Volume 1 Issue 4, December 2022
ISSN: 2810-9635 (Online)

Materials Science in Additive Manufacturing

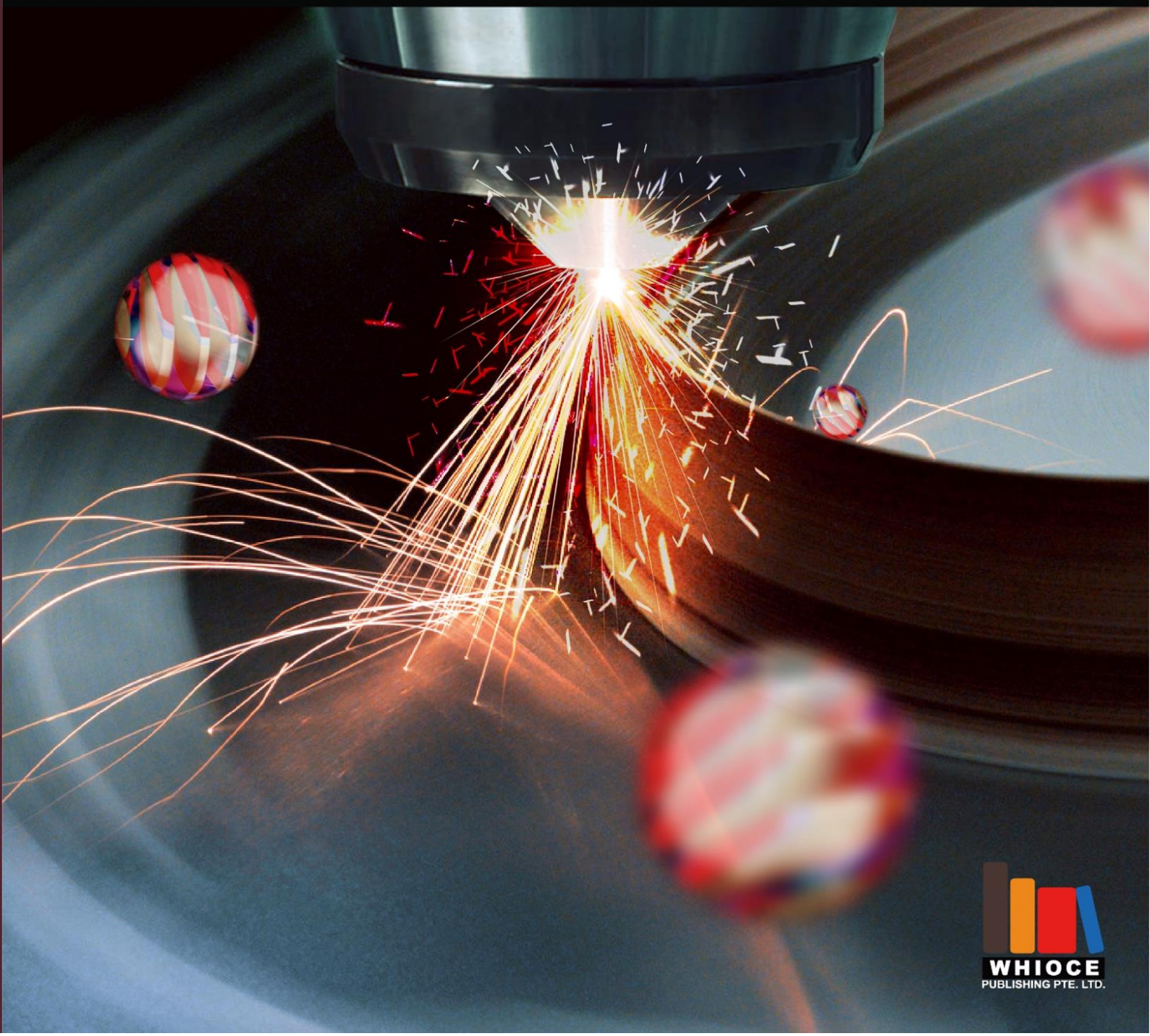

WHIOCE PUBLISHING PTE. LTD.

Materials Science in Additive Manufacturing

Online ISSN: 2810-9635

Materials Science in Additive Manufacturing aims to bridge the cutting-edge research between additive manufacturing and the entire spectrum of materials science. The journal covers all applied and fundamentals of processing, synthesis, structure, composition, properties and performance of materials designed or manipulated for additive manufacturing. The journal covers a wide scope of innovative techniques, processes, methods, and applications.

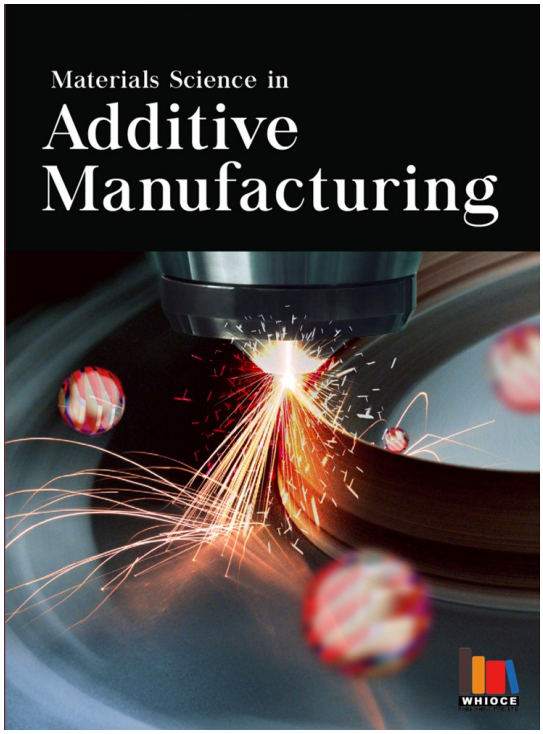

Scan to access website:

Scan to submit papers:

About Whioce Publishing

Whioce Publishing is a publishing company based in Singapore. We have in our portfolio a range of high-quality, open-access, peer-reviewed journals and books.

Contact Us

Managing Editor
Ian Wong
msam.editor@whioce.com

Whioce Publishing
8 Burn Road, #15-03 Trivex, Singapore 369977.

Editorial Office of *Materials Science in Additive Manufacturing*
30-2, Jalan BS 1/2, Olive Hill Business Park, 43300 Seri Kembangan, Selangor. Malaysia.

Volume 1 Issue 4 • December 2022
ISSN 2810-9635 (online)

MATERIALS SCIENCE IN ADDITIVE MANUFACTURING

Editor-in-Chief

Chee Kai Chua

Singapore University of Technology and Design, Singapore

WHIOCE PUBLISHING PTE. LTD.

MATERIALS SCIENCE IN ADDITIVE MANUFACTURING

ISSN: 2810-9635 (online)

Editorial and Production Credits

Publisher – Whioce Publishing
Managing Editor – Ian Wong
Editorial Assistant – Flora Kang
Production Editor – Ian Wong
Journal Development Editor – Felicia Wang
Article Layout and Typeset: Sinjore Technologies (India)
Cover Design: BUTTON GRAPHIC DESIGN STUDIO (Malaysia)

For all advertising queries, contact info@whioce.com.

Supplementary file

Supplementary files of articles can be obtained at https://accscience.com/journal/MSAM/1/4.

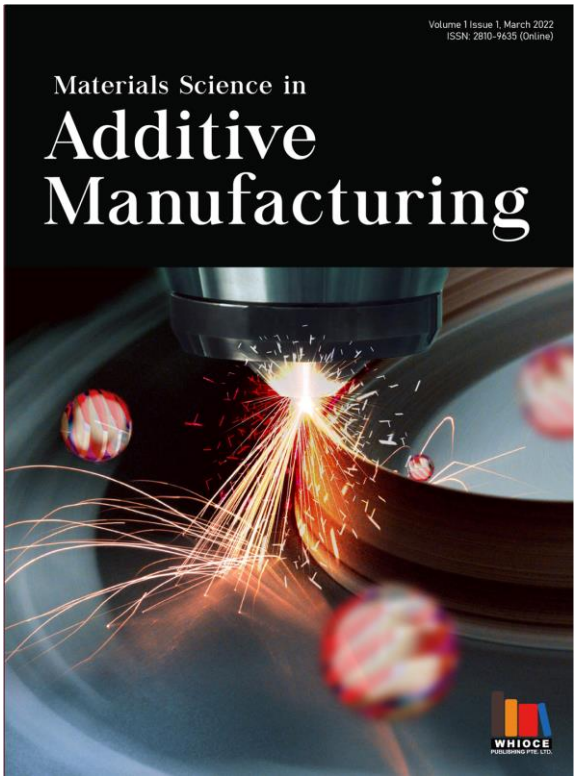

About the Cover

Directed energy deposition in progress

Disclaimer

Whioce Publishing is not liable to the statements, perspectives, and opinions contained in the publications. The appearance of advertisements in the journal shall not be construed as a warranty, endorsement, or approval of the products or services advertised and/or the safety thereof. Whioce Publishing disclaims responsibility for any injury to persons or property resulting from any ideas or products referred to in the publications or advertisements. Whioce Publishing remains neutral with regard to jurisdictional claims in published maps and institutional affiliations.

Materials Science in Additive Manufacturing

Editorial Board

December 2022 | Volume 1 | Issue 4 |

Materials Science in Additive Manufacturing

https://msam.whioce.com/index.php/MSAM/index

CONTENTS

1 **Influence of Y_2O_3 reinforcement particles during heat treatment of IN718 composite produced by laser powder bed fusion** *ORIGINAL RESEARCH ARTICLE*
Duy Nghia Luu, Wei Zhou, Sharon Mui Ling Nai
https://doi.org/10.18063/msam.v1i4.25

2 **Process optimization and mechanical property investigation of Inconel 718 manufactured by selective electron beam melting** *ORIGINAL RESEARCH ARTICLE*
Heng Dong, Feng Liu, Lin Ye, Xiaoqiong Ouyang, Qiangbing Wang, Li Wang, Lan Huang, Liming Tan, Xiaochao Jin, Yong Liu
https://doi.org/10.18063/msam.v1i4.23

3 **Experimental and numerical studies on the acoustic performance of simple cubic structure lattices fabricated by digital light processing** *ORIGINAL RESEARCH ARTICLE*
Zhejie Lai, Miao Zhao, Chong Heng Lim, Jun Wei Chua
https://doi.org/10.18063/msam.v1i4.22

4 **Laser additive manufacturing of magnesium alloys and its biomedical applications** *REVIEW ARTICLE*
Chuyi Liu, Chengrong Ling, Cheng Chen, Dongsheng Wang, Youwen Yang, Deqiao Xie, Cijun Shuai
https://doi.org/10.18063/msam.v1i4.24

5 **A survey of additive manufacturing reviews** *REVIEW ARTICLE*
Xiaoya Zhai, Liuchao Jin, Jingchao Jiang
https://doi.org/10.18063/msam.v1i4.21

Materials Science in Additive Manufacturing

ORIGINAL RESEARCH ARTICLE

Influence of Y_2O_3 reinforcement particles during heat treatment of IN718 composite produced by laser powder bed fusion

Duy Nghia Luu[1], Wei Zhou[1,2]*, Sharon Mui Ling Nai[3]*

[1]School of Mechanical and Aerospace Engineering, Nanyang Technological University, 50 Nanyang Avenue, Singapore 639798, Singapore

[2]Singapore Centre for 3D Printing, School of Mechanical and Aerospace Engineering, Nanyang Technological University, 50 Nanyang Avenue, Singapore 639798, Singapore

[3]Singapore Institute of Manufacturing Technology (SIMTech), Agency for Science, Technology and Research (A*STAR), Additive Manufacturing Division, 5 Cleantech Loop, CleanTech Two Block B, Singapore 636732, Singapore

Abstract

A metal matrix composite with Inconel 718 as the base metal and yttrium oxide (Y_2O_3) as the reinforcement particles was fabricated by the laser powder bed fusion technology. This paper presents a comprehensive study on the influence of the Y_2O_3 reinforcement particles on the microstructures and mechanical properties of the heat-treated printed composite. Complex precipitates formation between the Y_2O_3nanoparticles and the carbonitride precipitates were shown. The complex precipitates separated into individual Y_2O_3 and titanium nitride (TiN) nanoparticles after heat treatment. Nano-sized Y-Ti-O precipitates were observed after solutionization due to the release of supersaturated Y in the metal matrix. Grain refinement was also observed in the heat-treated composites due to the high number of nano-sized precipitates. After solutionizing and aging, the grain size of the Y_2O_3-reinforced sample is 28.2% and 33.9% smaller, respectively, than that of the monolithic Inconel 718 sample. This effectively reduced the segregation of Nbat the grain boundaries and thus, γ′ and γ′′ precipitates were distributed in the metal matrix more homogeneously. Combined with the increased Orowan strengthening from a significantly higher number of nano-sized precipitates and grain boundary strengthening, the composite achieved higher yield strength, and ultimate tensile strength (1099.3 MPa and 1385.5 MPa, respectively) than those of the monolithic Inconel 718 (1015.5 MPa and 1284.3 MPa, respectively).

Keywords: Laser powder bed fusion; Additive manufacturing; Inconel 718; Y_2O_3 reinforcement; Heat treatment

***Corresponding authors:**
Wei Zhou
(mwzhou@ntu.edu.sg)
Sharon Mui Ling Nai
(mlnai@simtech.a-star.edu.sg)

Citation: Luu DN, Zhou W, Nai SML, 2022, Influence of Y_2O_3 reinforcement particles during heat treatment of IN718 composite produced by laser powder bed fusion. *Mater Sci Add Manuf,* 1(4): 25.
https://doi.org/10.18063/msam.v1i4.25

Received: October 10, 2022

Accepted: December 7, 2022

Published Online: December 22, 2022

1. Introduction

Fabricating metalmatrix composites (MMCs) with discontinuous reinforcements have beensteadily gaining interest over the years to improve existing materials and tackle new challenges. The MMCs usually have high modulus, strength, and stiffness, good fatigue properties, and high-temperature performance[1,2]. This is made possible due to the exceptional ability of the MMCs to combine the ductile and tough characteristics of

metals with the wear resistance, stiffness, and rigidness of ceramic materials. One of the prime material candidates to be used as the base metal is Inconel 718 (IN718) due to its excellent strength, ductility, and creep resistance at high temperatures[3]. Thus, the material is in high demand in the aerospace industry, presenting the need to further enhance its mechanical properties to widen its industry applications.

The traditional manufacturing methods for MMCs can be categorized into either solid-state or liquid-state methods[4]. For solid-state methods, the alloying of individual components takes place by repeatedly welding and fracturing the raw powder, which takes a very long time to complete. Friction stir processing (FSP) is another promising solid-state method that is able to produce MMCs. However, this method is primarily used to produce surface composites[5,6] and requires extensive process optimization and simulation to understand the effects of those parameters on the homogeneity of the composite[7]. Liquid-state methods usually involve different ways of introducing the reinforcement particles into the liquid melt[8]. This can be done by simply adding the reinforcement particles into a molten metal followed by mechanical agitation such as stirring. The primary problems are to ensure the homogeneous dispersion of the particles within the liquid melt as well as to ensure good wettability between the reinforcement and the matrix, which can be challenging[9]. On the other hand, the liquid melt can also be infiltrated into a ceramic preform to manufacture MMCs[10]. However, the properties of the MMCs manufactured by this method depend on the characteristics of the preform, which requires monitoring the size, shape, and interconnectedness of the pores or cells. As such, it is often substantially complex and expensive to design and manufacture the preform[11].

It should also be noted that the final product from the traditional manufacturing methods usually has simple forms such as tube, sheet, or ingot. Due to the high strength of IN718, it is difficult and costly to produce complex parts from those simple forms. Fortunately, due to the excellent weldability of IN718, the material and its composites are suitable to be fabricated by additive manufacturing (AM), a method that has revolutionized the traditional manufacturing industry. In this study, laser powder bed fusion (LPBF) is utilized to fabricate IN718 MMCs to overcome the drawbacks of traditional manufacturing methods. For instance, the technology is well known for its ability to produce near-net shape products. Furthermore, homogeneously dispersed reinforcement particles could be achieved using the technology by making use of its short melt-pool lifetime and high cooling rate. However, despite the advantages of using AM for IN718 MMCs, the development of printed IN718 MMCs is quite recent and only limited to a few groups of researchers[12-15].

One of the most commonly used types of reinforcements is oxides due to several of their outstanding properties[16]. This paper presents a comprehensive microstructural and mechanical property study of the IN718 MMC reinforced with yttrium oxide (Y_2O_3). The study was done in heat-treated MMC because IN718 must be heat treated to make use of its precipitation hardening characteristic. Thus, it is of utmost importance to understand the effect of the reinforcement particles on the different phases in IN718. Unfortunately, studies regarding the heat-treated IN718/Y_2O_3 material system have not been presented. There are only a handful of studies related to the heat treatment of oxide-reinforced Ni-based alloys[17,18] while most of the studies are for Fe-based alloys[19–21]. As such, this study will provide a comprehensive comparison of the microstructures and mechanical properties between the Y_2O_3-reinforced IN718 Ni-based alloys and the monolithic IN718 in the as-printed state as well as after each stage of the heat treatment. This study also showed the importance of heat treatment to the Y_2O_3-reinforced IN718 as the value added of the Y_2O_3 nanoparticles could not be showcased in the as-printed state.

2. Methods and materials

2.1. Powder preparation and LPBF process

Commercially available IN718 powder (20 – 63 μm) was purchased from Höganäs. The chemical compositions of the powder are listed in Table 1. The scanning electron microscopy (SEM) images of the IN718 and nano-Y_2O_3 (30 – 100 nm) powder are shown in Figure 1A and B, respectively.

The reinforcement particles were mixed with the IN718 powder using the Inversina 20L tumbler mixer for 8 h. The amount of reinforcement particles was 1 wt.%. Steel balls were added with a 1 – 3, ball-to-powder, ratio during mixing to enhance the dispersion homogeneity. A uniform mixture of powder was obtained as shown in Figure 1C. It can be seen that the Y_2O_3 particles were able to attach themselves to the surface of the IN718 powder particles.

The time needed for a homogeneous powder mixture was first determined visually using a camera by observing the mixture after 2, 4, 6, and 8 h of mixing as shown in Figure 2A-D. It was observed that the white Y_2O_3 nanoparticles were still agglomerated after 2 h of mixing. As the mixing time increased, the nanoparticles were distributed more homogeneously in the mixture, and they were no longer in large clusters after 6 h and were fully

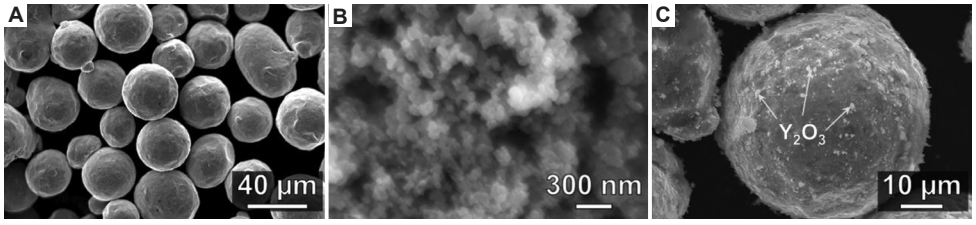

Figure 1. Scanning electron microscopy (SEM) images of IN718 (A) and nano-Y_2O_3 (B). SEM image of IN718 mixed with nano-Y_2O_3 (C).

Table 1.Chemical compositions (wt.%) of IN718 powder

Ti	Nb	Mo	Cr	C	B	P	Ni	Fe	O	N	Si	S	Mn	Al	Co
0.73	5.33	3.03	18.6	0.01	0.014	0.002	54	Bal.	0.03	0.16	0.51	0.002	0.18	0.39	0.02

blended with the IN718 powder after 8 h. The resultant homogeneously mixed powder was then examined under SEM. The white Y_2O_3 nanoparticles were observed on the surface of all the IN718 powder particles as shown in Figure 2E. The chemical compositions of the white nanoparticles at 15 distinct locations were analyzed using energy dispersive X-ray (EDX) and the average wt.% of the major elements is listed in Table 2. The presence of Y and O was detected, further confirming the nanoparticles to be Y_2O_3.

The samples were printed using the ProX300 machine (3D Systems) using 50 µm hatch spacing and 40 µm layer thickness. As referenced from our previous works[22,23], after extensive process parameters optimization, the optimal laser power and scan speed are listed in Table 3. A fiber laser, with a 1070 nm wavelength and 75 µm spot size, was used. An island printing strategy was employed, with each island being a hexagon with a 25000 µm radius. The scanning tracks were rotated 90° for each consecutive layer.

2.2. Heat treatment profiles

All the samples were solutionized and aged in a vacuum tube furnace (Lenton, UK). The solutionizing treatment for tensile specimens was carried out at 1075°C at a heating up rate of 15°C/min, held for 1 h, followed by furnace cooling at a rate of 10°C/min. The aging treatment of the samples was also carried out in a vacuum tube furnace at a heating rate of 10°C/min to 720°C, held for 8 h, followed by furnace cooling at a rate of 10°C/min to 620°C, held for another 8 h, followed by furnace cooling at a rate of 10°C/min to room temperature. This aging treatment profile is similar to the one used in other studies[24-27].

However, to understand the reasons behind the differences in the mechanical properties of the samples after aging treatment, all the samples were also subjected to solutionizing treatment at 1275°C using the same heating

Table 2. Chemical compositions (wt.%) of the white nanoparticles in the powder mixture after 8 h of mixing

O	Cr	Fe	Ni	Y
5.46±1.54	19.06±1.08	17.61±0.79	47.95±1.87	9.91±1.51

Table 3. Laser power and scan speed for the LPBF process of IN718 samples

Reinforcement	Laser power (W)	Scan speed (mm/s)
Nil	238	1000
1 wt.% Y_2O_3	260	1000

rate, holding time, and cooling rate as the solutionizing treatment at 1075°C before aging. The percentage of the area occupied by the γ′ and γ″ precipitates is calculated using the ImageJ software. The samples are labeled as shown in Table 4. The heat treatment profiles are shown in Figure 3.

2.3. Material characterization

The samples were ground and polished along the building direction using the typical procedure. Microstructural analysis was carried out after the samples were etched with Kalling's No. 2 reagent. The SEM of the$Y_2O_{3\ sample}$ was prepared by dispersing the powder in ethanol and drop-cast into a Si substrate. Imaging and energy dispersive X-ray (EDX) analyses were carried out using the field emission scanning electron microscope (FESEM) JEOL-JSM-7600F and the Ultra Plus FESEM from Carl Zeiss FESEM machines. The printed samples were wire-cut into tensile coupons with dimensions with a gauge length of 14 mmas shown in Figure 4. Tensile testing was carried out using the INSTRON 5982 machine, at a strain rate of 0.01/sat room temperature. The tensile direction was perpendicular to the building direction. The chosen dimensions and processing parameters of the tensile coupons would result

in comparable or better mechanical properties than those reported by other literature as shown in our previous study Luu *et al.*[22].

The grain size was calculated using the line intersection method. The width and length of the grains would then be calculated by dividing the length of the line by its number of intersections. The diameter of the grain would then be equal to the diameter of the circle that has the same area as the width × length.

The size distributions of the precipitates were measured using the ImageJ software. Multiple SEM images were taken and the size of the precipitates in the images was measured. The volume fraction, f_p, of the precipitates in the samples was measured using Equation I.

$$f_p = \frac{\frac{4}{3}\pi\left(\frac{d_p}{2}\right)^3 N_p}{Ad_p} \quad \text{(I)}$$

Where d_p is the mean diameter of the precipitates, N_p is the number of precipitates in a given area, and A is the area of the given area.

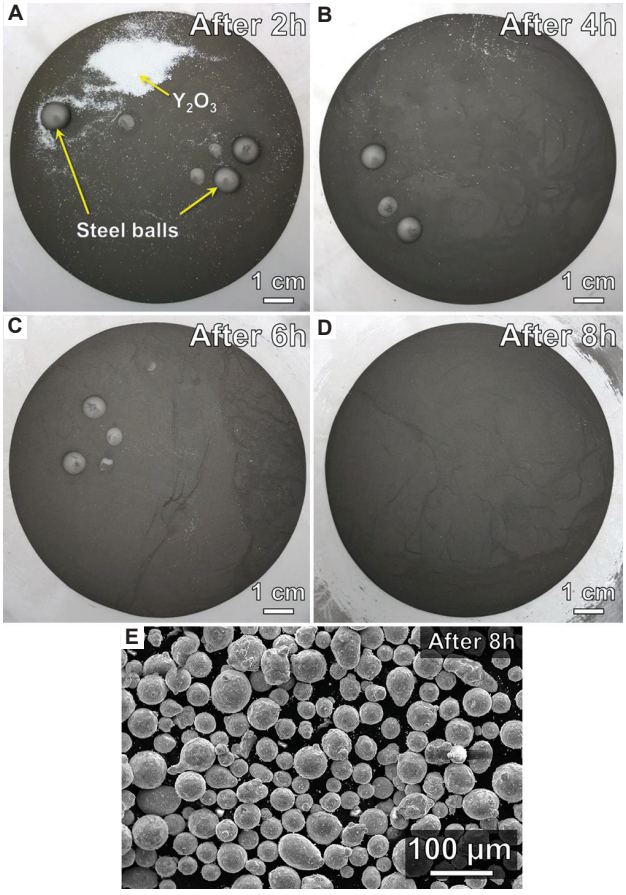

Figure 2. Photos of the powder mixture after 2(A), 4(B), 6(C), and 8(D) hours of mixing. SEM image of the powder mixture after 8 h of mixing (E).

3. Results and discussion

3.1. Microstructures of as-printed samples

SEM images comparing the microstructures of as-printed samples are shown in Figure 5A and B. The microstructures of both samples consist of a white color phase with a

Table 4. Labeling of IN718 and the composite samples

Sample ID	Heat treatment	Reinforcement
AP-0	As-printed	Nil
AP-Y		Y_2O_3
1075-0	Solutionized at 1075°C	Nil
1075-Y		Y_2O_3
1075A-0	Solutionized at 1075°C+Aged	Nil
1075A-Y		Y_2O_3
1275A-0	Solutionized at 1275°C+Aged	Nil
1275A-Y		Y_2O_3

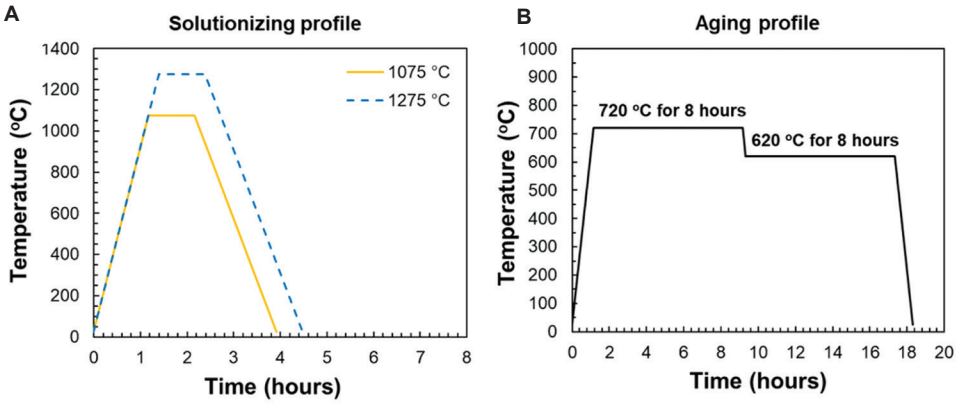

Figure 3. Solutionizing (A) and aging (B) profiles.

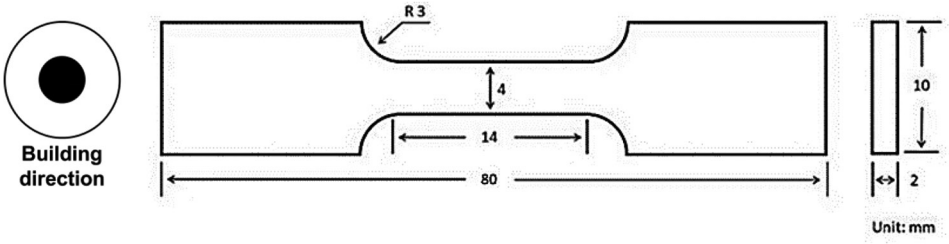

Figure 4. Dimensions of the tensile coupons used. The building direction is pointing out of the page.

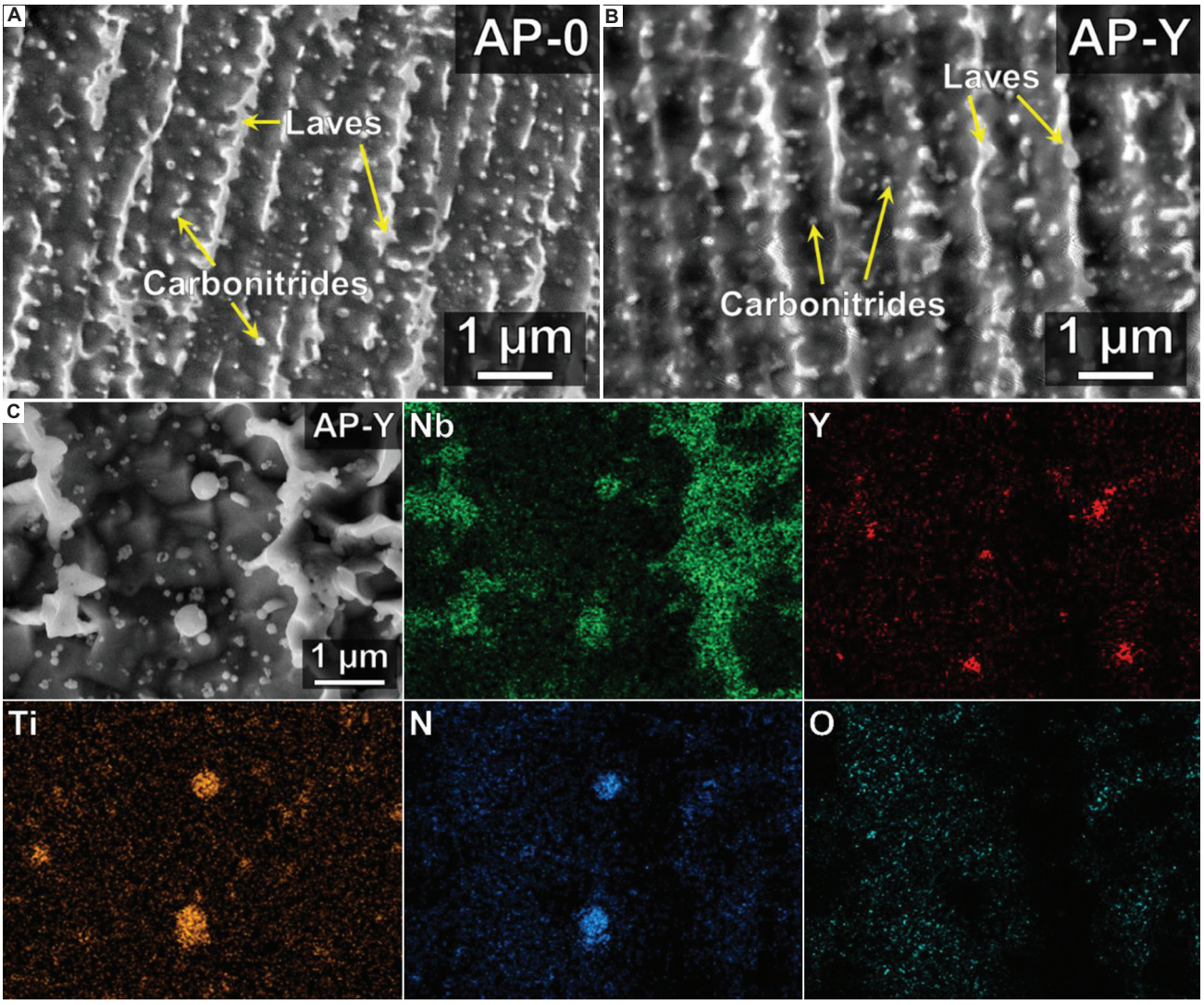

Figure 5. Scanning electron microscopy images of the microstructures of samples AP-0 (A) and AP-Y (B). EDX analysis of the phases in sample AP-Y (C).

long chain morphology and several nano-sized particles distributed throughout the microstructures. EDX analysis of sample AP-Y (Figure 5C) shows that the long chain phase consists of primarily Nb and Mo. On the other hand, the nano-sized particles are made up of primarily Ti, N, and Nb.

According to the phase transformation route during solidification of IN718, which is L ⇒ L + γ ⇒ L + γ + NbC ⇒ L + γ + NbC + Laves[28], the Laves phase is the last phase to form when there is a high concentration of Nb and Mo in the liquid melt due to the low solubility limit of these elements in IN718[29]. Due to the long chain phase

having high concentrations of Nb and Mo, it is identified to be Laves phase. This phase is usually located in the interdendritic region after solidification[30]. Consequently, the nano-sized particles are identified to be NbC carbide precipitates. Even though element C is difficult to index, the identification of the phase is further supported by the presence of elements Ti and N in the precipitates. This is because the pre-existing TiN in the melt often acts as nucleation sites for the NbC precipitates due to favorable lattice match[31]. Due to the presence of both C and N in the precipitates, they are also referred to as carbonitride precipitates. Moreover, Figure 5C shows that the Y_2O_3 nanoparticles are segregated at the interdendritic regions where the Laves phase is usually located.

The distributions of particle size in all as-printed samples are shown in Figure 6. It can be seen that the addition of the reinforcement particles increases the size of the precipitates in the IN718 matrix, which reflects the results shown in our previous study that Y_2O_3 nanoparticles have a high tendency to combine with the existing carbonitride precipitates and increase in size[23]. The majority of the precipitates in sample AP-0 are in the range of 45 – 65 nm in diameter while it is 55 – 95 nm in diameter in sample AP-Y as shown in Figure 6A. Furthermore, the cumulative percentage graph of sample AP-0 is always above that of sample AP-Y as shown in Figure 6B. This shows that at any particular particle diameter size, there is a higher proportion of precipitates in sample AP-0 that are smaller than and equal to that diameter size. The specific d_{10}, d_{50}, d_{90}, and the mean particle diameter, d_p, values of the size of the precipitates are listed in Table 5.

Table 5. Comparison of d_{10}, d_{50}, d_{90}, and d_p values of the size of the precipitates in the as-printed samples

Sample ID	d_{10} (nm)	d_{50} (nm)	D_{90} (nm)	d_p (nm)
AP-0	37.2	51.5	84.7	62.5
AP-Y	50.6	72.3	114.9	83.7

3.2. Microstructures of printed samples after 1075°C solutionized and aged

Both monolithic and Y_2O_3-reinforced samples solutionized at 1075°C are deeply etched to reveal their microstructures as shown in Figure 7. It can be seen that the grain structures of both samples consist of mostly columnar grains with some equiaxed grains distributed throughout, both after solutionizing and after aging treatments. The optical micrographs also reveal that the grains' interior (in between the black dashed lines that indicate the grain boundaries) of the samples after aging (Figure 7B and D) is darker than that of the samples before aging (Figure 7A and C).

SEM analysis in Figure 8 shows that the grains' interior consists of numerous precipitates either arranged in straight lines or randomly distributed. Since a higher number of these precipitates are observed in both samples after aging, the darker grains' interior observed in Figure 7 corresponds to this increase in precipitate formation. SEM analysis reveals that the Laves phase at the grain boundaries (as indicated in Figure 8) has a discrete and blocky morphology. This phenomenon is observed in both the monolithic IN718 sample (Figure 8A) and the composite (Figure 8C). However, the morphology of the Laves phase does not change significantly after aging as shown in (Figure 8B and D). It should be noted that the grain boundaries Laves phase in both samples 1075-0 and 1075A-0 appears to be larger and more concentrated compared to samples 1075-Y and 1075A-Y.

A closer look using SEM shows that the interdendritic Laves phase transforms from a straight, long-chain, and continuous morphology (Figure 5A and B) to also a discrete and blocky morphology after solutionizing treatment, similar to the one located at grain boundaries but smaller in size. The microstructures of both samples1075-0 and 1075-Y (Figure 9) consist of mostly Laves phase and δ phase. The presence of the δ phase after solutionizing treatment is due to the following reasons. First, as Laves

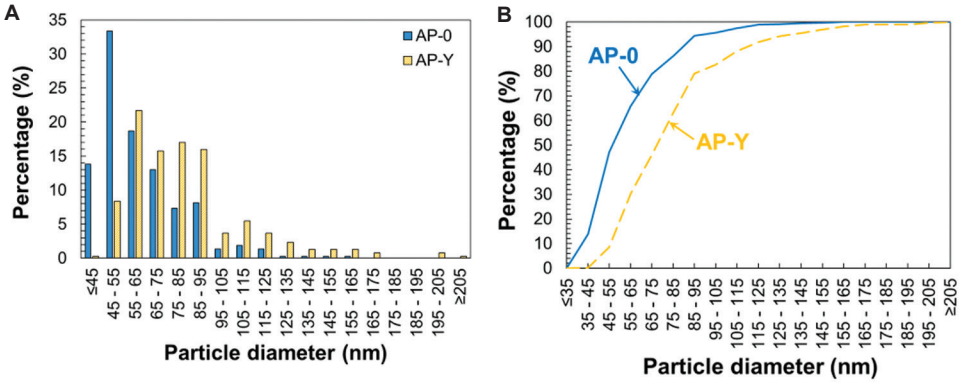

Figure 6. The size distribution (A) and the cumulative percentage (B) of the precipitates in the as-printed samples.

phase dissolves during the heat treatment, the amount of Nb available in the matrix increases. This provides extra material for the formation ofδ phase, which has a chemical formula of Ni_3Nb. Second, according to the TTT diagram of IN718, the δ phase starts to form at approximately 980°C, which is below the solutionizing temperature.

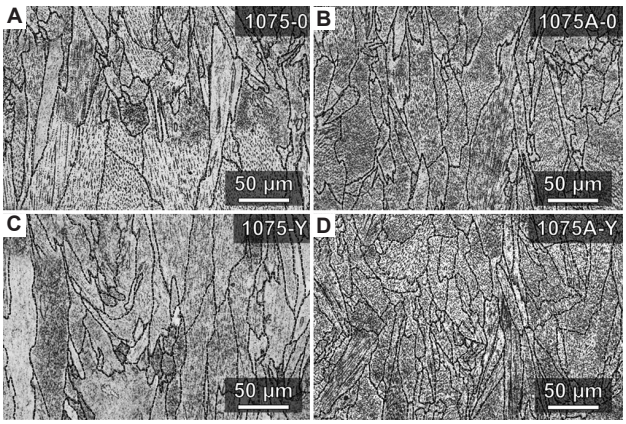

Figure 7. Optical micrographs of etched samples 1075-0 (A), 1075A-0 (B), 1075-Y (C), and 1075A-Y (D). The black dashed lines indicate the grain boundaries.

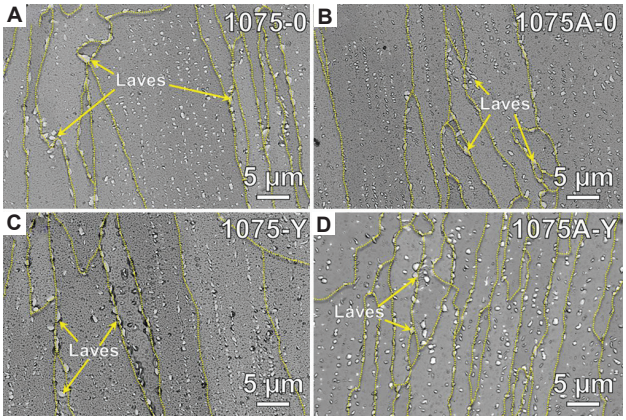

Figure 8. Scanning electron microscopy images showing the microstructures of samples 1075-0 (A), 1075A-0 (B), 1075-Y (C), and 1075A-Y (D). The yellow dashed lines indicate the grain boundaries.

Due to the sample being furnace-cooled at the end of the solutionizing treatment, this provides extra time for the δ phase to form.

Further analysis of sample 1075-Y shows that multiple nano-sized precipitates can be observed near or embedded inside the Laves phase particles as shown in Figure 10A. Extensive analysis by line scan EDX shows that the compositions of the precipitates are a combination of Nb, Ti, Y, N, and O elements. The precipitates that are embedded in the Laves phase particles have 1 common trait, which is the presence of Ti and N in all of them, as shown in Region 2 in Figure 10B and Region 1 in Figure 10D. On the other hand, Y may or may not be detected in those precipitates as shown in the presence of Y peak in Region 1 in Figure 10D but not in Region 2 in Figure 10B. However, it can also be seen that O can be detected in both cases of embedded precipitates, suggesting that Y could also be present but only in a minute amount. Most of the time, the precipitates that exist outside of the Laves phase have both Y and Ti as well as O, while N is not detected. This can be observed in Region 1 in Figure 10B and Region 2 in Figure 10D. Due to the lack of element N, these precipitates that are observed in sample 1075-Y are the Y-Ti-O complex precipitates that were reported in other literature[32,33].

However, the precipitate formation that is similar to the observed precipitates in sample AP-Y can still be found in sample 1075-Y as shown in Region 3 in Figure 10D. In addition, large Y_2O_3 particles and large TiN particles can be detected next to each other as shown in Regions 1 and 2 in Figure 10C. As such, all these observations further support the conclusion made previously in which Y_2O_3 nanoparticles have a high tendency to combine with other elements in the IN718 to form complex precipitates.

After the IN718/Y_2O_3 composite has been solutionized, two additional observations can be made. First, the presence of embedded precipitates within the Laves phase suggests that reprecipitation of Laves phase during cooling has occurred and trapped other precipitates within

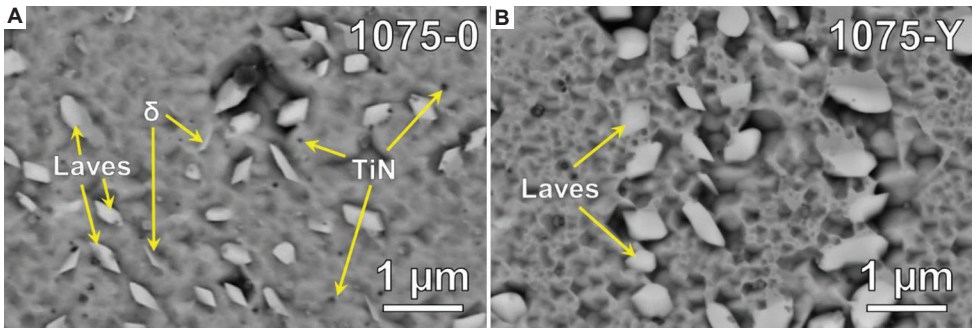

Figure 9. Scanning electron microscopy images showing the microstructures of samples 1075-0 (A) and 1075-Y (B).

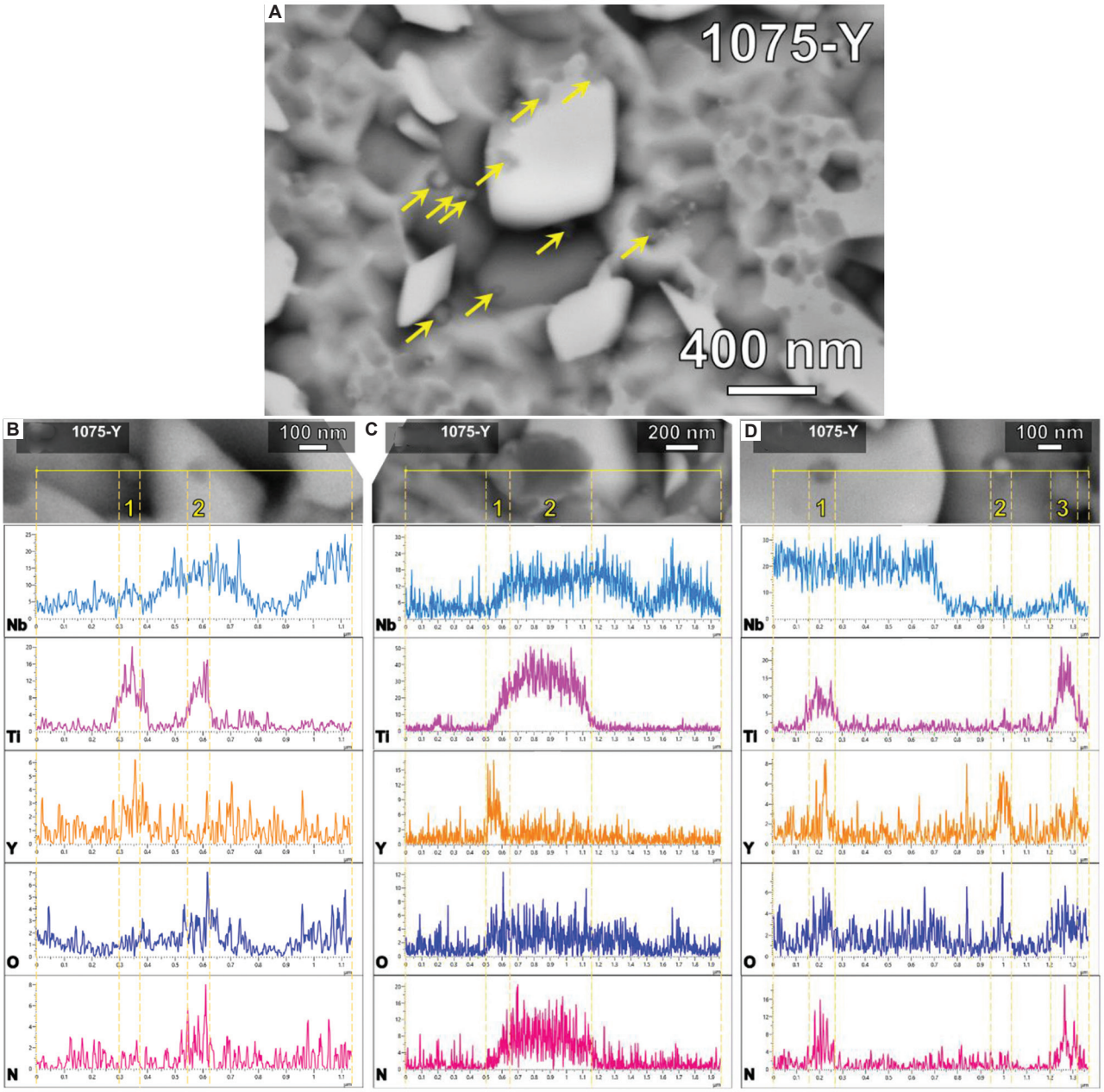

Figure 10. Scanning electron microscopy image showing precipitates (yellow arrows) present in the microstructure of sample 1075-Y (A). Line scan EDX (B–D) analysis showing the variation of chemical compositions (wt.%) across different precipitates in sample 1075-Y.

them. As Y_2O_3 has a high tendency to combine with Ti, these elements are often found together in the Laves phase. Second, the appearance of numerous nano-sized Y-Ti-O precipitates with diameters <100 nm suggests that those precipitates were formed during the solutionizing treatment. Shi *et al.*[34] observed a similar phenomenon in heat-treated Zr-containing ODS-FeCrAl in which nano-sized Y-Al-O precipitates were formed during solutionizing treatment. The authors attributed this to the supersaturated state of Y in the matrix in the as-printed sample. When the as-printed sample is subjected to solutionizing treatment, the element Y is released, forming the observed nano-sized precipitates. Moreover, the absence of N in the complex precipitates when they are not embedded inside the Laves phase particle prevents the NbC shell from forming properly due to the lack of a favorable TiN nucleation site. Thus, the size of the complex precipitate is significantly smaller.

The grain sizes of the printed samples after different stages of heat treatment are listed in Table 6. It can be seen that the grain size of the as-printed IN718/Y_2O_3 composite sample is slightly larger than that of the as-printed monolithic IN718 sample. The limited grain refinement effect in the as-printed IN718/Y_2O_3 composite sample is the result of the low wettability between the Y_2O_3 nanoparticles and the IN718 matrix, which makes them not effective as nucleation sites[35]. However, after solutionizing and aging, there is an increase in equiaxed grains formation in the Y_2O_3-reinforced sample after heat treatment as shown in Figure 7C and D. Due to this, the average grain size of the Y_2O_3-reinforced sample decreases from 19.1 ± 3.1 (before heat treatment) to 17.1 ± 7.2 μm (after solutionizing) to 12.5 ± 4.1 μm (after aging). On the other hand, the grain size of the monolithic sample increases from 18.9 ± 1.9 μm to 23.8 ± 8.2 μm after solutionizing and decreases to 18.9 ± 4.4 μm after aging. It should be noted that both samples achieve grain refinement after aging but the effect is stronger in the Y_2O_3-reinforced sample as the grain size decreases by 26.9% compared to 20.6% in the monolithic sample. This suggests that both the existing carbonitride precipitates and the newly form nano-sized Y-Ti-O precipitates contribute to the grain refinement. These precipitates aid the grain recrystallization at high temperature by acting as nucleation centers. As such, due to the absence of the Y-Ti-O precipitates in the monolithic samples, the carbonitride precipitates alone are not enough to suppress grain growth due to the high temperature[36] during solutionizing treatment. This results in a bigger grain size in the solutionized monolithic sample.

Table 6. Grain sizes (μm) of the printed samples at different stages of heat treatment

Reinforcement	As-printed	1075°C solutionized	1075°C solutionized+aged
Nil	18.9±1.9	23.8±8.2	18.9±4.4
1 wt.% Y_2O_3	19.1±3.1	17.1±7.2	12.5±4.1

3.3. Mechanical properties of heat-treated IN718 composites

A comparison of the mechanical properties between monolithic samples and Y_2O_3-reinforced samples is shown in Figure 11A. All samples were fabricated using their

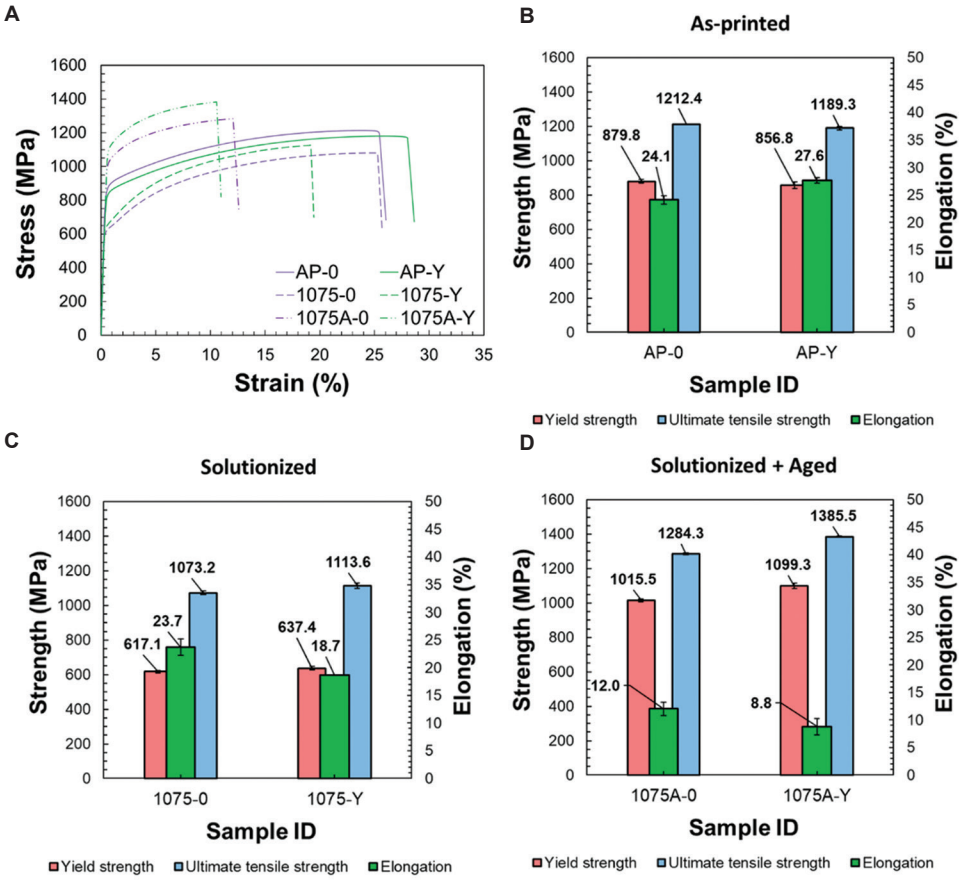

Figure 11. Stress-strain curves comparing monolithic samples with Y_2O_3-reinforced samples (A). Tensile properties of as-printed (B), after solutionized (C), and after solutionized + aged (D) Y_2O_3-reinforced samples in comparison with monolithic samples.

optimized parameters and solutionized at 1075°C so that the best mechanical properties could be obtained. This is because at this temperature, the Laves phase is dissolved almost completely and the remaining Laves phase has a particulate morphology instead of a long chain morphology. Furthermore, the amount of δ phase precipitates in the microstructure is kept relatively low as this phase also has several negative impacts on the mechanical properties[37]. The strength and elongation values after each heat treatment stage are shown in Figure 11B to D.

It can be seen that sample AP-Y has higher elongation than that of sample AP-0 (27.6% compared to 24.1%) while the strength of sample AP-Y (yield strength [YS] and ultimate tensile strength [UTS] are 856.8 and 1189.3 MPa, respectively) is slightly lower than that of sample AP-0 (YS and UTS are 879.8 and 1212.4 MPa, respectively). After being solutionized, a significant decrease in strength is observed in the monolithic sample in which YS and UTS both decrease by 29.9% and 11.5%, respectively. However, the extent of the reductions in YS and UTS in the Y_2O_3-reinforced sample is lesser, which are 25.6% and 6.4%, respectively. After both solutionizing and aging treatments are done, the strength of the Y_2O_3-reinforced sample (YS and UTS are 1099.3 and 1385.5 MPa, respectively) continues to be higher than that of the monolithic sample (YS and UTS are 1015.5 and 1284.3 MPa, respectively).

By considering the contribution of different strengthening factors, the minor differences in the strength of the as-printed samples can be explained as follows. First, as nanoscale carbonitride precipitates are also present in the base material, it is reasonable to also include their Orowan strengthening contribution. The contribution of Orowan strengthening, σ_{Orowan}, is calculated using Equation II[38].

$$\sigma_{Orowan} = \frac{0.538Gb\sqrt{f_p}}{d_p}\ln\left(\frac{d_p}{2b}\right) \quad \text{(II)}$$

Where G is the shear modulus and b is the Burgers vector. For IN718, G = 63 Gpa[39] and $b = \frac{a}{2}110$ [40], where a is the lattice parameter of IN718, which a = 0.359 nm[41]. Thus, b = 0.2539 nm.

However, the increase in strength due to Orowan strengthening in sample AP-Y is calculated to be only 12.34 MPa higher than that of sample AP-0.As such, due to the presence of the carbonitride precipitates in sample AP-0, the contribution of Orowan strengthening in sample AP-Y is only significant if it is noticeably higher than the contribution of the carbonitride precipitates. However, it can be seen that the addition of reinforcement particles increases the size of the carbonitride precipitates. Thus, the increase in Orowan strengthening is small.

Second, the strength of the as-printed samples is also affected by the grain size through grain boundary strengthening or the Hall-Petch strengthening effect. However, due to the small difference in the grain size of samples AP-0 and AP-Y as shown in Table 6, the difference in the Hall-Petch strengthening effect is also negligible.

In addition to the stated strengthening mechanisms, other mechanisms such as the coefficient of thermal expansion (CTE) mismatch strengthening mechanism or the load transfer mechanism can also strengthen the material. The CTE mismatch strengthening, $\Delta\sigma_{CTE}$, can be calculated using Equation III[42].

$$\Delta\sigma_{CTE} = kGb\sqrt{\frac{12" T(\alpha_m - \alpha_p)f_p}{bd_p(1-f_p)}} \quad \text{(III)}$$

Where k is a constant approximately equal to 1.25, ΔT is the difference between the processing and testing temperatures, α_m and α_p are the coefficient of thermal expansion of matrix and reinforcement particles, respectively. The theoretical volume fraction of the nanoparticles will be used for calculation. The processing temperature for LPBF can be taken to be 2100 K[43], thus ΔT = 2100 – 300 = 1800 K. Using the theoretical vol% of the added nano-Y_2O_3 particles, $d_{p(Y_2O_3)} = 65nm$, α_m = 13.1 × $10^{-6}K^{-1}$[44], and $\alpha_{p(Y_2O_3)} = 8.1\times10^{-6}K^{-1}$ [45], the contribution of $\Delta\alpha_{CTE}$ in sample AP-Y is calculated to be 207.85 MPa.

Thus, based on the calculated results, CTE mismatch is indeed one of the important strengthening mechanisms in the IN718/Y_2O_3 composite due to the significant increase in the sample strength. This is also verified by Wang *et al.*[42] in which the calculated contribution of CTE mismatch strengthening is the highest. However, it has been reported that the inclusion of CTE mismatch strengthening often overestimates the actual strength of the sample. As such, several papers agreed that the activation of CTE mismatch strengthening is questionable and thus could be negligible[46–50]. Furthermore, it has also been shown that CTE mismatch strengthening can only be significant when the reinforcement particles are above a certain size[51] and volume fraction[52]. The critical diameter, d_c can be calculated using Equation IV.

$$d_c = \frac{b}{\Delta\alpha\Delta T} \quad \text{(IV)}$$

In this case, the d_c of the nano-Y_2O_3 particles is calculated to be 91.4 nm. As the mean diameter of the Y_2O_3 nanoparticles is 65 nm, the majority of them are

below the critical diameter. In addition, due to the small volume fraction of the added nanoparticles, the fraction of the nanoparticles that can contribute to strengthening is also small.

Furthermore, the previously calculated results of the strengthening contribution are based on the CTE mismatch between the Y_2O_3 nanoparticles and the IN718 matrix. However, it has been pointed out that the nanoparticles have a high tendency to combine with the carbonitride shell to form a complex precipitate. As such, it would be more appropriate to compare the CTE mismatch between the Y_2O_3 nanoparticles and the carbonitride shell. Since the CTE of the shell is in the range of $6.65 \times 10^{-6}K^{-1}$ to $8.48 \times 10^{-6}K^{-1}$[53], which is much closer to that of the Y_2O_3 nanoparticles than IN718 is, the actual increase in strength is again expected to be small. Due to these reasons, the contribution of CTE mismatch strengthening in the IN718/Y_2O_3 composite will be omitted.

Finally, the load transfer mechanism, $\Delta\sigma_{load}$ can be calculated using Equation V[42,54].

$$\Delta\sigma_{load} = 0.5 f_p \sigma_m \quad \text{(V)}$$

Where σ_m is the yield strength of the matrix. It can be seen from Equation V that the contribution of the load transfer mechanism is expected to be small as the volume fraction, f_p, of the reinforcement particles is very small. Coupling with the 0.5 coefficient, the load transferring mechanism is believed to be not at play, which is also verified by Wang *et al.*[42]

Thus, it can be seen that the majority of the strengthening mechanisms do not result in a significant improvement in the strength of sample AP-Y. In fact, the strength of sample AP-Y is slightly lower than that of sample AP-0. This is because the theoretical calculation does not consider the agglomeration of the Y_2O_3 nanoparticles. This further supports the observations made in Section 3.1 in which there is a high concentration of Y_2O_3 in the interdendritic regions. As a result, this overestimated the strengthening contribution of the Orowan mechanism. Furthermore, several other factors could potentially overestimate the Orowan strengthening mechanism such as not all the particles being spherical and the mean particle diameter values being inaccurate to represent the entire size distribution. Thus, due to the similar grain sizes, the small volume fraction of reinforcement particles, and the presence of carbonitride precipitates in sample AP-0, the strengths of the as-printed samples only differ slightly.

However, in this study, the value added of the reinforcement particles in strengthening IN718 can only be realized after heat treatment as seen in Figure 11. A thorough quantitative analysis of the Orowan strengthening is challenging in heat-treated samples since there are numerous types of nano-sized precipitates (carbonitride precipitates, Y_2O_3 nanoparticles, Y-Ti-O nanoparticles, γ′ and γ′′ precipitates, and δ and blocky Laves phase) that each contributes to the strength of the material differently. Furthermore, the morphology of the majority of the precipitates is not spherical and their distribution in the matrix may not be homogeneous. Thus, these factors make quantifying the contribution of the precipitates to the strength of the material highly challenging. However, an appropriate qualitative analysis to explain the differences in the material's strength can still be carried out.

First, the number of nano-sized precipitates in the Y_2O_3-reinforced sample is expected to be higher than in the monolithic sample due to the formation of the Y-Ti-O precipitates after solutionizing treatment (Figure 10A). As such, these precipitates increase the strength of the IN718/Y_2O_3 composite after heat treatment. Furthermore, these precipitates also contribute to grain refinement after heat treatment since they act as nucleation centers for the recrystallization of grains at high temperatures and at the same time, suppress grain growth. Hence, this further enhances the material's strength through grain boundary strengthening.

Second, it is theorized that the difference in the Laves phase morphology at the grain boundaries between the Y_2O_3-reinforced samples and the monolithic samples as shown in Figure 8 also contributes to the difference in the mechanical properties. However, after solutionizing treatment at 1075°C,the microstructural changes resulting from additional aging treatment are not obvious. Thus, it is challenging to accurately characterize the differences. As such, to accurately characterize the differences in the microstructures that arise from aging treatment and to understand the reasons behind any changes in mechanical properties after aging treatment, both samples are solutionized at 1275°C before aging. This is because when the samples are solutionized at this temperature, the diffusion of different alloying elements is significantly enhanced[55]. As such, the movements of the alloying elements during heat treatment can be visualized.

SEM analysis of sample 1275A-Y shows that the addition of Y_2O_3 has resulted in grain refinement. This is evident in Figure 12 showing a significantly higher number of smaller equiaxed grains in sample 1275A-Y compared to sample 1275A-O. It is also observed that the segregated regions (red color) are thinner in sample 1275A-Y than those in sample 1275A-0. This further reinforced the phenomenon in which the addition of Y_2O_3 reduces the segregation at the grain boundaries as shown in Figure 8.

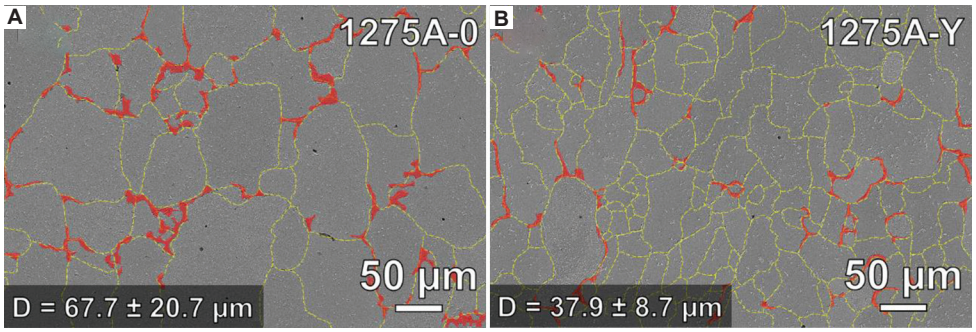

Figure 12. SEM images of samples 1275A-0 (A) and 1275A-Y (B) showing the grain boundaries (yellow dashed lines) and segregated regions (red areas). D: grain size.

In-depth analysis of the grain boundary of sample 1275A-Y (Figure 13) revealed that the segregated region consists of numerous small precipitates embedded within the segregated material as shown in Figure 13B On the other hand, the non-segregated region consists of a cluster of several white color precipitates as shown in Figure 13C.

EDX analysis shows that in segregated regions, the embedded is either Y_2O_3 or TiN particles. In addition, Nb is not detected in any of the particles. A similar observation can be made in the non-segregated region in which individual Y_2O_3 and TiN particles cluster together. Combined with the information in Figure 10, this shows that the complex precipitates that exist in the as-printed sample are not stable at high temperatures for a prolonged period and gradually separate into individual Y_2O_3 and TiN particles.

The increase in the number of precipitates increases the effectiveness of the Zener pinning effect, suppressing grain growth[56]. As such, significant grain refinement is observed in sample 1275A-Yas the grain size decreases from 67.7 ± 20.7 μm to 37.9 ± 8.7 μm as shown in Figure 12. The grain refinement in sample 1075A-Y suggests that the same phenomenon could have occurred in that sample. As there are more grain boundaries in sample 1275A-Y than in sample 1275A-0, there are more sites for the material to diffuse toward, resulting in thinner segregated regions as shown in Figure 12B.

It is also observed that the distribution of the γ′ and γ′′ precipitates in sample 1275A-Y have less of a difference as compared to those in sample 1275A-0 as shown in Figure 14. It is generally accepted that the γ′ phase has a cube-shaped morphology[57] while the γ′′ phase has a disc-shaped morphology[58]. The precipitates are indicated in Figure 14A and C. The γ′ and γ′′ precipitates are seen abundantly near the grain boundaries in sample 1275A-0 (Figure 14A). It is calculated that the precipitates occupied 71.0% of the total area of the image. However, in the region that is far from the grain boundaries, few precipitates are seen (Figure14B), which only occupied 52.0%. On the other hand, the difference in the occupied area of the precipitates between near and far from the grain boundaries in sample 1275A-Y is only 2.4%, which is significantly smaller than the 19.0% in sample 1275A-0.

The reason for the differences is as follows. It has been established that the segregation of Nb at the grain boundaries is much more severe in sample 1275A-0. In addition, the grain size of sample 1275A-0 is also much larger than that of sample 1275A-Y. Figure 15 shows the schematics that visualize the difference in the distribution of Nb in the microstructures between samples 1275A-0 and 1275A-Y. Due to the larger grain size and the segregation of Nb at the grain boundaries in sample 1275A-0, there is an Nb concentration gradient from the center of the grain to the edge of the grain as Nb diffuses towards the grain boundaries. Thus, this creates regions of low concentration of Nb at the center of the grains (red color) and regions of high concentration of Nb near the segregated materials at the grain boundaries (blue color). On the other hand, due to the smaller grain size of sample 1275A-Y, while having much less segregation at the grain boundaries, the concentration gradient of Nb in the microstructure is also much less significant. Thus, the distribution of Nb in sample 1275A-Y is relatively homogeneous. As Nb is needed for the formation of both the γ′ and γ′′ precipitates, there will be more and bigger precipitates in the blue regions in sample 1275A-0 due to the abundance of Nb. On the other hand, there is not enough Nb in the red region for the precipitates to form properly. Thus, this explains the difference observed in Figure 14A and B. Due to the relatively homogeneous distribution of Nb in sample 1275A-Y, the difference observed in Figure 14C and D is not significant. Because sample 1075A-Y also has a smaller grain size and less segregation at the grain boundaries compared to sample

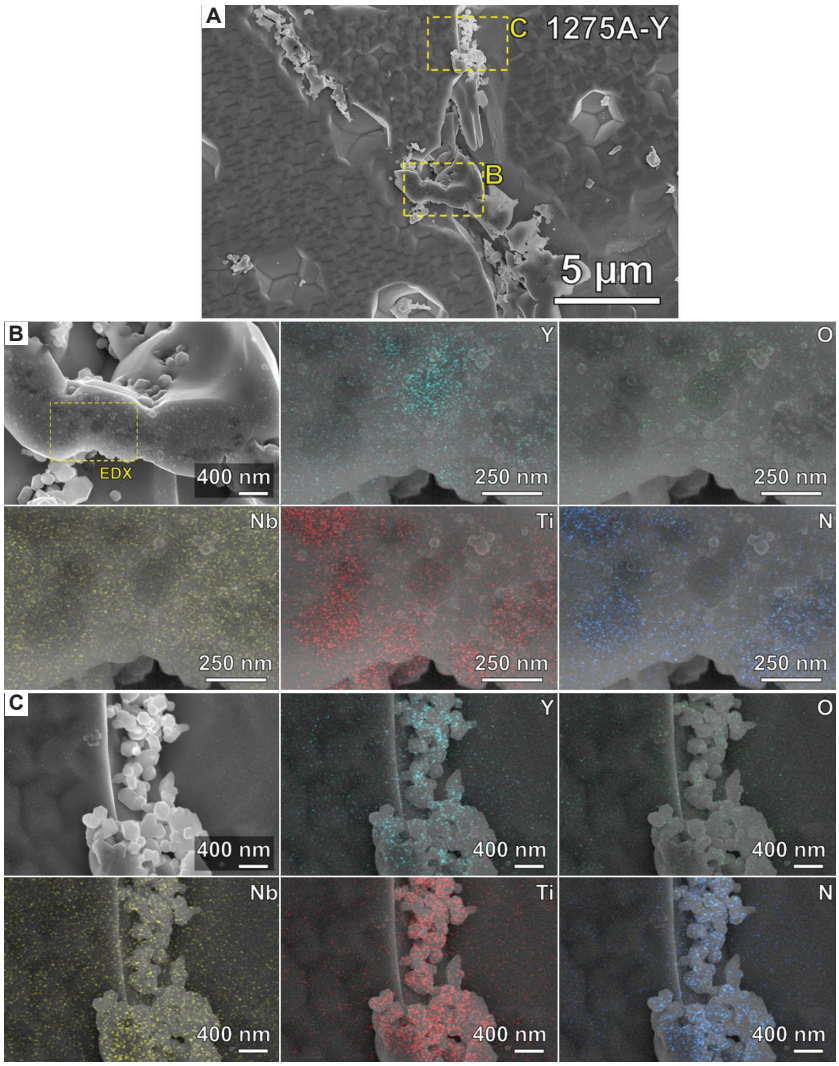

Figure 13. Scanning electron microscopy (SEM) images showing the grain boundary of sample 1275A-Y (A). High-magnification SEM images with EDX mapping spectra of the segregated (B) and non-segregated (C) areas.

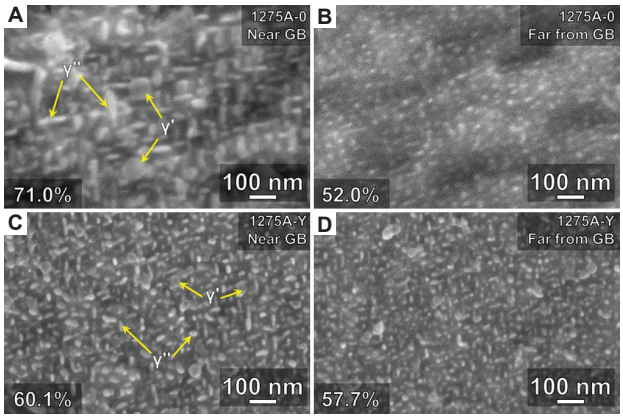

Figure 14. Scanning electron microscopy images showing the precipitates in sample 1275A-0 near grain boundary (A) and far from grain boundary (B), and in sample 1275A-Y near grain boundary (C) and far from grain boundary (D). GB: grain boundary.

1075A-0, the distribution of the γ′ and γ′′ precipitates is expected to follow the same trend.

Thus, while it is true that the presence of γ′ and γ′′ precipitates after aging treatment increases the strength of both Y_2O_3-reinforced and monolithic samples significantly, the distribution of the precipitates is shown to be affected by the addition of the reinforcement particles, which, in turn, affects their effectiveness. The lack of proper precipitation in the region far away from the grain boundaries in sample 1275A-0 affects the mechanical properties of the heat-treated monolithic sample negatively. Taken together, the higher strengths of the composites are the result of the increased Orowan strengthening from a significantly higher number of nano-sized precipitates, the grain boundary strengthening effect, and the γ′ and γ′′ precipitates being distributed more homogeneously.

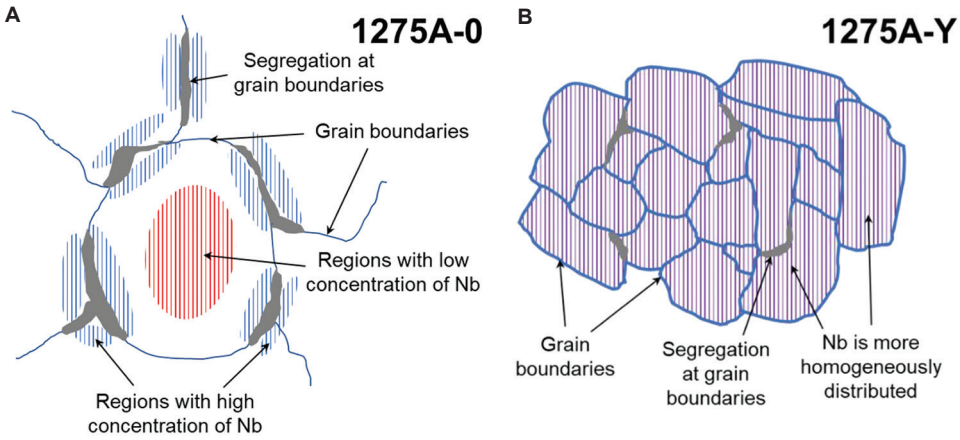

Figure 15. Schematics showing the difference in the distribution of Nb in the microstructures between samples 1275A-0 (A) and 1275A-Y (B).

4. Conclusions

The influence of Y_2O_3 addition on the microstructures of heat-treatedLPBFIN718 samples is investigated, and the results are as follows.

(i) Y_2O_3 nanoparticles have a high tendency to combine with carbonitride precipitates to form complex precipitates. These complex precipitates separate into individual Y_2O_3 and TiN nanoparticles after heat treatment. At the same time, Y-Ti-O precipitates form during the heat treatment due to the release of supersaturated Y in the matrix.

(ii) Grain refinement is observed in the Y_2O_3-reinforced composite after heat treatment due to the high number of nano-sized precipitates acting as nucleation centers for the recrystallization of grains and suppressing grain growth as a result of the Zener pinning effect.

(iii) Thinner segregated regions are observed at the grain boundaries of the heat-treated Y_2O_3-reinforced composite. This leads to a more homogeneous distribution of Nb in the microstructures and results in a smaller difference in the γ′ and γ″ precipitates distribution between the regions near and far from the grain boundaries.

(iv) The value added of the reinforcement particles in strengthening IN718 is only realized after heat treatment. The higher strengths of the composites are the result of the increased Orowan strengthening from a significantly higher number of nano-sized precipitates, the grain boundary strengthening effect, and the γ′ and γ″ precipitates being distributed more homogeneously.

Acknowledgments

The work is supported by the A*STAR Graduate Academy (A*GA) and by the Nanyang Technological University (NTU). The authors would like to thank Mr. Min Hao Goh for his assistance with the SEM-EDX analysis and Dr. Li Tao for his assistance with the heat treatment.

Funding

The financial support from the A*STAR Structural and Metal Alloys Program (SMAP): Work Package II with project No. A18B1b0061 is acknowledged.

Conflict of interest

The authors declare that they have no known competing financial interests or personal relationships that could have appeared to influence the work reported in this paper.

Author contributions

Conceptualization: Duy Nghia Luu and Wei Zhou
Formal analysis: Duy Nghia Luu
Investigation: Duy Nghia Luu
Methodology: Duy Nghia Luu
Project administration: Wei Zhou and Sharon Mui Ling Nai
Resources: Wei Zhou and Sharon Mui Ling Nai
Supervision: Wei Zhou and Sharon Mui Ling Nai
Validation: Wei Zhou and Sharon Mui Ling Nai
Visualization: Duy Nghia Luu
Writing – original draft: Duy Nghia Luu
Writing – review and editing: Wei Zhou and Sharon Mui Ling Nai

References

1. Ibrahim IA, Mohamed FA, Lavernia EJ, 1991, Particulate reinforced metal matrix composites-a review. *J Mater Sci*, 26: 1137–1156.

https://doi.org/10.1007/BF00544448

2. Gu DD, Meiners W, Wissenbach K, *et al.*, 2012, Laser additive manufacturing of metallic components: Materials,

processes and mechanisms. *Int Mater Rev*, 57: 133–164.

https://doi.org/10.1179/1743280411Y.0000000014

3. Zhang YC, Li ZG, Nie PL, *et al*., 2013, Effect of ultrarapid cooling on microstructure of laser cladding IN718 coating. *Surf Eng*, 29: 414–418.

https://doi.org/10.1179/1743294413Y.0000000142

4. Singh L, Singh B, Saxena KK, 2020, Manufacturing techniques for metal matrix composites (MMC): An overview. *Adv Mater Process Technol*, 6: 224–240.

https://doi.org/10.1080/2374068X.2020.1729603

5. Sharma V, Prakash U, Kumar BV, 2015, Surface composites by friction stir processing: A review. *J Mater Process Technol*, 224: 117–134.

https://doi.org/10.1016/j.jmatprotec.2015.04.019

6. Akbari M, Asadi P, Asiabaraki HR, 2022, Investigation of wear and microstructural properties of A356/TiC composites fabricated by FSP. *Surf Rev Lett*, 29: 1–10.

https://doi.org/10.1142/S0218625X2250130X

7. Akbari M, Asadi P, 2021, Simulation and experimental investigation of multi-walled carbon nanotubes/aluminum composite fabrication using friction stir processing. *Proc Inst Mech Eng Part E J Process Mech Eng*, 235: 2165–2179.

https://doi.org/10.1177/09544089211034029

8. Rohatgi PK, Asthana R, Das S, 1986, Solidification, structures, and properties of cast metal-ceramic particle composites. *Int Met Rev*, 31: 115–139.

https://doi.org/10.1179/imtr.1986.31.1.115

9. Shi Z, Han F, 2015, Microstructures and properties of cast T91-ODS alloys. *Mater Res Innov*, 19: S5832–S5835.

https://doi.org/10.1179/1432891714Z.0000000001202

10. Etemadi R, Wang B, Pillai KM, *et al*., 2018, Pressure infiltration processes to synthesize metal matrix composites-A review of metal matrix composites, the technology and process simulation. *Mater Manuf Process*, 33: 1261–1290.

https://doi.org/10.1080/10426914.2017.1328122

11. S-De-la-muela AM, Cambronero LE, Ruiz-Román JM, 2020, Molten metal infiltration methods to process metal matrix syntactic foams. *Metals* (*Basel*), 10: 149.

https://doi.org/10.3390/met10010149

12. Kong D, Dong C, Ni X, *et al*., 2019, Effect of TiC content on the mechanical and corrosion properties of Inconel 718 alloy fabricated by a high-throughput dual-feed laser metal deposition system. *J Alloys Compd*, 803: 637–648.

https://doi.org/10.1016/j.jallcom.2019.06.317

13. Gu D, Zhang H, Dai D, *et al*., 2019, Laser additive manufacturing of nano-TiC reinforced Ni-based nanocomposites with tailored microstructure and performance. *Compos Part B Eng*, 163: 585–597.

https://doi.org/10.1016/j.compositesb.2018.12.146

14. Tang B, Tan Y, Zhang Z, *et al*., 2020, Effects of process parameters on geometrical characteristics, microstructure and tribological properties of TiB_2 reinforced Inconel 718 alloy composite coatings by laser cladding. *Coatings*, 10: 76.

https://doi.org/10.3390/coatings10010076

15. Dhanya MS, Shukla AK, Dineshraj S, *et al*., 2019, Processing and characterization of yttria-dispersed Inconel 718 ODS alloy. *Trans Indian Inst Met*, 72: 1395–1398.

https://doi.org/10.1007/s12666-019-01649-5

16. Khalaj O, Mašek B, Jirková H, *et al*., 2017, Experimental study on thermomechanical properties of new-generation ODS alloys. *Zenodo*, 11: 501–504.

https://doi.org/10.5281/zenodo.1131439

17. Wang G, Huang L, Zhao P, *et al*., 2020, Effect of heat treatment on microstructure and mechanical properties of ODS nickel-based superalloy via strengthening mechanism. *JOM*, 72: 3279–3287.

https://doi.org/10.1007/s11837-020-04220-6

18. Chun YB, Mao X, Han CH, *et al*., 2017, Microstructural evolution and tensile properties of oxide dispersion strengthened Alloy 617 at elevated temperatures. *Mater Sci Eng A*, 706: 161–171.

https://doi.org/10.1016/j.msea.2017.09.009

19. Auger MA, Leguey T, Muñoz A, *et al*., 2011, Microstructure and mechanical properties of ultrafine-grained Fe-14Cr and ODS Fe-14Cr model alloys. *J Nucl Mater*, 417: 213–216.

https://doi.org/10.1016/j.jnucmat.2010.12.060

20. Fintová S, Kuběna I, Luptáková N, *et al*., 2020, Development of advanced Fe-Al-O ODS alloy microstructure and properties due to heat treatment. *J Mater Res*, 35: 2789–2797.

https://doi.org/10.1557/jmr.2020.278

21. De Sanctis M, Fava A, Lovicu G, *et al*., 2017, Mechanical characterization of a nano-ODS steel prepared by low-energy mechanical alloying. *Metals* (*Basel*), 7: 283.

https://doi.org/10.3390/met7080283

22. Luu DN, Zhou W, Nai SM, 2022, Mitigation of liquation cracking in selective laser melted Inconel 718 through optimization of layer thickness and laser energy density. *J Mater Process Technol*, 299: 117374.

https://doi.org/10.1016/j.jmatprotec.2021.117374

23. Luu DN, Zhou W, Nai SM, 2022, Influence of nano-Y_2O_3 addition on the mechanical properties of selective laser melted Inconel 718. *Mater Sci Eng A*, 845: 143233.

https://doi.org/10.1016/j.msea.2022.143233

24. Yeh AC, Lu KW, Kuo CM, *et al*., 2011, Effect of serrated grain

boundaries on the creep property of Inconel 718 superalloy. *Mater Sci Eng A*, 530: 525–529.

https://doi.org/10.1016/j.msea.2011.10.014

25. Deng DW, Wang CG, Liu QQ, *et al*., 2015, Effect of standard heat treatment on microstructure and properties of borided Inconel 718. *Trans Nonferrous Met Soc China*, 25: 437–443.

https://doi.org/10.1016/S1003-6326(15)63621-4

26. Zhang Y, Li Z, Nie P, *et al*., 2013, Effect of heat treatment on niobium segregation of laser-cladded IN718 alloy coating. *Metall Mater Trans A Phys Metall Mater Sci*, 44: 708–716.

https://doi.org/10.1007/s11661-012-1459-z

27. Sui S, Chen J, Ma L, *et al*., 2019, Microstructures and stress rupture properties of pulse laser repaired Inconel 718 superalloy after different heat treatments. *J Alloys Compd*, 770: 125–135.

https://doi.org/10.1016/j.jallcom.2018.08.063

28. Zhao Y, Li K, Gargani M, *et al*., 2020, A comparative analysis of Inconel 718 made by additive manufacturing and suction casting: Microstructure evolution in homogenization. *Addit Manuf*, 36: 101404.

https://doi.org/10.1016/j.addma.2020.101404

29. Kumara C, Balachandramurthi AR, Goel S, *et al*., 2020, Toward a better understanding of phase transformations in additive manufacturing of Alloy 718. *Materialia*, 13: 100862.

https://doi.org/10.1016/j.mtla.2020.100862

30. Mills WJ, 1984, Effect of heat treatment on the tensile and fracture toughness behavior of Alloy 718 weldments. *Weld J*, 63(8): 237s-245s.

31. Cao Y, Bai P, Liu F, *et al*., 2019, Investigation on the precipitates of IN718 alloy fabricated by selective laser melting. *Metals* (*Basel*), 9: 1128.

https://doi.org/10.3390/met9101128

32. Li X, Chu H, Chen Y, *et al*., 2019, Microstructure and properties of the laser cladding ODS layers on CLAM steel. *Surf Coatings Technol*, 357: 172–179.

https://doi.org/10.1016/j.surfcoat.2018.10.006

33. Guo Y, Li M, Chen C, *et al*., 2020, Oxide dispersion strengthened FeCoNi concentrated solid-solution alloys synthesized by mechanical alloying. *Intermetallics*, 117: 106674.

https://doi.org/10.1016/j.intermet.2019.106674

34. Shi Y, Lu Z, Yu L, *et al*., 2020, Microstructure and tensile properties of Zr-containing ODS-FeCrAl alloy fabricated by laser additive manufacturing. *Mater Sci Eng A*, 774: 138937.

https://doi.org/10.1016/j.msea.2020.138937

35. Wilms MB, Streubel R, Frömel F, *et al*., 2018, Laser additive manufacturing of oxide dispersion strengthened steels using laser-generated nanoparticle-metal composite powders. *Procedia CIRP*, 74: 196–200.

https://doi.org/10.1016/j.procir.2018.08.093

36. Zöllner D, 2022, Impact of a strong temperature gradient on grain growth in films. *Model Simul Mater Sci Eng*, 30: 025010.

https://doi.org/10.1088/1361-651X/ac44a8

37. Rao GA, Kumar M, Srinivas M, *et al*., 2003, Effect of standard heat treatment on the microstructure and mechanical properties of hot isostatically pressed superalloy Inconel 718. *Mater Sci Eng A*, 355: 114–125.

https://doi.org/10.1016/S0921-5093(03)00079-0

38. Gladman T, 1999, Precipitation hardening in metals. *Mater Sci Technol*, 15: 30–36.

https://doi.org/10.1179/026708399773002782

39. Sabelkin VP, Cobb GR, Doane BM, *et al*., 2020, Torsional behavior of additively manufactured nickel alloy 718 under monotonic loading and low cycle fatigue. *Mater Today Commun*, 24: 101256.

https://doi.org/10.1016/j.mtcomm.2020.101256

40. Roper CM, Heczel A, Bhattiprolu VS, *et al*., 2022, Effect of laser heating on microstructure and deposition properties of cold sprayed SS304L. *Materialia*, 22: 101372.

https://doi.org/10.1016/j.mtla.2022.101372

41. Amato KN, Gaytan SM, Murr LE, *et al*., 2012, Microstructures and mechanical behavior of Inconel 718 fabricated by selective laser melting. *Acta Mater*, 60: 2229–2239.

https://doi.org/10.1016/j.actamat.2011.12.032

42. Wang Y, Shi J, Deng X, *et al*., 2012, Contribution of Different Strengthening effects in Particulate-reinforced Metal Matrix Nanocomposites Prepared by Additive Manufacturing. In: Proceeding Advanced Manufacturing. American Society of Mechanical Engineers. Vol. 2; 2016. p1–7. Available from: https://www.asmedigitalcollection.asme.org/IMECE/proceedings/IMECE2016/50527phoenix,arizona, USA/265241 [Last accessed on 2017 Mar 22].

43. Zhang Z, Chen DL, 2006, Consideration of Orowan strengthening effect in particulate-reinforced metal matrix nanocomposites: A model for predicting their yield strength. *Scr Mater*, 54: 1321–1316.

https://doi.org/10.1016/j.scriptamat.2005.12.017

44. EOS NickelAlloy IN718 Material Data Sheet; 2020.

45. Martienssen W, Warlimont H, 2005, *Springer Handbook of Condensed Matter and Materials Data*. Berlin: Springer.

https://doi.org/10.1007/3-540-30437-1

46. Ferguson JB, Schultz BF, Venugopalan D, *et al*., 2014, On the superposition of strengthening mechanisms in dispersion strengthened alloys and metal-matrix nanocomposites:

Considerations of stress and energy. *Met Mater Int*, 20: 375–388.

https://doi.org//10.1007/s12540-014-2017-6

47. Ferguson JB, Sheykh-Jaberi F, Kim CS, *et al*., 2012, On the strength and strain to failure in particle-reinforced magnesium metal-matrix nanocomposites (Mg MMNCs). *Mater Sci Eng A*, 558: 193–204.

https://doi.org/10.1016/j.msea.2012.07.111

48. Vogt R, Zhang Z, Li Y, *et al*., 2009, The absence of thermal expansion mismatch strengthening in nanostructured metal-matrix composites. *Scr Mater*, 61: 1052–1055.

https://doi.org/10.1016/j.scriptamat.2009.08.025

49. Nardone VC, Prewo KM, 1986, On the strength of discontinuous silicon carbide reinforced aluminum composites. *Scr Metall*, 20: 43–48.

https://doi.org/10.1016/0036-9748(86)90210-3

50. Kim CS, Sohn I, Nezafati M, *et al*., 2013, Prediction models for the yield strength of particle-reinforced unimodal pure magnesium (Mg) metal matrix nanocomposites (MMNCs). *J Mater Sci*, 48: 4191–4204.

https://doi.org/10.1007/s10853-013-7232-x

51. Redsten AM, Klier EM, Brown AM, *et al*., 1995, Mechanical properties and microstructure of cast oxide-dispersion-strengthened aluminum. *Mater Sci Eng A*, 201: 88–102.

https://doi.org/10.1016/0921-5093(94)09741-0

52. Chawla N, Habel U, Shen YL, *et al*., 2000, The effect of matrix microstructure on the tensile and fatigue behavior of SiC particle-reinforced 2080 Al matrix composites. *Metall Mater Trans A*, 31: 531–540.

https://doi.org//10.1007/s11661-000-0288-7

53. Wang S, Zheng Y, Zhang G, *et al*., 2019, Effect of NbC addition on the microstructure, mechanical properties and thermal shock resistance of Ti(C,N)-based cermets. *Mater Res Express*, 6: 056557.

https://doi.org/10.1088/2053-1591/ab07e9

54. Ceschini L, Dahle A, Gupta M, *et al*., 2017, *Aluminum and Magnesium Metal Matrix Nanocomposites*. Singapore: Springer Singapore.

https://doi.org/10.1007/978-981-10-2681-2

55. Patil RV, Kale GB, 1996, Chemical diffusion of niobium in nickel. *J Nucl Mater*, 230: 57–60.

https://doi.org/10.1016/0022-3115(96)80010-9

56. Rohrer GS, 1948, Introduction to grains, phases, and interfaces-an interpretation of microstructure. *Metall Mater Trans A Phys Metall Mater Sci*, 175: 15–51.

https://doi.org/10.1007/s11661-010-0215-5

57. Cozar R, Pineau A, 1973, Morphology of γ' and γ" precipitates and thermal stability of Inconel 718 type alloys. *Metall Trans*, 4: 47–59.

https://doi.org/10.1007/BF02649604

58. Burke MG, Miller MK, 2012, Precipitation in Alloy 718: A Combined AEM and APFIM Investigation. Tennessee: Oak Ridge National Laboratory. p337–50.

Materials Science in Additive Manufacturing

ORIGINAL RESEARCH ARTICLE

Process optimization and mechanical property investigation of Inconel 718 manufactured by selective electron beam melting

Heng Dong[1,2], Feng Liu[1,2], Lin Ye[1,2], Xiaoqiong Ouyang[1,2], Qiangbing Wang[3], Li Wang[1,2], Lan Huang[1,2]*, Liming Tan[1,2]*, Xiaochao Jin[4], Yong Liu[1,2]

[1]State Key Laboratory of Powder Metallurgy, Central South University, Changsha 410083, China

[2]Powder Metallurgy Research Institute, Central South University, Changsha 410083, China

[3]Guangzhou Sailong Additive Manufacturing Co., Ltd., Guangzhou 510700, China

[4]State Key Laboratory for Strength and Vibration of Mechanical Structures, Xi'an Jiaotong University, Xi'an 710049, China

Abstract

To accelerate the optimization of selective electron-beam melting (SEBM) processing parameters, two machine learning models, Gaussian process regression, and support vector regression were applied in this work to predict the relative density of Inconel 718 from experimental data. The experimental validation indicated that the trained algorithms can precisely predict the relative density of SEBM samples. Moreover, the effects of different parameters on surface integrity, internal defects, and mechanical properties are discussed in this paper. The Inconel 718 samples with high density (>99.5%) prepared by the same SEBM energy density exhibit different mechanical properties, which are related to the existence of the unmelted powder, Laves phase, and grain structure. Finally, Inconel 718 sample with superior strength and plasticity was fabricated using the optimized processing parameters.

Keywords: Electron beam melting; Inconel 718; Machine learning; Parameter optimization; Defects; Tensile property

***Corresponding authors:**
Liming Tan
(limingtan@csu.edu.cn)
Lan Huang
(lhuang@csu.edu.cn)

Citation: Dong H, Liu F, Ye L, *et al*., 2022, Process optimization and mechanical property investigation of Inconel 718 manufactured by selective electron beam melting. *Mater Sci Add Manuf,* 1(4): 23.
https://doi.org/10.18063/msam.v1i4.23

Received: September 22, 2022

Accepted: October 31, 2022

Published Online: November 23, 2022

1. Introduction

Compared with traditional subtractive manufacturing techniques, additive manufacturing (AM) techniques are getting increasing attention due to their flexibility in designing and fabricating complex parts through incremental layer-by-layer manufacturing method[1-3]. Selective electron-beam melting (SEBM) is one of the most promising powder bed fusion AM techniques for metal part fabrication[4]. Compared with another powder bed fusion technology, that is, selective laser melting (SLM)[5], SEBM has higher energy utilization rate and production efficiency, and it could reduce the risk of oxide and nitride formation due to its vacuum environment[4,6]. Moreover, SEBM reduces the temperature gradient and residual stresses through preheating and, thus, avoids the strain-induced distortion[7,8]. Therefore, SEBM has advantage in fabricating high-performance materials with high active elements or which are difficult to process, such as Ti6Al4V[9], superalloy[10], copper and copper alloys[11], and tungsten[12].

To accelerate the application of the SEBM, the generation of defects during the print processing must be solved in the first place since macroscopical cracks preferentially nucleate from defects region, which affect the overall property of materials[13]. The types of internal defects reported generally in SEBM process include entrapped gas porosity, lack of fusion porosity[14], shrinkage porosity,[15] and hot cracking[16]. In Ni-based superalloys, the formation of detrimental intermetallic phases, such as laves phases, δ phases, carbides, and nitrides, is also a kind of defect, because they reduce the number of elements used for solid solution and γ′/γ″ precipitation[17-20]. Although some post-processing treatment methods, such as hot isostatic pressing (HIP), could reduce the defect density, not all defects can be repaired[21,22]. Therefore, it is of great significance to control defect generation during AM process by optimizing processing parameters. Various researchers have optimized processing parameters through experiment, such as taguchi method[23], energy density[24], processing window[25] and dimensionless number[26], and performed physical calculation simulation[27-29] to build defect-free parts with a flat surface successfully. However, the processing parameters optimization is still a big challenge due to the high-dimensionality and complex combination of parameters, during which complex physical processes and interactions also need to be considered.

Recently, with the development of materials informatics, machine learning method has been broadly adopted to facilitate composition and process optimization for complex alloys[30-36]. Liu *et al.*[37] developed a machine learning approach based on Gaussian process regression (GPR) to identify the processing window for AlSi10Mg alloy by laser powder bed fusion, wherein the fully dense alloy with high strength and ductility was manufactured. Aoyagi *et al.*[38] proposed a simple method that combines uniform design and support vector machine to correlate processing parameters with surface conditions and generated a processing map that can obtain the best densification for SEBM CoCr alloy by fewer samples. Thereafter, Lei *et al.*[39,40] optimized multiple processing parameters of SEBM for superalloy Alloy713ELC. Sah *et al.*[41] trained multiple machine learning algorithms to predict the density and defect formation in LBPF sample.

In this study, the most commonly used superalloy Inconel 718 was selected to investigate the effects of different parameters on the surface morphology and internal defects. The beam current and scan speed were used as the input of GPR and support vector regression (SVR) to establish the relationship between different processing parameters and relative density, and the optimized processing window is determined. Then, four high-density Inconel 718 samples with different microstructures and properties were built according to the processing window. The relationship among SEBM processing parameters, defect, microstructure, and property of Inconel 718 was studied.

2. Methodology

2.1. Inconel 718 powder and SEBM process

Pre-alloyed powders were supplied by Guangzhou Sailong Additives Manufacturing. Co., Ltd., Guangzhou, China. The chemical composition of powder is listed in Table 1. Figure 1 shows the surface morphology and microstructure of the Inconel 718 alloy powder. The powders mostly exhibit a spherical shape (>90%), only few satellites (red arrow) and non-spherical powders (white arrow) were observed, as indicated in Figure 1A. On the smooth surface of the powder, dendrite structure can be seen, as shown in Figure 1B. Inconel 718 powder consists of fine equiaxed grains with average grain size of 5.8 μm

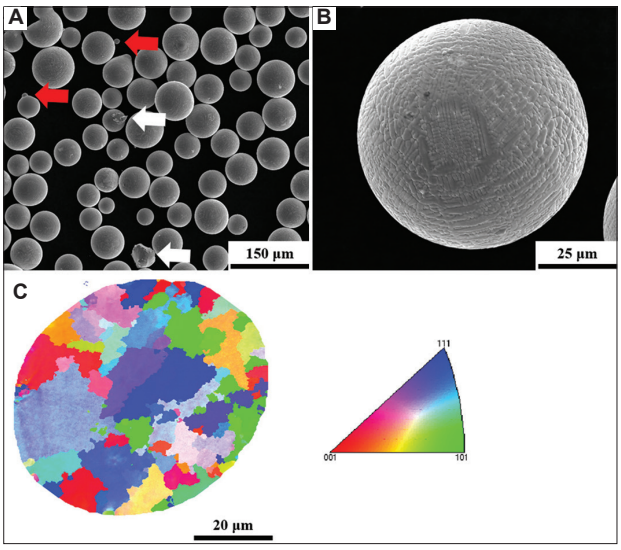

Figure 1. Surface morphologies and microstructures of pre-alloyed Inconel 718 powder. (A) SEM in low magnifications. (B) SEM high magnifications. (C) IPF map are based on EBSD measurements with a step size of 0.3 μm.

Table 1. Chemical composition of Inconel 718 powder.

Ni	Cr	Fe	Nb	Mo	Ti	Al	Co	Cu	Si	C	O	N
Bal.	21	17.2	5.12	3.21	0.85	0.45	0.2	0.089	0.039	0.032	0.0149	0.0146

and random orientation, as shown in Figure 1C. The average powder particle size is approximately 35 μm, as illustrated in Figure 2. A flow time of 12.0 ± 0.1 s for 50 ± 0.1 g of powders is determined by going through a 2.5 mm diameter Hall flowmeter orifice. Therefore, the pre-alloyed powders with the above-mentioned properties are suitable for the selective electron-beam melting.

The SEBM was conducted on a commercial SEBM machine (Sailong-Y150 SEBM System) provided by Xi'an Sailong Metal Materials. Co, Ltd., Xi'an, China. During SEBM, the powder bed was preheated to 900°C to prevent "smoking" phenomenon. Then, the contour scanning was performed before hatching. The scanning direction of the electron beam was rotated by 90° after each successive layer. In this study, beam current and scan speed were chosen as variables with a certain acceleration voltage of 60 kV, a line offset of 100 μm, a layer thickness of 50 μm, and a spot size of 150 μm. Cuboid samples with a size of 20 × 20 × 10 mm^3 were built using the processing parameters, as shown in Table 2, which generate 63 parameter combinations in total. The volume energy density (J/mm^3) is calculated as follows:

$$E_{volume} = \frac{P}{v \times l \times t} \quad \text{(I)}$$

where v is scan speed (mm/s), l is line offset (mm), t is layer thickness (mm), and the power P is determined by

$$P = U \times I \quad \text{(II)}$$

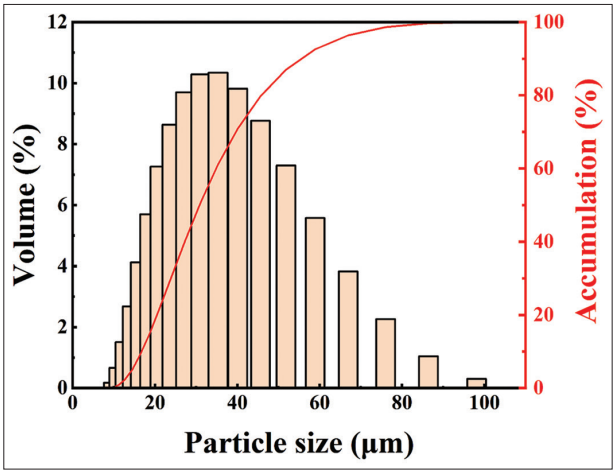

Figure 2. The powder size distribution of the studied Inconel 718 alloy.

Table 2. Selective electron beam melting processing parameters.

Processing parameter	Values
Beam current (mA)	7.5, 10, 12.5, 15, 17.5, 20, 22.5, 25, 27.5
Scan speed (mm/s)	2000, 3000, 4000, 5000, 6000, 7000, 8000

where U is acceleration voltage (V), and I represent beam current (mA).

2.2. Machine learning

SVR and GPR are two classical regression algorithms of machine learning in the field of process optimization. Both models have advantage in update and suitable for small data set. It is necessary to evaluate, in which one is suitable for data in this work. Other common algorithms have been evaluated. Linear regression and logistic regression were too simple to learn effectively. Artificial neural network was so complex that it can easily cause overfitting. Although Decision Trees, Random Forest, and K-Nearest Neighbor obtained an optimized processing window, they did not obtain a smoothed boundary curve between different relative density due to their characteristics. The SVR constructs a hyper-plane or set of hyper-planes in a high or infinite dimensional space, and the nearest data points on either side of the hyper-plane are termed as support vectors which are used to plot the boundary line[41]. All data in a set are closest to the regression plane. The model produced by SVR only depends on a subset of the training data, because the cost function ignores samples whose prediction is close to their target[42]. The GPR implements Gaussian processes (a generic supervised learning method) for regression purposes. The collection of random variables has a joint Gaussian distribution with a continuous domain and the prediction interpolates the observations[37]. In this study, beam current and scan speed are input, while relative density is output, and SVR and GPR were used to predict relative density and generate processing windows.

The raw data set will affect the results of machine learning algorithms. Data preprocessing methods, including unbalanced data, data partitioning, and standardization, were applied to reduce the impact of raw data distribution and improve the accuracy of prediction. As shown in Figure 3, relative density values are mostly concentrated between 98% and 100%, and only a few original data are lower than 98%, resulting in unbalanced data. Unbalanced data reduce the prediction accuracy of low-density areas. To improve the prediction accuracy, the data of relative density lower than 98% were copied once to improve the weight of low-density data. The total data set was increased to 65 (remove unformed build). Machine learning parameters are divided into parameter and hyper-parameter. Parameter obtains value by the process of training data, but hyper-parameter is set manually. The choice of hyper-parameter will change the learning ability of machine learning model. When the data and hyper-parameter are fixed, the machine learning model is usually fixed. Therefore, raw data set should be partitioned to obtain the appropriate hyper-parameter, and the train-set

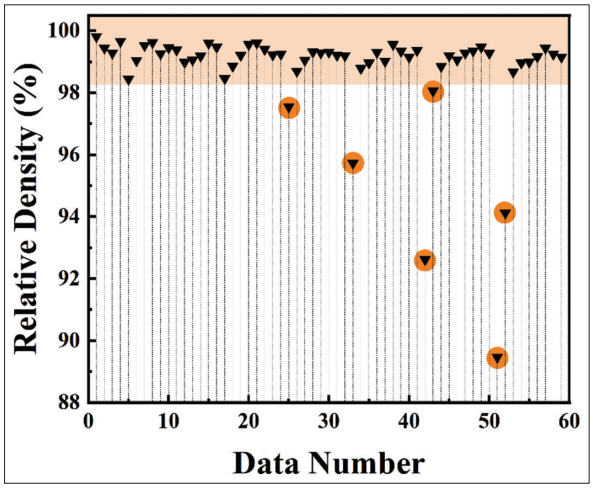

Figure 3. Data set distribution.

to test-set ratio is 8:2. If the variance difference between each feature is large, the machine learning algorithm cannot learn from each feature well, resulting in poor learning effect. Standardization of data can improve the learning ability of the machine learning algorithm and further enhance the prediction accuracy. Two methods of regression scoring were used to evaluate the prediction accuracy of the machine learning model, including the mean squared error (*MSE*):

$$MSE = \frac{1}{n}\sum_{i=1}^{n}(y_i - \hat{y}_i)^2 \quad \text{(III)}$$

and the R-Squared (R^2):

$$R^2 = 1 - \frac{\frac{1}{n}\sum_{i=1}^{n}\left(y_i - \hat{y}_i\right)^2}{\frac{1}{n}\sum_{i=1}^{n}\left(y_i - \bar{y}\right)^2} \quad \text{(IV)}$$

where n is the number of data, y_i is the true value, $\hat{y}_i$ is the predicted value, and $\bar{y}$ is the average of true values. A smaller *MSE* and a R^2 that is closer to 1 indicate superior model performance.

All machine learning algorithms were implemented by Python 3.8 programming language and Scikit-learn (sklearn) API.

2.3. Materials characterization and mechanical property test

The relative density of the as-built samples was measured using the Archimedes method. Theoretical density of Inconel 718 used in this work is 8.24 g/cm^3, which is higher than that reported in other literature[43-45]. The surface flatness and cross-sectional integrity were evaluated based on optical images. Inconel 718 alloy samples with four different processing parameters were selected for characterization from the processing window. All the sectioned samples were mounted and metallographically ground and polished using typical metallographic procedure. The backscattered electron (BSE) images of as-built samples microstructure were observed using scanning electron microscopy (SEM, FEI Quanta 650). Inverse pole figure (IPF) maps of the SEBM Inconel 718 were characterized by electron back-scattered diffraction (EBSD) analysis. The observation region is in the middle of the sample and parallel to the building direction (BD). The hardness of each as-built sample was measured by the Vickers microhardness tester (THV-10), with load and dwell time of 1 kgf and 10 s, respectively. Average hardness value of 10 points was used. To evaluate the mechanical strength of printed samples, dog-bone-shaped samples with a gauge length of 8 mm were taken from the as-built samples for tensile testing. The tensile direction was parallel to the build direction with a displacement rate of 0.5 mm/s at room temperature.

3. Results

3.1. Processing parameters on surface integrity

There is a total of 63 combination of scan speed (m/s) and beam current (mA) in this study. The samples were divided into four types: even, uneven, porous, and unformed, according to the surface morphology observed from the optical images, as shown in Figure 4A. According to processing parameters window of surface morphology, porous surface was observed in the samples built with low beam current and high scan speed, while uneven or unformed surface was observed in the samples built with high beam current and low scan speed. Most samples can obtain a flat and even surface. Figure 4B-D shows the typical surface morphology and corresponding cross-sections of samples. There were two different cross sections of uneven surface. Large irregular pores were inside undular surface, while no pores were inside arched surface, as shown in Figure 4B. The even surface had a cross-section without defects or with a few defects, as shown in Figure 4C. There were a large number of lack-of-fusion pores beneath the porous surface, and the lack-of-fusion defects were generally perpendicular to the build direction, as shown in Figure 4D.

The energy input or energy density is often used to investigate the influence of SEBM processing parameters. Figure 5A shows the relationship among surface morphology, energy density, and beam current. To a certain extent, the energy density reflects the

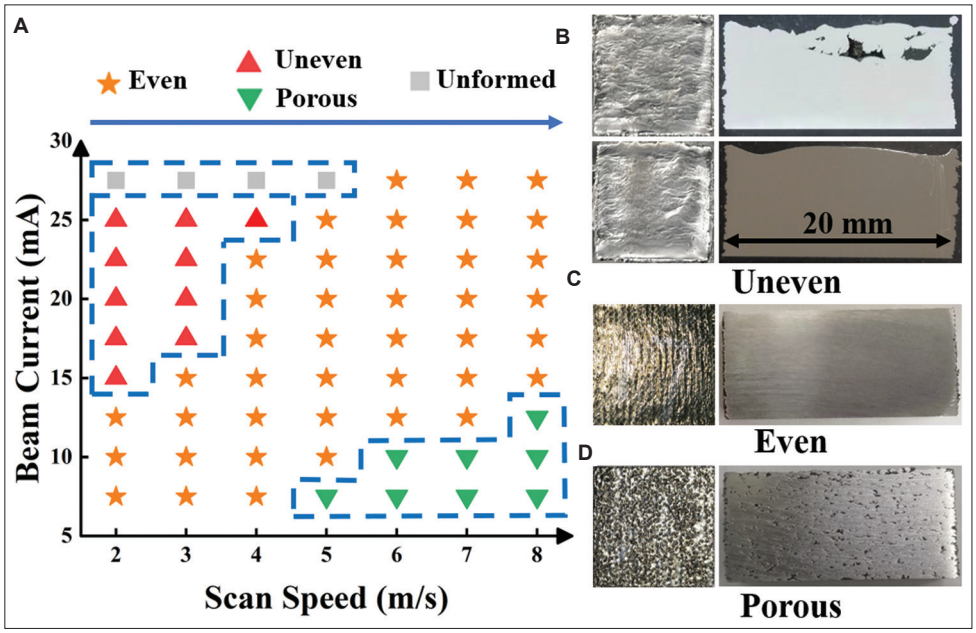

Figure 4. Classification of surface morphology. (A) Processing parameters window of surface morphology. (B–D) Typical surface morphology and corresponding cross sections of samples: (B) 15 mA and 2 m/s (top), 25mA and 3m/s (bottom); (C) 15 mA and 4 m/s; and (D) 7.5 mA and 7 m/s.

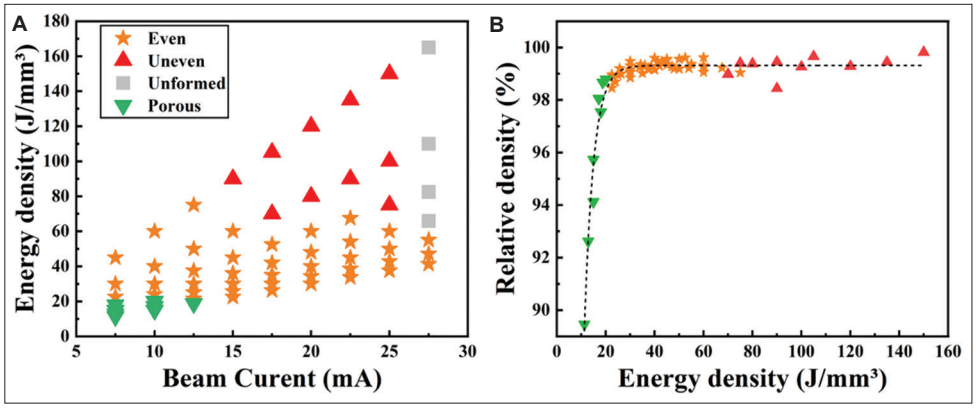

Figure 5. Surface morphology analysis. (A) Effect of energy density and beam current on surface morphology. (B) Relationship between energy density, relative density and surface morphology.

characteristics of surface morphology. Low-energy density results in porous surfaces, while high-energy density results in uneven surfaces. Despite the same energy density, it is still easy to get uneven or unformed surfaces when the beam current is too high. The surface morphology is also related with the relative density, as shown in Figure 5B. The porous surface has a low relative density due to the lack-of-fusion defects mentioned above. Samples with even surfaces usually own higher relative density, compared to those with uneven surfaces. Different from SLM which uses laser as energy source, there was no reduction in relative density due to keyhole when the energy density is too high[46].

3.2. Prediction of relative density by machine learning

In this study, SVR and GPR machine learning algorithms were trained to predict the relative density. There were 65 groups of basic data (including six repeated low relative density data), in which 52 data were for training, while 13 data were for testing, as shown in Figure 3. Training the machine learning model by the method is described in section 2.2. The appropriate hyper-parameter was selected by the Grid-Search method. Hyper-parameter is critical to machine learning's performance. SVR has the radial basis function kernel and hyper-parameters $C = 300$, $\gamma = 3.5$, and GPR has squared exponential kernel and hyper-parameter

alpha = 5×10^{-3}. Kernel and hyper-parameters affect the learning ability and generalization of the model[47]. The predicted value matched well with the measured value, indicating that the selection of hyper-parameter was appropriate, as shown in Figure 6A and 6C. Compared with the "big data" in the field of artificial intelligence, the data volume obtained by SEBM was small. To make full use of the limited data, all data were taken as input to train the machine learning model with the same hyperparameters. New machine learning model predicted the relative density from the parameter space. There were 61 discrete scan speed values from 2000 mm/s to 8000 mm/s with an interval of 100 mm/s and 201 discrete beam current values from 7.5 mA to 27.5 mA with an interval of 0.1 mA. The combination of these parameters gave rise to a parameter space of 12261. The scoring of SVR model and GPR model is shown in Table 3. Both models have learned data well and exhibited good performance. The relative density contour map was produced by GPR model and SVR model, as shown in Figure 6B and D. Both maps displayed similar structure, while a high relative density region of low beam current and high scan speed predicted by SVR did not exist. Hence, the map obtained by GPR model may be more applicable.

3.3. Optimized SEBM processing window for Inconel 718

The SEBM processing window for Inconel 718 was obtained by the combination of GPR relative density contour map and processing parameters window of surface morphology, as shown in Figure 7A. The area with high relative density and even surface is the optimized SEBM processing window. The low, middle, and high scan speed areas in the processing window were used to fabricate Inconel 718 samples with a high relative density and even surface. Compared with SVR model, an apparent feature

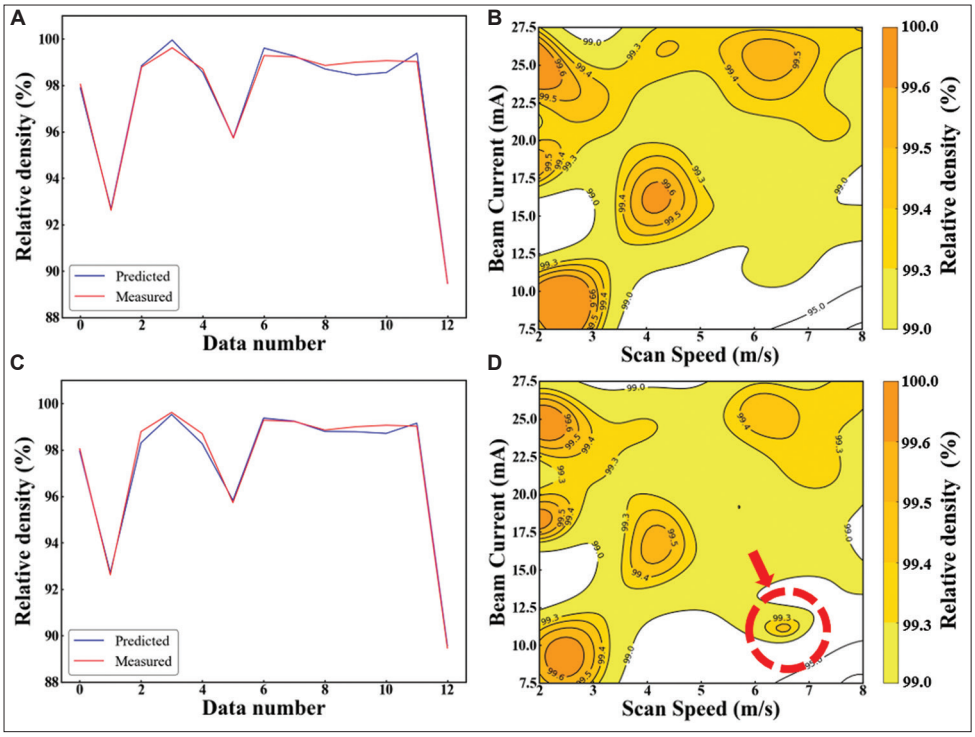

Figure 6. Relative density value prediction results: Comparison between predicted value and measured value from test-set (A) GPR and (C) SVR, and relative density contour map with beam current and scan speed (B) GPR and (D) SVR (the red circle is the area of error prediction). GPR: Gaussian process regression, SVR: Support vector regression.

Table 3. Scoring of SVR and GPR.

Machine learning algorithm	R^2			MSE		
	Train-set	Test-set	All-data	Train-set	Test-set	All-data
SVR	0.9975	0.9942	0.9982	0.00906	0.0506	0.0506
GPR	0.9994	0.9913	0.9986	0.00201	0.0763	0.0763

GPR: Gaussian process regression, SVR: Support vector regression

of GPR is that it can output prediction error directly. The error of relative density prediction in parameter space is provided in Figure 7B. All the area had low error except for the unformed surface area.

Four new points of processing conditions within the area with high relative density and even surface in this optimized processing window were selected to validate the GPR model. It should be noted that P1, P2, and P3 have the same energy density. New samples were fabricated with corresponding processing parameters. The specific SEBM processing parameters of new samples and the results of measured and predicted values are shown in the Table 4. In the 95% confidence interval (error × 1.96), the predicted value matched with the measured value and exhibited high accuracy, as shown in Figure 7C. In addition, the relative density obtained under the new processing parameter was generally higher than the previous training data. The microstructure and mechanical properties of the four new samples were further characterized.

3.4. Microstructure of the SEBM-fabricated Inconel 718

As shown in Figure 8, no cracks and lack-of-fusion pores were found in the building samples. BSE images at low

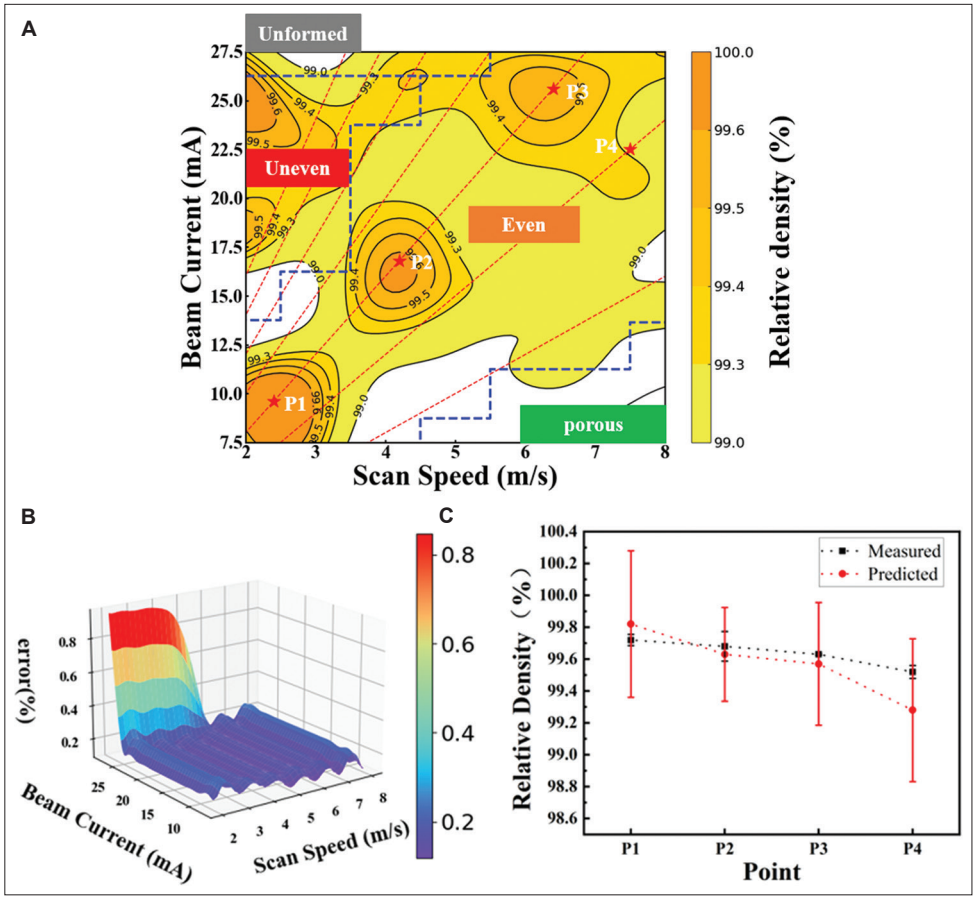

Figure 7. (A) The selective electron beam melting processing window for Inconel 718 and selected four new points for validation. (B) The error of elative density prediction by GPT model. (C) The measured relative density values compared to the predicted relative density values by Gaussian process regression model from four new points of parameter combination.

Table 4. Processing parameter of new samples for validation and relative density of measured and predicted value.

Point	Beam current (mA)	Scan speed (m/s)	Energy density (J/mm≥)	Measured relative density	Predicted relative density	Error
P1	9.6	2.4	48	99.72%	99.82%	−0.10%
P2	16.8	4.2	48	99.68%	99.63%	+0.05%
P3	25.6	6.4	48	99.63%	99.57%	+0.06%
P4	22.5	7.5	36	99.52%	99.29%	+0.23%

magnification present the similar microstructure of slender columnar grains from SEBM-fabricated Inconel 718 with processing parameters, as shown in Table 4. The columnar grains were parallel to the BD, which was also observed in other works about SEBM process[25,45,48].

Further, characterization shows that the main defect in the sample with even surface morphology was the voids parallel to the BD, as shown in Figure 9A. This defect was also observed in samples with uneven and porous surface morphology. The voids were distributed at the inter-dendritic region with a width of 2–3 μm and a length of 20 μm. These voids are considered the shrinkage porosity[49].

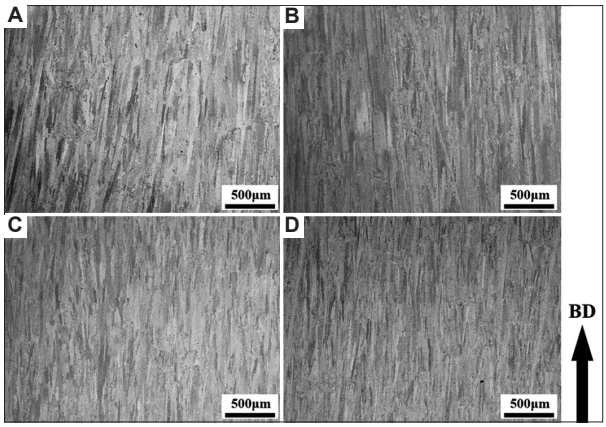

Figure 8. BSE images at low magnification showing the similar slender columnar grains in different samples: (A) P1, (B) P2, (C) P3, (D) P4.

The reason for the formation of shrinkage porosity was that insufficient liquid reached the channel that was isolated by dendrite bridging during solidification[50]. Three precipitates can be observed in the matrix of these samples, as shown in Figure 9B, and Figure 9C is the corresponding EDS map. According to the morphology and element enrichment, the block shape precipitate "a" is enriched in Nb and Mo, which is determined as Laves phase[17]. The long plate shape precipitate "b" is the δ phase. Laves phase is mainly formed on the grain boundaries and mixed with a few of δ phase somewhere. The polygonal precipitate "c" is enriched in N and Ti, indicating the existence of TiN phase. The spherical precipitate "d" in the core of TiN is rich in Al and O, which suggests that the precipitate is the Al_2O_3 phase. No gas pore defects were observed inside the sample.

The difference between grains was observed by EBSD. Figure 10 shows the EBSD-IPF maps on the cross-section parallel to the BD. Strong texture in the as-built samples along the BD was observed in the EBSD-IPF maps. The as-EBM-built samples mainly consist of columnar grains with preferential orientation <001>, decorated with few equiaxed fine grains. Figure 11 shows the pole figures and multiple of uniform density (MUD) maximum of four samples. Sample P2 shows a strong texture in BD with a MUD maximum of 30.73, sample P1 and P3 shows a reduced texture, and sample P4 has the lowest MUD maximum, which is 17.21. Completely equiaxed grain

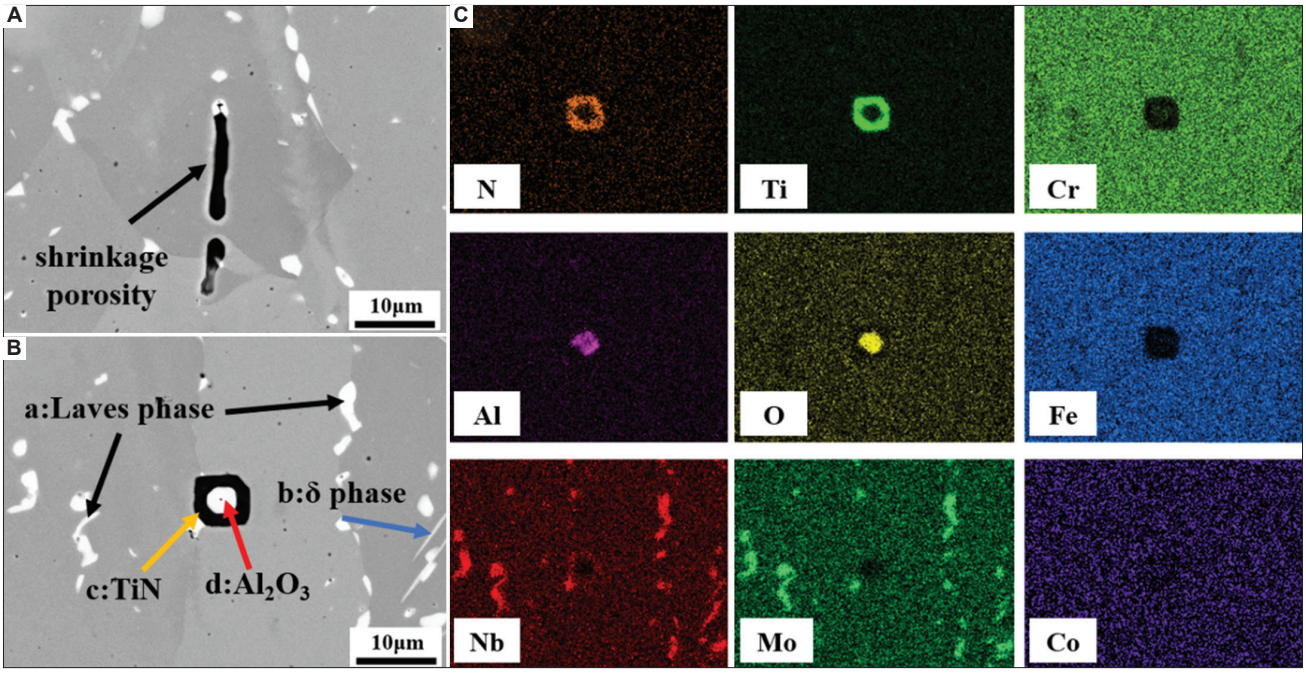

Figure 9. BSE images of defects and phase in selective electron beam melting -fabricated Inconel 718: (A) shrinkage porosity, (B) Laves phase, δ phase, and TiN/Al2O3 phase, (C) EDS map of the inclusion in (B).

structure has a MUD value of 1. In comparison, sample P2 has the least area of grains in random orientations.

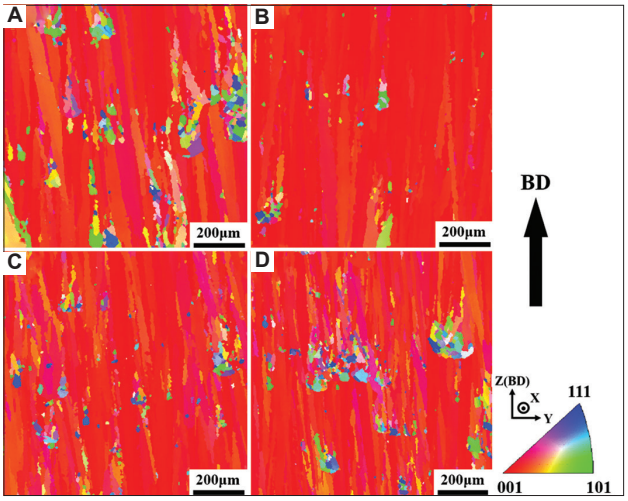

Figure 10. Electron back-scattered diffraction-Inverse pole figure maps on cross-section of as-built samples: (A) P1, (B) P2, (C) P3, and (D) P4.

The bottom half of these regions reserved a hemispherical shape. Compared with the microstructure of pre-alloyed powder, it indicated that the fine grains may be inherited from the incompletely melted powder[51]. Columnar grains were formed after <100> preferential growth on equiaxed grains. The columnar grains are interrupted when coming across the next unmelted powder. Variations of the columnar grain width measured using the interception method according to ASTM E112-2013 standard are listed in Table 5. Samples P1, P2, and P3 with the same energy density had similar columnar grain width, and sample P4 with the fastest scanning speed and smaller energy density had finer columnar grains.

3.5. Mechanical properties of SEBM-fabricated Inconel 718

The hardness of Inconel 718 fabricated by SEBM with the parameters listed in Table 4 is shown in Table 5. It can be seen that the as-built samples without heat treatment had high hardness, because high temperature was maintained

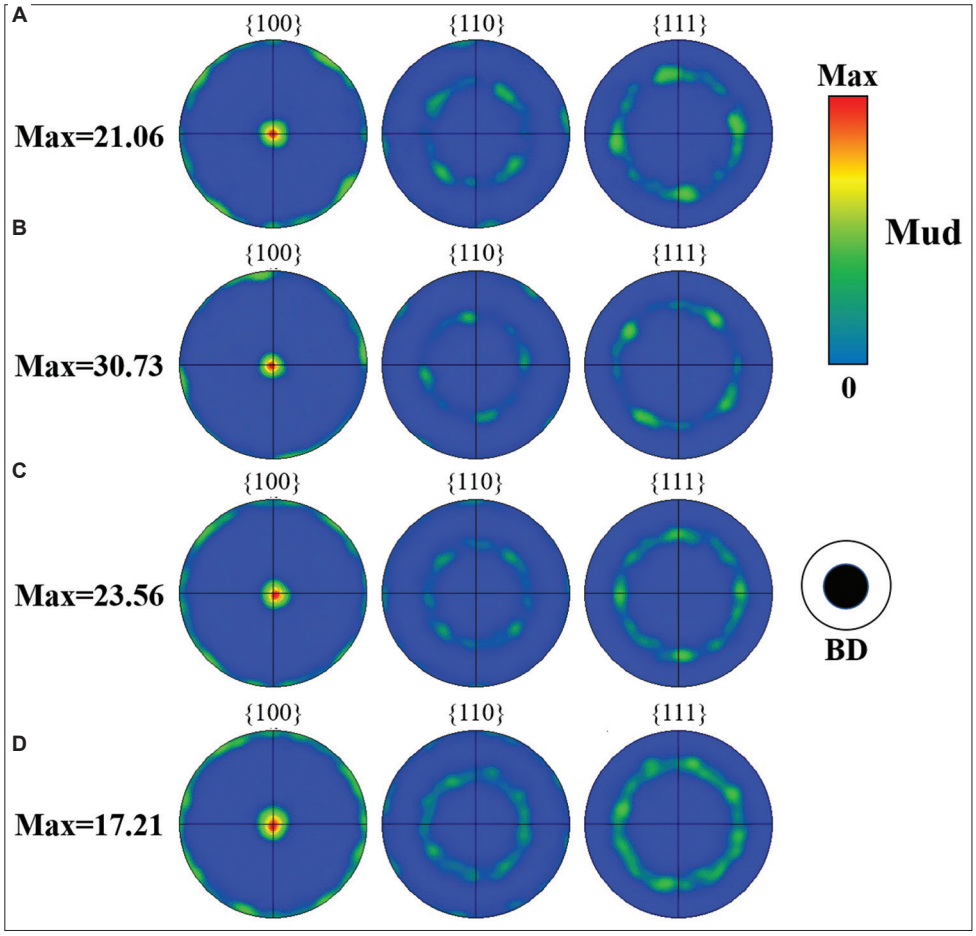

Figure 11. Pole figures in the XY-plane: (A) P1, (B) P2, (C) P3, (D) P4.

Table 5. Columnar grain width, hardness, and mechanical properties at room temperature of Inconel 718 fabricated by selective electron beam melting with the parameters listed in Table 4.

Sample	Columnar grain width (μm)	Hardness (Hv)	Yield strength (MPa)	Tensile strength (MPa)	Elongation (%)
P1	20.71±(16.51)	427.70±(32.59)	908.0±(5.0)	1009±(50)	7.6±(1.3)
P2	22.36±(16.85)	440.15±(15.81)	954.5±(14.5)	1270±(9)	34.0±(1.7)
P3	19.11±(15.30)	424.09±(17.34)	914.5±(10.5)	1215±(22)	22.1±(6.5)
P4	14.36±(10.30)	410.82±(12.88)	876.0±(4.0)	1216±(30)	17.5±(3.9)

during SEBM process resulting in precipitation of γ′ and γ″ phase. However, the deviation indicates that the microstructures and the precipitates were not uniform. The tensile strength, yield strength, and elongation at room temperature of the as-built samples are shown in Figure 12, and the detailed values are shown in Table 5. Although the four samples fabricated by optimized processing parameters obtained high relative density, the mechanical properties were different. Sample P1 had the worst mechanical properties, while sample P2 had the best, although both P1 and P2 were fabricated with the same energy density. Samples P1 and P3 had relatively higher relative density and similar hardness values, but the mechanical properties of sample P3 were significantly higher than that of sample P1, especially the elongation. Thereby, as for the SEBM-fabricated fully dense Inconel 718 specimens, it is far from adequate to take energy density or relative density into consideration to optimize the mechanical properties.

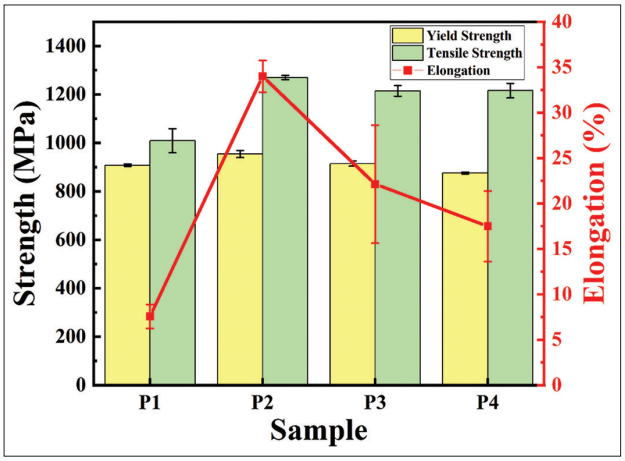

Figure 12. Tensile tests at room temperature of as-built Inconel 718 samples with the parameters listed in Table 4.

4. Discussion

4.1. Relationships between surface morphology and internal defects

The pre-alloyed powder in this study was prepared by plasma rotating electrode process; hence, the gas pore inside the powder and gas pore induced defects can be ignored. As shown in Figure 4, different combinations of parameters will give rise to different surface morphology in SEBM process. Different surface morphology is related to various types of internal defects. Uneven surface included lack-of-fusion defect or no defects, even surface included shrinkage porosity defect, while porous surface included lack-of-fusion defect.

Figure 13A shows the effect of beam current on relative density, and input energy increases with the increase of current by fixing scanning speed. When the input energy gradually increases, the surface morphology changes from even to uneven, and the relative density first decreases and then increases. The combined effect of the Marangoni effect, vapor recoil pressure, and electron-beam agitation results in an uneven surface[52]. The convex and concave of the uneven surface led to a large difference in the thickness of the powder layer, and the input energy (beam current < 15 mA) is not enough to melt the thicker powder layer, resulting in a huge lack-of-fusion defects, as shown in Figure 4B. With the further increase of input energy (15 mA < beam current < 25 mA), the molten pool is enough to pass through the thick powder layer and prevent lack-of-fusion defects, and the relative density increases correspondingly. When the input energy (beam current > 25 mA) is too high, the splashing of metal liquid or metal vapor makes it impossible to form. Figure 13B shows the effect of scan speed on relative density, and input energy decreases with the increase of scan speed by fixing beam current. When the input energy gradually decreases, the surface morphology changes from even to porous, and the relative density decreases. As shown in Figure 14, the sample with porous surface had a large number of lack-of-fusion defects, which is the main reason for the low relative density. Small and shallow molten pool was generated due to the low input energy. The molten pool cannot effectively penetrate the new layer of powder and combine with the previous solidified layer. Balling effect causes the partially melted powder to form an isolated molten liquid. Due to surface tension and rapid solidification, molten liquid could not flow into pores and thus combine with nearby powder[53]. Therefore, the lack-of-fusion defects

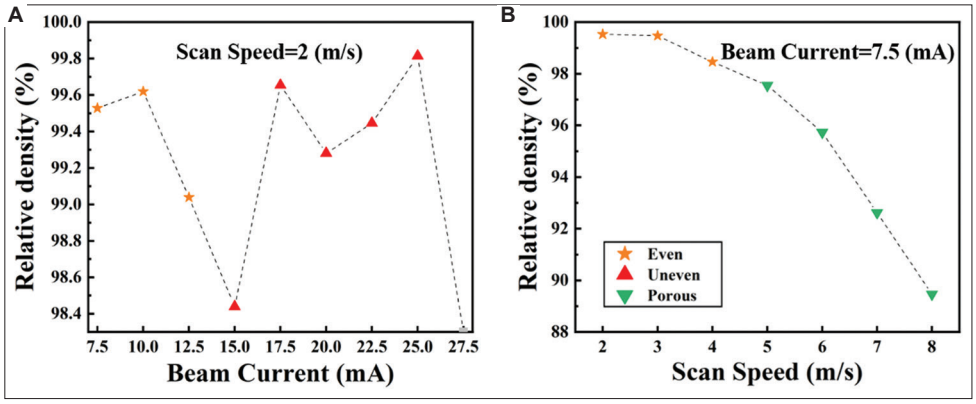

Figure 13. The effect of (A) beam current and (B) scan speed on relative density.

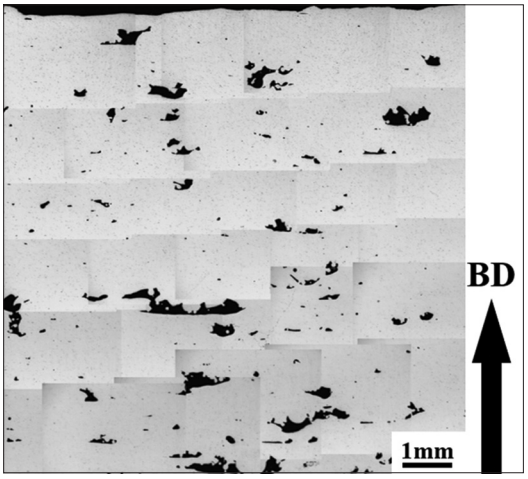

Figure 14. Lack-of-fusion defects inside Inconel 718 sample with porous surface, 7.5 mA and 6 m/s.

are generally irregular, and the defect direction may be either vertical to the powder layer or parallel to the powder layer. When the input energy is appropriate, the surface morphology is even. Although the surface is even and free of defects, the properties of the Inconel 718 fabricated by SEBM vary greatly when specific parameters are different. Therefore, the internal defects can be roughly judged by the surface morphology, while the mechanical properties need further evaluation.

4.2. Machine learning models for optimizing SEBM processing window

SVR and GPR models have exhibited good ability of learning and prediction in this study. As shown in Figure 6, SVR model incorrectly predicted that Inconel 718 fabricated in the region with low beam current and high scan speed had high relative density. Error in prediction may be caused by overfitting. Overfitting led to wrong prediction in the test-set in spite of good performance of the machine learning model in the train-set. The composition and preprocessing of data set or the inappropriate hyper-parameters could result in overfitting. Compared with GPR, SVR had better $R^2$and MSE in the test-set, but the robustness and generalization were worse. Therefore, the results of GPR model were better in this study to represent the predicted value of relative density in parameter space. However, it does not mean that any data set related to SEBM process is applicable to GPR model. Complex machine learning model does not necessarily have better learning performance. Model selection is based on the performance, interpretability, complexity of model, size, dimension of data set, and training time and cost. For a new data set, especially when the feature number is large, it is necessary to conduct performance tests on different machine learning algorithms to select the appropriate algorithm, such as ten-fold cross-validation. SVR and GPR chosen here are suitable for few-shot learning, because the data are limited in this study. Another feature deserved that more attention of GPR model is that the prediction error can be directly obtained. Updated GPR model is also convenient for small databases obtained in engineering application. When more measured data are obtained, the new data can be further added to the data set, and the model can be trained again to enhance the prediction performance and accuracy.

The SEBM processing window established through machine learning model with limited data has larger parameter selection range than before[15,25,48], which is conducive to selecting the appropriate processing parameters and controlling microstructure. High beam current and scan speed could improve production efficiency. Moreover, using machine learning to predict, the surface integrity is meaningful. There is a high relative density area at high-energy density, but this area is not suitable to manufacture due to the severe loss of dimensional accuracy. Four new samples that were manufactured according to processing window proved

the reliability of processing window. Although the sample manufactured by the optimized processing parameters still contain some defects, post-treatment such as HIP could heal those defects, and the original grain structure can be maintained as much as possible[21]. The formation of shrinkage porosity defects in Figure 9A may be ascribed to the existence of some imperfect spherical powders in the pre-alloyed powders, which resulted in low-energy absorption rate and thermal conductivity, and it prevented the liquid flowing into the inter-dendritic region to compensate voids[49].

4.3. Mechanical properties and fracture mechanisms

Inconel 718 samples, especially samples P1 and P2, with high relative density (>99.5%) were fabricated by SEBM after process optimization, which displayed different strength and elongation. Samples P1 and P2 had the same energy density. Although P1 had the highest density in this study, its mechanical properties were the worst. As shown in Figure 10, the difference in mechanical properties may be caused by different microstructures. According to the analysis of section 3.4, the unmelted powder resulted in equiaxed grains. The fracture surfaces of P1 and P2 were analyzed to explore the reason, as shown in Figure 15A-F. The samples exhibited dimple fracture, which indicates the ductile fracture mode. Both of them showed fine and equiaxed dimples in the center, and there were no significant differences between the size and depth of dimples. This is consistent with high elongation of P2, while P1 showed low elongation. Brittle fracture was observed at the boundary in Figure 15G, and complete and broken powders in P1 were observed, as shown in Figure 15H and I, respectively. The size of complete powder particle is about 88 μm, which is relatively large among pre-alloyed powder. These unmelted powders did not reduce the relative density of the sample, but retained the original structure of the pre-alloy powder. This, further, suggests that the equiaxed grains in Figure 10 may stem from the unmelted powder. The unmelted powder also resulted in the decrease of plasticity of Inconel 718 sample, because the smooth surface reduced the intergranular bonding force, and Laves phase inside powder perpendicular to the tensile direction also decreased the strength. The unmelted powder in each part of the sample became the breach of fracture. Although P3 and P4 had finer columnar grains, the increase in the number of mixed-equiaxed grain reduced its strength and plasticity. The large area of mixed-equiaxed grain that appeared randomly is the reason for the large variance of the elongation in P3 and P4. Sun *et al.*[51] fabricated the Inconel 718 by SEBM with similar microstructure to P1, whose strength and plasticity were also poor. Therefore, it is necessary to improve energy input to fully melt the original pre-alloyed powder. Reducing the particle size distribution is

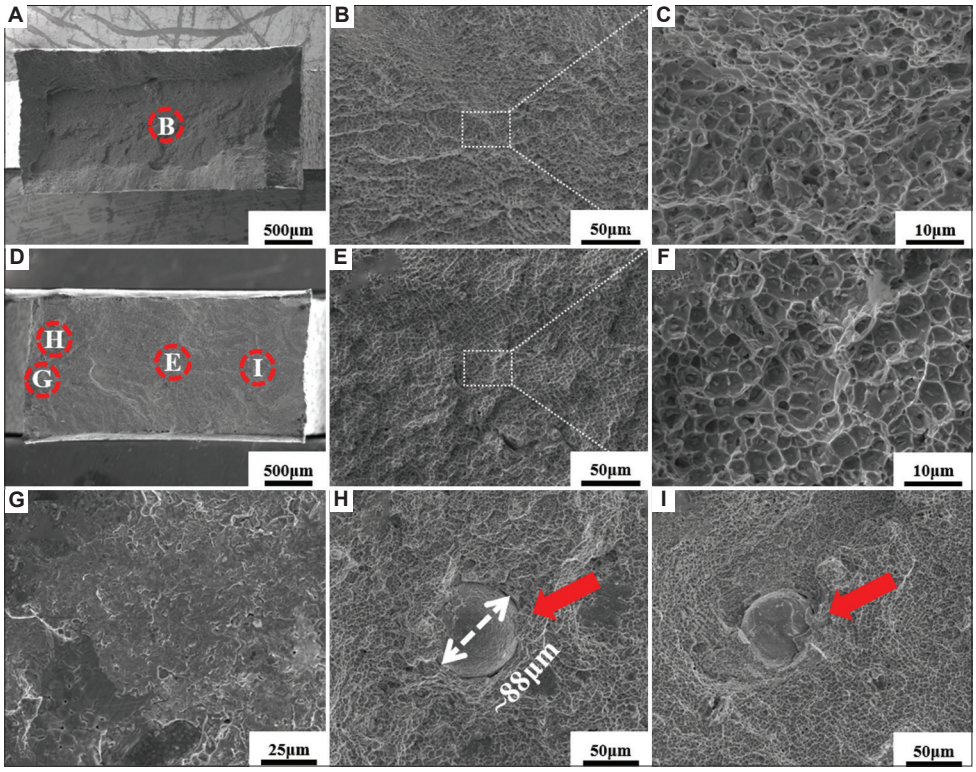

Figure 15. SEM images of fracture surface: (A–C) P2; (D–F) P1; (G), (H) and (I) are the corresponding regions in (D).

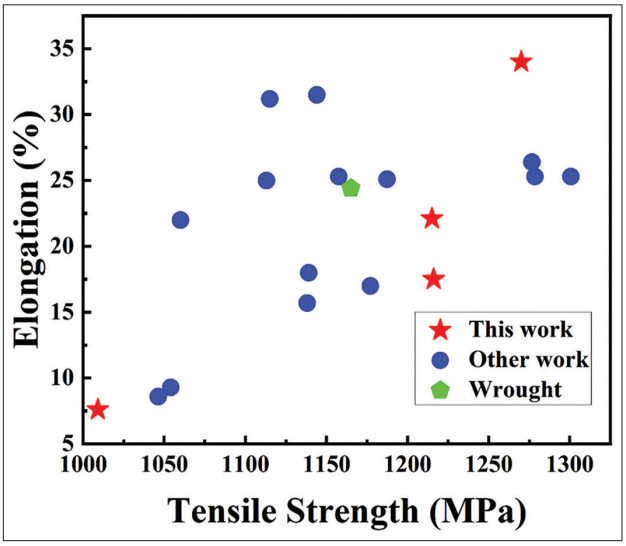

Figure 16. Summary of the tensile strength and elongation of as-built Inconel 718 by selective electron-beam melting from other work[48,54-57] and Wrought[56] Inconel 718, compared to the as-built Inconel 718 sample in this work.

also beneficial to the energy absorption of the powder. The above results suggest that energy density is not good enough to represent the energy absorbed by the powder.

In this study, the mechanical properties were measured in the as-built state. As shown in Figure 16, compared with SEBM and wrought Inconel 718 in other reports, P2 had considerable strength and elongation, because the sample with no defects and finer columnar grains was fabricated in processing window. Laves phase and δ phase (Figure 9B) were rich in strengthening elements such as Nb and Mo which reduced the effect of solid solution strengthening and inhibited the precipitation of γ′ and γ″ strengthening phase[17]. The bulk Laves phase is also the initiation region of the crack. Under normal conditions, solution treatment can make Laves phase dissolve into the matrix, and aging treatment can make strengthening phase precipitate uniformly. Therefore, heat treatment is suggested to further improve mechanical property of Inconel 718.

5. Conclusions

In this study, SEBM processing window was established for Inconel 718 using machine learning model to obtain high relative density. The relationship between the SEBM processing parameters, surface morphology, defects, microstructure, and mechanical properties has been investigated. The main conclusions are as follows:

(i) Excessive energy input leads to uneven surfaces or unshaped samples. Insufficient energy input results in porous surface with lack-of-fusion defects, which is the main reason for low density.

(ii) SVR and GPR models were trained to predict the relative density, and GPR model presents superior predictability. The SEBM processing window for Inconel 718 was obtained by combining GPR relative density contour map with processing parameter window of surface morphology. Machine learning model allows the high-density area to be predicted from a data set which contains a few samples, and the parameter space is larger than before.

(iii) Inconel 718 samples with high relative density (>99.5%) were fabricated by SEBM. Mechanical properties and plasticity are different while at the same energy density. Although the unmelted powder particles did not reduce the relative density of the sample, the smooth surface and the Laves phase inside, which are perpendicular to the tensile direction of the powder, aggravate the properties.

(iv) Sample P2 with few defects and finer columnar grains was prepared using the optimized parameters, and further, mechanical test indicated its excellent combination of strength and ductility.

Acknowledgment

None.

Funding

This work is supported by National Science and Technology Major Project (J2019-IV-0003-0070), National Natural Science Foundation of China (91860105, 52074366, 52001334), China Postdoctoral Science Foundation (2019M662799), Natural Science Foundation of Hunan Province of China (2021JJ40757), Science and Technology Innovation Program of Hunan Province (2021RC3131), and Project Supported by State Key Laboratory of Powder Metallurgy, Central South University, Changsha, China.

Conflict of interest

The authors declared no potential conflicts of interest with respect to the research, authorship, and/or publication of this article.

Author contributions

Conceptualization: Heng Dong, Feng Liu, Liming Tan
Formal analysis: Heng Dong
Funding acquisition: Yong Liu, Li wang
Investigation: Heng Dong, Lin Ye, Xiaoqiong Ouyang
Methodology: Heng Dong, Lin Ye, Xiaoqiong Ouyang
Resources: Qiangbing Wang
Supervision: Liming Tan, Lan Huang
Validation: Heng Dong, Feng Liu
Writing – original draft: Heng Dong, Feng Liu

Writing – review & editing: Heng Dong, Liming Tan, Lan Huang, Xiaochao Jin

All authors have read and agreed to the published version of the manuscript.

References

1. Herzog D, Seyda V, Wycisk E, *et al.*, 2016, Additive manufacturing of metals. *Acta Materialia*, 117: 371–392.

   https://doi.org/10.1016/j.actamat.2016.07.019

2. Sanchez S, Smith P, Xu Z, *et al.*, 2021, Powder Bed Fusion of nickel–based superalloys: A review. *Int J Mach Tools Manuf*, 165: 103729.

   https://doi.org/10.1016/j.ijmachtools.2021.103729

3. Ang YT, Sing SL, Lim JC, 2022, Process study for directed energy deposition of 316L stainless steel with TiB2 metal matrix composites. *Mater Sci Addit Manuf*, 1: 13.

   https://doi.org/10.18063/msam.v1i2.13

4. Körner C, 2016, Additive manufacturing of metallic components by selective electron beam melting–a review. *Int Mater Rev*, 61: 361–377.

   https://doi.org/10.1080/09506608.2016.1176289

5. He M, Ni Y, Wang S, 2021, On the microstructure and tensile properties of Inconel 718 alloy fabricated by selective laser melting and conventional casting. *J Micromech Mol Phys*, 6: 2141003.

   https://doi.org/10.1142/s2424913021410034

6. Hashemi SM, Parvizi S, Baghbanijavid H, *et al.*, 2021, Computational modelling of process–structure–property–performance relationships in metal additive manufacturing: A review. *Int Mater Rev*, 67: 1–46.

   https://doi.org/10.1080/09506608.2020.1868889

7. Sochalski–Kolbus LM, Payzant EA, Cornwell PA, *et al.*, 2015, Comparison of residual stresses in inconel 718 simple parts made by electron beam melting and direct laser metal sintering. *Metall Mater Trans A*, 46: 1419–1432.

   https://doi.org/10.1007/s11661–014–2722–2

8. Leung CL, Tosi R, Muzangaza E, *et al.*, 2019, Effect of preheating on the thermal, microstructural and mechanical properties of selective electron beam melted Ti-6Al-4V components. *Mater Des* 174: 107792.

   https://doi.org/10.1016/j.matdes.2019.107792

9. Liu S, Shin YC, 2019, Additive manufacturing of Ti6Al4V alloy: A review. *Mater Des*, 164: 107552.

   https://doi.org/10.1016/j.matdes.2018.107552

10. Hosseini E, Popovich VA, 2019, A review of mechanical properties of additively manufactured Inconel 718. *Addit Manuf*, 30: 100877.

    https://doi.org/10.1016/j.addma.2019.100877

11. Raab SJ, Guschlbauer R, Lodes MA, *et al.*, 2016, Thermal and electrical conductivity of 99.9% pure copper processed via selective electron beam melting. *Adv Eng Mater*, 18: 1661–1666.

    https://doi.org/10.1002/adem.201600078

12. Yang G, Yang P, Yang K, *et al.*, 2019, Effect of processing parameters on the density, microstructure and strength of pure tungsten fabricated by selective electron beam melting. *Int J Refract Metals Hard Mater*, 84: 105040.

    https://doi.org/10.1016/j.ijrmhm.2019.105040

13. Bond DM, Zikry MA, 2020, Effects of electron beam manufacturing induced defects on fracture in Inconel 718. *Addit Manuf*, 32: 101059.

    https://doi.org/10.1016/j.addma.2020.101059

14. Cunningham R, Narra SP, Ozturk T, *et al.*, 2016, Evaluating the effect of processing parameters on porosity in electron beam melted Ti-6Al-4V via synchrotron X-ray microtomography. *J Miner Metals Mater Soc*, 68: 765–771.

    https://doi.org/10.1007/s11837-015-1802-0

15. Ding X, Koizumi Y, Aoyagi K, *et al.*, 2019, Microstructural control of alloy 718 fabricated by electron beam melting with expanded processing window by adaptive offset method. *Mater Sci Eng A*, 764: 138058.

    https://doi.org/10.1016/j.msea.2019.138058

16. Chandra S, Tan X, Narayan RL, *et al.*, 2021, A generalised hot cracking criterion for nickel-based superalloys additively manufactured by electron beam melting. *Addit Manuf*, 37:101633.

    https://doi.org/10.1016/j.addma.2020.101633

17. Deng D, Peng RL, Söderberg H, *et al.*, 2018, On the formation of microstructural gradients in a nickel-base superalloy during electron beam melting. *Mater Des*, 160: 251–261.

    https://doi.org/10.1016/j.matdes.2018.09.006

18. Deng D, Peng RL, Brodin H, *et al.*, 2018, Microstructure and mechanical properties of Inconel 718 produced by selective laser melting: Sample orientation dependence and effects of post heat treatments. *Mater Sci Eng A*, 713: 294–306.

    https://doi.org/10.1016/j.msea.2017.12.043

19. Chandra S, Tan X, Narayan RL, *et al.*, 2021, Nanometer-scale precipitations in a selective electron beam melted nickel-based superalloy. *Scr Mater*, 194: 113661.

    https://doi.org/10.1016/j.scriptamat.2020.113661

20. Polonsky AT, Echlin MP, Lenthe WC, *et al.*, 2018, Defects and 3D structural inhomogeneity in electron beam additively manufactured Inconel 718. *Mater Char*, 143: 171–181.

    https://doi.org/10.1016/j.matchar.2018.02.020

21. Goel S, Zaninelli E, Gårdstam J, *et al.*, 2020, Microstructure evolution-based design of thermal post-treatments for

EBM-built Alloy 718. *J Mater Sci*, 56: 5250–5268.

https://doi.org/10.1007/s10853-020-05595-2

22. Peng H, Shi Y, Gong S, *et al.*, 2018, Microstructure, mechanical properties and cracking behaviour in a γ'-precipitation strengthened nickel-base superalloy fabricated by electron beam melting. *Mater Des*, 159: 155–169.

https://doi.org/10.1016/j.matdes.2018.08.054

23. Gong H, Rafi K, Gu H, *et al.*, 2014, Analysis of defect generation in Ti-6Al-4V parts made using powder bed fusion additive manufacturing processes. *Addit Manuf*, 1–4: 87–98.

https://doi.org/10.1016/j.addma.2014.08.002

24. Moussaoui K, Rubio W, Mousseigne M, *et al.*, 2018, Effects of Selective Laser Melting Additive manufacturing parameters of Inconel 718 on porosity, microstructure and mechanical properties. *Mater Sci Eng A*, 735: 182–190.

https://doi.org/10.1016/j.msea.2018.08.037

25. Helmer HE, Körner C, Singer RF, 2014, Additive manufacturing of nickel-based superalloy Inconel 718 by selective electron beam melting: Processing window and microstructure. *J Mater Res*, 29: 1987–1996.

https://doi.org/10.1557/jmr.2014.192

26. Rankouhi B, Agrawal AK, Pfefferkorn FE, *et al.*, 2021, A dimensionless number for predicting universal processing parameter boundaries in metal powder bed additive manufacturing. *Manuf Lett*, 27: 13–17.

https://doi.org/10.1016/j.mfglet.2020.12.002

27. Yan W, Qian Y, Ge W, *et al.*, 2018, Meso-scale modeling of multiple-layer fabrication process in Selective Electron Beam Melting: Inter-layer/track voids formation. *Mater Des*, 141: 210–219.

https://doi.org/10.1016/j.matdes.2017.12.031

28. Ammer R, Markl M, Ljungblad U, *et al.*, 2014, Simulating fast electron beam melting with a parallel thermal free surface lattice Boltzmann method. *Comput Math Appl*, 67: 318–330.

https://doi.org/10.1016/j.camwa.2013.10.001

29. Adhitan RK, Raghavan N, 2017, Transient thermo-mechanical modeling of stress evolution and re-melt volume fraction in electron beam additive manufacturing process. *Proc Manuf*, 11: 571–583.

https://doi.org/10.1016/j.promfg.2017.07.151

30. Liu F, Wang Z, Wang Z, *et al.*, 2022, High-throughput method-accelerated design of Ni-based superalloys. *Adv Funct Mater*, 32: 2109367.

https://doi.org/10.1002/adfm.202109367

31. Wang Z, Zhang L, Li W, *et al.*, 2020, High throughput experiment assisted discovery of new Ni-base superalloys. *Scr Mater*, 178: 134–138.

https://doi.org/10.1016/j.scriptamat.2019.11.019

32. Wen C, Zhang Y, Wang C, *et al.*, 2019, Machine learning assisted design of high entropy alloys with desired property. *Acta Mater*, 170: 109–117.

https://doi.org/10.1016/j.actamat.2019.03.010

33. Liu P, Huang H, Antonov S, *et al.*, 2020, Machine learning assisted design of γ'-strengthened Co-base superalloys with multi-performance optimization. *NPJ Comput Mater*, 6: 62.

https://doi.org/10.1038/s41524-020-0334-5

34. Liu F, Xiao X, Huang L, *et al.*, 2022, Design of NiCoCrAl eutectic high entropy alloys by combining machine learning with CALPHAD method. *Mater Today Commun*, 30: 103172.

https://doi.org/10.1016/j.mtcomm.2022.103172

35. Liu F, Wang Z, Wang Z, *et al.*, 2020, Evaluating yield strength of Ni-based superalloys via high throughput experiment and machine learning. *J Micromech Mol Phys*, 5: 2050015.

https://doi.org/10.1142/s2424913020500150

36. Gong X, Zeng D, Groeneveld-Meijer W, *et al.*, 2022, Additive manufacturing: A machine learning model of process-structure-property linkages for machining behavior of Ti-6Al-4V. *Mater Sci Addit Manuf*, 1: 6.

https://doi.org/10.18063/msam.v1i1.6

37. Liu Q, Wu H, Paul MJ, *et al.*, 2020, Machine-learning assisted laser powder bed fusion process optimization for AlSi10Mg: New microstructure description indices and fracture mechanisms. *Acta Mater*, 201: 316–328.

https://doi.org/10.1016/j.actamat.2020.10.010

38. Aoyagi K, Wang H, Sudo H, *et al.*, 2019, Simple method to construct process maps for additive manufacturing using a support vector machine. *Addit Manuf*, 27: 353–362.

https://doi.org/10.1016/j.addma.2019.03.013

39. Lei Y, Aoyagi K, Cui Y, *et al.*, 2020, Process optimization and mechanical property investigation of non-weldable superalloy Alloy713ELC manufactured with selective electron beam melting. *Mater Sci Eng A*, 787: 139485.

https://doi.org/10.1016/j.msea.2020.139485

40. Lei Y, Aoyagi K, Aota K, *et al.*, 2021, Critical factor triggering grain boundary cracking in non-weldable superalloy Alloy713ELC fabricated with selective electron beam melting. *Acta Mater*, 208: 116695.

https://doi.org/10.1016/j.actamat.2021.116695

41. Sah AK, Agilan M, Dineshraj S, *et al.*, 2022, Machine learning-enabled prediction of density and defects in additively manufactured Inconel 718 alloy. *Mater Today Commun*, 30: 103193.

https://doi.org/10.1016/j.mtcomm.2022.103193

42. Smola AJ, Schölkopf B, 2004, A tutorial on support vector regression. *Stat Comput*, 14: 199–222.

https://doi.org/10.1023/b: stco.0000035301.49549.88

43. Luu DN, Zhou W, Nai SM, 2022, Mitigation of liquation cracking in selective laser melted Inconel 718 through optimization of layer thickness and laser energy density. *J Mater Process Technol*, 299: 117374.

https://doi.org/10.1016/j.jmatprotec.2021.117374

44. Balbaa M, Mekhiel S, Elbestawi M, *et al*., 2020, On selective laser melting of Inconel 718: Densification, surface roughness, and residual stresses. *Mater Design*, 193: 108818.

https://doi.org/10.1016/j.matdes.2020.108818

45. Im SY, Jun SY, Lee JW, *et al*., 2020, Unidirectional columnar microstructure and its effect on the enhanced creep resistance of selective electron beam melted Inconel 718. *J Alloys Comp*, 817: 153320.

https://doi.org/10.1016/j.jallcom.2019.153320

46. Zhang L, Li Y, Zhang S, *et al*., 2021, Selective laser melting of IN738 superalloy with a low Mn+Si content: Effect of energy input on characteristics of molten pool, metallurgical defects, microstructures and mechanical properties. *Mater Sci Eng A*, 826: 141985.

https://doi.org/10.1016/j.msea.2021.141985

47. Pedregosa F, Varoquaux G, Gramfort A, *et al*., 2011, Scikit-learn: Machine learning in python. *JMLR*, 12: 2825–2830.

48. Lee HJ, Kim HK, Hong HU, *et al*., 2019, Influence of the focus offset on the defects, microstructure, and mechanical properties of an Inconel 718 superalloy fabricated by electron beam additive manufacturing. *J Alloys Comp*, 781: 842–856.

https://doi.org/10.1016/j.jallcom.2018.12.070

49. Zhao Y, Aoyagi K, Daino Y, *et al*., 2020, Significance of powder feedstock characteristics in defect suppression of additively manufactured Inconel 718. *Addit Manuf*, 34: 101277.

https://doi.org/10.1016/j.addma.2020.101277

50. Chauvet E, Kontis P, Jägle EA, *et al*., 2018, Hot cracking mechanism affecting a non-weldable Ni-based superalloy produced by selective electron Beam Melting. *Acta Mater*, 142: 82–94.

https://doi.org/10.1016/j.actamat.2017.09.047

51. Sun SH, Koizumi Y, Saito T, *et al*., 2018, Electron beam additive manufacturing of Inconel 718 alloy rods: Impact of build direction on microstructure and high-temperature tensile properties. *Addit Manuf*, 23: 457–470.

https://doi.org/10.1016/j.addma.2018.08.017

52. Gui Y, Aoyagi K, Bian H, *et al*., 2022, Detection, classification and prediction of internal defects from surface morphology data of metal parts fabricated by powder bed fusion type additive manufacturing using an electron beam. *Addit Manuf*, 54: 102736.

https://doi.org/10.1016/j.addma.2022.102736

53. Bauereiß A, Scharowsky T, Körner C, 2014, Defect generation and propagation mechanism during additive manufacturing by selective beam melting. *J Mater Process Technol*, 214: 2522–2528.

https://doi.org/10.1016/j.jmatprotec.2014.05.002

54. Strondl A, Palm M, Gnauk J, *et al*., 2011, Microstructure and mechanical properties of nickel based superalloy IN718 produced by rapid prototyping with electron beam melting (EBM). *Mater Sci Technol*, 27: 876–883.

https://doi.org/10.1179/026708309x12468927349451

55. Deng D, Moverare J, Peng RL, *et al*., 2017, Microstructure and anisotropic mechanical properties of EBM manufactured Inconel 718 and effects of post heat treatments. *Mater Sci Eng A*, 693: 151–163.

https://doi.org/10.1016/j.msea.2017.03.085

56. Kirka MM, Medina F, Dehoff R, *et al*., 2017, Mechanical behavior of post-processed Inconel 718 manufactured through the electron beam melting process. *Mater Sci Eng A*, 680: 338–346.

https://doi.org/10.1016/j.msea.2016.10.069

57. Goel S, Zaninelli E, Gundgire T, *et al*., 2021, Microstructure evolution and mechanical response–based shortening of thermal post-treatment for electron beam melting (EBM) produced Alloy 718. *Mater Sci Eng A*, 820: 141515.

https://doi.org/10.1016/j.msea.2021.141515

Materials Science in Additive Manufacturing

ORIGINAL RESEARCH ARTICLE

Experimental and numerical studies on the acoustic performance of simple cubic structure lattices fabricated by digital light processing

Zhejie Lai, Miao Zhao, Chong Heng Lim, Jun Wei Chua*

Department of Mechanical Engineering, National University of Singapore, 117575, Singapore

Abstract

Sound absorption is one of the important properties of porous materials such as foams and lattices. Many mathematical models in the literature are capable of modeling the acoustic properties of lattices. However, appropriate models need to be chosen for specific lattice structures on a case-by-case basis and require significant experience in acoustic modeling. This work aims to provide simplified insights into different mathematical models for the simple cubic lattice. The strut lengths and radii of the unit cells were varied, and the sound absorption properties were measured using an impedance tube. The sound absorption coefficients of the lattices generally increased and exhibited more resonant-like behavior as the strut radius increased. The Delany-Bazley (DB) model and the multi-layered micropore-cavity (MMC) model were used to simulate the acoustic properties of the lattices. The correction factors in the MMC were calculated based on empirical relations fitted using experimental data of the design geometry parameters. Results show that the DB model was able to model the sound absorption coefficients for lattice samples with porosities as low as 0.7, while the MMC with resonator theory is a more appropriate acoustics approach for lattices with porosities lower than 0.7. This work will be highly useful for materials researchers who are studying the acoustic properties of novel porous materials, as well as manufacturers of acoustic materials interested in the additive manufacturing of lattice structures for sound absorption and insulation applications.

Keywords: Lattice structures; Sound absorption; Delany-Bazley model; Transfer matrix method; Resonance

***Corresponding author:**
Jun Wei Chua
(chua.junwei@u.nus.edu)

Citation: Lai Z, Zhao M, Lim CH, *et al*., 2022, Experimental and numerical studies on the acoustic performance of simple cubic structure lattices fabricated by digital light processing. *Mater Sci Add Manuf,* 1(4): 22.
https://doi.org/10.18063/msam.v1i4.22

Received: October 6, 2022

Accepted: October 28, 2022

Published Online: November 17, 2022

1. Introduction

Porous materials have become a desired type of materials in several fields, such as sound absorption and insulation[1-5], heat exchange, chemical processing, bioengineering, and energy storage[3], due to their specific properties, including lightweight, high specific surface area, low bulk density, and microstructure controllability[6,7]. The lattice is one of the three types of porous structural categories, which is an ordered and location-specific structure that repeats the unit cell in a certain manner. In addition, the research of the theories and optimization of lattice are developed due to the additive manufacturing (AM) processing that emerged, which makes lattice fabrication possible.

One of the critical properties is acoustic performance, including sound absorption and sound insulation, which is highly structural-dependent for lattice material. In the history of AM development, various technologies emerged to overcome the difficulties of the AM processes. They can be divided into three large groups, mainly liquid-based, powder-based, and solid-based processes. In general, the liquid-based processes use photosensitive polymers as raw materials and ultraviolet (UV) light as energy source. These liquid-based technologies generally have some advantages, such as cost-effectiveness, high dimension accuracy, good surface finish, and a wide range of available materials. But they also have some shortcomings, such as post-processing requirements, relatively small build volumes, and no multi-materials capability. For solid-based processes such as material extrusion, thermoplastics filaments and metal wires are primarily used as base materials, and heat energy or electron beams are used as an energy source. The advantages of these processes include multi-material parts fabrication, ease of structure removal and minimal material wastage. However, these processes tend to suffer from relatively poor dimensional accuracies and surface finishes, limited material choices and relatively high energy consumption. In addition, as for powder-based technologies, they mainly exploit the high-energy laser and electron beam as an energy source and powder form material including thermoplastics and metals, with the latter being the more common class of materials. These technologies can present fast, with no support structure, large build volume and have additional part function processing. Furthermore, due to the lack of development, the materials are limited and surface finish and accuracy are relatively poor, and the energy consumption is the highest among the total technologies, which are the main disadvantages of the powder-based processes. The detailed information for liquid-, solid-, and powder-based technologies are summarized in Supplementary Text 1 (in Supplementary File).

While the complex interior structure of engineered lattices makes it difficult to analyze their acoustic properties, there exist many mathematical models that aim to characterize the sound absorption or transmission properties of porous materials. These models include the classical Delany-Bazley (DB) model[8], the Johnson-Champoux-Allard model[1,9], the Biot theory[10,11], and the transfer matrix method (TMM)[12,13]. Furthermore, the parameters for the above models may be obtained through measurements, analytical, or empirical methods[1,14-16]. For instance, research on the sound absorption efficiency of IN625 foams has been proposed by Zhai *et al.*[17] The classical DB model using a tetrakaidekahedral unit cell was employed to predict the performance of foams, which are fabricated through template replication processing. A good agreement between the numerical and experimental results was observed. The model was also used alongside the TMM with minor modifications to model the sound absorption properties of functionally graded metal foams with a finite number of layers with great accuracy[18].

A less conventional approach in the acoustic modeling of lattice structures is to view such lattices as resonant materials similar to Helmholtz resonators[19,20] and microperforated panels (MPP)[21,22]. In a recent work on the sound absorption performances of microlattices, the sound and energy absorption of four classes of plate and truss microlattices based on the faced-centered cubic (FCC) crystal structure were investigated[23]. Sound absorption measurements on metal lattice samples of various geometries and the number of layers revealed that there exist various numbers of resonance peaks with absorption coefficients near one. The number of resonance peaks in the frequency range corresponds to the number of layers, with the first peak occurring at the lower frequencies when the number of layers is increased. It was proposed in the work that the modeling of the characteristic impedance based on a modification of major research work by Maa *et al.*[21], which assumes the cavities as a set of micro-perforations, was a viable method that can model such lattices with great accuracies.

From the above case studies, the mechanisms of sound propagation and dissipation can be modeled by methods that may vary significantly in physics. It takes a trained researcher in the acoustics community to determine with confidence the most appropriate mathematical model to model the acoustic properties of lattice structures of a particular geometry, especially if the geometry is novel. Even for the same lattice design, the physics of sound propagation can vary widely with changes in its design parameters such as unit cell size and strut width. Such difficulty in determining the most appropriate modeling approach arises as there is very few concrete acoustics design guidelines dedicated to lattice structures in the literature.

In this work, the acoustic properties of truss lattice structures based on the simple cubic (SC) crystal structure were investigated. Many samples of SC-Truss lattices of varying unit cell lengths and strut radii were fabricated using vat photopolymerization and their sound absorption properties were measured using an impedance tube. This work also investigated the use of both the DB model and the TMM with resonator theory, referred to herein as the multi-layered micropore-cavity (MMC) model, to model the sound absorption performances of the SC-Truss lattices and compared them with the experimental results. Thereafter, some numerical models and guidelines were proposed to

accurately characterize the acoustic properties of the lattices by first choosing the correct model by a design criterion, and then calculating the most appropriate geometrical parameters or correction factors for the model based on the lattice geometry. This work will be of significant utility to materials researchers who are studying the acoustic properties of novel porous materials, as well as manufacturers of acoustic materials interested in the AM of lattice structures for sound absorption and insulation applications.

2. Experimental and numerical methods

2.1. Fabrication of simple cubic lattices

The unit cell design of the SC-Truss lattices in this work is shown in Figure 1. The unit cell is in the form of a cube with a side length D, and the struts of the unit cell is made of cylindrical rods of radius R. The unit cell was then repeated to form a lattice structure of diameter 30 mm and height 30 mm, with truncations done to model the structure as a cylindrical structure. The cylindrical shape of the lattice structures was chosen for sound absorption measurements using an impedance tube of cylindrical cross-section, as detailed in section 2.2. The ranges of strut lengths used in this work were $D \in \{3.0, 5.0, 6.0, 7,5\}$, which gave a total of 10, 6, 5, and 4 layers of unit cells in the structure, respectively. The base case in this work is one that had unit cell dimensions of D = 5.0 mm and r = 1.03 mm, which gave a relative density of 0.3 for the lattice structure. This choice of dimensions allows for comparisons with other related lattice sound absorption works done by our research team in the past[23]. The strut radii r were varied in steps of 0.2 mm such that the porosities of the lattice structures fall between 0.4 and 0.9. The list of strut lengths and radii for the lattice structures in this work is tabulated in Table 1.

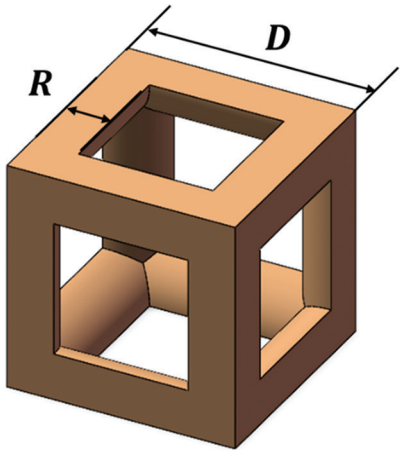

Figure 1. Schematic diagram for SC RUC with dimensions strut length D and strut radius R.

The cylindrical lattice samples were manufactured using vat photopolymerization using the Voxelab Proxima 6.0 printer. The choice of the process was derived from the comparison of the various AM processes as discussed in section 1. The solid-based and powder-based technologies, such as material extrusion and powder bed fusion, are not suited for our fabrication due to the poor surface quality of the printed samples. Moreover, compared among the market-available technologies and machines, vat photopolymerization is the most suitable AM process to be used in this work due to its reasonable material costs, a small quantity of resin during the build as well as minimal shrinkage. The resin used was the standard 405 nm UV resin from NOVA3D, chosen due to its high toughness and strength. A layer thickness of 0.05 mm and an exposure time of 2 s were used during printing. These printing parameters were determined based on the experimental determination of the optimal parameters for the printing of samples using the chosen printer and resin. As-printed parts were cleaned by immersing in isopropyl alcohol and post-cured in a UV curing chamber.

2.2. Acoustic performance characterization

The sound absorption coefficient (α) and sound transition loss were tested by the BSWA SW477 impedance tube

Table 1. Design parameters of samples

Sample	Strut length D (mm)	Strut radius R (mm)
1	3.0	0.43
2	3.0	0.63
3	3.0	0.83
4	5.0	0.63
5	5.0	0.83
6	5.0	1.03
7	5.0	1.23
8	5.0	1.43
9	6.0	0.83
10	6.0	1.03
11	6.0	1.23
12	6.0	1.43
13	6.0	1.63
14	6.0	1.83
15	7.5	1.03
16	7.5	1.23
17	7.5	1.43
18	7.5	1.63
19	7.5	1.83
20	7.5	2.03
21	7.5	2.23

based on the ISO-10534-2 standard. The average room temperature and relative humidities are 26°C and 60%, respectively. Every cylindrical SC lattice was inserted into the 30 mm diameter holder of the impedance tube. About five measurements of the sound absorption coefficients were recorded and averaged. The frequency range of interest is between 1000 Hz and 6300 Hz.

2.3. Numerical modeling of acoustic properties

In this work, the acoustic properties of the SC-Truss lattice cells were analyzed analytically using two different modeling approaches: the DB model[8,12] for porous materials and the TMM[24,25] of which some sub-domains of the air within the cells were modeled as resonant materials.

2.3.1. Delany-Bazley (DB) model

To use the DB model to simulate the sound absorption properties of the SC-Truss lattices, knowledge of their flow resistivity σ is required. These values were calculated by considering the SC-Truss unit cell as a representative unit cell (RUC) as shown in Figure 2.

According to Fourie and Du Plessis's work[26], the RUC dimension d can be calculated as a function of air volume V_a, pore size d_p, and tortuosity χ of the unit cell, given by:

$$d_{RUC} = \frac{V_a}{\chi d_p^2}. \quad \text{(I)}$$

The tortuosity χ is a geometry-dependent parameter of porous materials that characterizes the dispersion of microscopic velocity of a flowing fluid within the materials[12,26]. It can be derived in terms of the porosity φ as following:

$$\chi = 2 + 2\cos\left[\frac{4\pi}{3} + \frac{1}{3}\cos^{-1}\left(2\phi - 1\right)\right]. \quad \text{(II)}$$

Moreover, the pore dimension d_p, which is derived from the simple cubic structure, is the function of the strut length D and strut radius R as follows:

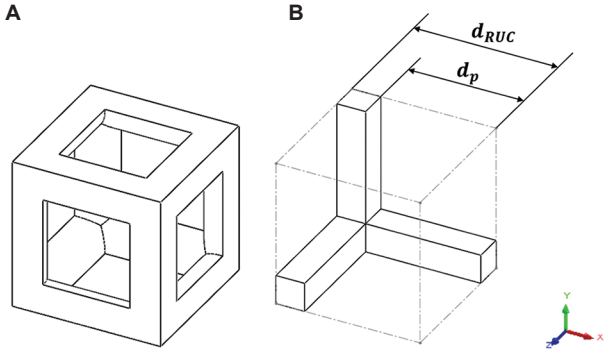

Figure 2. (A) Simple cubic unit cell. (B) Representative unit cell.

$$d_p = \frac{D}{2} - R. \quad \text{(III)}$$

The airflow resistivity σ of the SC-Truss lattices was obtained as follows[17]:

$$\sigma = \frac{36\eta\chi\left(\chi - 1\right)}{\phi^2 d_{RUC}^2}, \quad \text{(IV)}$$

Where η is the dynamic viscosity of the air at 26°C, taken as $\eta = 1.84\times10^{-5}$ kg/(m.s). Based on Equations I to IV, the airflow resistivity σ of the SC-Truss lattices was determined based on the air volume V_f, strut lengths and radii, porosity φ and the dynamic viscosity of the air within the lattice cells. Calculated values of the tortuosity χ, representative unit cell dimension d_{RUC} and airflow resistivity σ are tabulated in Supplementary Text 2 in the Supplementary File.

2.3.2. Multi-layered micropore-cavity (MMC) model

The MMC model is a mathematical model that integrates the use of the TMM and the theories of MPPs to model the sound propagation in multi-layered Helmholtz Resonator structures. Unlike the DB model that views the SC-Truss lattices as homogeneous porous materials, this model views the lattices as multiple layers of micropores with air cavities in between. The TMM is a powerful analytical method to model the propagation of acoustic waves in one-dimensional problems involving multiple discrete layers of acoustic material[12,27]. The general expression of the TMM for n heterogeneous layers in series is as follows:

$$\begin{Bmatrix} p \\ v_y \end{Bmatrix}_{x=0} = \left[\boldsymbol{T}_{layer\,1}\right]\left[\boldsymbol{T}_{layer\,2}\right]\cdots\left[\boldsymbol{T}_{layer\,n}\right]\begin{Bmatrix} p \\ v_y \end{Bmatrix}_{x=L}, \quad = \left[\boldsymbol{T}_{total}\right]\begin{Bmatrix} p \\ v_y \end{Bmatrix}_{x=t} = \begin{bmatrix} T_{11} & T_{12} \\ T_{21} & T_{22} \end{bmatrix}\begin{Bmatrix} p \\ v_y \end{Bmatrix}_{x=L} \quad \text{(V)}$$

where $\left[\boldsymbol{T}_{layer\,x}\right]$ is the transfer matrix for Layer x. To model the acoustic properties of the SC-Truss lattices using the TMM, the air domain within the SC-Truss unit cell, as shown in Figure 1, needs to be discretized into sub-domains and the acoustic properties determined individually. The sub-domains consist of two narrow tubes of square cross-section and a central open cavity similar to that of the unit cell, as shown in Figure 3. The narrow tubes on both ends of the cavity have a side length of $d_{tube} = D - 2R$ and a thickness of $t_{tube} = \frac{R}{\sqrt{2}}$. The latter dimension results from the cylindrical cross-sectional geometry of the individual struts. The cavity is then modeled as a layer of air of thickness $l_{cav} = D - 2t_{tube} = D - \sqrt{2}R$.

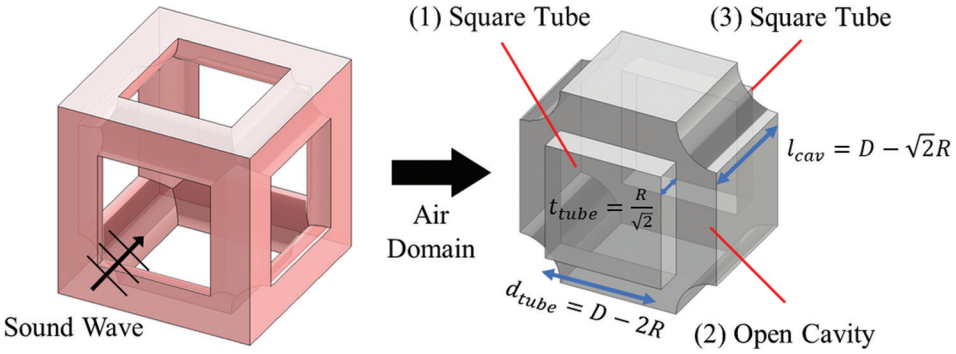

Figure 3. Discretization of the air domain of the SC-Truss unit cell for the acoustic modeling using the MMC model.

By assuming the closed tubes of square cross-section as a set of resonant materials, the transfer matrix is given by[25]

$$\boldsymbol{T}_r = \begin{bmatrix} 1 & Z_r \\ 0 & 1 \end{bmatrix}, \tag{VI}$$

Where Z_r is the characteristic impedance of the closed tube. Based on the works by Maa, Morse and Ingard[21,22] on microperforated panel absorbers, Z_r can be expressed as follows:

$$Z_r = \frac{32\eta t_{tube}}{\varepsilon d_{tube}^2}\left(\sqrt{1+\frac{k^2}{32}} + 2\delta_1 R_s\right) + j\frac{\omega\rho_0 t_{tube}}{\varepsilon}\left(1+\frac{1}{\sqrt{9+\frac{k^2}{2}}} + \delta_2\frac{d_{tube}}{t_{tube}}\right), \tag{VII}$$

Where η, ρ_0 refer to the dynamic viscosity and density of air at 25°C respectively, ω is the angular frequency of the sound waves, j is the imaginary unit such that $j^2 = -1$, ε is the perforation ratio of the square tubes given by $\varepsilon = \left(\frac{d_{tube}}{D}\right)^2$, $k = \left(\frac{d_{tube}}{2}\right)\sqrt{\frac{\rho\omega}{\eta}}$ is the perforate constant, and $R_s = \frac{1}{2}\sqrt{2\eta\rho_0\omega}$ is the resistive end-correction factor that accounts for the air friction arising from the oscillatory viscous flow on the surface of the perforated panel. δ_1 and δ_2 are the resistive and reactive correction factors to be determined from experimentally determined sound absorption coefficient results from this work.

For the open cavity of the SC-Truss unit cell, the layer was simply modeled as a layer of air of density ρ_0 and speed of sound c_0, similar to the air outside the lattice cells. The transfer matrix of the cavity is given by[25].

$$\boldsymbol{T}_c = \begin{bmatrix} \cos(k_0 l_{cav}) & jZ_0\sin(k_0 l_{cav}) \\ j\frac{1}{Z_0}\sin(k_0 l_{cav}) & \cos(k_0 l_{cav}) \end{bmatrix}, \tag{VIII}$$

Where $Z_0 = \rho_0 c_0$ and $k_0 = \frac{\omega}{c_0}$ are the characteristic impedance and the wave number of the air layer, respectively. Thereafter, the transfer matrix of one layer of SC-Truss unit cells is given by,

$$\left[\boldsymbol{T}_{layer\,x}\right] = \boldsymbol{T}_r\boldsymbol{T}_c\boldsymbol{T}_r = \begin{bmatrix} 1 & Z_r \\ 0 & 1 \end{bmatrix} \begin{bmatrix} \cos(k_0 l_{cav}) & jZ_0\sin(k_0 l_{cav}) \\ j\frac{1}{Z_0}\sin(k_0 l_{cav}) & \cos(k_0 l_{cav}) \end{bmatrix} \begin{bmatrix} 1 & Z_r \\ 0 & 1 \end{bmatrix}. \tag{IX}$$

The sound absorption coefficient is a measure of the proportion of sound energy absorbed and dissipated by a material when a sound wave is incident on it and is commonly used to quantify the sound absorption capability of a material[28]. An estimate of the sound absorption coefficient α_{TMM} for each frequency f for the multi-layered material can be determined directly for T_{total} by the following expression[25]:

$$\alpha_{TMM}(f) = 1 - \left|\frac{T_{11} - \frac{\rho_0 c_0 T_{21}}{\cos\theta}}{T_{11} + \frac{\rho_0 c_0 T_{21}}{\cos\theta}}\right|^2, \tag{X}$$

Where θ is the angle of incidence of the sound wave. For normal incidence, $\theta = 0°$ and hence $\cos\theta = 1$.

Based on experimental data, the optimal values of the correction factors δ_1 and δ_2 were determined and their relations to the geometric parameters of the SC-Truss unit cell were proposed. Thereafter, α_{TMM} for each case were

calculated with δ_1 and δ_2 calculated from the proposed models. The mean absolute error of the absorption coefficients over the entire frequency range was obtained for each case. The calculated values of tube side length d_{tube}, tube thickness t_{tube}, cavity layer thickness l_{cav}, and the perforation ratio ε are tabulated in Supplementary Text 2 in the Supplementary File.

3. Results

3.1. Manufacturing of samples and dimensional analysis

Representative macroscopic and microscopic sample images are presented in Figure 4A and 4B, respectively. The rest of the macroscopic and microscopic sample images are presented in Supplementary Texts 3 and 4, respectively. The strut lengths and radii of the samples were measured under the digital microscope using pixel measurement. At least three measurements of both the strut lengths and radii were taken, and the arithmetic averages were obtained. The percentage error in dimensions was calculated using Equation XI below.

$$Percentage\,error = \frac{\left|\text{Measured dimension} - \text{Design dimension}\right|}{\text{Design dimension}} \times 100\% \quad \text{(XI)}$$

The design dimensions, actual dimensions, and dimension error percentages are tabulated in Table 2. It is obvious that all the actual dimension values were close to the designed values the error percentages were approximately 0%–2% and several cases were about 3%–4%. In general, the percentage dimension errors were acceptable and hence the design dimensions may be used in subsequent analytical analysis without a need for error corrections.

3.2. Sound absorption coefficients of SC-Truss lattice structures

The sound absorption coefficients of all the SC-Truss lattices are plotted in Figure 5. Each of the plots of sound frequencies with sound absorption coefficients was of the same strut length. The mean and standard deviations of the absorption coefficients are also plotted in Figure 5.

Overall, for fixed strut lengths, the average sound absorption performance of the SC-Truss lattice was enhanced when the strut radius was increased. The mean absorption coefficients generally increased with increasing strut radius. The variations in sound absorption coefficients became more fluctuating with increasing strut radius with fixed strut length. This can also be observed from the higher standard deviations of the absorption coefficients with increasing strut radii. In addition, when the curves showed the peak and valley characteristics, increasing the strut radius resulted in the reduced frequency of the first peak absorption coefficient and a higher coefficient value at the first peak frequency.

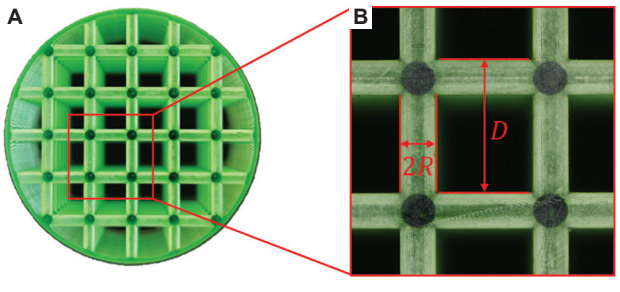

Figure 4. (A) Macroscopic sample image. (B) Microscopic sample image. Abbreviations: *D*, strut length; *R*, strut radius.

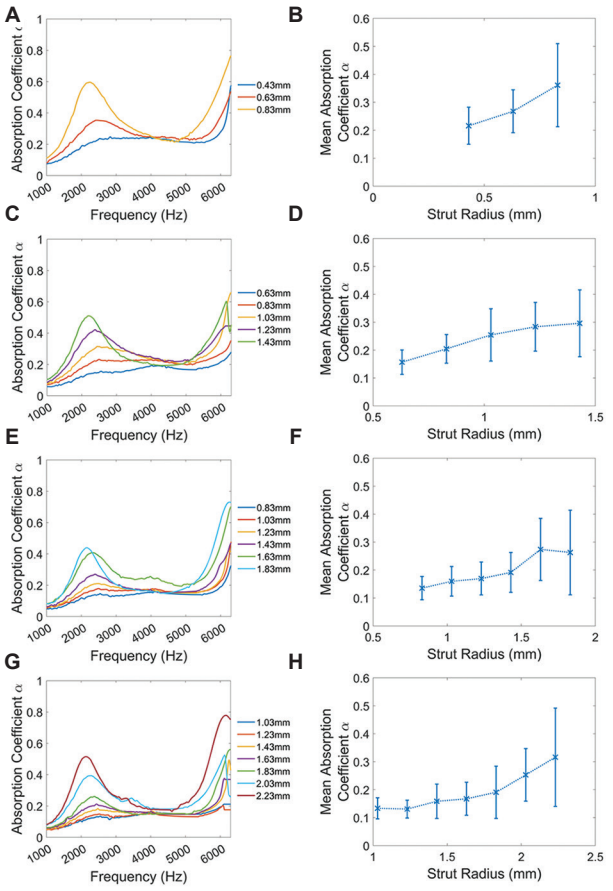

Figure 5. Plots of the sound absorption coefficients obtained from experimental measurements. (A) and (B) correspond to the cases for D = 3 mm, (C) and (D) correspond to the cases for D = 5 mm, (E) and (F) correspond to the cases for D = 6 mm, and (G) and (H) correspond to the cases for D = 7.5 mm. (A), (C), (E), and (G) correspond to the cases where d is the smallest among cases with the same D, while (B), (D), (F), and (H) correspond to the cases where d is the largest amongst cases with the same D.

Table 2. Dimension analysis of the fabricated lattice samples

Sample	Strut length *D* (mm)			Strut radius *R* (mm)		
	Design	Measured	Percentage error	Design	Measured	Percentage error
1	3.0	2.99	0.22	0.43	0.44	1.55
2	3.0	3.00	0.11	0.63	0.65	3.44
3	3.0	2.98	0.78	0.83	0.83	0.20
4	5.0	4.99	0.27	0.63	0.66	4.76
5	5.0	5.00	0.00	0.83	0.81	2.41
6	5.0	5.01	0.13	1.03	1.02	1.29
7	5.0	5.00	0.00	1.23	1.22	1.08
8	5.0	4.97	0.53	1.43	1.44	0.70
9	6.0	6.02	0.39	0.83	0.86	3.01
10	6.0	6.03	0.44	1.03	1.04	0.65
11	6.0	6.01	0.22	1.23	1.25	1.76
12	6.0	6.04	0.61	1.43	1.45	1.17
13	6.0	6.02	0.28	1.63	1.65	1.12
14	6.0	6.03	0.50	1.83	1.84	0.27
15	7.5	7.53	0.40	1.03	1.05	2.10
16	7.5	7.53	0.40	1.23	1.25	1.76
17	7.5	7.53	0.44	1.43	1.46	1.75
18	7.5	7.53	0.40	1.63	1.64	0.51
19	7.5	7.51	0.18	1.83	1.86	1.73
20	7.5	7.53	0.36	2.03	2.07	1.72
21	7.5	7.51	0.13	2.23	2.25	0.67

3.3. Numerical modeling of sound absorption performances

3.3.1. Delany-Bazley (DB) model

Representative plots of the sound absorption coefficients obtained from the DB model are shown in Figure 6. For each strut length, the strut radii used for the plots are the smallest and largest among the cases of the same strut length. The comparison plots for all the test cases in this work are collated in Supplementary Text 5 in the Supplementary File. It can be seen that for small strut radii, the DB model generally modeled the general increase in absorption coefficients with increasing frequencies reasonably well. That being said, the model tends to underestimate the sound absorption coefficients, especially at high frequencies. These under-estimation issues were more apparent for higher strut lengths. For large strut radii, the DB model was able to model the peak absorption behaviors at low frequencies. However, the peak absorption coefficients predicted by the DB model tend to be slightly larger than the experimental values. Furthermore, the DB model was not able to correctly model the high sound absorption peaks at higher frequencies above 5000 Hz, instead the model predicted significantly lower sound absorption coefficients at those frequencies. It is noted that the DB model was derived to model the sound absorption performances of porous materials of high porosity such as synthetic foams. Therefore, it was likely that the DB model was not able to accurately model the sound absorption performances of porous materials of moderate porosity, such as the lattices in this work with high strut radii.

3.3.2. Multi-layered micropore-cavity (MMC) model

Using different pairs of values for the correction factors δ_1 and δ_1, the sound absorption coefficients over the frequency range of interest were calculated using the MMC model as described in section 2.3.2. Thereafter, the optimal $\{\delta_1, \delta_2\}$ pair was chosen based on the mean absolute errors in sound absorption coefficients as compared with the experimental values. The optimal values of δ_1 and δ_2 for each test case were collated in Supplementary Text 6 in the Supplementary File. It was proposed that the correction factors δ_1 and δ_2 may be dependent on the geometry of the narrow tubes or the lattice samples, such as the tube side length d_{tube}, tube thickness t_{tube}, perforation ratio ε, and the

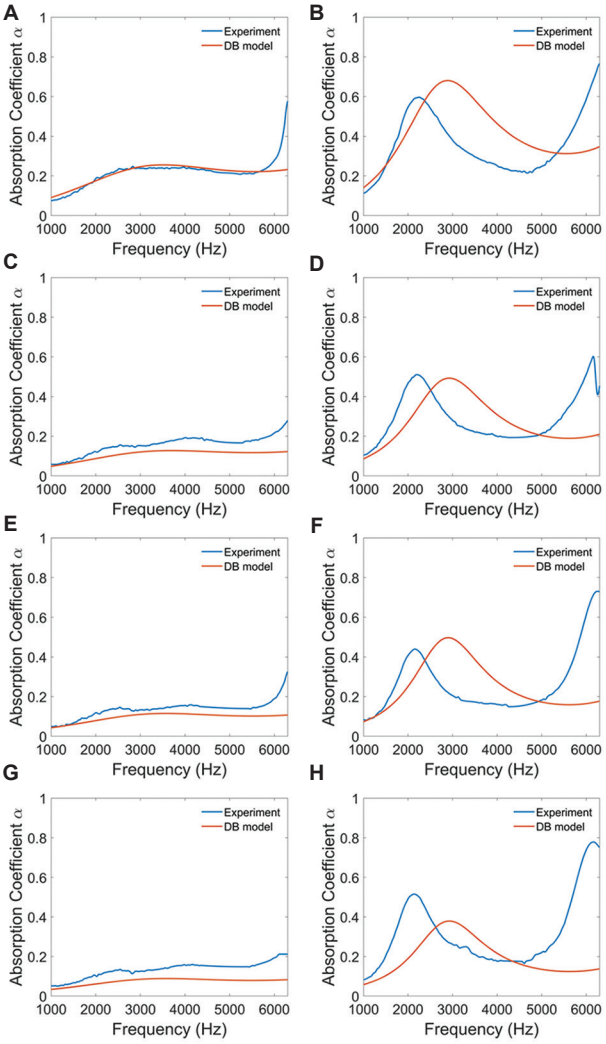

Figure 6. Plots of the sound absorption coefficients obtained from both experimental measurements and numerical modeling using the DB model. (A) and (B) correspond to the cases for D = 3 mm, (C) and (D) correspond to the cases for D = 5 mm, (E) and (F) correspond to the cases for D = 6 mm, and (G) and (H) correspond to the cases for D = 7.5 mm. (A), (C), (E), and (G) correspond to the cases where d is the smallest amongst cases with the same D, while (B), (D), (F), and (H) correspond to the cases where d is the largest amongst cases with the same D.

number of unit cell layers N in the lattice samples. Observations of the data revealed that δ_1 could be a function of $\frac{d_{tube}}{t_{tube}}$ and N, as shown in the plot of $\frac{d_{tube}}{t_{tube}}$ against $N\delta_1$ in Figure 7A. Linear regression was done on the data points and the data points seem to lie close to the regression line with $R^2 = 0.8547$. The regression line has the following equation:

$$N\delta_1 = 183.0961\frac{d_{tube}}{t_{tube}} - 109.0583 \quad \text{(XII)}$$

Similarly, δ_1 could be a function of the perforation ratio ε (Figure 7B). Such a hypothesis is because the reactance correction factor is already a function of $\frac{d_{tube}}{t_{tube}}$ and similar hypothesis on δ_2 were made in the previous works[29]. However, it can be seen that δ_2 was zero when the perforation ratio was too low or too high, while δ_2 peaks when the perforation ratio is around 0.35. Henceforth, it was proposed that the data points are divided into two equal subsets based on the porosity φ of the lattice samples. By applying linear regression on each of the subsets, the following empirical piecewise relation for δ_2 was obtained:

$$\delta_2 = \begin{cases} 1.9320\varepsilon - 0.3012 \; for \phi < 0.6893 \\ -0.7545\varepsilon + 0.5879 \; for \phi < 0.6893 \end{cases} \quad \text{(XIII)}$$

The coefficients of determination R^2 for the two linear regression lines were 0.8629 and 0.4782, respectively. While the first regression line fits the data points well, the linear correlation between the perforation ratio and δ_2 was relatively weak, owing to the large variations in values of δ_2 at higher porosities.

Representative plots of the sound absorption coefficients obtained from the DB model are shown in Figure 8. Similar to Figure 6, the strut radii used for the plots are the smallest and largest strut radii among the cases of the same strut length. The comparison plots for all the test cases in this work were collated in Supplementary Text 7 in the Supplementary File. Based on the observation from the figure for small strut radii, the MMC model was also appropriate in simulating the sound absorption behavior throughout the frequency range. However, the deviations from the experimental results were slightly larger than that of the DB model due to the higher peak frequencies at frequencies below 4000 Hz predicted by the MMC model. Unlike the DB model, the MMC model was able to model the sound absorption properties of lattices of larger strut radii more closely to the experimental results. Such good fitting of experimental results can be reasoned that the cross-sectional area of the square tubes in Figure 3 was sufficiently small such that they bear closer resemblances to conventional MPPs in the literature. Moreover, the use of empirical relations in Equations XII and XIII assisted in shifting the sound absorption curves closer to the experimental data due to how the relations were derived. Hence, it can be concluded that the MMC model was a better mathematical model to model the sound absorption properties of lattices with large strut radii.

3.3.3. Mean absolute errors in absorption coefficients

The plot of the mean percentage errors of the absorption coefficients based on the DB model and the MMC model is

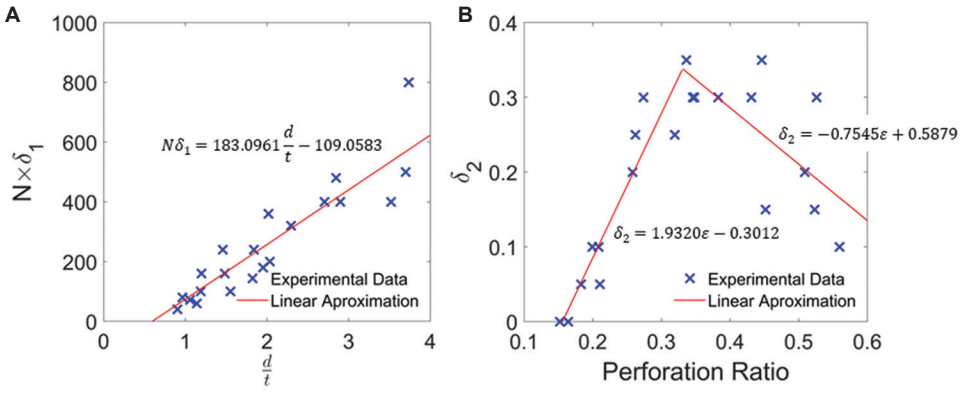

Figure 7. (A) Plot of $\frac{d_{tube}}{t_{tube}}$ against $N\delta_1$, with the plot and equation of the linear approximation of the experimental data. (B) The plot of the perforation ratio ε against δ_2, with the plots and equations of the piecewise linear approximations of the experimental data.

shown in Figure 9. Values of the mean percentage errors are provided in Supplementary Text 8 in the Supplementary File. It can be seen that the DB model resulted in percentage errors of mostly between 5% and 60%, with most of the errors being around 20%–30%. Notably, the mean percentage error is the lowest at 8.5% for the sample with D = 3.0 mm and R = 0.43 mm. The percentage errors for low porosity lattices (φ < 0.5) were noticeably high at above 40%. This is expected considering the low accuracy of the DB model for low-porosity materials. In contrast, the percentage errors from the MMC model were relatively lower than that of the DB model at around 10%–20% for most lattice samples. Moreover, the MMC model predicted the sound absorption performances significantly better than the DB model for lattice samples with porosities below 0.7, while the percentage errors were comparable to the DB model for porosities above 0.7. Hence, one can infer that for SC-Truss lattices with porosities below 0.7, the MMC model is a more accurate model to calculate the sound absorption coefficients. For SC-Truss lattices with porosities above 0.7, both the DB model and the MMC model work similarly well in predicting the sound absorption coefficients. That being said, it is recommended to use the DB model over the MMC model due to the simplicity of the DB model.

4. Discussion

First, this work demonstrated the good dimensional accuracies of the SC-Truss lattice samples fabricated using the vat photopolymerization process. As compared to other AM processes such as material extrusion, powder bed fusion, and material jetting, the major manufacturing defects such as surface roughness and micro-porosities are less apparent in the fabricated samples[5]. Therefore, this observation proved useful in the characterization of the acoustic properties of lattice structures manufactured using AM, as the design geometrical parameters may be used in the mathematical models without much concern over corrections to the geometry. Furthermore, the photopolymer resin used in this work was notable for its high toughness and strength and has been used in previous works with high build quality and high dimensional accuracies[30,31]. Hence, the sound absorption of these lattices by structural vibrations and material damping may be neglected[12,32], which simplifies the acoustic analysis significantly.

Second, it is understood that there exists a set of criteria in which the DB model is valid[12,33]. In particular, it is acknowledged that the DB model works well only when the porosity of the porous material is close to one. Through this work, it is determined that the DB model may be able to model the acoustic properties of SC-Truss lattices for porosities above 0.7, though percentage errors of about 20% are expected. Hence, to fabricate such lattices on a large scale for industrial applications, the DB model is still applicable and can be used to determine a general trend in the variation of sound absorption coefficients with frequency. The simplicity of the DB model expressions, as well as the availability of several methods of determining the airflow resistivity of the fabricated lattices[26,34], ensures that the model is a more attractive mathematical model to use as compared to other more complicated models, such as the JCA model[12].

Finally, the determination of both δ_1 and δ_2 through experimentation and statistical regression is an approach that is less reported in the modeling of acoustic materials using the theories related to the MPP absorbers. One of the first works to do so is the work by Maa, Morse and Ingard, which assigned discrete values to δ_1 and δ_2 based on the general morphology of the narrow perforations[21,22]. Common values for δ_1 are 2 and 4, depending on whether

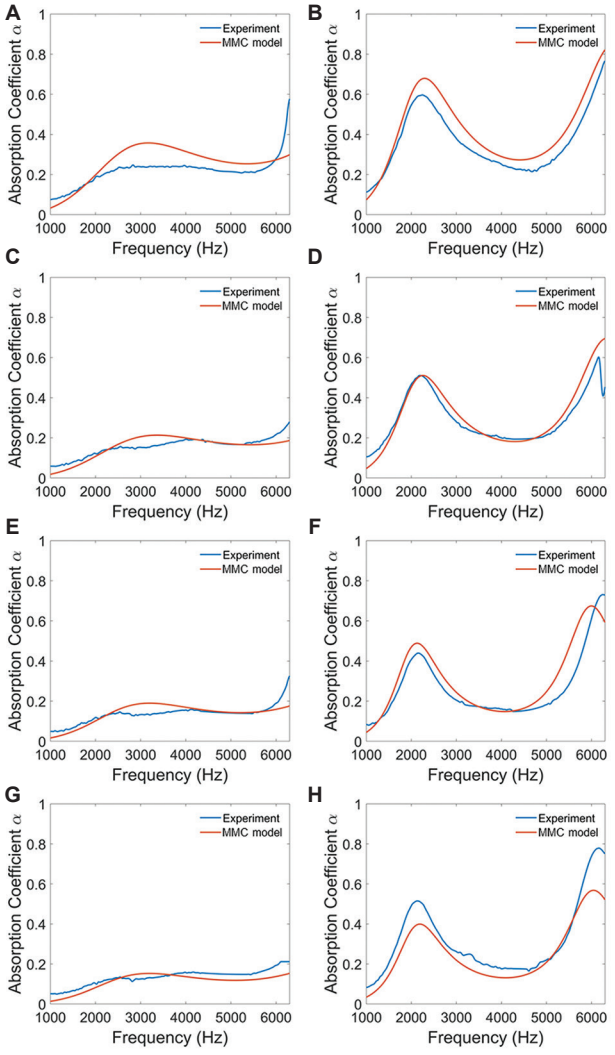

Figure 8. Plots of the sound absorption coefficients obtained from both experimental measurements and numerical modeling using the MMC model. (A) and (B) correspond to the cases for D = 3 mm, (C) and (D) correspond to the cases for D = 5 mm, (E) and (F) correspond to the cases for D = 6 mm, and (G) and (H) correspond to the cases for D = 7.5 mm. (A), (C), (E), and (G) correspond to the cases where d is the smallest amongst cases with the same D, while (B), (D), (F), and (H) correspond to the cases where d is the largest amongst cases with the same D.

the edges of the holes were round or sharp, respectively, which several prior works using Maa's formulation set δ_2 as 0.85[21,30,31,35]. However, this work has shown that such crude choices of δ_1 and δ_2 may not be effective in the context of lattice structures due to the vast difference in length scales and pore shapes. Rather, the values may be related to the detailed geometry of the lattice unit cells and pores and must be determined on a case-by-case basis. For the SC-Truss, no research works have documented the process of determining appropriate expressions for δ_1 and δ_2 for the MMC model to model the sound absorption

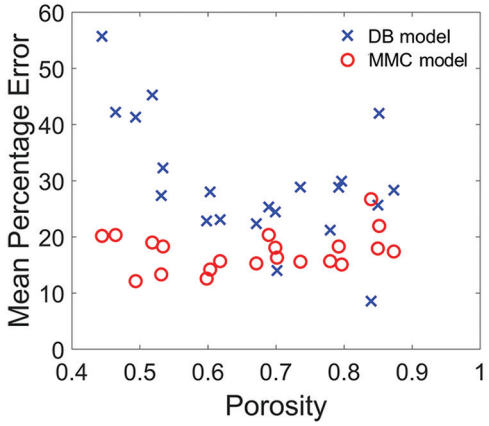

Figure 9. Plot of the porosity of the SC-Truss lattices against the mean percentage errors of the sound absorption coefficients obtained from experiments and numerical models.

properties with high accuracies. Therefore, this work is a valuable contribution to both the acoustics and materials community in determining appropriate expressions of the correction factors so that researchers and manufacturers may use the MMC model to predict the sound absorption or transmission properties of the SC-Truss lattices without having to be too concerned about the correctness of the correction factors in the model.

5. Conclusions

In this work, the acoustic properties of truss lattice structures based on the SC crystal structure were investigated. Many samples of SC-Truss lattices of varying unit cell lengths and strut radii were fabricated using vat photopolymerization, and their sound absorption properties were measured using an impedance tube. It was shown that as the strut radius increases, the sound absorption performances generally increase and become more resonant-like. This work also investigated the use of both the DB model and the MMC model to model the sound absorption performances of the SC-Truss lattices and compared them with the experimental results. It was determined that the correction factors in the MMC model may be calculated based on the empirical relation given in Equations XII and XIII, using present design geometry parameters. Furthermore, it was determined that the DB model was able to model the sound absorption coefficients for lattice samples with porosities as low as 0.7, hence seemingly stretching the limits of the validity of the model. For lattices with porosities lower than 0.7, the MMC model is a more appropriate acoustics approach than the DB model. This work will be of significant utility to materials researchers who are studying the acoustic properties of novel porous materials, as well as manufacturers of

acoustic materials interested in the AM of lattice structures for sound absorption and insulation applications.

Acknowledgments

The authors would also like to acknowledge Dr. Wei Zhai, Dr. Xinwei Li, and Dr. Xiang Yu for their supervision and valuable suggestions on the research work.

Funding

This research is supported by the NUS R&G Postdoc Fellowship Program (Project No. A-0000065-25-00).

Conflict of interest

The authors declare that they have no known competing financial interests or personal relationships that could have appeared to influence the work reported in this paper. Any opinions, findings, and conclusions or recommendations expressed in this material are those of the author(s) and do not reflect the views of National University of Singapore (NUS).

Author contributions

Conceptualization: Zhejie Lai, Jun Wei Chua
Investigation: Zhejie Lai, Miao Zhao, Chong Heng Lim
Methodology: Zhejie Lai, Miao Zhao, Chong Heng Lim, Jun Wei Chua
Resources: Chong Heng Lim
Supervision: Jun Wei Chua
Validation: Zhejie Lai, Jun Wei Chua
Writing – original draft: Zhejie Lai, Jun Wei Chua
Writing – review & editing: Jun Wei Chua

References

1. Cao L, Fu Q, Si Y, *et al*., 2018, Porous materials for sound absorption. *Composites Commun,* 10: 25–35

   https://doi.org/10.1016/j.coco.2018.05.001

2. Jia C, Li L, Liu Y, *et al*., 2020, Highly compressible and anisotropic lamellar ceramic sponges with superior thermal insulation and acoustic absorption performances. *Nat Commun*, 11: 3732.

   https://doi.org/10.1038/s41467-020-17533-6

3. Yu X, Lu Z, Zhai W, 2021, Enhancing the flow resistance and sound absorption of open-cell metallic foams by creating partially-open windows. *Acta Mater,* 206: 116666.

   https://doi.org/10.1016/j.actamat.2021.116666

4. Yang W, An J, Chua CK, *et al*., 2020, Acoustic absorptions of multifunctional polymeric cellular structures based on triply periodic minimal surfaces fabricated by stereolithography. *Virtual Phys Prototyp*, 15: 242–249.

   https://doi.org/10.1080/17452759.2020.1740747

5. Zieliński TG, Opiela KC, Pawłowski P, *et al*., 2020, Reproducibility of sound-absorbing periodic porous materials using additive manufacturing technologies: Round robin study. *Additive Manuf,* 36: 101564.

   https://doi.org/10.1016/j.addma.2020.101564

6. Cheng Y, Xu Z, Chen S, *et al*., 2021, The influence of closed pore ratio on sound absorption of plant-based polyurethane foam using control unit model. *Appl Acoust*, 180: 108083.

   https://doi.org/10.1016/j.apacoust.2021.108083

7. Doutres O, Atalla N, Dong K, 2011, Effect of the microstructure closed pore content on the acoustic behavior of polyurethane foams. *J Appl Phys,* 110: 064901.

   https://doi.org/10.1063/1.3631021

8. Delany ME, Bazley EN, 1970, Acoustical properties of fibrous absorbent materials. *Appl Acoust,* 3: 105–116.

   https://doi.org/10.1016/0003-682X(70)90031-9

9. Kino N, 2015, Further investigations of empirical improvements to the Johnson-Champoux-Allard model. *Appl Acoust,* 96: 153–170.

   https://doi.org/10.1016/j.apacoust.2015.03.024

10. Biot MA, 1956, Theory of propagation of elastic waves in a fluid-saturated porous solid. II. Higher frequency range. *J Acoust Soc Am,* 28: 179–191.

    https://doi.org/10.1121/1.1908241

11. Dib L, Bouhedja S, Amrani H, 2015, Mechanical parameters effects on acoustic absorption at polymer foam. *Adv Mater Sci Eng,* 2015: 1–10.

    https://doi.org/10.1155/2015/896035

12. Allard JF, Atalla N, 2009, Propagation of Sound in Porous media: Modelling Sound Absorbing Materials. 2nd ed. Wiley, Hoboken, N.J. p358.

13. Verdiere K, Panneton R, Elkoun S, *et al*., Transfer matrix method applied to the parallel assembly of sound absorbing materials. *J Acoust Soc Am*, 134: 4648.

    https://doi.org/10.1121/1.4824839

14. Niskanen M, Groby JP, Duclos A, *et al*., 2017, Deterministic and statistical characterization of rigid frame porous materials from impedance tube measurements. *J Acoust Soc Am,* 142: 2407.

    https://doi.org/10.1121/1.5008742

15. Boulvert J, Cavalieri T, Costa-Baptista J, *et al*., Optimally graded porous material for broadband perfect absorption of sound. *J Appl Phys*, 126: 175101.

    https://doi.org/10.1063/1.5119715

16. Chen S, Lei S, Zhu J, *et al*., 2021, The influence of microstructure on sound absorption of polyurethane foams through numerical simulation. *Macromol Theory Simul,* 30: 2000075.

https://doi.org/10.1002/mats.202000075

17. Zhai W, Yub X, Song X, *et al.*, 2018, Microstructure-based experimental and numerical investigations on the sound absorption property of open-cell metallic foams manufactured by a template replication technique. *Mater Design*, 137: 108–116.

    https://doi.org/10.1016/j.matdes.2017.10.016

18. Chua JW, Li X, Li T, *et al.*, 2022, Customisable sound absorption properties of functionally graded metallic foams. *J Mater Sci Technol*, 108: 196–207.

    https://doi.org/10.1016/j.jmst.2021.07.056

19. Gai XL, Xing T, Li XY, *et al.*, 2016, Sound absorption of microperforated panel mounted with helmholtz resonators. *Appl Acoust,* 114: 260–265.

    https://doi.org/10.1016/j.apacoust.2016.08.001

20. Komkin AI, Mironov MA, Bykov AI, 2017, Sound absorption by a Helmholtz resonator. *Acoust Phys,* 63: 385–392.

    https://doi.org/10.1134/s1063771017030071

21. Maa DY, 1998, Potential of microperforated panel absorber. *J Acoust Soc Am,* 104: 2861–2866.

    https://doi.org/10.1121/1.423870

22. Morse PM, Ingard KU, 1968, Theoretical Acoustics (International Series in Pure and Applied Physics). McGraw-Hill, New York.

23. Li X, Yu X, Chua JW, *et al.*, 2021, Microlattice metamaterials with simultaneous superior acoustic and mechanical energy absorption. *Small,* 17: e2100336.

    https://doi.org/10.1002/smll.202100336

24. Doutres O, Atalla N, Osman H, 2015, Transfer matrix modeling and experimental validation of cellular porous material with resonant inclusions. *J Acoust Soc Am,* 137: 3502–3513.

    https://doi.org/10.1121/1.4921027

25. Jiménez N, Umnova O, Groby JP, 2021, Acoustic Waves in Periodic Structures, Metamaterials, and Porous Media (Topics in Applied Physics). Springer, Germany.

26. Fourie JG, Du Plessis JP, 2002, Pressure drop modelling in cellular metallic foams. *Chem Eng Sci*, 57: 2781–2789.

    https://doi.org/10.1016/s0009-2509(02)00166-5

27. Verdière K, Panneton R, Elkoun S, *et al.*, 2013, Transfer matrix method applied to the parallel assembly of sound absorbing materials. *J Acoust Soc Am,* 134: 4648–4658.

    https://doi.org/10.1121/1.4824839

28. Ashby M, Evans T, Fleck NA, 2000, Metal Foams: A Design Guide. Elsevier, Burlington.

29. Okuzono T, Nitta T, Sakagami K, 2019, Note on microperforated panel model using equivalent-fluid-based absorption elements. *Acoust Sci Technol*, 40: 221–224.

    https://doi.org/10.1250/ast.40.221

30. Li X, Yu X, Zhai W, 2021, Additively manufactured deformation-recoverable and broadband sound-absorbing microlattice inspired by the concept of traditional perforated panels. *Adv Mater,* 33: e2104552.

    https://doi.org/10.1002/adma.202104552

31. Li X, Yu X, Zhai W, 2022, Less is more: Hollow-truss microlattice metamaterials with dual sound dissipation mechanisms and enhanced broadband sound absorption. *Small,* 18: e2204145.

    https://doi.org/10.1002/smll.202204145

32. Rahimabady M, Statharas EC, Yao K, *et al.*, Hybrid local piezoelectric and conductive functions for high performance airborne sound absorption. *Appl Phys Lett,* 111: 241601.

    https://doi.org/10.1063/1.5010743

33. Egab L, Wang X, Fard M, 2014, Acoustical characterisation of porous sound absorbing materials: A review. *Int J Veh Noise Vib* 10: 129–149.

    https://doi.org/10.1504/IJVNV.2014.059634

34. Institution BS, 1993, Acoustics. Materials for Acoustical Applications. Determination of Airflow Resistance. British Standards Institution, United Kingdom.

35. Khosravani MR, Reinicke T, 2021, Experimental characterization of 3D-printed sound absorber. *Eur J Mech A Solids*, 89: 104304.

    https://doi.org/10.1016/j.euromechsol.2021.104304

Materials Science in Additive Manufacturing

REVIEW ARTICLE

Laser additive manufacturing of magnesium alloys and its biomedical applications

Chuyi Liu[1], Chengrong Ling[2], Cheng Chen[2], Dongsheng Wang[3], Youwen Yang[1,2]*, Deqiao Xie[4]*, Cijun Shuai[2,5]*

[1]College of Mechanical and Electrical Engineering, Jiangxi University of Science and Technology, Ganzhou 341 000, China

[2]Institute of Additive Manufacturing, Jiangxi University of Science and Technology, Nanchang 330 013, China

[3]Key Laboratory of Construction Hydraulic Robots of Anhui Higher Education Institutes, Tongling University, Tongling 244 061, China

[4]College of Mechanical and Electrical Engineering, Nanjing University of Aeronautics and Astronautics, Nanjing 210 016, China

[5]State Key Laboratory of High Performance Complex Manufacturing, Central South University, Changsha 410 083, China

Abstract

Biomedical magnesium (Mg) alloy with unique biodegradability and excellent biocompatibility is one of the most sought after materials in medical field for orthopedics applications. Nevertheless, the high corrosion rate and inadequate mechanical properties hinder its development. Apart from that, to obtain the best surgical result, the size and shape of the fixation implant need to be adapted to the individual case. Thus, additive manufacturing (AM) processes, such as laser powder bed fusion (LPBF), are used to overcome these issues. This work reviews the recent advancements in biodegradable Mg-based alloys prepared by LPBF for biomedical applications. The influence of feedstock features and manufacturing parameters on the formability and quality is delineated in detail. The mechanical performances, degradation behaviors, and biological behavior of the LPBF-processed parts are discussed. Furthermore, we also made some suggestions for the challenges of Mg alloys in LPBF processing and applications in biomedical.

Keywords: Magnesium alloy; Additive manufacturing; Biological behavior; Biomedical

***Corresponding authors:**
Youwen Yang
(yangyouwen@jxust.edu.cn)
Deqiao Xie
(dqxie@nuaa.edu.cn)
Cijun Shuai
(shuai@csu.edu.cn)

Citation: Liu C, Ling C, Chen C, *et al.*, 2022, Laser additive manufacturing of magnesium alloys and its biomedical applications. *Mater Sci Add Manuf,* 1(4): 24. https://doi.org/10.18063/msam.v1i4.24

Received: October 30, 2022

Accepted: November 23, 2022

Published Online: December 14, 2022

1. Introduction

1.1. Potential of magnesium in biomedical applications

With the increase in elderly population and the frequent traffic accidents, more and more people are suffering from bone defect[1]. At present, statistics shows that the cumulative number of cases exceeds 20 million in China, with an increment of 3 million new cases every year[2]. The regeneration and reconstruction of damaged tissues have great strategic importance[3]. Medical metal materials, such as titanium alloys, tantalum alloys, and stainless steel, are commonly used as implant to replace the damaged parts in bones due to their excellent mechanical properties and good biocompatibility[4].

However, their elastic modulus and mechanical strength are much higher than natural bone, which cause the "stress occlusion" effect after implantation, thus leading to the atrophy of natural bone tissue and even migration failure[5]. Moreover, they might release some toxic metal ions, which induce inflammation. Unfortunately, the implants do not easily degrade, and thus, they need to be removed in secondary surgery after implantation[6]. In this case, this could the patients will undoubtedly have to endure huge pain and shoulder extra economic burden. Therefore, it is imperative to develop new metal scaffolds for repairing bone defect[7].

Recently, biodegradable metals such as magnesium (Mg), zinc (Zn), and iron (Fe) alloys have become a hot research topic in tissue repair because of their mechanical strength, unique degradation properties, and good biocompatibility[8,9]. After implantation, these biodegradable metals have the sufficient mechanical strength to provide support during the healing process[10]. Importantly, they can be completely degraded *in vivo*, and their degradation products will be metabolized by the human body without any toxic side effects[11]. Compared to Zn and Fe alloys, Mg alloy has received wide attention from experts and scholars since it has the following three significant advantages:

(i) Mechanical compatibility. Mg alloy is a light alloy with low density and high specific strength. Its density (1.8 – 2.1 g/cm^3) and elastic modulus (40 – 45 GPa) are similar to those of human bone, indicating that they can effectively reduce the stress shielding effect[12,13]. It has excellent application prospects in bone tissue defect repair.

(ii) Biodegradability. The standard electrode potential of Mg is −2.37 V. Mg alloy can completely degrade the body by self-corrosion. The degradation products have no apparent side effects on the human body and can be excreted through human metabolic processes[14,15].

(iii) Biocompatibility. Mg, which is involved in synthesizing a variety of proteases and nucleic acids, is one of the essential nutritional elements for humans. Mg ion is conducive to the dilatation of blood vessels and the healing of bone tissue. Therefore, biodegradable Mg alloy is hailed as the new-generation medical metal materials. The comparison between Mg alloy and other bone implants is shown in Table 1.

1.2. Development of Mg-based implants

Mg and its alloys, as the promising implants, are mainly used in bone fixation devices, cardiovascular scaffolds, and tissue engineering scaffolds[20-22]. The advantages of Mg implants and its clinical applications are presented in Figure 1. The development of Mg-based implants has gone through two stages, with the 21st century as the dividing line. Before the 21st century, Mg alloys were mainly used in bone fixation devices. In 1900, Payr *et al.*[23] pioneered the use of Mg as a bone connector for the fixation of injured bone, and the Mg plate produced no adverse effects in animals. In 1906, Lambotte extended the animal *in vivo* experiment to a human clinical study, using Mg plates and steel nails to fix the calf fracture of patients[24]. Still, the Mg plate and steel nails formed galvanic corrosion, which produced a large amount of hydrogen. The implantation site appeared to have a gas swelling phenomenon. In 1938, McBride *et al.*[25] used a bone fixation device made of Mg-Al-Mn alloy to treat multiple fractures, and no negative effects were observed in the fracture tissue after implantation. However, due to the rapid degradation rate of Mg alloy in the human body, the clinical research of Mg alloy as a bone fixation device has stalled in the late 20th century[26].

Due to the rapid development of science and technology after the 21st century, some Mg alloy bone fixation devices have passed clinical trials and obtained regional certification. In 2008, the United States established a research center to study biodegradable biomaterials. In 2013, Syntellix AG successfully developed degradable Mg alloy screws, which passed clinical trials and obtained CE certification[27]. In 2014, the China Food and Drug Administration certified the Mg-Zn-Ca bone nail developed in South Korea because of its relatively slow degradation rate[14]. In recent years, Mg alloys have gradually been used to manufacture cardiovascular and tissue engineering scaffolds. Chaya *et al.*[28] used Mg bone plates and screws and titanium alloy plates and screws to repair bone cracks in rabbits. The results showed that the degradation of Mg bone plate was beneficial to bone healing. Zhao *et al.*[29] used Mg screws to fix vascularized bone grafts with femoral head necrosis and found that released Mg ions could stimulate the generation of fresh bone. Wang *et al.*[30] used Mg-Zn-Y-Nd alloy scaffolds to treat esophageal cancer. The data showed that Mg alloy had good biocompatibility and degradation performance and could kill the esophageal cancer cells.

1.3. Advantages of laser powder bed fusion (LPBF) for the fabrication of implants

To meet the requirements of clinical applications, bone implants should possess not only appropriate mechanical strength and good biocompatibility but also personalized shape to match different damaged parts. The traditional preparation methods of Mg alloy components are mainly casting and powder metallurgy. Although the formed Mg alloy components have good mechanical properties,

Table 1. Comparison of physical performance between Mg alloys and other bone implants

Materials	Density (g/cm^3)	Modulus (GPa)	Compressive yield (MPa)	Elongation (%)
Human bone[12,16,17]	1.8 – 2.1	10 – 30	130 – 180	3 – 6
Mg alloys[16,17]	1.79 – 2.0	37.5 – 65	70 – 140	2 – 11
Ti alloys[17,18]	4.2 – 4.5	79 – 110	795 – 908	6 – 16
Co alloys[17,18]	8.3 – 9.2	220 – 230	450 – 1500	5 – 30
316 L steel[17,18]	8.0	193	172 – 690	12 – 40
Tantalum[17,18]	16.7	188 – 190	138 – 345	1 – 30
Hap[18,19]	3.1	80 – 110	0.03 – 0.3	/
TCP[18,19]	/	24 – 39	2 – 3.5	/
Fe alloys[17-19]	7.8 – 7.9	200 – 205	170 – 690	12 – 40

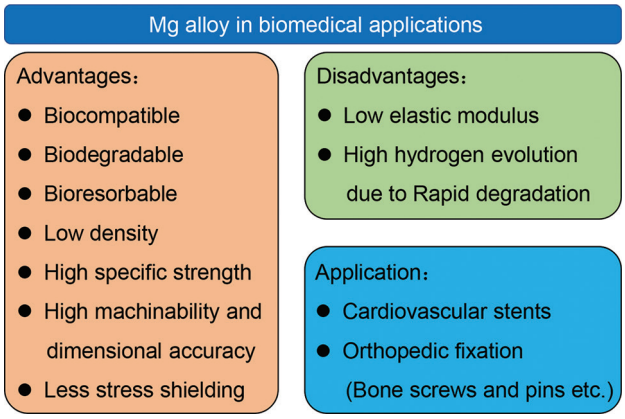

Figure 1. The advantages of Mg implants and its clinical applications.

the process has an extended processing cycle and low material utilization. Unfortunately, these methods cannot easily control the pore size to obtain complex geometric shapes. Additive manufacturing (AM), commonly known as three-dimensional (3D) printing, is a manufacturing technology that integrates computer-aided design, material processing, and molding technologies and uses digital model files as a basis. Meanwhile, through software and CNC systems, special materials are stacked layer by layer in accordance with extrusion, sintering, melting, light curing, or spraying to fabricate block parts[31]. Compared with traditional manufacturing technology, AM could provide a reliable way to obtain personalized complex 3D structures, which can efficiently and reliably replicate anatomical morphology related to tissues and organs. It could prepare precisely controlled pore structure to meet the personalized customization needs of patients. In particular, LPBF is commercially known as selective laser melting (SLM), which uses metallic and non-metallic powders as the raw material[32]. In contrast to other AM technologies, SLM can process a very wide variety of materials. In addition, it is possible to recycle and reuse unmelted metal powder, which allows the efficient use of the material. Due to its characteristics, SLM can be effectively applied as a prospective production technique for valuable materials and components, through cutting down the cost and lead time of fabrication and reducing the loss of material. Therefore, it has attracted increasing interest and attention in fabricating biodegradable Mg-based implants.

In 2011, Ng *et al.*[33] used the SLM process to prepare pure Mg, which was the first report about the Mg alloy for custom biomedical implants. Since then, Mg and its alloys for the degradable implants has become hotspot research in biomedical field. In this review, we present a systematic analysis and discussion on the recent literature on LPBF-processed Mg alloy. In addition, the effect of the comprehensive powder properties, parameters optimization, and post-treatment on their mechanical and degradable properties will be highlighted, along with the current challenges in LPBF-processed Mg alloys. The review also presents insights into the future of Mg alloys and their use in biomedical applications.

2. LPBF-processed Mg alloys

The fabrication of Mg and its alloys through LPBF is deemed to be extremely challenging. On the one hand, due to the inherent inflammability and explosiveness, the preparation conditions of Mg powders are extremely demanding. On the other hand, low evaporation temperature and high vapor pressure of Mg tend to trigger micro-crack during LPBF processing, causing poor structural integrity of parts. Thus, until now, there is no relevant report on LPBF-processed ultrapure Mg (>99.9%). A great deal of current research on Mg prepared by LPBF has focused on its alloys. This is due to their good workability and low risk.

2.1. Preparation of the feedstock

It is well known that LPBF is a typical powder metallurgy technology. Powder properties are an essential part of the LPBF industry chain. The powder should possess a

spherical morphology to form a homogeneous layer of continuously deposited powder. This feature is vital to improve the flowability and packing density. At present, the methods for preparing Mg alloys powder mainly include water, gas, and plasma atomization, plasma rotating electrode (PRE) atomization, and evaporation-condensation. Among them, aerosolization is widely used for the preparation of Mg powder for LPBF processing with a particle size distribution between 20 and 70 μm. Moreover, the sphericity of the powder can reach 98%. Usually, high sphericity means superior flowability, which is conducive to powder spreading with scraper and as-built parts with high quality.

2.1.1. Water atomization

Water atomization is an atomization method that uses water as the atomization medium to break the molten metal. The advantages of water atomization include simple equipment structure, high efficiency, and low atomization cost. However, the disadvantage of water atomization is that the prepared powder has high impurity and poor sphericity. It was due to the fact that the reaction between active metal and atomization medium at high temperature increases oxygen content. In addition, the metal droplets formed by water atomization breaking in the rapid solidification stage are irregular due to the large specific heat capacity of water.

2.1.2. Gas atomization

The aerosolization method uses high-speed airflow to crush the liquid metal stream, forming tiny droplets, and then quickly condensing to obtain the formed powder. Compared with water atomization, gas atomization uses inert gas (i.e., argon and nitrogen) as atomization medium. The metal prepared by this method has the advantages of small powder (particle size <150 μm), uniform composition, and high sphericity. Gas atomization is suitable for producing most metals and alloys, which is the primary production method for spherical metal powders in AM processing. At present, most of the powder is produced and prepared by the gas atomization method, accounting for 30%–50% of the powder produced in the world[29]. The density and microstructure of 17-4PH stainless steel parts prepared from gas-atomized and water-atomized powders were comprehensively investigated by Irrinki *et al.*[34]. The morphology of water-atomized powder and gas-atomized powder is shown in Figure 2.

2.1.3. Plasma atomization

Plasma atomization was reported by Entezarian *et al.* in 1996 for the production of highly spherical powders with an average particle size of 40 μm[36]. This approach uses the

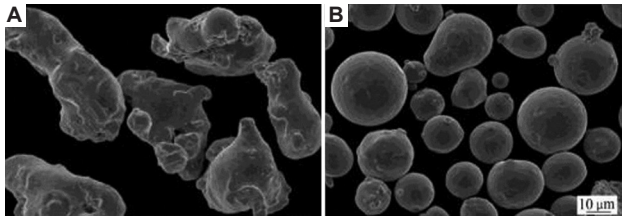

Figure 2. The SEM image of (A) water-atomized powders and (B) gas-atomized powders[35].

focused argon plasma jet generated by a plasma torch to melt the wire as initial material, which then results in the formation of tiny metal droplets. The plasma torch produces an extremely high-temperature argon plasma, which can inhibit the rapid solidification of molten and superheated metal droplets into irregular shapes[36]. Therefore, the droplets spend sufficient time in the superheated state and adopt an equilibrium shape (ideal spheres) driven by the surface tension during the falling process. The atomization and condensation process of the metal powder is carried out in an inert atmosphere.

2.1.4. Plasma rotating electrode atomization

Plasma rotating electrode (PRE) atomization is a centrifugal atomization process. It uses the plasma arc generated by a plasma gun as a high-temperature heat source to melt the raw material, which is in the form of an electrode rod and rotate at approximately 15,000 rpm. Meanwhile, centrifugal force separates the molten material from the rod, which then results in the formation of tiny metal droplets. The metal droplets solidify into spherical powders before they hit the chamber walls. This method was invented to reduce the volume of gas consumed to prepare each unit weight of atomized powder, as well as to address the generally low yield of fine powders prepared by conventional gas atomization processes. Notably, the yield for the process was closely related to this centrifugal force, that is, the rotation speed. In addition, the process can eliminate the risk of ceramic contamination due to melting of reactive metals in ceramic crucibles, thus obtaining high-purity spherical metal powder. Zheng *et al.*[37] reported that Mg-15Gd-0.4Zr (wt%) alloy powders with the size ranging from 75 to 250 μm were prepared by PRE atomization. As compared with aluminum (Al) powder prepared by gas atomization, it exhibited relatively high sphericity, as shown in Figure 3. The Mg alloy powder was adopted as the base material, and corresponding samples were successfully prepared by laser-directed energy deposition.

Based on the above description, the powder preparation methods are capable of producing spherical powders tailored for AM process. Recently, the rapid development of AM significantly increased the demand for spherical

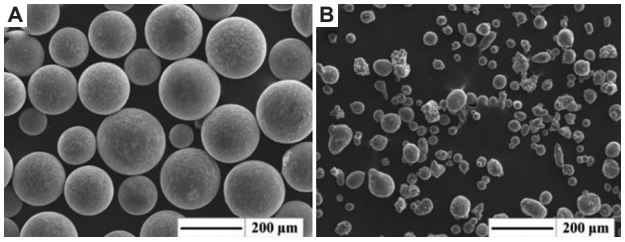

Figure 3. Morphology of (A) the pre-atomized Mg-15Gd-0.4Zr (wt%) alloy powder and (B) the gas-atomized Al powder.

metal powders in the market. The efficient preparation of high-quality spherical metal powders is vital to promote AM technology upgrades and industrial applications. Therefore, the existing powder preparation methods need to be improved. For the gas atomization method, optimizing the structure of the atomizer and improving the kinetic efficiency of the atomized gas are the most effective means to improve the quality and production efficiency of metal powders. For the PRE atomization method, to efficiently prepare high-quality spherical powders, the rotation speed of the electrode bar is increased, while the reasonable plasma heat source and power are also fed.

2.2. Parameters optimization

The performance of SLM prepared product strongly depends on the processing parameters, such as laser power, scanning speed, hatch spacing, and layer thickness. The previous studies have shown that the process parameters are considered appropriate when the following requirements are fulfilled in scanning tracks and layers[38]: (π) The scanning tracks should be continuity, (θ) each layer has to be high enough to build up the part cumulatively, (ρ) every layer should be high enough, and (σ) the connection angle between two adjacent layers should be close to 90°.

2.2.1. Laser power

High laser power can improve the wettability of the molten pool and provide more power for powder consolidation. Ji *et al.*[39] reported an analytical model to predict the grain size of the part after LPBF process. Results show that the maximum surface temperature of the component is not influenced by the scanning speed. In addition, the average grain size reduced with the increasing of laser power. He *et al.*[40] prepared AZ61 alloy with a relative density of 98%. The forming zone of AZ61 with input laser power from 60 W to 90 W was determined. The results show that the increase in laser power helps improve the densification of the material and the formation of equiaxed grains, thus improving the resistance to degradation and microhardness. However, too high laser power can lead to grain coarsening and a decrease of Al solid solution in the Mg matrix, resulting in increased mass loss and decreased microhardness.

2.2.2. Scanning speed

The appropriate scanning rate can increase the heating time of metal powder. The fabrication of compact component can be achieved with low scanning speed, as it allows longer contact time between powder and laser, thereby increasing the rate of energy transfer to the powder bed. With the scanning speed increasing, less energy is transferred to powder, which always results in incomplete melting of the particles. Shuai *et al.*[41] reported the influence of SLM processing parameters on the corrosion performance of ZK60 alloy. At an energy density of 600 J/mm^3, the final as-built part with a relative density of 97.3% was obtained. Spierings *et al.*[42] analyzed the impact of different laser scanning speeds on the static mechanical properties of SLM-treated scandium (Sc) and zirconium (Zr)-modified Al-Mg alloys. The results showed that the scanning speed could affect the hardness and mechanical performance of the alloy, while yield strength was barely affected by the laser scanning speed.

2.2.3. Laser energy density

Although the variety of laser powers or scanning speeds can significantly influence the forming quality and performance of AM-processed part, it is difficult to describe their effects individually. An empirical formula for evaluating the input energy of laser additive using laser energy density[43] is given below:

$$E_V = \frac{P}{V.H.D}$$

Where, E_v represents energy density (J/mm^3), P is the laser power (W), V is the scanning speed (mm/s), H is the hatch spacing (mm), and D is the layer thickness (mm). After forming, the forming quality of samples is measured by density and surface roughness. In general, the surface of the sample with high density is relatively flat and has a low surface roughness, as shown in Figure 4. In the case of low laser energy density, the temperature in the molten pool is also relatively low so that the metal powder cannot be fully melted, and noticeable unmelted powder particles and a large number of pores can be observed between the adjacent molten layers, which result in low density. When the laser energy density is too high, the temperature in the molten pool easily exceeds the boiling point of magnesium powder because the melting and boiling point of magnesium powder is relatively close, resulting in a large amount of powder evaporation, which leads to the formation of local vapor pressure, powder splashing phenomenon, and formation of a large number of pores, as displayed in Figure 5.

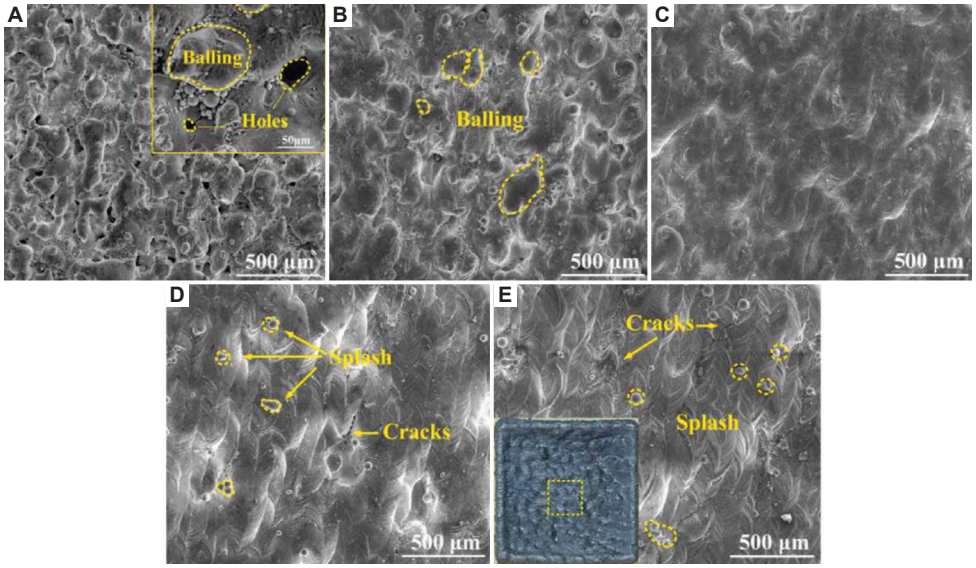

Figure 4. (A-E) SEM images of SLMed ZK60 alloy surface morphologies at different energy density[44].

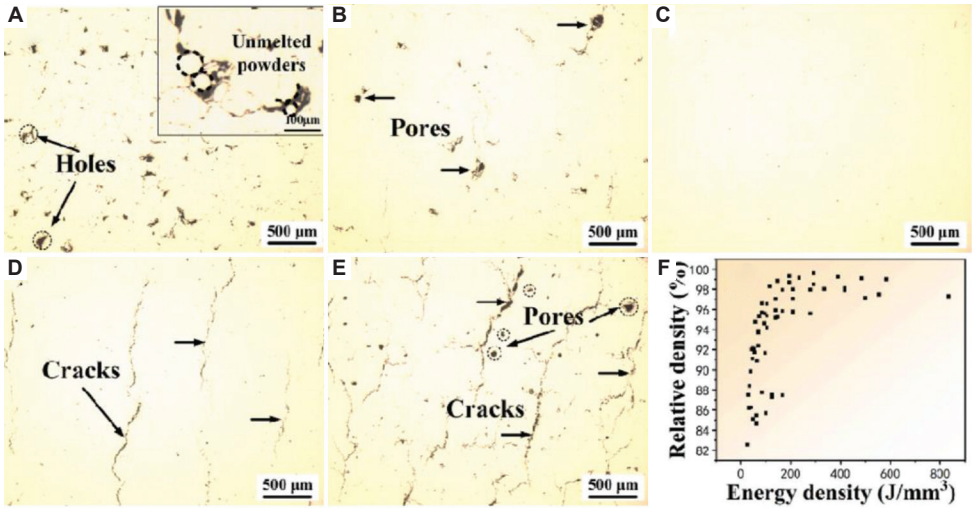

Figure 5. (A-F) Optical micrographs of the SLMed ZK60 Mg alloy at different energy density[44].

Esmaily *et al.*[45] reported the influence of laser energy density on the forming quality of WE43 magnesium alloy by changing the laser power and scanning rate and obtained the sintering process window diagram. WE43 has many pores and unmelted metal powders in the low-energy density region, resulting in a very low material density and poor mechanical properties. In the high-energy density area, due to the high temperature, there is apparent burning and evaporation phenomenon, resulting in the keyhole and other phenomena, and the forming quality is poor. The stable molten pool can only be obtained under the appropriate laser energy density in the forming area, which ensures good forming quality and dimensional accuracy and achieves 98.3% density.

Wei *et al.*[46] studied the influence of different laser energy densities on the forming properties, microstructure, and mechanical performance of AZ91D samples. They found that the forming parts with high density and no obvious macroscopic defects could be obtained between 83 and 167 J/mm^3. When the laser energy input is over 214 J/mm^3, the sample cannot be deposited due to solid evaporation, and there is a severe burning phenomenon. When the laser energy input is <77 J/mm^3, the powder cannot be completely melted, resulting in many holes in the sample. Therefore, only in the appropriate processing window can high-density parts be prepared. The optimization parameters obtained from the current literature are collated in Table 2.

Table 2. Additive manufacturing process parameters for magnesium and its alloy

Material	Laser power (W)	Laser spot size (μm)	Scanning speed (mm/s)	Layer thickness (μm)	Hatch spacing (μm)
Mg[47]	100	50	10	100	/
Mg-xZn[48]	70	50	100	100–200	/
AZ61[49]	150	70	400	40	60
AZ91D[46]	200	/	500	40	90
ZK30[48]	75	150	15	50	50
ZK60[41]	50	150	8	100	100
ZK60-xCu[48]	60	150	10	/	100
Mg-Ca[50]	80	10	/	40	150
ZK60-BG[51]	80	140	/	60	60
ZK61[52]	100	/	100	40	1500
WE43[45]	280	1200	/	30	40
GWZ1031K[53]	80	200	/	30	100

2.3. Post treatments

SLM, as a typical AM technology, can reliably prepare Mg-based products, which especially own complex geometries and do not require molds and accessories[54]. Besides, it also possesses these advantages, such as small machining allowances and high material utilization. Notably, Mg is susceptible to oxidation due to its high chemical reactivity and relatively low melting and boiling points to cause high evaporation during melting[55,56]. Therefore, SLM-processed Mg alloy parts exhibit many defects such as high surface roughness, porosity, residual stresses, anisotropy, and undesired microstructures, which can greatly reduce the overall performance of the parts. The removal of the defects is of great practical importance, where some post-treatments are commonly performed, especially hot isostatic pressing (HIP) and calcium hydrogen phosphate dihydrate (DCPD).

2.3.1. Hot isostatic pressing (HIP)

HIP is a frequently used thermomechanical treatment method that eliminates the porosity and relieves the residual stresses, thus improving ductility, fatigue resistance, and microstructure. The method is performed under high-temperature and -pressure conditions, in which the temperature and pressure usually reach 1000 – 2000°C and 200 MPa, respectively. The working pressure generated by a high-pressure inert gas in a closed vessel is close to the yield point of the as-built parts, thus causing plastic deformation. The parts are pressed evenly in all directions with high temperature and pressure, which eliminates these defects to form a dense and uniform microstructure. Therefore, the treated parts can show high density, good uniformity, and excellent performance. Esmaily *et al.*[45] processed WE43 Mg alloy through SLM and found that HIP treatment is an effective method to eliminate the processing defects, thereby obtaining almost fully dense parts, as shown in Figure 6. Gangireddy *et al.*[57] showed that at higher initial porosity, HIP treatment was beneficial for the densification of LPBF formed WE43 magnesium alloys, but could not improve the densification of samples with smaller porosity due to the closed nature of the pores. The cooling rate of laser AM is much higher than that of traditional casting, and an excessively fast cooling rate may be detrimental to the precipitation of strengthening phases. A large amount of residual stress caused by excessive cooling rate, texture, and mechanical anisotropy generated along the direction of heat flow can be eliminated by heat treatment[58].

2.3.2. Calcium hydrogen phosphate dihydrate (DCPD)

The surface roughness of as-built parts affects the mechanical properties and degradation rate. Coatings can modulate the degradation behavior and improve the biological properties. Wang *et al.*[59] applied DCPD to the surface coating of JDBM porous scaffolds with helical tetrahedral structural units, as shown in Figure 7. DCPD treatment slowed down the degradation rate of the scaffolds and improved their biocompatibility. Dou *et al.*[60] used the sol-gel impregnation method to prepare 45S bioactive ceramic coatings on AZ31 Mg alloy substrates and found that the corrosion resistance was significantly improved. Rojaee *et al.*[61] synthesized hydroxyapatite coating on AZ91 alloy by electrophoretic deposition process, which significantly improved its corrosion resistance and biological properties. Razavi *et al.*[62] prepared nanostructured magnesite and diopside coatings by electrophoretic deposition, which also improved the corrosion resistance and biological activity of magnesium alloys. Kopp *et al.*[63] used plasma electrolytic oxidation (PEO) to treat the surfaces of WE43 Mg alloy scaffolds with different pore sizes prepared by

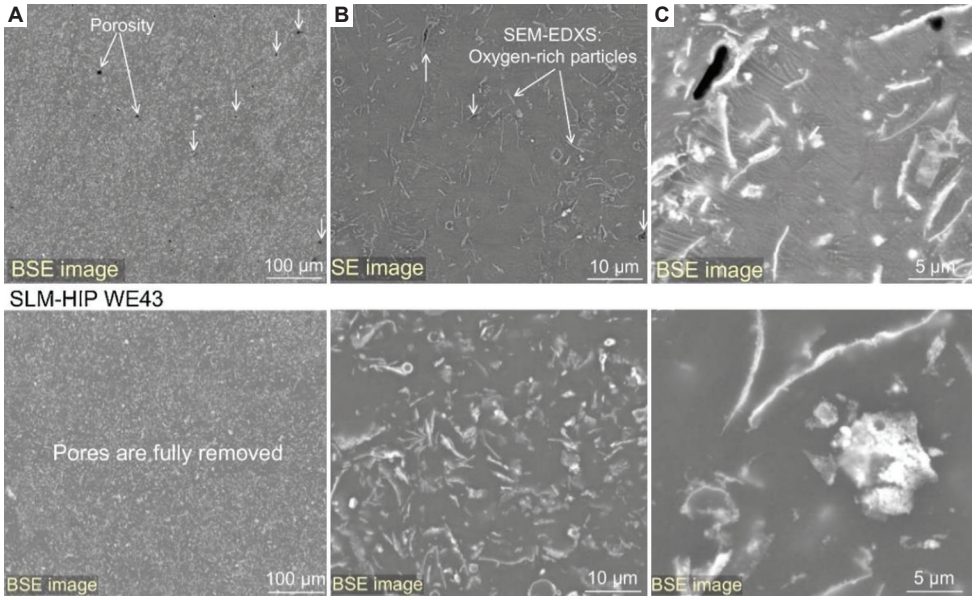

Figure 6. (A-C) BSE-SEM micrographs revealing the microstructure of the sample in the SLM-prepared WE43 with and without HIP treatment.

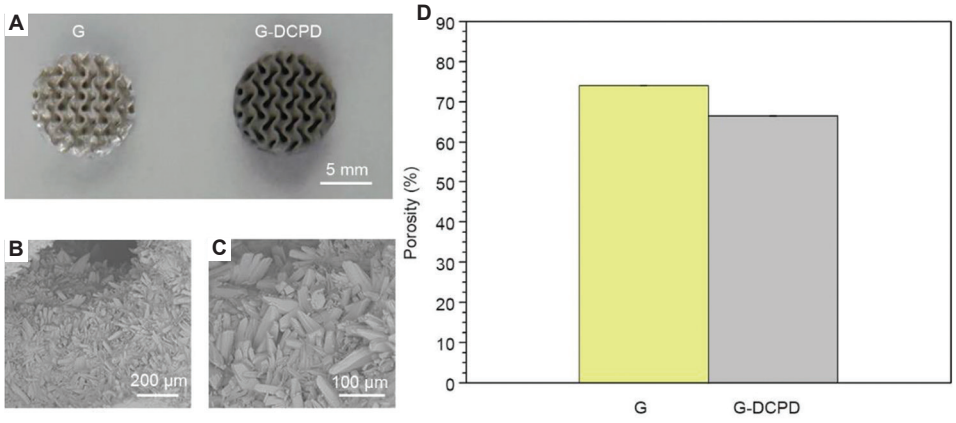

Figure 7. (A) Macrograph, (B and C) SEM, and (D) porosity of the G-DCPD scaffold.

LPBF technique. The results showed that PEO significantly reduced the degradation rate of the scaffolds at the initial stage of DMEM soaking. After soaking for 21 days, the stability of the PEO-modified surface decreased, and the weak parts were eroded and cracked.

2.3.3. Friction stir processing

In recent years, severe plastic deformation (SPD), which is an emerging technology, has been widely used to the post-treatments of SLMed parts. Friction stirring processing (FSP) is a typical SPD technique, with its basic principle derived from friction stir welding (FSW), as shown in Figure 8. It is able to simultaneously use high strains, high strain rates, and high temperatures to fully move the material, which results in grain refinement, second phase fragmentation, homogenization, and densification within the stirring zone[64]. Huang *et al.*[65] used FSP to reduce the porosity and

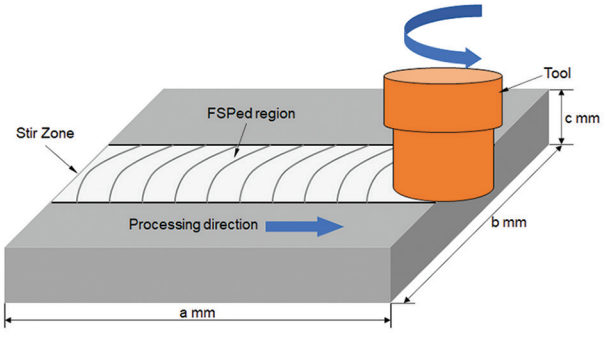

Figure 8. Schematic diagram of friction stirring processing.

homogenize the microstructure of the SLMed Ti_6Al_4V alloy, the results showed that fracture strain increased from 0.21 to 0.65 after FSP. In addition, FSP improves the ductility and fatigue life of the SLMed-$AlSi_{10}Mg$ alloy, due to the spheroidization of the eutectic phase, the homogenization of the microstructure, and the reduction in porosity[66]. However, to the best of our knowledge, there are only a very limited number of studies relating to the adjustment of the microstructure and enhanced mechanical properties of SLMed-Mg alloys by FSP. Deng *et al.*[67] found that FSP treatment of SLMed-Mg alloys resulted in a reduction of porosity from 0.779% to 0.015%, disappearance of melt pool boundaries, columnar to equiaxed transformation, and grain refinement, which significantly improved the mechanical properties of the Mg-Gd-Zr alloy.

2.3.4. Laser beam polishing

Laser polishing is an efficient, non-contact, and fully automated post-treatment technology that provides excellent performance in reducing the surface roughness of SLMed parts. In the past two decades, laser polishing has been widely used to reduce the surface roughness of polymers, metals, ceramics, and other materials. In contrast to conventional polishing processes, laser polishing smoothens rough surfaces using thermal energy to melt a thin layer of material, as shown in Figure 9. In laser polishing, a precisely controlled laser beam is guided onto the surface of the part for polishing. By controlling the energy of the laser beam, the peak on the surface is just melted, and the molten metal is generated due to the multi-directional surface tension and gravity, and then, it is filled into the valley. In this case, there is no material loss during laser polishing. The laser power, spot size, and scanning speed are the main control parameters to obtain a smooth surface[68]. At present, laser polishing has demonstrated its ability to polish various materials, from reflective materials such as aluminum to high strength materials such as Inconel and titanium alloys[69]. Unfortunately, there are no relevant reports on laser polishing for SLMed Mg alloys.

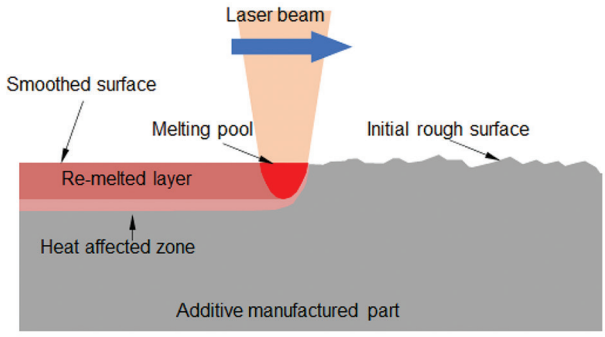

Figure 9. Schematic diagram of laser beam polishing.

3. Performance of LPBF developed Mg alloys

3.1. Mechanical properties

An ideal orthopedic implant should have sufficient mechanical strength and excellent stress conduction capability, matches with the surrounding bone tissue, and provides mechanical support during the healing process of bone tissue. Processing method directly affects the mechanical properties of Mg alloys. Compared with cast Mg alloys, due to the influence of grain refinement, solid solution strengthening, and other factors, the mechanical properties of Mg alloys manufactured by laser AM have been improved to varying degrees in various aspects. The mechanical properties of bone are closely related to age, bone health, and bone type. Zhang *et al.*[70] prepared porous Mg scaffolds with porosity of 33 – 54% using fiber deposition hot pressing technology, and their Young's modulus and compressive strength were comparable to those of human cancellous bone.

Hyer *et al.*[71] used LPBF to prepare a dense WE43 alloy. Under the compressive action, the average yield strength of the newly built WE43 structure was 224 MPa, the compressive strength was 417 MPa, and the failure strain was 9.5%. Under tension, the newly constructed LPBF WE43 has an average yield strength of 215 MPa, a tensile strength of 251 MPa, and a failure strain of 2.6%. A study by Fang *et al.*[72] on the mechanical properties of hot rolled and WAAM-GTA prepared AZ31 samples showed that the performance of WAAM-GTA AZ31 along the direction of travel was always better than that along the build direction. Whether there were large pores within the specification length of the processed tensile samples, its mechanical properties will vary. Deng *et al.*[53] systematically analyzed the effect of different solution conditions and aging heat treatment on the microstructure and mechanical properties of SLM GZ112K alloy. Appropriate post-heat treatment is an effective measure to improve the microstructure and mechanical properties of SLMed alloy. SLM-T6 alloy meets the requirements of high tensile strength, SLM-T4 alloy meets the requirements of high ductility, and SLMed alloy achieves a good combination of tensile strength and ductility. The ultra-high yield strength of SLM-T6 GZ112K alloy mainly comes from the following four aspects: Fine-grain strengthening with average grain size <3.1 μm, precipitation strengthening of β′-aging precipitation, secondary phase strengthening of long-period stacking-ordered (LPSO) structure and X phase, and the extra composite strengthening from the coexistence of basal and prismatic precipitates. Wang *et al.*[73] studied the effect of geometric design on the dynamic response of additively fabricated Mg scaffolds, and the results showed that geometric design had a significant effect on

the compression fatigue performance of Mg scaffolds. A summary of the mechanical properties of the additively manufactured biodegradable Mg alloys from the literature is presented in Table 3.

3.2. Degradation performance

The previous studies have shown that AM prepared Mg and its alloys possess fine grain size and homogeneous microstructure, which can obtain lower degradation rates, mainly due to improved passivation properties and reduced micro-galvanic corrosion[77]. Despite that, their corrosion rate in the body fluid environment is still unable to meet the needs of bone implants. For an ideal biodegradable bone metal implant, they have a corrosion rate of <0.5 mm/year and need to provide mechanical support for 12 – 24 weeks to meet the clinical requirements[78,79]. This means that the AM-processed biodegradable Mg and its alloys implants need to be regulated. The corrosion resistance of the additively manufactured Mg and its alloys in the current studies is summarized in Table 4.

3.2.1. Scavenging effect

Many impurities, such as iron, nickel, and copper, in Mg and its alloy commonly exhibit relatively high potential. This causes the micro-galvanic corrosion with matrix and thus increases their degradation rate. In this case, the corrosion resistance of Mg alloys can be significantly improved by adopting high purification methods or reducing the impurity concentration by improving the processing technology. Han *et al.*[80] found that the degradation rate of high purity Mg *in vivo* was much lower than that of Mg-containing iron impurities. Cao *et al.*[81] slowed down the corrosion rate of Mg alloys by adding a certain amount of Zr to the molten Mg alloy to remove the impurity iron. Studies have shown that Zr and iron can easily form a precipitate phase, which precipitate at the bottom of the melt, thereby achieving purification effect. Peng *et al.*[82] used a zone solidification method to prepare Mg alloys and found that the corrosion rate of the alloys purified by this method was lower than that of conventionally cast Mg alloys.

3.2.2. Alloying treatment

Alloying treatment is an effective way to improve the corrosion resistance of Mg alloys by changing the microstructure and the type of precipitates. At present, researchers have developed a series of biological Mg alloys by alloying methods, and their properties have been studied. Shuai *et al.*[83] found that with the increase of Al content, α-Mg dendrites and intermetallic compounds

Table 3. Mechanical performances of the LPBF-manufactured biodegradable Mg alloys

Type			Mechanical properties	Improvement mechanisms
Shapes	Materials	Dimensions		
Block	ZK60[41]	Cubic 6 × 6 × 6 mm³	Microhardness: 89.2 Hv	High densification, fine-grain strengthening, and solution strengthening
	AZ91D[46]	Bone-shaped gauge 25 × 6 × 2 mm³	UTS: 296 MPa, UYS: 254 MPa Microhardness: 100 HV	Fine-grain strengthening
	AZ61[49]	Bone-shaped gauge 25 × 6 × 1.5 mm³	UTS: 287.1 MPa, UYS: 233.4 MPa, EL: 3.12%	Fine-grain and solid solution strengthening
	GWZ1031K[53]	Bone-shaped gauge 18 × 3 × 10 mm³	UTS: 347 MPa UYS: 310 MPa EL: 4.1%	Fine-grain strengthening
	Mg-8Zn[74]	Cuboid 5 × 5 × 3 mm³	Hardness: 71.5 Hv	Fine-grain strengthening
Porous	Mg-Ca[50]	Cuboid 6 × 6 × 9 mm³	UCS: 111.19 MPa Elastic modulus: 1.26 GPa	Optimizing the laser parameters
	ZK61[52]	Cuboid 6 × 6 × 9 mm³	Microhardness: 106.75 Hv UCS: 50.95 MPa Elastic modulus: 0.91 GPa	Fine-grain strengthening, solution strengthening, and precipitation strengthening
	WE43[75]	Cylindrical D (6 mm), H (6 mm)	Hardness: 77.41 Hv UCS: 21.21 MPa Elastic modulus: 0.79 GPa	Optimized structure of porous units
	WE43[76]	Cubic fluorite	UCS: 71.48 MPa	Optimized structure of porous units

Table 4. Corrosion resistance of the LPBF-manufactured Mg and its alloys

Material	Soaking time	Degradation behaviors
Mg[47]	1 day	pH in SBF: ~10.5
Mg-6Zn[74]	7 day	Evolved H_2 volume in SBF: 32.2 mL/cm^2
ZK60[41]	2 day	H_2 volume evolution rate in SBF: 0.006 mL/cm^2/h
ZK60-0.2Cu[92]	7 day	pH in SBF: 9.49 CR in SBF: ~1.01 mm/year
ZK60-BG[51]	7 day	CR in SBF: 0.51 mm/year
WE43[45]	20 h	CR in 0.1 M NaCl solution: 5 mm/year
Amorphous Mg-Zn-Ca[88]	/	CR for current density in SBF: 0.35 mm/year

SBF and CR represent simulated body fluid and corrosion rate, respectively

were effectively refined. Li *et al.*[84] reported that Zn addition refined the grain size to promote the formation of passivation films on the substrate, thus providing effective protection for the Mg substrate. Luo *et al.*[85] found that the alloying of rare earths significantly reduced the proportion of β phase and promoted the formation of γ phase with a larger active potential, which reduced the micro-galvanic corrosion with the Mg matrix. In addition, the introduction of alloying elements improves the stability or structural integrity of corrosion product layer on the substrate surface with strong protective ability. Leleu *et al.*[86] introduced alloying element Y into Mg alloys, which formed a dense surface film after immersion in chloride rinsing solution and played a significant protective role. Willbold *et al.*[87] added rare earth elements (La, Nd, and Ce) to Mg matrix and found that the rare earth oxides formed on the surface of the Mg alloy to improve the passivation ability of the surface film. Notably, most of rare earth elements have low solid solubility in Mg matrix, thus excessive addition of rare earths can cause galvanic corrosion to accelerate the degradation and bring about cytotoxicity problems.

3.2.3. Amorphous alloy

Amorphous alloy, also known as metallic glass, is a non-equilibrium metal material with excellent corrosion resistance. Wang *et al.*[88] prepared $Mg_{60}Zn_{33}Ca_7$ amorphous alloy by melt spin quenching method. The corrosion potential shifts positively and the corrosion current density decreases, thus showing excellent corrosion resistance. Chen *et al.*[89] reported the research on Mg-based amorphous alloys, which were processed by traditional copper mold casting process. The amorphous alloys possess great glass forming ability, high fracture strength and surface hardness, and good plasticity. Zhang *et al.*[90] prepared Mg-based amorphous alloys by rapid cooling. The results show that the corrosion resistance of the amorphous alloy is obviously better than that of the crystalline alloy with the same composition. Zberg *et al.*[91] also studied the degradation process of Mg-Zn-Ca amorphous alloy as a biodegradable medical material and found that the corrosion resistance was significantly improved. Moreover, there was no obvious hydrogen evolution reaction during the degradation process.

3.3. Biological behavior

Medical implants need to have excellent biocompatibility to avoid toxic effects on the human body[93]. At present, there are little reports on the biocompatibility of additively manufactured metal implants. The biocompatibility evaluation of Mg-based degradable metals for AM is still at the cellular and *in vitro* levels. The factors affecting biocompatibility are mainly its chemical properties and degradation products. Ouyang *et al.*[94] reported that the large pores of the metal scaffolds were favorable for nutrient supply, while the small pores were favorable for cell growth.

Bioactive ceramics have excellent osteoconductive and bioactivity. Rojaee *et al.*[95] synthesized hydroxyapatite coating on AZ91 alloy by electrophoretic deposition process, and its corrosion resistance and biological properties were significantly improved. Razavi *et al.*[62] prepared nanostructured magnesite and diopside coatings by electrophoretic deposition, which also improved the corrosion resistance and bioactivity of magnesium alloys. Tian *et al.*[96] used ammonium bicarbonate particles as a pore-forming agent, and then prepared porous Mg scaffolds by powder metallurgy process, and coated bioactive ceramics on the surface of Mg scaffolds in a low vacuum environment. The results showed that the coated Mg scaffolds have obvious biological activity, and the coating effectively delays the degradation rate of magnesium stents and improves its mechanical integrity.

Rahimi *et al.*[97] successfully prepared chitosan and nanofiber coatings on the surface of AZ31 Mg alloy by anodizing combined with electrospinning. The coating not only has good corrosion resistance but also has good cell adhesion and proliferation ability. However, due to the large differences in physical properties and mismatched degradation rates, the surface coating is easy to crack or even falls off after implantation, making it difficult to achieve long-term effective protection. Dutta *et al.*[98] prepared Mg/bioglass composites by microwave sintering, and the results showed that the corrosion resistance, mechanical properties, and biocompatibility were

improved. Obviously, the introduction of bioactive ceramics can not only induce the formation of calcium and phosphorus layers, providing long-term stable protection, but also greatly improve the biological performance.

Recently, the use of mesoporous bioglass as a reinforcing phase to prepare Mg-based composites for bone repair has been proposed. Mesoporous bioglass has uniform and ordered mesoporous channels (2 – 50 nm) and high specific surface area (500 – 800 m^2/g)[99]. More importantly, as a silicon-containing active ceramic, a large number of silanol groups will be formed on the interface at the initial stage of degradation, thereby forming a negatively charged silica gel layer. Under alkaline conditions, the silica gel layer acts electrostatically to adsorb Ca^{2+} and HPO_4^{2-} in the solution, thereby inducing *in situ* deposition of apatite. *In vitro* degradation tests showed that this *in situ* deposited calcium-phosphorus layer effectively enhanced the biological activity of Mg alloy substrates.

4. Challenges for the future

4.1. Challenges of LPBF-processed Mg Alloys

Due to the inherent characteristics of Mg alloys such as low evaporation temperatures, high vapor pressures, and a high propensity to oxidize, the manufacture of degradable Mg-based implants through AM presents a great number of challenges.

(i) The preparation of Mg powder that can be used for AM processing and degradable Mg-based implants is difficult. The preparation conditions of Mg powders are extremely demanding and the slightest inadvertence can lead to explosive accidents. Moreover, in the current market, the Mg alloy powders commonly used in AM processing are pure Mg, AZ91D, and WE43 powders. Due to the biological toxicity of Al element, AZ91D alloy contains 9% (mass fraction) of Al; therefore, only pure Mg and WE43 powders are suitable for degradable Mg-based implants.

(ii) The AM processing for Mg alloys always produces severe powder splashes due to low evaporation temperature and high vapor pressure of Mg alloys, and this phenomenon is very different from AM processing steel, Ti, or Al. Powder spattering can significantly reduce the stability of the Mg alloy during AM processing, as some Mg powder is removed by steam along the scan path, where defects are likely to occur in subsequent scan passes. In this case, a strategy of powder replenishment is necessary for Mg alloys during AM processing. However, there are no relevant studies on the interaction between Mg powder evaporation, gas flow, and laser input.

(iii) The quality of components prepared by LPBF is difficult to maintain consistently. Due to the complexity of the process chain, many potential fluctuations may occur during manufacturing process, which leads to variable quality of LPBF parts. Recently, a large number of scholars have explored the use of machine learning (ML) algorithms to overcome this obstacle using datasets obtained at various stages of the LPBF process chain[100]. Before LPBF, ML algorithms can be used for part design and document preparation. During the LPBF process, ML can be applied for process parameter optimization and *in situ* monitoring[101]. In addition, ML can also be integrated into post-processing. Therefore, in the future, it is promising to attempt to integrate ML algorithms into different stages of the LPBF process chain to better control the quality of LPBF Mg alloys.

4.2. Challenges of Mg alloys in biomedical applications

In the early stage, most of the medical Mg alloys were in the basic research stage, and the types of alloys that can be clinically applied are rare. At present, there are only high-purity Mg and WE43. Other Mg alloys still face great challenges in clinical applications, including the following problems.

(i) The degradation rate is too fast. Since the electrode potential of magnesium is −2.37 V, it usually appears as an active anode. Corrosion reaction occurs in the body fluid environment, and more $Mg(OH)_2$ is generated on the Mg matrix. The corrosion layer has a loose structure and poor corrosion resistance. In addition, bodily fluids contain a large amount of Cl^-, which will further react with $Mg(OH)_2$ to form the more soluble $MgCl_2$, thereby accelerating the degradation rate.

(ii) The mechanical strength and toughness are insufficient. For materials used in bone fixation and support, high strength and moderate plasticity are required, such as yield strength ≥300 MPa and elongation ≥10%; and for materials used in coronary stents and balloon dilators, high plasticity and medium strength are required, such as elongation ≥20% and yield strength ≥150 MPa. Mg alloys are difficult to enhance plasticity with increasing strength.

(iii) Biocompatibility verification is insufficient. Mg has good biocompatibility, but other alloying elements are inevitably added in the smelting process, which is potentially toxic to the human body. For example, Al can cause chronic neurotoxicity and lead to Alzheimer's disease; some rare earth elements (Y, Nd, Pr, etc.) are potentially toxic after implantation. The corrosion process will be accompanied by the production of a large amount of OH^- and H_2, which can easily trigger an inflammatory response.

Usually, the regeneration cycle of bone tissue is very long, and the implant needs to remain in the body for about 6 – 12 months to fully the reconstruct bone tissue. Bone healing goes through three necessary stages: Inflammation, repair, and bone remodeling. In the first two stages, the bone defect site cannot bear weight, and implants are needed to provide sufficient support to prevent secondary injury. Therefore, in the early stage of healing, Mg alloy implants are required to have high mechanical strength to provide sufficient support; at the same time, a low degradation rate must be maintained to maintain the integrity of the mechanical structure and prevent mechanical failure due to excessive degradation. In addition, it can avoid problems such as swelling and local alkalinity caused by the production of a large amount of H_2, which results in inflammation of the implantation site. Therefore, improving the corrosion resistance of Mg alloys has become a top priority.

5. Conclusions

This paper reviews the research progress in the field of laser AM of Mg alloys, and summarizes and compares their powder preparation, process parameters, and post-processing. Biological Mg alloys show great application potential in the field of tissue engineering due to their good mechanical properties, natural degradability, and biocompatibility. However, under the complex human physiological environment, the corrosion rate cannot be effectively controlled. The follow-up research can start from the following aspects:

(i) Further studying the influence of alloying elements on the mechanical properties of Mg alloys, analyzing the changing trend of the mechanical properties of magnesium alloys during the corrosion process, and establishing the alloying criteria for biological Mg alloys.

(ii) Carrying out an in-depth study on the corrosion properties of biological Mg alloys in simulated body fluids and blood to find out the influencing factors, corrosion mechanism and corrosion laws in the corrosion process, and to provide scientific basis for the development and clinical applications of biological Mg alloys.

(iii) Setting up dynamic simulation environment, simulating the degradation behavior of Mg alloys *in vivo*, and collecting and analyzing *in vivo* experimental data.

Acknowledgments

The authors would also like to thank the Institute of AM of Jiangxi University of Science and Technology.

Funding

This study was supported by the following funds: (1) National Natural Science Foundation of China (51935014, 52165043, 82072084); (2) JiangXi Provincial Natural Science Foundation of China (20212BAB214026); and (3) Jiangsu Provincial Key Research and Development Program (BE2019002).

Conflict of interest

The authors declare that they have no competing financial interests that could have influenced the work reported in this paper.

Author contributions

Conceptualization: Chuyi Liu, Chengrong Ling, and Dongsheng Wang
Funding acquisition: Youwen Yang
Supervision: Youwen Yang and Cijun Shuai
Writing – original draft: Chuyi Liu
Writing – review & editing: Chengrong Ling, Cheng Chen, Youwen Yang, Deqiao Xie, and Cijun Shuai

All authors have read and agreed to the published version of the manuscript.

References

1. Xing F, Li S, Yin D, *et al.*, 2022, Recent progress in Mg-based alloys as a novel bioabsorbable biomaterials for orthopedic applications. *J Magnes Alloys*, 10: 1428–1456.

   https://doi.org/10.1016/j.jma.2022.02.013

2. Tschon M, Boanini E, Sartori M, *et al.*, 2022, Antiosteoporotic nanohydroxyapatite zoledronate scaffold seeded with bone marrow mesenchymal stromal cells for bone regeneration: A 3d *in vitro* model. *Int J Mol Sci*, 23: 5988.

   https://doi.org/10.3390/ijms23115988

3. Xia B, Chen G, 2022, Research progress of natural tissue-derived hydrogels for tissue repair and reconstruction. *Int J Biol Macromol*, 214: 480–491.

   https://doi.org/10.1016/j.ijbiomac.2022.06.137

4. Ni J, Ling H, Zhang S, *et al.,* 2019, Three-dimensional printing of metals for biomedical applications. *Mater Today Bio*, 3: 100024.

   https://doi.org/10.1016/j.mtbio.2019.100024

5. Li J, Qin L, Yang K, *et al.*, 2020, Materials evolution of bone plates for internal fixation of bone fractures: A review. *J Mater Sci Technol*, 36: 190–208.

   https://doi.org/10.1016/j.jmst.2019.07.024

6. Zhang B, Su Y, Zhou J, *et al.*, 2021, Toward a better regeneration through implant-mediated immunomodulation: Harnessing the immune responses. *Adv Sci*, 8: 2100446.

   https://doi.org/10.1002/advs.202100446

7. Bairagi D, Mandal S 2022, A comprehensive review on

biocompatible Mg-based alloys as temporary orthopaedic implants: Current status, challenges, and future prospects. *J Magnes Alloys*, 10: 627–669.

https://doi.org/10.1016/j.jma.2021.09.005

8. Venezuela JJ, Johnston S, Dargusch MS, 2019, The prospects for biodegradable zinc in wound closure applications. *Adv Healthc Mater*, 8: 1900408.

https://doi.org/10.1002/adhm.201900408

9. Kabir H, Munir K, Wen C, *et al.*, 2021, Recent research and progress of biodegradable zinc alloys and composites for biomedical applications: Biomechanical and biocorrosion perspectives. *Bioact Mater*, 6: 836–879.

https://doi.org/10.1016/j.bioactmat.2020.09.013

10. Qin Y, Wen P, Guo H, *et al.*, 2019, Additive manufacturing of biodegradable metals: Current research status and future perspectives. *Acta Biomater*, 98: 3–22.

https://doi.org/10.1016/j.actbio.2019.04.046

11. Venezuela J, Dargusch MS, 2019, The influence of alloying and fabrication techniques on the mechanical properties, biodegradability and biocompatibility of zinc: A comprehensive review. *Acta Biomater*, 87: 1–40.

https://doi.org/10.1016/j.actbio.2019.01.035

12. Shahin M, Wen C, Munir K, *et al.*, 2022, Mechanical and corrosion properties of graphene nanoplatelet-reinforced Mg-Zr and Mg-Zr-Zn matrix nanocomposites for biomedical applications. *J Magnes Alloys*, 10: 458–477.

https://doi.org/10.1016/j.jma.2021.05.011

13. Bommala VK, Krishna MG, Rao CT, 2019, Magnesium matrix composites for biomedical applications: A review. *J Magnes Alloys*, 7: 72–79.

https://doi.org/10.1016/j.jma.2018.11.001

14. Wang JL, Xu JK, Hopkins C, *et al.*, 2020, Biodegradable magnesium-based implants in orthopedics-a general review and perspectives. *Adv Sci*, 7: 1902443.

https://doi.org/10.1002/advs.201902443

15. Chandra G, Pandey A, 2020, Biodegradable bone implants in orthopedic applications: A review. *Biocybern Biomed Eng*, 40: 596–610.

https://doi.org/10.1016/j.bbe.2020.02.003

16. Wu CL, Xie WJ, Man HC, 2022, Laser additive manufacturing of biodegradable Mg-based alloys for biomedical applications: A review. *J Magnes Alloys*, 10: 915–937.

https://doi.org/10.1016/j.jma.2021.12.014

17. Wu S, Liu X, Yeung KW, *et al.*, 2014, Biomimetic porous scaffolds for bone tissue engineering. *Mater Sci Eng R Rep*, 80: 1–36.

https://doi.org/10.1016/j.mser.2014.04.001

18. Yang Y, He C, Dianyu E, *et al.*, 2020, Mg bone implant: Features, developments and perspectives. *Mater Design,* 185: 108259.

https://doi.org/10.1016/j.matdes.2019.108259

19. Li X, Liu X, Wu S, *et al.*, 2016, Design of magnesium alloys with controllable degradation for biomedical implants: From bulk to surface. *Acta Biomater*, 45: 2–30.

https://doi.org/10.1016/j.actbio.2016.09.005

20. Yazdimamaghani M, Razavi M, Vashaee D, *et al.*, 2017, Porous magnesium-based scaffolds for tissue engineering. *Mater Sci Eng C*, 71: 1253–1266.

https://doi.org/10.1016/j.msec.2016.11.027

21. Li C, Guo C, Fitzpatrick V, *et al.*, 2020, Design of biodegradable, implantable devices towards clinical translation. *Nat Rev Mater,* 5: 61–81.

https://doi.org/10.1038/s41578-019-0150-z

22. Malladi L, Mahapatro A, Gomes AS, 2018, Fabrication of magnesium-based metallic scaffolds for bone tissue engineering. *Mater Technol,* 33: 173–182.

https://doi.org/10.1080/10667857.2017.1404278

23. Payr E, 1900, Beitrage zur Technik der Blutgesfass und Nervennaht nebst Mittheilungen die Verwendung eines Resorbierharen Metalles in der Chirurgie. *Arch Klin Chir*, 62: 67–71.

24. Lambotte A, 1909, Technique et indication des protheses dans le traitement des fractures. *Presse Me*d, 17: 321.

25. Mcbride ED, 1938, Absorbable metal in bone surgery: A further report on the use of magnesium alloys. *J Am Med Assoc*, 111: 2464–2467.

https://doi.org/10.1001/jama.1938.02790530018007

26. Witte F, 2010, The history of biodegradable magnesium implants: A review. *Acta Biomater*, 6: 1680–1692.

https://doi.org/10.1016/j.actbio.2010.02.028

27. Biber R, Pauser J, Geßlein M, *et al.*, 2016, Magnesium-based absorbable metal screws for intra-articular fracture fixation. *Case Rep Orthop*, 2016: 9673174.

https://doi.org/10.1155/2016/9673174

28. Chaya A, Yoshizawa S, Verdelis K, *et al.*, 2015, *In vivo* study of magnesium plate and screw degradation and bone fracture healing. *Acta Biomater*, 18: 262–269.

https://doi.org/10.1016/j.actbio.2015.02.010

29. Zhao D, Huang S, Lu F, *et al.*, 2016, Vascularized bone grafting fixed by biodegradable magnesium screw for treating osteonecrosis of the femoral head. *Biomaterials*, 81: 84–92.

https://doi.org/10.1016/j.biomaterials.2015.11.038

30. Wang Z, Sun Z, Han B, *et al.*, 2020, Biological behavior

exploration of a paclitaxel-eluting poly-l-lactide-coated Mg-Zn-Y-Nd alloy intestinal stent *in vivo*. *RSC Adv*, 10: 15079–15090.

https://doi.org/10.1039/C9RA10156J

31. Sing SL, 2022, Perspectives on additive manufacturing enabled beta-titanium alloys for biomedical applications. *Int J Bioprint*, 8: 478.

https://doi.org/10.18063/ijb.v8i1.478

32. Chen Z, Han C, Gao M, *et al.*, 2022, A review on qualification and certification for metal additive manufacturing. *Virtual Phys Prototyp*, 17: 382–405.

https://doi.org/10.1080/17452759.2021.2018938

33. Ng CC, Savalani M, Man HC, 2011, Fabrication of magnesium using selective laser melting technique. *Rapid Prototyp J*, 17: 479–490.

https://doi.org/10.1108/13552541111184206

34. Irrinki H, Nath SD, Alhofors M, *et al.*, 2019, Microstructures, properties, and applications of laser sintered 17-4PH stainless steel. *J Am Ceram Soc*, 102: 5679–5690.

https://doi.org/10.1111/jace.16372

35. Hoeges S, Zwiren A, Schade C, 2017, Additive manufacturing using water atomized steel powders. *Metal Powder Rep*, 72: 111–117.

https://doi.org/10.1016/j.mprp.2017.01.004

36. Moghimian P, Poirié T, Habibnejad-Korayem M, *et al.*, 2021, Metal powders in additive manufacturing: A review on reusability and recyclability of common titanium, nickel and aluminum alloys. *Addit Manuf,* 43: 102017.

https://doi.org/10.1016/j.addma.2021.102017

37. Zheng D, Li Z, Jiang Y, *et al.*, 2022, Effect of multiple thermal cycles on the microstructure evolution of GA151K alloy fabricated by laser-directed energy deposition. *Addit Manuf*, 57: 102957.

https://doi.org/10.1016/j.addma.2022.102957

38. Aboulkhair NT, Simonelli M, Parry L, *et al.*, 2019, 3D printing of aluminium alloys: Additive manufacturing of aluminium alloys using selective laser melting. *Prog Mater Sci*, 106: 100578.

https://doi.org/10.1016/j.pmatsci.2019.100578.

39. Ji X, Mirkoohi E, Ning J, *et al.*, 2020, Analytical modeling of post-printing grain size in metal additive manufacturing. *Opt Lasers Eng*, 124: 105805.

https://doi.org/10.1016/j.optlaseng.2019.105805

40. He C, Bin S, Wu P, *et al.*, 2017, Microstructure evolution and biodegradation behavior of laser rapid solidified Mg-Al-Zn alloy. *Metals*, 7: 105.

https://doi.org/10.3390/met7030105

41. Shuai C, Yang Y, Wu P, *et al.*, 2017, Laser rapid solidification improves corrosion behavior of Mg-Zn-Zr alloy. *J Alloys Compd*, 691: 961–969.

https://doi.org/10.1016/j.jallcom.2016.09.019

42. Spierings AB, Dawson K, Dumitraschkewitz P, *et al.*, 2018, Microstructure characterization of SLM-processed Al-Mg-Sc-Zr alloy in the heat treated and HIPed condition. *Addit Manuf*, 20: 173–181.

https://doi.org/10.1016/j.addma.2017.12.011

43. Buhairi MA, Foudzi FM, Jamhari FI, *et al.*, 2022, Review on volumetric energy density: Influence on morphology and mechanical properties of Ti6Al4V manufactured via laser powder bed fusion. *Prog Addit Manuf*,

https://doi.org/10.1007/s40964-022-00328-0

44. Liang J, Lei Z, Chen Y, *et al.*, 2022, Formability, microstructure, and thermal crack characteristics of selective laser melting of ZK60 magnesium alloy. *Mater Sci Eng A*, 839: 142858.

https://doi.org/10.1016/j.msea.2022.142858

45. Esmaily M, Zeng Z, Mortazavi AN, *et al.*, 2020, A detailed microstructural and corrosion analysis of magnesium alloy WE43 manufactured by selective laser melting. *Addit Manuf*, 35: 101321.

https://doi.org/10.1016/j.addma.2020.101321

46. Wei K, Gao M, Wang Z, Zeng X, 2014, Effect of energy input on formability, microstructure and mechanical properties of selective laser melted AZ91D magnesium alloy. *Mater Sci Eng A*, 611: 212–222.

https://doi.org/10.1016/j.msea.2014.05.092

47. Yang Y, Wu P, Lin X, *et al.*, 2016, System development, formability quality and microstructure evolution of selective laser-melted magnesium. *Virtual Phys Prototyp*, 11: 173–181.

https://doi.org/10.1080/17452759.2016.1210522

48. Sezer N, Evis Z, Koç M, 202, Additive manufacturing of biodegradable magnesium implants and scaffolds: Review of the recent advances and research trends. *J Magnes Alloys*, 9: 392–415.

https://doi.org/10.1016/j.jma.2020.09.014

49. Liu S, Yang W, Shi X, *et al.*, 2019, Influence of laser process parameters on the densification, microstructure, and mechanical properties of a selective laser melted AZ61 magnesium alloy. *J Alloys Compd*, 808: 151160.

https://doi.org/10.1016/j.jallcom.2019.06.261

50. Liu C, Zhang M, Chen C, 2017, Effect of laser processing parameters on porosity, microstructure and mechanical properties of porous Mg-Ca alloys produced by laser additive manufacturing. *Mater Sci Eng A*, 703: 359-371.

https://doi.org/10.1016/j.msea.2017.07.031

51. Yang Y, Lu C, Peng S, *et al.*, 2020, Laser additive manufacturing of Mg-based composite with improved degradation behaviour. *Virtual Phys Prototyp*, 15: 278–293.

    https://doi.org/10.1080/17452759.2020.1748381

52. Zhang M, Chen C, Liu C, *et al.*, Study on porous Mg-Zn-Zr ZK61 alloys produced by laser additive manufacturing. *Metals*, 8: 635.

    https://doi.org/10.3390/met8080635

53. Deng Q, Wu Y, Wu Q, *et al.*, 2022, Microstructure evolution and mechanical properties of a high-strength Mg-10Gd-3Y-1Zn-0.4Zr alloy fabricated by laser powder bed fusion. *Addit Manuf*, 49: 102517.

    https://doi.org/10.1016/j.addma.2021.102517

54. Wang T, Meng Q, Araby S, *et al.*, 2021, Non-oxidized graphene/metal composites by laser deposition additive manufacturing. *J Alloys Compd,* 882: 160724.

    https://doi.org/10.1016/j.jallcom.2021.160724

55. Cao X, Jahazi M, Immarigeon JP, *et al.*, 2006, A review of laser welding techniques for magnesium alloys. *J Mater Process Technol*, 171: 188–204.

    https://doi.org/10.1016/j.jmatprotec.2005.06.068

56. Manakari V, Parande G, Gupta M, 2017, Selective laser melting of magnesium and magnesium alloy powders: A review. *Metals*, 7: 2.

    https://doi.org/10.3390/met7010002

57. Gangireddy S, Gwalani B, Liu K, *et al.*, 2019, Microstructure and mechanical behavior of an additive manufactured (AM) WE43-Mg alloy. *Addit Manuf*, 26: 53–64.

    https://doi.org/10.1016/j.addma.2018.12.015

58. Hosseini E, Popovich VA, 2019, A review of mechanical properties of additively manufactured Inconel 718. *Addit Manuf*, 30: 100877.

    https://doi.org/10.1016/j.addma.2019.100877

59. Wang Y, Fu P, Wang N, *et al.*, 2020, Challenges and solutions for the additive manufacturing of biodegradable magnesium implants. *Engineering*, 6: 1267–1275.

    https://doi.org/10.1016/j.eng.2020.02.015

60. Dou Y, Cai S, Ye X, *et al.*, 2013, 45S5 bioactive glass-ceramic coated AZ31 magnesium alloy with improved corrosion resistance. *Surf Coat Technol*, 228: 154–161.

    https://doi.org/10.1016/j.surfcoat.2013.04.022

61. Rojaee R, Fathi M, Raeissi K 2013, Electrophoretic deposition of nanostructured hydroxyapatite coating on AZ91 magnesium alloy implants with different surface treatments. *Appl Surf Sci*, 285: 664–673.

    https://doi.org/10.1016/j.apsusc.2013.08.108

62. Razavi M, Fathi M, Savabi O, *et al.*, 2014, Controlling the degradation rate of bioactive magnesium implants by electrophoretic deposition of akermanite coating. *Ceram Int*, 40: 3865–3872.

    https://doi.org/10.1016/j.ceramint.2013.08.027

63. Kopp A, Derra T, Müther M, *et al.*, 2019, Influence of design and postprocessing parameters on the degradation behavior and mechanical properties of additively manufactured magnesium scaffolds. *Acta Biomater*, 98: 23–35.

    https://doi.org/10.1016/j.actbio.2019.04.012

64. Han J, Chen J, Peng L, *et al.*, 2017, Microstructure, texture and mechanical properties of friction stir processed Mg-14Gd alloys. *Mater Design*, 130: 90–102.

    https://doi.org/10.1016/j.matdes.2017.05.046

65. Huang C, Yan X, Zhao L, *et al.*, 2019, Ductilization of selective laser melted Ti6Al4V alloy by friction stir processing. *Mater Sci Eng A*, 755: 85–96.

    https://doi.org/10.1016/j.msea.2019.03.133

66. Macías JG, Elangeswaran C, Zhao L, *et al.*, 2019, Ductilisation and fatigue life enhancement of selective laser melted AlSi10Mg by friction stir processing. *Scr Mater*, 170: 124–128.

    https://doi.org/10.1016/j.scriptamat.2019.05.044

67. Deng Q, Wu Y, Su N, *et al.*, 2021, Influence of friction stir processing and aging heat treatment on microstructure and mechanical properties of selective laser melted Mg-Gd-Zr alloy. *Addit Manuf*, 44: 102036.

    https://doi.org/10.1016/j.addma.2021.102036

68. Alfieri V, Argenio P, Caiazzo F, *et al.*, 2017, Reduction of surface roughness by means of laser processing over additive manufacturing metal parts. *Materials*. 10: 30.

    https://doi.org/10.3390/ma10010030

69. Basha SM, Bhuyan M, Basha MM, *et al.*, 2020, Laser polishing of 3D printed metallic components: A review on surface integrity. *Mater Today Proc*, 26: 2047–2054.

    https://doi.org/10.1016/j.matpr.2020.02.443

70. Zhang X, Li XW, Li JG, *et al.*, 2014, Preparation and mechanical property of a novel 3D porous magnesium scaffold for bone tissue engineering. *Mater Sci Eng C*, 42: 362–367.

    https://doi.org/10.1016/j.msec.2014.05.044

71. Hyer H, Zhou L, Benson G, *et al.*, 2020, Additive manufacturing of dense WE43 Mg alloy by laser powder bed fusion. *Addit Manuf*, 33: 101123.

    https://doi.org/10.1016/j.addma.2020.101123

72. Fang X, Yang J, Wang S, *et al.*, 2022, Additive manufacturing of high performance AZ31 magnesium alloy with full equiaxed grains: Microstructure, mechanical property, and electromechanical corrosion performance. *J Mater Proc*

Technol, 300: 117430.

https://doi.org/10.1016/j.jmatprotec.2021.117430

73. Wang Y, Huang H, Jia G, *et al.*, 2021, Fatigue and dynamic biodegradation behavior of additively manufactured Mg scaffolds. *Acta Biomater*, 135: 705–722.

https://doi.org/10.1016/j.actbio.2021.08.040

74. Chen J, Wu P, Wang Q, *et al.*, 2016, Influence of alloying treatment and rapid solidification on the degradation behavior and mechanical properties of Mg. *Metals*, 6: 259.

https://doi.org/10.3390/met6110259

75. Liu J, Liu B, Min S, *et al.*, 2022, Biodegradable magnesium alloy WE43 porous scaffolds fabricated by laser powder bed fusion for orthopedic applications: Process optimization, *in vitro* and *in vivo* investigation. *Bioact Mater*, 16: 301–319.

https://doi.org/10.1016/j.bioactmat.2022.02.020

76. Hyer H, Zhou L, Liu Q, *et al.*, 2021, High strength WE43 microlattice structures additively manufactured by laser powder bed fusion. *Materialia*, 16: 101067.

https://doi.org/10.1016/j.mtla.2021.101067

77. Zhang WN, Wang LZ, Feng ZX, *et al.*, 2020, Research progress on selective laser melting (SLM) of magnesium alloys: A review. *Optik*, 207: 163842.

https://doi.org/10.1016/j.ijleo.2019.163842

78. Shuai C, Li S, Peng S, *et al.*, 2019, Biodegradable metallic bone implants. *Mater Chem Front*, 3: 544–562.

https://doi.org/10.1039/C8QM00507A

79. Liu J, Lin Y, Bian D, *et al.*, 2019, *In vitro* and *in vivo* studies of Mg-30Sc alloys with different phase structure for potential usage within bone. *Acta Biomater*, 98: 50–66.

https://doi.org/10.1016/j.actbio.2019.03.009

80. Han HS, Loffredo S, Jun I, *et al.*, 2019, Current status and outlook on the clinical translation of biodegradable metals. *Mater Today*, 23: 57–71.

https://doi.org/10.1016/j.mattod.2018.05.018

81. Cao F, Shi Z, Song GL, *et al.*, 2013, Corrosion behaviour in salt spray and in 3.5% NaCl solution saturated with Mg(OH)2 of as-cast and solution heat-treated binary Mg-X alloys: X=Mn, Sn, Ca, Zn, Al, Zr, Si, Sr. *Corros Sci*, 76: 60–97.

https://doi.org/10.1016/j.corsci.2013.06.030

82. Peng Q, Huang Y, Zhou L, *et al.*, 2010, Preparation and properties of high purity Mg-Y biomaterials. *Biomaterials*, 31: 398–403.

https://doi.org/10.1016/j.biomaterials.2009.09.065

83. Shuai S, Guo E, Zheng Q, *et al.*, 2016, Three-dimensional α-Mg dendritic morphology and branching structure transition in Mg-Zn alloys. *Mater Charact*, 118: 304–308.

https://doi.org/10.1016/j.matchar.2016.06.009

84. Li J, Xie D, Yu H, *et al.*, 2020, Microstructure and mechanical property of multi-pass low-strain rolled Mg-Al-Zn-Mn alloy sheet. *J Alloys Compd*, 835: 155228.

https://doi.org/10.1016/j.jallcom.2020.155228

85. Luo Q, Guo Y, Liu B, *et al.*, 2020, Thermodynamics and kinetics of phase transformation in rare earth-magnesium alloys: A critical review. *J Mater Sci Technol*, 44: 171–190.

https://doi.org/10.1016/j.jmst.2020.01.022

86. Leleu S, Rives B, Bour J, *et al.*, 2018, On the stability of the oxides film formed on a magnesium alloy containing rare-earth elements. *Electrochim Acta,* 290: 586–594.

https://doi.org/10.1016/j.electacta.2018.08.093

87. Willbold E, Gu X, Albert D, *et al.*, 2015, Effect of the addition of low rare earth elements (lanthanum, neodymium, cerium) on the biodegradation and biocompatibility of magnesium. *Acta Biomater*, 11: 554–562.

https://doi.org/10.1016/j.actbio.2014.09.041

88. Wang C, Shuai Y, Yang Y, *et al.*, 2022, Amorphous magnesium alloy with high corrosion resistance fabricated by laser powder bed fusion. *J Alloys Compd*, 897: 163247.

https://doi.org/10.1016/j.jallcom.2021.163247

89. Chen S, Tu J, Hu Q, *et al.*, 2017, Corrosion resistance and *in vitro* bioactivity of Si-containing coating prepared on a biodegradable Mg-Zn-Ca bulk metallic glass by micro-arc oxidation. *J Non Cryst Solids*, 456: 125–131.

https://doi.org/10.1016/j.jnoncrysol.2016.11.011

90. Zhang D, Qin Y, Feng W, *et al.*, 2019, Microstructural evolution of the amorphous layers on Mg-Zn-Ca alloy during laser remelting process. *Surf Coat Technol*, 363: 87–94.

https://doi.org/10.1016/j.surfcoat.2019.02.051

91. Zberg B, Arata ER, Uggowitzer PJ, *et al.*, 2009, Tensile properties of glassy MgZnCa wires and reliability analysis using Weibull statistics. *Acta Mater*, 57: 3223–3231.

https://doi.org/10.1016/j.actamat.2009.03.028

92. Shuai C, Liu L, Zhao M, *et al.*, 2018, Microstructure, biodegradation, antibacterial and mechanical properties of ZK60-Cu alloys prepared by selective laser melting technique. *J Mater Sci Technol*, 34: 1944–1952.

https://doi.org/10.1016/j.jmst.2018.02.006

93. Spriano S, Yamaguchi S, Baino F, *et al.*, 2018, A critical review of multifunctional titanium surfaces: New frontiers for improving osseointegration and host response, avoiding bacteria contamination. *Acta Biomater*, 79: 1–22.

https://doi.org/10.1016/j.actbio.2018.08.013

94. Ouyang P, Dong H, He X, *et al.*, 2019, Hydromechanical mechanism behind the effect of pore size of porous titanium scaffolds on osteoblast response and bone ingrowth. *Mater Design*, 183: 108151.

https://doi.org/10.1016/j.matdes.2019.108151

95. Rojaee R, Fathi M, Raeissi K, 2013, Controlling the degradation rate of AZ91 magnesium alloy via sol-gel derived nanostructured hydroxyapatite coating. *Mater Sci Eng C*, 33: 3817–3825.

https://doi.org/10.1016/j.msec.2013.05.014

96. Tian M, Cai S, Ling L, *et al.*, 2022, Superhydrophilic hydroxyapatite/hydroxypropyltrimethyl ammonium chloride chitosan composite coating for enhancing the antibacterial and corrosion resistance of magnesium alloy. *Prog Org Coat*, 165: 106745.

https://doi.org/10.1016/j.porgcoat.2022.106745

97. Roshan NR, Hassannejad H, Nouri A, 2021, Corrosion and mechanical behaviour of biodegradable PLA-cellulose nanocomposite coating on AZ31 magnesium alloy. *Surf Eng*, 37: 236–245.

https://doi.org/10.1080/02670844.2020.1776093

98. Dutta S, Devi KB, Mandal S, *et al.,* 2019, *In vitro* corrosion and cytocompatibility studies of hot press sintered magnesium-bioactive glass composite. *Materialia*, 5: 100245.

https://doi.org/10.1016/j.mtla.2019.100245

99. Kang YG, Wei J, Shin JW, *et al.*, 2018, Enhanced biocompatibility and osteogenic potential of mesoporous magnesium silicate/polycaprolactone/wheat protein composite scaffolds. *Int J Nanomed*, 13: 1107–1117.

https://doi.org/10.2147/ijn.S157921

100. Gong X, Zeng D, Groeneveld-Meijer W, *et al.*, 2022, Additive manufacturing: A machine learning model of process-structure-property linkages for machining behavior of Ti-6Al-4V. *Mater Sci Addit Manuf*, 1: 6.

https://doi.org/10.18063/msam.v1i1.6

101. Sing SL, Kuo CN, Shih CT, *et al.*, 2021, Perspectives of using machine learning in laser powder bed fusion for metal additive manufacturing. *Virtual Phys Prototyp*, 16: 372–386.

https://doi.org/10.1080/17452759.2021.1944229

Materials Science in Additive Manufacturing

REVIEW ARTICLE

A survey of additive manufacturing reviews

Xiaoya Zhai[1], Liuchao Jin[2], Jingchao Jiang[2]*

[1]School of Mathematical Sciences, University of Science and Technology of China, China

[2]Department of Mechanical and Automation Engineering, The Chinese University of Hong Kong, Shatin, Hong Kong, China

Abstract

Nowadays, additive manufacturing (AM) technologies have been widely used in construction, medical, military, aerospace, fashion, etc. The advantages of AM (e.g., more design freedom, no restriction on the complexity of parts, and rapid prototyping) have attracted a growing number of researchers. Increasing number of papers are published each year. Until now, thousands of review papers have already been published in the field of AM. It is, therefore, perhaps timely to perform a survey on AM review papers so as to provide an overview and guidance for readers to choose their interested reviews on some specific topics. This survey gives detailed analysis on these reviews, divides these reviews into different groups based on the AM techniques and materials used, highlights some important reviews in this area, and provides some discussions and insights.

Keywords: Additive manufacturing; 3D printing; Review

***Corresponding author:**
Jingchao Jiang
(jjia547@aucklanduni.ac.nz)

Citation: Zhai X, Jin L, Jiang J, 2022, A survey of additive manufacturing reviews. *Mater Sci Addi Manuf.* 1(4): 21.
https://doi.org/10.18063/msam.v1i4.21

Received: October 10, 2022

Accepted: October 28, 2022

Published Online: November 16, 2022

1. Introduction

Thirty years into its development, additive manufacturing (AM, also known as 3D printing) has become a mainstream manufacturing process. AM fabricates parts by adding materials layer-by-layer directly based on a 3D model. It is able to manufacture complex parts and allows more freedom of design optimization compared with traditional manufacturing techniques[1]. According to ISO/ASTM, AM can be divided into seven groups: vat photopolymerization, material jetting, binder jetting, powder bed fusion, material extrusion, directed energy deposition, and sheet lamination[2]. AM has its distinctive advantages over conventional manufacturing processes, for example, reduced product development time, lower cost, and ability to fabricate almost any complex shape. Therefore, AM has now been widely used in construction, medical, military, aerospace, fashion, etc. Until now, thousands of review papers have already been published in the field of AM, let alone the published research papers in this field. Figure 1 shows the number of published review papers in AM in each year. As can be seen, there are too many AM review papers published in recent years, with huge increasing rate. It is, therefore, perhaps timely to conduct a survey on AM review papers so as to provide an overview and guidance for readers to choose their interested reviews on some specific topics. This survey gives detailed analysis on these reviews, divides these reviews into different groups, and highlights some important reviews in this area along with discussions.

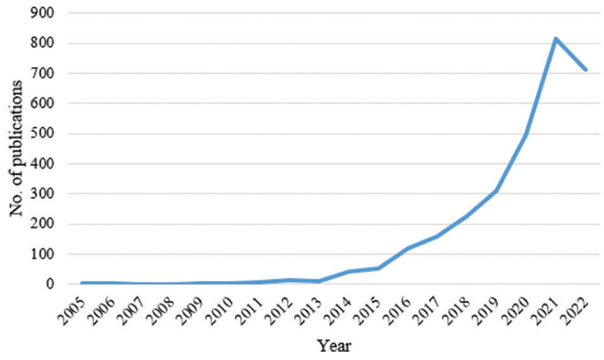

Figure 1. Number of publications of AM review papers in each year (statistics from Scopus database; search keywords: "additive manufacturing" in the title, abstract or keywords, then limited to review; access date: October 19, 2022).

2. Additive manufacturing technologies

This section gives a brief introduction on AM technologies. According to ISO/ASTM[2], AM can be divided into seven categories: (i) Material extrusion, (ii) powder bed fusion, (iii) material jetting, (iv) binder jetting, (v) directed energy deposition, (vi) vat photopolymerization, and (vii) sheet lamination. Each AM technique will be introduced briefly before going into the review papers published in this area.

2.1. Material extrusion

Material extrusion is an AM process that selectively distributes material through nozzles or orifices[3-6]. In 1988, Scott Crump, co-founder of Stratasys Ltd., developed the AM process, which forms a layer by mechanically extruding molten thermoplastic materials (e.g., acrylonitrile butadiene styrene (ABS) and polylactic acid (PLA)) onto the substrate[7]. This AM process was subsequently coined as fused deposition modeling (FDM), which requires a high operating temperature to melt the material[8]. The manufacturing process of FDM starts from a 3D model, which is then translated into gcode data that can be read by FDM machines. After the data is sent to the machine, the machine can manufacture parts in a point-by-point and then layer-by-layer manner, from the bottom of the part to the top, until the whole part is completed. The material (filament) is first melted in the liquefier/extrusion head and then deposited carefully through a nozzle to platform of the printer. The extrusion head moves along the X and Y axes, while the construction platform operates up and down on the Z axis. At present, a lot of materials have been developed for material extrusion AM, including acrylonitrile-butadiene-styrene (ABS), nylon, high impact polystyrene (HIPS), polyethylene terephthalate (PET), polylactic acid (PLA), polyethylene terephthalate glycol (PETG), polyether ether ketone (PEEK), and thermoplastic polyester (TPC). In general, support removal and post-processing may be needed after fabrication[9].

2.2. Powder bed fusion

Powder bed fusion is another AM process. Typically, powder bed fusion selectively melts the powder in the tank using an energy beam (laser or electron)[10]. After scanning and finishing one layer of powder, the rolling mechanism helps spread the next layer of the powder. Then, the next layer is scanned, melted, and fused, until the entire part is completed. In the mid-1980s, Deckard and Beaman developed the polymer powder bed fusion technology, which is used to process polymer powders[11]. Now, more materials can also be used in this technology, such as ceramics or metals[12,13]. Selective laser melting (SLM)[14,15], selective laser sintering (SLS)[16], direct metal laser sintering (DMLS)[17,18], and electron beam melting (EBM)[19] are among the most popular metal powder bed fusion technologies. DMLS and SLM use focused laser beams as power sources[20-22], while EBM uses scanning electron beams (up to 60 kV) as the power source[23]. The actual printing process is completed in a vacuum or inert environment to avoid powder oxidation.

2.3. Material jetting

Material jetting is similar to inkjet printing. Inkjet printing deposits ink droplets onto a substrate drop by drop, while material jetting process directly deposits wax and/or photopolymer droplets onto the substrate by on-demand inkjet[24,25]. Light curing or heating is the driving force of the phase change of the sprayed droplets. A lot of research has been carried out on material jetting, including direct ink jetting of nanoink suspensions of ceramics[26,27], semiconductor[28], and metals[29].

2.4. Binder jetting

In binder jetting, a liquid polymer is selectively deposited onto a bed of powder[30]. The jetted polymer droplet infiltrates the powder surface, leading to a printed powder agglomerate primitive. Powder spreading promotes recoating, as is done in powder bed fusion processes. The finished parts are composed of bound powder, which requires infiltration through post-processing to gain enough strength. Any powdered material that can be successfully spread and wet by the jetted binder can be used in this technique. Different materials have been studied using this technique, for example, foundry sand[31], metal[32], polymer materials[33], and ceramic[34]. The binding mechanism of this technique is chemical and/or thermal reaction bonding. Depending on the bonding agent, chemical reaction is generally the source of activation. After completing the fabrication, post-processing may be necessary, including removal of loose powder and impregnation/infiltration of

suitable liquid material depending on the powder material and intended application.

2.5. Directed energy deposition

In directed energy deposition (DED), metallic powder or wire is fed directly into the focal point of an energy beam to create a molten pool[35]. Laser Engineered Net Shaping (LENS), belonging to DED, was first developed at Sandia National Laboratories in 1995 and commercialized by Optomec[36]. Parts printed by LENS accommodate graded multi-materials[37] and allow microstructures with complex inner features[38]. DED systems with wire-fed methods have been achieved[39], and DED of powder directly has also been successful[40,41]. Lasers and electron beams are the most commonly used energy source.

2.6. Vat photopolymerization

The definition of Vat photopolymerization is an "additive manufacturing process in which liquid photopolymer in a vat is selectively cured by light-activated polymerization"[2]. Vat photopolymerization uses a (liquid) photopolymer resin which is able to cure (solidify) under a light source[42,43]. Stereolithography (SLA) and digital light processing (DLP) are the most used techniques which belong to Vat photopolymerization. The scanning speed of vat photopolymerization is relatively high and minimum layer thickness is adjustable depending on the curing depth[44]. Once finishing the printing, post-processing may be needed, for example, support material removal and/or post-curing by further UV exposure.

2.7. Sheet lamination

Sheet lamination is an AM process in which sheets of material are bonded to form a part[45]. The process works by scrubbing each layer together with pressure and/or binders continuously. In this technique, the raw material typically is paper, metal foil, polymers or composite sheets predominately formed of metal, or ceramic powder material. Thermal reaction, chemical reaction bonding, or ultrasound can be used for binding. The source of activation includes localized or large-scale heating, chemical reaction, and ultrasonic transducers.

3. Analysis and discussion of AM review papers

This section gives the detailed analysis of review papers published within the field of AM. Top authors, source journals, affiliations of authors, and countries, are discussed. Then, the review papers are analyzed and discussed based on their different focuses, for example, different AM techniques (as briefly introduced in the previous section) and materials used. The database used is Scopus. Scopus is one of the most used databases, and it includes more papers than the Web of science.

3.1. Top 10 authors

As shown in Figure 2, Ramakrishna Seeram from National University of Singapore has the most review papers (21) published within AM field, followed by Chua Chee Kai from Singapore University of Technology and Design, and Yeong Wai Yee from Nanyang Technological University. It is interesting that all the top three authors are from Singapore. Researchers may refer their publications to catch up the up-to-date research in the AM field.

3.2. Top ten journals

Looking at the sources of these review papers (Figure 3), most of these AM review papers are published in journal *Additive Manufacturing*, followed by *Materials* and *International Journal of Advanced Manufacturing Technology*. Researchers may check these journals' websites to see the state-of-the-art developments of AM technologies.

3.3. Top 10 affiliations

As shown in Figure 4, most of the review papers in additive manufacturing are from Nanyang Technological University, followed by Singapore Centre for 3D Printing.

3.4. Top ten countries

Looking at the countries of the authors from, United States has the most review papers in AM, with 756 review papers published, followed by China with 617 publications (Figure 5).

3.5. Review papers in the seven AM techniques

Dividing these review papers into the seven AM techniques as introduced in section 2, it can be found that most review papers are about powder bed fusion, and no review paper is found in sheet lamination (Figure 6). This is probably because powder bed fusion is the most focused research area within AM, due to its application potential in aerospace, engineering, and biomedicine. While, sheet lamination seems a little bit out of focus at this moment. Note that, the review papers collected in this subsection only consider the broad review in these seven AM techniques, excluding the review papers focused on a specific topic (e.g., process parameters' influence, fatigue analysis, and path planning). For the broad reviews in these seven AM techniques, the most cited papers are listed in Table 1. Readers can check these papers based on their interests. Table 2 gives more review papers focusing on the specific topics in each AM technique. For example, Nohut and Schwentenwein[46] focuses on functionally graded materials in vat photopolymerization, while Xu *et al.*[47] focuses on drug

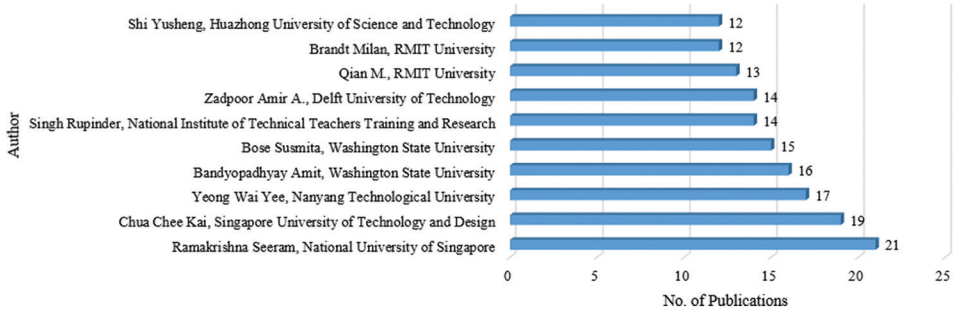

Figure 2. Top ten authors of AM review papers (statistics from Scopus database; search keywords: "additive manufacturing" in the title, abstract or keywords, then limited to review; access date: October 19, 2022).

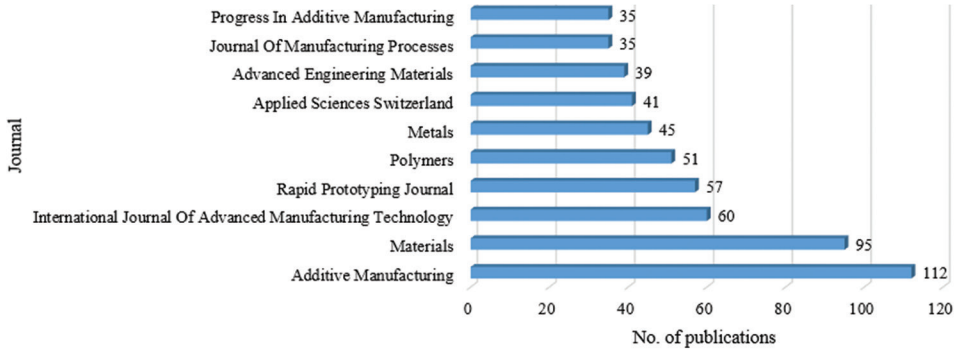

Figure 3. Top ten journals of AM review papers published in (statistics from Scopus database; search keywords: "additive manufacturing" in the title, abstract or keywords, then limited to review; access date: October 19, 2022).

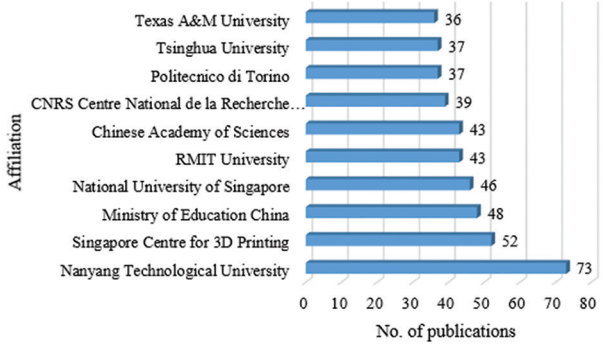

Figure 4. Top ten affiliations of authors of AM review papers (statistics from Scopus database; search keywords: "additive manufacturing" in the title, abstract or keywords, then limited to review; access date: October 19, 2022).

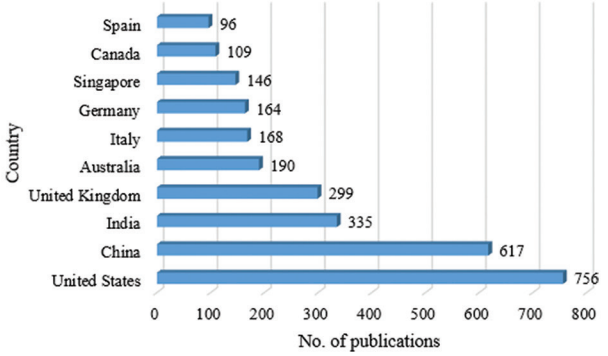

Figure 5. Top ten countries of authors of AM review papers (statistics from Scopus database; search keywords: "additive manufacturing" in the title, abstract or keywords, then limited to review; access date: October 19, 2022).

delivery and medical device in Vat photopolymerization. In terms of powder bed fusion, Luo and Zhao[48] focuses on thermal stress, while McCann *et al.*[49] focuses on process monitoring and machine control. More details on the topics these review papers focus on are shown in Table 2.

3.6. Review paper categories based on materials

From the point view of materials, there are also various review papers in additive manufacturing focusing on different materials. In this survey, the materials are categorized into ten groups, including metal, ceramic, polymer, biomaterial, concrete, fiber, food, smart material, glass, and wood for AM. As shown in Figure 7, most review papers revolve around polymer and metal. This is probably because both polymer and metal are the most commonly used materials and have already been studied a lot. Table 3 lists the most cited review papers in each type of material. Table 4 presents more review papers in

Table 1. Top cited review papers in the seven AM categories

Category	First author	Published year	Article title	No. of citations	References
Material extrusion	Wickramasinghe *et al.*	2020	FDM-Based 3D printing of polymer and associated composite: A review on mechanical properties, defects and treatments	199	[50]
	Dey and Yodo	2019	A systematic survey of FDM process parameter optimization and their influence on part characteristics	173	[51]
Binder jetting	Ziaee and Crane	2019	Binder jetting: A review of process, materials, and methods	221	[52]
Vat photopolymerization	Pagac *et al.*	2021	A review of vat photopolymerization technology: Materials, applications, challenges, and future trends of 3d printing	74	[53]
Material jetting	Gülcan *et al.*	2021	The state of the art of material jetting-a critical review	18	[54]
Powder bed fusion	Grasso and Colosimo	2017	Process defects and *in situ* monitoring methods in metal powder bed fusion: A review	384	[55]
Directed energy deposition	Dass and Moridi	2019	State of the art in directed energy deposition: From additive manufacturing to materials design	150	[56]
	Ahn	2021	Directed Energy Deposition (DED) Process: State of the Art	44	[57]

Statistics from Scopus database; access date: October 19, 2022

Table 2. AM review papers with different topics in each AM technique

Category	Keywords	Article title	First author	References
Vat photopolymerization	Tissue scaffolds	A review on fabricating tissue scaffolds using vat photopolymerization	Chartrain *et al.*	[58]
	Drug delivery; medical device	Vat photopolymerization 3D printing for advanced drug delivery and medical device applications	Xu *et al.*	[47]
	4D printing	4D printing materials for vat photopolymerization	Andreu *et al.*	[59]
	Functionally graded materials	Vat Photopolymerization Additive Manufacturing of Functionally Graded Materials: A Review	Nohut and Schwentenwein	[46]
	Shape-conformable batteries	Toward High Resolution 3D Printing of Shape-Conformable Batteries via Vat Photopolymerization: Review and Perspective	Maurel *et al.*	[60]
	Functional materials	A Review of Multi-Material 3D Printing of Functional Materials via Vat Photopolymerization	Shaukat *et al.*	[61]
Powder bed fusion	Residual stress	An overview of residual stresses in metal powder bed fusion	Bartlett *et al.*	[62]
	Thermal stress	A survey of finite element analysis of temperature and thermal stress fields in powder bed fusion Additive Manufacturing	Luo and Zhao	[48]
	Process physics; material screening	A review of the process physics and material screening methods for polymer powder bed fusion additive manufacturing	Chatham *et al.*	[63]
	Aluminum alloys	New aluminum alloys specifically designed for laser powder bed fusion: A review	Aversa *et al.*	[64]
	Repeatability; reproducibility	A review of critical repeatability and reproducibility issues in powder bed fusion	Dowling *et al.*	[65]
	Formation and impact of flaws	Invited Review Article: Review of the formation and impact of flaws in powder bed fusion additive manufacturing	Snow *et al.*	[66]

(Contd...)

Table 2. *(Continued)*

Category	Keywords	Article title	First author	References
	drug delivery; healthcare	Advances in powder bed fusion 3D printing in drug delivery and healthcare	Awad *et al.*	[67]
	Process monitoring; machine control	In-situ sensing, process monitoring and machine control in Laser Powder Bed Fusion: A review	McCann *et al.*	[49]
Binder jetting	Stainless steel	A review on binder jet additive manufacturing of 316L stainless steel	Mirzababaei and Pasebani	[68]
Material extrusion	Process–Structure–Properties	Process–Structure–Properties in Polymer Additive Manufacturing via Material Extrusion: A Review	Goh *et al.*	[69]
	Dimensional inaccuracy; warpage	Material extrusion-based additive manufacturing of polypropylene: A review on how to improve dimensional inaccuracy and warpage	Spoerk *et al.*	[70]
	Fiber-reinforced polymers	Fused filament fabrication of fiber-reinforced polymers: A review	Brenken *et al.*	[71]
	Plant biopolymers	Material extrusion of plant biopolymers: Opportunities & challenges for 3D printing	Chaunier *et al.*	[72]
	Design methods	A survey of design methods for material extrusion polymer 3D printing	Huang *et al.*	[73]
	Continuous fiber	Material extrusion additive manufacturing of continuous fiber reinforced polymer matrix composites: A review and outlook	Zhuo *et al.*	[5]
	Wood; lignocellulosic	Material extrusion additive manufacturing of wood and lignocellulosic filled composites	Lamm *et al.*	[74]
	Process monitoring	Process monitoring for material extrusion additive manufacturing: a state-of-the-art review	Oleff *et al.*	[75]
	Plant protein	Plant protein in material extrusion 3D printing: Formation, plasticization, prospects, and challenges	Rowat *et al.*	[76]
Directed energy deposition	Repair	Application of directed energy deposition-based additive manufacturing in repair	Saboori *et al.*	[77]
	In situ monitoring	A review on *in situ* monitoring technology for directed energy deposition of metals	Tang *et al.*	[78]
	Slicing	A review of slicing methods for directed energy deposition based additive manufacturing	Xu *et al.*	[79]
	Adaptive control	Review on adaptive control of laser-directed energy deposition	Wang *et al.*	[80]
	High-quality	Preventing evaporation products for high-quality metal film in directed energy deposition: A review	Kim *et al.*	[81]
	Process parameters; Ti	Selective laser manufacturing of Ti-based alloys and composites: impact of process parameters, application trends, and future prospects	Singh *et al.*	[82]
	Heat treatments; quality; residual stress	A review of heat treatments on improving the quality and residual stresses of the Ti–6Al–4V parts produced by additive manufacturing	Teixeira *et al.*	[83]

Statistics from Scopus database; access date: October 19, 2022

AM, focusing on different materials. We have concluded and listed some of the typical review papers in different materials. For the category of materials in Table 4, ABS, PLA, and PEEK are listed separately as these three types of materials are widely used nowadays and there are a lot of published review papers on these three materials. Note that not all review papers are listed in this table as there are too many papers published nowadays. However, Tables 3 and 4 should be enough for readers to obtain the essential information.

Table 3. Top cited review papers in different materials

Category	First author	Published year	Article title	No. of citations	Reference
Metal	Frazier	2014	Metal additive manufacturing: A review	3289	[84]
	Sames *et al.*	2016	The metallurgy and processing science of metal additive manufacturing	1320	[85]
Ceramics	Deckers *et al.*	2014	Additive manufacturing of ceramics: A review	294	[86]
	Sing *et al.*	2017	Direct selective laser sintering and melting of ceramics: A review	197	[87]
Polymer	Ligon *et al.*	2017	Polymers for 3D printing and customized additive manufacturing	1626	[88]
Stainless steel	Kong *et al.*	2021	About metastable cellular structure in additively manufactured austenitic stainless steels	92	[89]
	Jin *et al.*	2020	Wire arc additive manufacturing of stainless steels: A review	83	[90]
Ni-based alloys	Attallah *et al.*	2016	Additive manufacturing of Ni-based super alloys: The outstanding issues	130	[91]
Ti-based alloys	Shipley *et al.*	2018	Optimization of process parameters to address fundamental challenges during selective laser melting of Ti-6Al-4V: A review	273	[92]
Biomaterial	Murphy and Atala	2014	3D bioprinting of tissues and organs	3847	[93]
Concrete	Buswell *et al.*	2018	3D printing using concrete extrusion: A roadmap for research	557	[94]
Fibre	Parandoush and Lin	2017	A review on additive manufacturing of polymer-fiber composites	581	[95]
	Kabir *et al.*	2020	A critical review on 3D printed continuous fiber-reinforced composites: History, mechanism, materials and properties	176	[4]
Multi-material	Bandyopadhyay and Heer	2018	Additive manufacturing of multi-material structures	349	[96]
ABS	Torrado Perez *et al.*	2014	Fracture surface analysis of 3D-printed tensile specimens of novel ABS-based materials	285	[97]
PLA	Ilyas *et al.*	2021	Polylactic acid (Pla) biocomposite: Processing, additive manufacturing and advanced applications	73	[98]
PEEK	Zanjanijam *et al.*	2020	Fused filament fabrication of peek: A review of process-structure-property relationships	54	[99]
Aluminium alloys	Aboulkhair *et al.*	2019	3D printing of aluminum alloys: Additive Manufacturing of aluminum alloys using selective laser melting	507	[100]
Copper	Tran *et al.*	2019	3D printing of highly pure copper	83	[101]
Food	Godoi *et al.*	2016	3d printing technologies applied for food design: Status and prospects	424	[102]
Smart Material	Mendes-Felipe *et al.*	2019	State-of-the-art and future challenges of UV curable polymer-based smart materials for printing technologies	128	[103]
Glass	Zhang *et al.*	2021	3D printing of glass by additive manufacturing techniques: a review	16	[104]
Wood	Lamm *et al.*	2020	Material extrusion additive manufacturing of wood and lignocellulosic filled composites	21	[74]

Statistics from Scopus database; access date: October 19, 2022

3.7. Review paper categories based on research area

In this section, AM review papers that focus on key/hottest areas (e.g., aerospace, tissue engineering) will be discussed. Nowadays, AM is widely used in different fields, including aerospace, tissue engineering, construction, drug delivery, topology optimization, etc. The most cited review papers focused on these areas are provided in this subsection, as shown in Table 5.

Table 4. Typical review papers in different materials

Category	Keywords	Article title	First author	Reference
Metal	Aerospace	A review on metal additive manufacturing for intricately shaped aerospace components	Madhavadas *et al.*	[105]
	Hybrid FDM	Additive manufacturing of metals and ceramics using hybrid fused filament fabrication	Ramkumar and Rijwani	[106]
	Defects	Multi-scale defects in powder-based additively manufactured metals and alloys	Fu *et al.*	[107]
	Symmetry	Symmetry and its application in metal additive manufacturing (MAM)	Uralde *et al.*	[108]
	Properties	Influence of powder characteristics on properties of parts manufactured by metal additive manufacturing	Muthuswamy	[109]
	Digital twin	A digital twin hierarchy for metal additive manufacturing	Phua *et al.*	[110]
	Modeling; simulation	Modeling and simulation of metal selective laser melting process: A critical review	Zhou *et al.*	[111]
	Hybrid AM	Metal hybrid additive manufacturing: state-of-the-art	Sefene *et al.*	[112]
	Functionally Graded Materials	Review of additive manufacturing techniques for large-scale metal functionally graded materials	Zhang *et al.*	[113]
	Electro polishing	Review-electro polishing of additive manufactured metal parts	Chaghazardi and Wüthrich	[114]
	Defects; anomalies	Defects and anomalies in powder bed fusion metal additive manufacturing	Mostafaei *et al.*	[115]
	Fatigue	Ultrasonic fatigue of laser beam powder bed fused metals: A state-of-the-art review	Avateffazeli and Haghshenas	[116]
	Machine learning; defect detection	Machine learning algorithms for defect detection in metal laser-based additive manufacturing: A review	Fu *et al.*	[117]
	Microstructure	Additive manufacturing of metals: Microstructure evolution and multistage control	Liu *et al.*	[118]
	Electrical Machines	Metal additive manufacturing for electrical machines: Technology review and latest advancements	Selema *et al.*	[119]
	Surface characteristics	Surface characteristics improvement methods for metal additively manufactured parts: A review	Hashmi *et al.*	[120]
	Load-Bearing Implants	Metal additive manufacturing for load-bearing implants	Bandyopadhyay and Heer	[121]
	Mirror	Design and fabrication technology of metal mirrors based on additive manufacturing: A review	Zhang *et al.*	[122]
	In situ monitoring	In-situ measurement and monitoring methods for metal powder bed fusion: An updated review	Grasso and Colosimo	[123]
	Fracture; fatigue	Fracture and fatigue in additively manufactured metals	Becker *et al.*	[124]
	AI; machine learning	Applications of artificial intelligence and machine learning in metal additive manufacturing	Ladani	[125]
	Digital twin	The case for digital twins in metal additive manufacturing	Gunasegaram *et al.*	[126]
	Surface finish; porosity; residual stresses; fatigue	Effects of post-processing on the surface finish, porosity, residual stresses, and fatigue performance of additive manufactured metals: A review	Ye *et al.*	[127]
	Biomedical	Biomedical applications of metal 3D printing	Velásquez-García and Kornbluth	[128]
	Renewable energy	3D printing of metal-based materials for renewable energy applications	Mooraj *et al.*	[129]
	Liquid metal	Current status of liquid metal printing	Ansell	[130]
	Machine learning	Perspectives of using machine learning in laser powder bed fusion for metal additive manufacturing	Sing *et al.*	[131]

(Contd...)

Table 4. *(Continued)*

Category	Keywords	Article title	First author	Reference
Ceramic	Dental	Additive manufacturing of ceramics for dental applications: A review	Galante *et al.*	[132]
	Bone tissue	3D printing of ceramic-based scaffolds for bone tissue engineering: An overview	Du *et al.*	[133]
	SiC ceramic	Progress and challenges toward additive manufacturing of SiC ceramic	He *et al.*	[134]
	Graphene	Direct ink writing technology (3d printing) of graphene-based ceramic nanocomposites: A review	Pinargote *et al.*	[135]
	Ceramic membrane	A comprehensive review of recent developments in 3D printing technique for ceramic membrane fabrication for water purification	Dommati *et al.*	[136]
	Cellular ceramic	Cellular ceramic architectures produced by hybrid additive manufacturing: A review on the evolution of their design	Pelanconi *et al.*	[137]
Polymer	Mechanical	Mechanical characterization of 3D-printed polymers	Dizon *et al.*	[138]
	Polymer-fiber	A review on additive manufacturing of polymer-fiber composites	Parandoush and Lin	[95]
	Nanocomposites	High performance polymer nanocomposites for additive manufacturing applications	De Leon *et al.*	[139]
		3D printing of polymer nanocomposites via stereolithography	Manapat *et al.*	[140]
	Natural fiber	Additive manufacturing of natural fiber reinforced polymer composites: Processing and prospects	Balla *et al.*	[141]
	Gradient scaffolds	3D printing for the design and fabrication of polymer-based gradient scaffolds	Bracaglia *et al.*	[142]
Stainless steel	Corrosion	Corrosion performance of additively manufactured stainless steel parts: A review	Ettefagh *et al.*	[143]
		The corrosion of stainless steel made by additive manufacturing: A review	Ko *et al.*	[144]
	Mechanical; thermal	Mechanical and thermal properties of stainless steel parts, manufactured by various technologies, in relation to their microstructure	Eshkabilov *et al.*	[145]
	Surface tension	Surface tension measurements of liquid pure iron and 304L stainless steel under different gas mixtures	Klapczynski *et al.*	[146]
	Mechanical; microstructure	Mechanical properties and microstructure of 316 stainless steel processed by pulsed micro-plasma additive manufacturing	Yuan *et al.*	[147]
	Pitting Corrosion	Pitting corrosion in 316L stainless steel fabricated by laser powder bed fusion additive manufacturing: A review and perspective	Voisin *et al.*	[148]
	Powder Reuse	The influence of powder reuse on the properties of laser powder bed-fused stainless steel 316L: A review	Douglas *et al.*	[149]
	Solidification	Solidification behaviour of austenitic stainless steels during welding and directed energy deposition	Hossein Nedjad *et al.*	[150]
Ni-based alloys	Fatigue	Overview: Additive manufacturing enabled accelerated design of Ni-based alloys for improved fatigue life	Shao *et al.*	[151]
	Microstructural constituent	Powder bed fusion additive manufacturing of Ni-based super alloys: A review of the main microstructural constituents and characterization techniques	Haines *et al.*	[152]
	Cracking resistance	Applications of alloy design to cracking resistance of additively manufactured Ni-based alloys	Markanday	[153]
	Residual stress; crack	Additive manufacturing of Ni-based super alloys: Residual stress, mechanisms of crack formation and strategies for crack inhibition	Guo *et al.*	[154]

(Contd...)

Table 4. *(Continued)*

Category	Keywords	Article title	First author	Reference
Ti-based alloys	Mechanical	Additive manufacturing and post-processing of Ti-6Al-4V for superior mechanical properties	Qian *et al.*	[155]
	Fatigue	A review of the as-built SLM Ti-6Al-4V mechanical properties towards achieving fatigue resistant designs	Agius *et al.*	[156]
	Biomedical	A review of powdered additive manufacturing techniques for Ti-6al-4v biomedical applications	Harun *et al.*	[157]
	Chemical polishing	Chemical polishing of scaffolds made of Ti-6Al-7Nb alloy by additive manufacturing	Lyczkowska *et al.*	[158]
	Mechanical	Mechanical properties of titanium-based Ti–6Al–4V alloys manufactured by powder bed additive manufacture	Tong *et al.*	[159]
	Process parameters	Selective laser manufacturing of Ti-based alloys and composites: impact of process parameters, application trends, and future prospects	Singh *et al.*	[82]
	Heat treatment	A review of heat treatments on improving the quality and residual stresses of the Ti–6Al–4V parts produced by additive manufacturing	Teixeira *et al.*	[83]
	Surface roughness	A review on the influence of process variables on the surface roughness of Ti-6Al-4V by electron beam powder bed fusion	de Campos Carolo and Ordoñez	[160]
Biomaterial	Bioink	Bioink properties before, during and after 3D bioprinting	Hölzl *et al.*	[161]
	Biomedical; tissue	3D bioprinting for biomedical devices and tissue engineering: A review of recent trends and advances	Derakhshanfar *et al.*	[162]
	Printability	Printability and Shape Fidelity of Bioinks in 3D Bioprinting	Schwab *et al.*	[163]
	Cell-Hydrogels	Design and printing strategies in 3D bioprinting of cell-hydrogels: A review	Lee *et al.*	[164]
	Skin	3D bioprinting of skin: A state-of-the-art review on modeling, materials, and processes	Vijayavenkataraman *et al.*	[165]
	Hydrogel	3D bioprinting of photo crosslinkable hydrogel constructs	Pereira *et al.*	[166]
	Cardiac tissue; cell	3D Bioprinting of cardiac tissue and cardiac stem cell therapy	Alonzo *et al.*	[167]
	Machine learning	A perspective on using machine learning in 3D bioprinting	Yu *et al.*	[168]
	Organ	The emergence of 3D bioprinting in organ-on-chip systems	Fetah *et al.*	[169]
	Liver transplantation	Bioprinting for liver transplantation	Kryou *et al.*	[170]
	Process parameters	Effects of processing parameters of 3D bioprinting on the cellular activity of bioinks	Adhikari *et al.*	[171]
Concrete	Simulation	Numerical simulations of concrete processing: From standard formative casting to additive manufacturing	Roussel *et al.*	[172]
	Extrusion-based	Extrusion-based additive manufacturing of concrete products: Revolutionizing and remodeling the construction industry	Valente *et al.*	[173]
	Biomimicry	Biomimicry for 3D concrete printing: A review and perspective	du Plessis *et al.*	[174]
	Functionally graded concrete	On-demand additive manufacturing of functionally graded concrete	Ahmed *et al.*	[175]
Fiber	Carbon fiber	Additively manufactured carbon fiber-reinforced composites: State of the art and perspective	van de Werken *et al.*	[176]
	Natural fiber	Recent advancements of plant-based natural fiber–reinforced composites and their applications	Li *et al.*	[177]
	Mechanical	The mechanical testing and performance analysis of polymer-fiber composites prepared through the additive manufacturing	Shanmugam *et al.*	[178]
	FDM	A review on fiber reinforced composite printing via FFF	Ferreira *et al.*	[179]
	Continuous fiber	Material extrusion additive manufacturing of continuous fiber reinforced polymer matrix composites: A review and outlook	Zhuo *et al.*	[5]

(Contd...)

Table 4. *(Continued)*

Category	Keywords	Article title	First author	Reference
	Process parameter	Influence of process parameters on the properties of additively manufactured fiber-reinforced polymer composite materials: A review	Ramesh *et al.*	[180]
Multi-material	Electronics	3D printing of multilayered and multimaterial electronics: A review	Goh *et al.*	[181]
	Powder bed fusion	Multimaterial powder bed fusion techniques	Mehrpouya *et al.*	[182]
	Direct ink writing	Direct ink writing advances in multi-material structures for a sustainable future	Rocha *et al.*	[183]
	Architecture; construction	Multi-material additive manufacturing in architecture and construction: A review	Pajonk *et al.*	[184]
	Polymer	Advances in polymers based multi-material additive-manufacturing techniques: State-of-art review on properties and applications	García-Collado *et al.*	[185]
	Functional material	A review of multi-material 3D printing of functional materials through vat photopolymerization	Shaukat *et al.*	[61]
ABS	Fracture surface	Fracture surface analysis of 3D-printed tensile specimens of novel ABS-based materials	Torrado Perez	[97]
	FDM	Review of acrylonitrile butadiene styrene in fused filament fabrication: A plastics engineering-focused perspective	Peterson	[186]
PLA	Biocomposite	Polylactic acid (Pla) biocomposite: Processing, additive manufacturing and advanced applications	Ilyas *et al.*	[98]
	Bone repair	Recent progress on 3D-printed polylactic acid and its applications in bone repair	Chen *et al.*	[187]
	4D printing	4D printing of shape memory polylactic acid (PLA)	Mehrpouya *et al.*	[188]
	Process Parameter; Mechanical	The influence of the process parameters on the mechanical properties of PLA specimens produced by fused filament fabrication—A review	Cojocaru *et al.*	[189]
PEEK	Process parameter	An overview on the influence of process parameters through the characteristic of 3D-printed PEEK and PEI parts	El Magri *et al.*	[190]
	FDM	Applications of 3D-printed peek via fused filament fabrication: A systematic review	Dua *et al.*	[191]
Aluminum alloys	Microstructure; mechanical	Microstructure and mechanical property considerations in additive manufacturing of aluminum alloys	Ding *et al.*	[192]
	Mechanical	Mechanical properties of SLM-printed aluminium alloys: A review	Ponnusamy *et al.*	[193]
	Heat treatment	Heat treatment of aluminium alloys produced by laser powder bed fusion: A review	Fiocchi *et al.*	[194]
	WAAM	Challenges associated with the wire arc additive manufacturing (WAAM) of aluminium alloys	Thapliyal	[195]
	Corrosion	Corrosion and corrosion protection of additively manufactured aluminium alloys—a critical review	Revilla *et al.*	[196]
Copper	Pure copper	A review on additive manufacturing of pure copper	Jiang *et al.*	[197]
Food	Functional	Toward the design of functional foods and biobased products by 3D printing: A review	Portanguen *et al.*	[198]
	Plant-based	3D food printing: Applications of plant-based materials in extrusion-based food printing	Wang *et al.*	[199]
	Food material	A review on 3D printable food materials: types and development trends	Li *et al.*	[200]
	4D printing	4D printing: a new approach for food printing; effect of various stimuli on 4D printed food properties. A comprehensive review	Navaf *et al.*	[201]

(Contd...)

Table 4. ***(Continued)***

Category	Keywords	Article title	First author	Reference
Smart materials	Manufacturing	Significant roles of 4D printing using smart materials in the field of manufacturing	Haleem *et al.*	[202]
	Wearable application	Potentials of additive manufacturing with smart materials for chemical biomarkers in wearable applications	Kwon *et al.*	[203]
Glass	Crystallization	Crystallization in additive manufacturing of metallic glasses: A review	Liu *et al.*	[204]
	Silica Glass	Overview of 3D-printed silica glass	Zhang *et al.*	[205]
Wood	Wood powders	A review on wood powders in 3D printing: processes, properties and potential applications	Das *et al.*	[206]

Statistics from Scopus database; access date: October 19, 2022

Table 5. Most cited review papers in key/hottest areas

Area	Article title	Citation	First author	References
Machine learning	Machine learning in additive manufacturing: State-of-the-art and perspectives	153	Wang *et al.*	[207]
Construction	3D printing using concrete extrusion: A roadmap for research	560	Buswell *et al.*	[94]
Biomedical	Bioink properties before, during and after 3D bioprinting	567	Hölzl *et al.*	[161]
Tissue engineering	3D bioprinting of tissues and organs	3872	Murphy and Atala	[93]
Topology optimization	Current and future trends in topology optimization for additive manufacturing	383	Liu *et al.*	[208]
Electrochemical	3D-printing technologies for electrochemical applications	554	Ambrosi and Pumera	[209]
Smart structures	Printing soft matter in three dimensions	838	Truby and Lewis	[210]
Food printing	3D printing technologies applied for food design: Status and prospects	428	Godoi *et al.*	[102]
Drug delivery	3D printing pharmaceuticals: Drug development to frontline care	243	Trenfield *et al.*	[211]
Aerospace	The present and future of additive manufacturing in the aerospace sector: A review of important aspects	279	Uriondo *et al.*	[212]

Statistics from Scopus database; access date: October 19, 2022

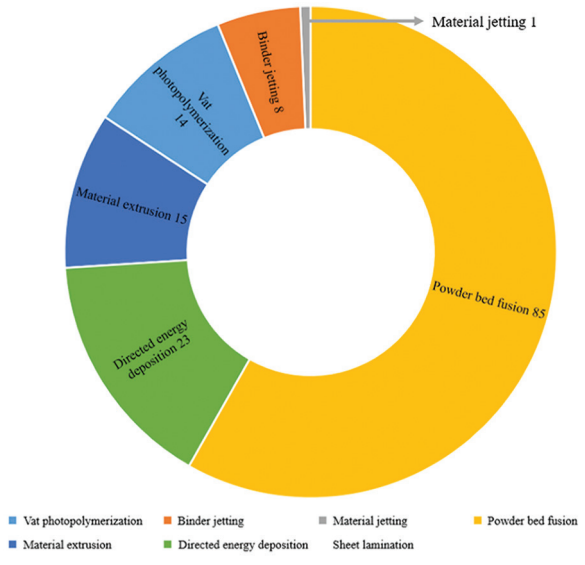

Figure 6. Number of review papers in different AM techniques (statistics from Scopus database; access date: October 19, 2022).

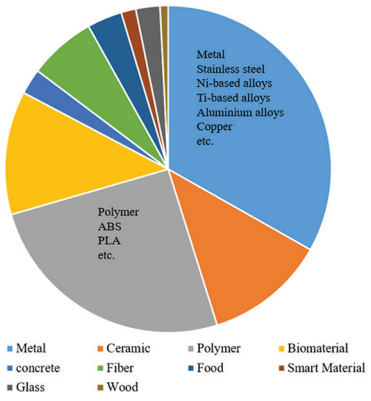

Figure 7. Review papers focusing on different materials (statistics from Scopus database; access date: October 19, 2022).

4. Conclusions

In this work, we conducted a survey on published review papers in AM. Analysis and discussion on reviews in

seven AM techniques are given (i.e., material extrusion, powder bed fusion, material jetting, binder jetting, directed energy deposition, vat photopolymerization, and sheet lamination). As can be seen, most of the review papers are in the categories of powder bed fusion and directed energy deposition. No review papers in sheet lamination were found. In the future, it is necessary to carry out a review on sheet lamination, although it is not a famous AM technique. In addition, typical review papers are categorized into different groups based on the materials these review papers focused on (e.g., metal, ceramic, polymer, biomaterial, concrete, fiber, food, smart material, glass, and wood). The specific objectives of each review paper are listed, as shown in Table 4. For example, He *et al.*[134] focuses on SiC ceramic in AM, and readers can refer accordingly based on their interests. The aim of this survey paper is to provide a guidance to the development of AM review papers, give a comprehensive analysis on the current available review papers in this field, and hopefully, provide some insights and inspire more ideas. As the review papers published in AM are increasing; nowadays, the selected review papers in this survey are based on the Scopus database, which might have some limitations. In addition, this survey only considers the most cited papers in each category based on the number of citations, while the published time of the review papers is not considered.

Acknowledgments

None.

Funding

The authors would like to acknowledge the fundings from the Provincial Natural Science Foundation of Anhui (2208085QA01) and the Fundamental Research Funds for the Central Universities (WK0010000075).

Conflict of interest

None.

Author contributions

Conceptualization: Jingchao Jiang
Data curation: Liuchao Jin
Formal analysis: Jingchao Jiang
Funding acquisition: Xiaoya Zhai
Investigation: Xiaoya Zhai
Methodology: Jingchao Jiang
Project administration: Xiaoya Zhai
Resources: Xiaoya Zhai
Writing – original draft: Xiaoya Zhai, Liuchao Jin
Writing – review & editing: Jingchao Jiang

References

1. Gibson I, Rosen DW, Stucker B, *et al*., 2021, Additive Manufacturing Technologies. 3rded. Berlin: Springer.

2. International Organization for Standardization/ASTM52900, 2021, Additive manufacturing-General principles-Terminology. West Conshohocken, PA: ASTM International.

3. Jiang J, Xu X, Stringer J, 2019, Optimization of process planning for reducing material waste in extrusion based additive manufacturing, robot. *Comput Integr Manuf*, 59: 317–325.

   https://doi.org/10.1016/j.rcim.2019.05.007

4. Kabir SM, Mathur K, Seyam AF, 2020, A critical review on 3D printed continuous fiber-reinforced composites: History, mechanism, materials and properties. *Compos Struct*, 232: 111476.

   https://doi.org/10.1016/J.COMPSTRUCT.2019.111476

5. Zhuo P, Li S, Ashcroft IA, *et al*., 2021, Material extrusion additive manufacturing of continuous fibre reinforced polymer matrix composites: A review and outlook, *Compos Part B Eng*, 224: 109143.

   https://doi.org/10.1016/J.COMPOSITESB.2021.109143

6. Goh GD, Neo SJ, Dikshit V, *et al*., 2021, Quasi-static indentation and sound-absorbing properties of 3D printed sandwich core panels. 24: 1206–1225.

   https://doi.org/10.1177/10996362211037015

7. Stratasys, 2017, United States: Stratasys. Avaialble from: https://www.investors.stratasys.com/news-events/press-releases/detail/418/inventor-of-fdm-3d-printing-and-co-founder-of-stratasys [Last accessed on 2018 Dec 09].

8. Jiang J, Xu X, Stringer J, 2019, Effect of Extrusion Temperature on Printable Threshold Overhang in Additive Manufacturing. In: 52nd CIRP Conference on Manufacturing Systems, Ljubljana.

9. Jiang J, Xu X, Stringer J, 2018, Support structures for additive manufacturing: A review. *J Manuf Mater Process*, 2: 64.

   https://doi.org/10.3390/jmmp2040064

10. Thompson SM, Bian L, Shamsaei N, *et al*., 2015, An overview of direct laser deposition for additive manufacturing; Part I: Transport phenomena, modeling and diagnostics. *Addit Manuf*, 8: 36–62.

    https://doi.org/10.1016/J.ADDMA.2015.07.001

11. Beaman JJ, Deckard CR, 1991, Selective Laser Sintering with Assisted Powder Handling. Available from: https://www.patents.google.com/patent/US4938816A/en [Last accessed on 2018 Dec 09].

12. Bertrand P, Bayle F, Combe C, *et al*., 2007, Ceramic components manufacturing by selective laser sintering. *Appl Surf Sci*, 254: 989–992.

https://doi.org/10.1016/j.apsusc.2007.08.085

13. Deckers J, Shahzad K, Vleugels J, *et al*., 2012, Isostatic pressing assisted indirect selective laser sintering of alumina components. *Rapid Prototyp J*, 18: 409–419.

https://doi.org/10.1108/13552541211250409

14. Mahmoud D, Elbestawi MA, 2019, Selective laser melting of porosity graded lattice structures for bone implants. *Int J Adv Manuf Technol*, 100: 2915–2927.

https://doi.org/10.1007/s00170-018-2886-9

15. Coeck S, Bisht M, Plas J, *et al*., 2019, Prediction of lack of fusion porosity in selective laser melting based on melt pool monitoring data. *Addit Manuf*, 25: 347–356.

https://doi.org/10.1016/J.ADDMA.2018.11.015

16. Kruth JP, Wang X, Laoui T, *et al*., 2003, Lasers and materials in selective laser sintering. *Assem Autom*, 23L 357–371.

https://doi.org/10.1108/01445150310698652

17. Siddiqui SF, Fasoro AA, Cole C, *et al*., 2019, Mechanical characterization and modeling of direct metal laser sintered stainless steel GP1. *J Eng Mater Technol*, 141: 031009.

https://doi.org/10.1115/1.4042867

18. Jiazhu W, Liu T, Chen H, *et al*., 2019, Simulation of laser attenuation and heat transport during direct metal deposition considering beam profile. *J Mater Process Technol*, 270: 92–105.

https://doi.org/10.1016/J.JMATPROTEC.2019.02.021

19. Nahmany M, Hadad Y, Aghion E, *et al.*, 2019, Microstructural assessment and mechanical properties of electron beam welding of AlSi10Mg specimens fabricated by selective laser melting. *J Mater Process Technol*, 270: 228–240.

https://doi.org/10.1016/J.JMATPROTEC.2019.02.025

20. Kruth JP, Mercelis P, Van Vaerenbergh J, *et al*., 2005, Binding mechanisms in selective laser sintering and selective laser melting. *Rapid Prototyp J*, 11: 26–36.

https://doi.org/10.1108/13552540510573365

21. Murr LE, Gaytan SM, Ramirez DA, *et al*., 2012, Metal fabrication by additive manufacturing using laser and electron beam melting technologies. *J Mater Sci Technol*, 28: 1–14.

https://doi.org/10.1016/S1005-0302(12)60016-4

22. Yang J, Ouyang H, Wang Y, 2010, Direct metal laser fabrication: Machine development and experimental work. *Int J Adv Manuf Technol*, 46: 1133–1143.

https://doi.org/10.1007/s00170-009-2174-9

23. Shellabear M, Nyrhilä O, 2004, DML-Development History and State of the Art. In: Proceeding 4th Laser Assisted Net Shape Engineering Conference. (LANE 2004). pp. 21–24.

https://doi.org/10.1016/j.molmed.2015.05.003

24. Calvert P, 2001, Inkjet printing for materials and devices. *Chem Mater*, 13: 3299–3305.

https://doi.org/10.1021/cm0101632

25. de Gans BJ, Duineveld PC, Schubert US, *et al*., 2004, Inkjet Printing of Polymers: State of the Art and Future Developments. Germany: WILEY-VCH Verlag.

https://doi.org/10.1002/adma.200300385

26. Blazdell PF, Evans JR, 2000, Application of a continuous ink jet printer to solid freeforming of ceramics. *J Mater Process Technol*, 99: 94–102.

https://doi.org/10.1016/S0924-0136(99)00392-1

27. Slade CE, Evans JR, 1998, Freeforming ceramics using a thermal jet printer. *J Mater Sci Lett*, 17: 1669–1671.

https://doi.org/10.1023/A:1006666718653

28. Elliott AM, Ivanova OS, Williams CB, 2013, Inkjet printing of quantum dots in photopolymer for use in additive manufacturing of nanocomposites. *Adv Eng Mater*, 15: 903–907.

https://doi.org/10.1002/adem.201300020

29. Ko SH, Chung J, Hotz N, *et al*., 2010, Metal nanoparticle direct inkjet printing for low-temperature 3D micro metal structure fabrication. *J Micromech Microeng*, 20: 125010.

https://doi.org/10.1088/0960-1317/20/12/125010

30. Polozov I, Sufiiarov V, Shamshurin A, 2019, Synthesis of titanium orthorhombic alloy using binder jetting additive manufacturing. *Mater Lett*, 243: 88–91.

https://doi.org/10.1016/J.MATLET.2019.02.027

31. Snelling D, Blount H, Forman C, *et al*., 2013, The effects of 3D pritned molds on metal castings. *2013 International Solid Freeform Fabrication Symposium,* 827–845.

32. Williams CB, Cochran JK, Rosen DW, 2011, Additive manufacturing of metallic cellular materials via three-dimensional printing. *Int J Adv Manuf Technol*, 53: 231–239.

https://doi.org/10.1007/s00170-010-2812-2

33. Lam CX, Mo XM, Teoh SH, *et al*., 2002, Scaffold development using 3D printing with a starch-based polymer. *Mater Sci Eng C*, 20: 49–56.

https://doi.org/10.1016/S0928-4931(02)00012-7

34. Yoo J, Cima MJ, Khanuja S, *et al*., 1993, Structural Ceramic Components by 3D Printing. In: International Solid Freeform Fabrication Symposium, University of Texas at Austin.

35. Eisenbarth D, Esteves PM, Wirth F, *et al*., 2019, Spatial powder flow measurement and efficiency prediction for laser direct metal deposition. *Surf Coatings Technol*, 362: 397–408.

https://doi.org/10.1016/J.SURFCOAT.2019.02.009

36. Sandia National Laboratories, 1997, Creating a Complex Metal Part in a Day is Goal of Commercial Consortium.

Available from: https://www.sandia.gov/media/lens.htm [Last accessed on 2018 Dec 09].

37. Griffith ML, Harwell LD, Romero J, *et al*., 1997, Multi-material Processing by LENS. In: Solid Freeform Fabrication Symposium Conference. Austin Texas. pp. 11–13.

https://doi.org/10.2966/scrip.040407.436

38. Griffith ML, Ensz MT, Puskar JD, *et al*., 2000, Understanding the Microstructure and Properties of Components Fabricated by Laser Engineered Net Shaping (LENS). In: MRS Proceeding. Cambridge: Cambridge University Pressp. pp9.

https://doi.org/10.1557/PROC-625-9

39. Taminger KM, Hafley RA, 2006, Electron Beam Freeform Fabrication for Cost Effective Near-Net Shape Manufacturing. In: NATO/RTO AVT-139 Spec. Meet Cost Effective Manufacturing. via Net Shape Process. Amsterdam. Available from: https://www.ntrs.nasa.gov/search.jsp?R=20080013538 [Last accessed on 2018 Dec 09].

40. Weng F, Gao S, Jiang J, *et al*., 2019, A novel strategy to fabricate thin 316L stainless steel rods by continuous direct metal deposition in Z direction. *Addit Manuf*, 27: 474–481.

https://doi.org/10.1016/j.addma.2019.03.024

41. Jiang J, Weng F, Gao S, *et al*., 2019, A support interface method for easy part removal in direct metal deposition. *Manuf Lett*, 20: 30–33.

https://doi.org/10.1016/j.mfglet.2019.04.002

42. Aduba DC, Margaretta ED, Marnot AE, *et al*., 2019, Vat photopolymerization 3D printing of acid-cleavable PEG-methacrylate networks for biomaterial applications. *Mater Today Commun*, 19: 204–211.

https://doi.org/10.1016/J.MTCOMM.2019.01.003

43. Cooper KG, 2001, Rapid prototyping technology: Selection and application. *Assem Autom*, 21: 358–359.

https://doi.org/10.1108/aa.2001.21.4.358.1

44. Pham DT, Ji C, 2000, Design for stereolithography. *Proc Inst Mech Eng Part C J Mech Eng Sci*, 214: 635–640.

https://doi.org/10.1243/0954406001523650

45. Himmer T, Nakagawa T, Anzai M, 1999, Lamination of metal sheets. *Comput Ind*, 39: 27–33.

https://doi.org/10.1016/S0166-3615(98)00122-5

46. Nohut S, Schwentenwein M, 2022, Vat photopolymerization additive manufacturing of functionally graded materials: A review. *J Manuf Mater Process*, 6: 17.

https://doi.org/10.3390/JMMP6010017

47. Xu X, Awad A, Robles-Martinez P, *et al*., 2021, Vat photopolymerization 3D printing for advanced drug delivery and medical device applications. *J Control Release*, 329: 743–757.

https://doi.org/10.1016/J.JCONREL.2020.10.008

48. Luo Z, Zhao Y, 2018, A survey of finite element analysis of temperature and thermal stress fields in powder bed fusion additive manufacturing. *Addit Manuf*, 21: 318–332.

https://doi.org/10.1016/J.ADDMA.2018.03.022

49. McCann R, Obeidi MA, Hughes C, *et al*., 2021, *In-situ* sensing, process monitoring and machine control in laser powder bed fusion: A review. *Addit Manuf*, 45: 102058.

https://doi.org/10.1016/J.ADDMA.2021.102058

50. Wickramasinghe S, Do T, Tran P, 2020, FDM-Based 3D printing of polymer and associated composite: A review on mechanical properties, defects and treatments. *Polymers*, 12: 1529.

https://doi.org/10.3390/POLYM12071529

51. Dey A, Yodo N, 2019, A systematic survey of FDM process parameter optimization and their influence on part characteristics. *J Manuf Mater Process*, 3: 64.

https://doi.org/10.3390/JMMP3030064

52. Ziaee M, Crane NB, 2019, Binder jetting: A review of process, materials, and methods. *Addit Manuf*, 28: 781–801.

https://doi.org/10.1016/J.ADDMA.2019.05.031

53. Pagac M, Hajnys J, Ma QP, *et al*., A review of vat photopolymerization technology: Materials, applications, challenges, and future trends of 3D printing. *Polymers*,13: 598.

https://doi.org/10.3390/POLYM13040598.

54. Gülcan O, Günaydın K, Tamer A, 2021, The state of the art of material jetting-a critical review. *Polymers*(*Basel*), 13: 2829.

https://doi.org/10.3390/POLYM13162829

55. Grasso M, Colosimo BM, 2017, Process defects and in situ monitoring methods in metal powder bed fusion: A review. *Meas Sci Technol*, 28: 044005.

https://doi.org/10.1088/1361-6501/AA5C4F

56. Dass A, Moridi A, 2019, State of the art in directed energy deposition: From additive manufacturing to materials design. *Coatings*, 9,: 418.

https://doi.org/10.3390/COATINGS9070418

57. Ahn DG, 2021, Directed energy deposition (DED) process: State of the art. *Int J Precis Eng Manuf Technol*, 8: 703–742.

https://doi.org/10.1007/S40684-020-00302-7

58. Chartrain NA, Williams CB, Whittington AR, 2018, A review on fabricating tissue scaffolds using vat photopolymerization. *Acta Biomater*, 74: 90–111.

https://doi.org/10.1016/J.ACTBIO.2018.05.010

59. Andreu A, Su PC, Kim JH, *et al*., 2021, 4D printing materials for vat photopolymerization. *Addit Manuf*, 44: 102024.

https://doi.org/10.1016/J.ADDMA.2021.102024

60. Maurel A, Martinez AC, Grugeon S, *et al*., 2021, Toward

high resolution 3D Printing of shape-conformable batteries via vat photopolymerization: Review and perspective. *IEEE Access*, 9: 140654–140666.

https://doi.org/10.1109/ACCESS.2021.3119533

61. Shaukat U, Rossegger E, Schlögl S, 2022, A review of multi-material 3D Printing of functional materials via vat photopolymerization. *Polymers*, 14: 2449.

https://doi.org/10.3390/POLYM14122449

62. Bartlett JL, Li X, 2019, An overview of residual stresses in metal powder bed fusion. *Addit Manuf*, 27 (2019) 131–149.

https://doi.org/10.1016/J.ADDMA.2019.02.020

63. Chatham CA, Long TE, Williams CB, A review of the process physics and material screening methods for polymer powder bed fusion additive manufacturing. *Prog Polym Sci*, 93: 68–95.

https://doi.org/10.1016/J.PROGPOLYMSCI.2019.03.003

64. Aversa A, Marchese G, Saboori A, *et al*., 2019, New Aluminum alloys specifically designed for laser powder bed fusion: A review. *Materials* (*Basel*), 12: 1007.

https://doi.org/10.3390/MA12071007

65. Dowling L, Kennedy J, O'Shaughnessy S, *et al*., 2020, A review of critical repeatability and reproducibility issues in powder bed fusion. *Mater Des*, 186: 108346.

https://doi.org/10.1016/J.MATDES.2019.108346

66. Snow Z, Nassar AR, Reutzel EW, 2020, Invited review article: Review of the formation and impact of flaws in powder bed fusion additive manufacturing. *Addit Manuf*, 36: 101457.

https://doi.org/10.1016/J.ADDMA.2020.101457

67. Awad A, Fina F, Goyanes A, *et al*., 2021, Advances in powder bed fusion 3D printing in drug delivery and healthcare. *Adv Drug Deliv Rev*, 174: 406–424.

https://doi.org/10.1016/J.ADDR.2021.04.025

68. Mirzababaei S, Pasebani S, 2019, A review on binder jet additive manufacturing of 316L stainless steel. *J Manuf Mater Process*, 3: 82.

https://doi.org/10.3390/JMMP3030082

69. Goh GD, Yap YL, Tan HK, *et al*., 2019, Process-structure-properties in polymer additive manufacturing via material extrusion: A review. *Crit Rev Solid State Mater Sci*, 45: 113–133.

https://doi.org/10.1080/10408436.2018.1549977

70. Spoerk M, Holzer C, Gonzalez-Gutierrez J, 2020, Material extrusion-based additive manufacturing of polypropylene: A review on how to improve dimensional inaccuracy and warpage. *J Appl Polym Sci*, 137: 48545.

https://doi.org/10.1002/APP.48545

71. Brenken B, Barocio E, Favaloro A, *et al*., 2018, Fused filament fabrication of fiber-reinforced polymers: A review. *Addit Manuf*, 21: 1–16.

https://doi.org/10.1016/J.ADDMA.2018.01.002

72. Chaunier L, Guessasma S, Belhabib S, *et al*., 2018, Material extrusion of plant biopolymers: Opportunities and challenges for 3D printing. *Addit Manuf*, 21: 220–233.

https://doi.org/10.1016/J.ADDMA.2018.03.016

73. Huang J, Chen Q, Jiang H, *et al*., 2020, A survey of design methods for material extrusion polymer 3D printing. *Virtual Phys Prototyp*, 15: 148–162.

https://doi.org/10.1080/17452759.2019.1708027

74. Lamm ME, Wang L, Kishore V, *et al*., 2020, Material extrusion additive manufacturing of wood and lignocellulosic filled composites. *Polymers* (*Basel*), 12: 2115.

https://doi.org/10.3390/POLYM12092115

75. Oleff A, Küster B, Stonis M, *et al*., 2021, Process monitoring for material extrusion additive manufacturing: A state-of-the-art review. *Prog Addit Manuf*, 64: 705–730.

https://doi.org/10.1007/S40964-021-00192-4

76. Rowat SJ, Legge RL, Moresoli C, 2021, Plant protein in material extrusion 3D printing: Formation, plasticization, prospects, and challenges. *J Food Eng*, 308: 110623.

https://doi.org/10.1016/J.JFOODENG.2021.110623

77. Saboori A, Aversa A, Marchese G, *et al*., 2019, Application of directed energy deposition-based additive manufacturing in repair. *Appl Sci*, 9: 3316.

https://doi.org/10.3390/APP9163316

78. Tang ZJ, Liu WW, Wang YW, *et al*., 2020, A review on in situ monitoring technology for directed energy deposition of metals. *Int J Adv Manuf Technol*, 108: 3437–3463.

https://doi.org/10.1007/S00170-020-05569-3

79. Xu J, Gu X, Ding D, *et al*., 2018, A review of slicing methods for directed energy deposition based additive manufacturing. *Rapid Prototyp J*, 24: 1012–1025.

https://doi.org/10.1108/RPJ-10-2017-0196/FULL/PDF

80. Wang H, Liu W, Tang Z, *et al*., 2020, Review on adaptive control of laser-directed energy deposition. *Optic Eng*, 59: 070901.

https://doi.org/10.1117/1.OE.59.7.070901

81. Kim KH, Jung CH, Jeong DY, *et al*., 2021, Preventing evaporation products for high-quality metal film in directed energy deposition: A review. *Metals*, 11: 353.

https://doi.org/10.3390/MET11020353

82. Singh N, Hameed P, Ummethala R, *et al*., 2020, Selective laser manufacturing of Ti-based alloys and composites: Impact of process parameters, application trends, and future prospects. *Mater Today Adv*, 8: 100097.

https://doi.org/10.1016/J.MTADV.2020.100097

83. Teixeira O, Silva FJ, Ferreira LP, *et al*., A review of heat

treatments on improving the quality and residual stresses of the Ti-6Al-4V parts produced by additive manufacturing. *Metals*, 10: 1006.

https://doi.org/10.3390/MET10081006

84. Frazier WE, 2014, Metal additive manufacturing: A review. *J Mater Eng Perform*, 23: 1917–1928.

https://doi.org/10.1007/S11665-014-0958-Z/FIGURES/9

85. Sames WJ, List FA, Pannala S, *et al*., The metallurgy and processing science of metal additive manufacturing. 61 (2016) 315–360.

https://doi.org/10.1080/09506608.2015.1116649

86. Deckers J, Vleugels J, Kruth JP, 2014, Additive manufacturing of ceramics: A review. *J Ceram Sci Technol*, 5: 245–260.

https://doi.org/10.4416/JCST2014-00032

87. Sing SL, Yeong WY, Wiria FE, *et al*., 2017, Direct selective laser sintering and melting of ceramics: A review. *Rapid Prototyp J*, 23: 611–623.

https://doi.org/10.1108/RPJ-11-2015-0178/FULL/PDF

88. Ligon SC, Liska R, Stampfl J, *et al*., 2017, Polymers for 3D printing and customized additive manufacturing. *Chem Rev*, 117: 10212–10290.

https://doi.org/10.1021/ACS.CHEMREV.7B00074/ASSET/IMAGES/LARGE/CR-2017-00074G_0037.JPEG

89. Kong D, Dong C, Wei S, *et al*., 2021, About metastable cellular structure in additively manufactured austenitic stainless steels. *Addit Manuf*, 38: 101804.

https://doi.org/10.1016/J.ADDMA.2020.101804

90. Jin W, Zhang C, Jin S, *et al*., 2020, Wire arc additive manufacturing of stainless steels: A review. *Appl Sci*, 10: 1563.

https://doi.org/10.3390/APP10051563

91. Attallah MM, Jennings R, Wang X, *et al*., 2016, Additive manufacturing of Ni-based superalloys: The outstanding issues. *MRS Bull*, 41: 758–764.

https://doi.org/10.1557/MRS.2016.211

92. Shipley H, McDonnell D, Culleton M, *et al*., 2018, Optimisation of process parameters to address fundamental challenges during selective laser melting of Ti-6Al-4V: A review. *Int J Mach Tools Manuf*, 128: 1–20.

https://doi.org/10.1016/J.IJMACHTOOLS.2018.01.003

93. Murphy SV, Atala A, 2014, 3D bioprinting of tissues and organs. *Nat Biotechnol*, 32: 773–785.

https://doi.org/10.1038/nbt.2958

94. Buswell RA, de Silva WR, Jones SZ, *et al*., 2018, 3D printing using concrete extrusion: A roadmap for research. *Cem Concr Res*, 112: 37–49.

https://doi.org/10.1016/J.CEMCONRES.2018.05.006

95. Parandoush P, Lin D, 2017, A review on additive manufacturing of polymer-fiber composites. *Compos Struct*, 182: 36–53.

https://doi.org/10.1016/J.COMPSTRUCT.2017.08.088

96. Bandyopadhyay A, Heer B, Additive manufacturing of multi-material structures. *Mater Sci Eng R Reports*, 129: 1–16.

https://doi.org/10.1016/J.MSER.2018.04.001

97. Perez AR, Roberson DA, Wicker RB, 2014, Fracture surface analysis of 3D-printed tensile specimens of novel ABS-based materials. *J Fail Anal Prev*, 14: 343–353.

https://doi.org/10.1007/S11668-014-9803-9/FIGURES/14

98. Ilyas RA, Sapuan SM, Harussani MM, *et al*., 2021, Polylactic acid (PLA) biocomposite: Processing, additive manufacturing and advanced applications. *Polymers*, 13: 1326.

https://doi.org/10.3390/POLYM13081326

99. Zanjanijam AR, Major I, Lyons JG, *et al*., Fused filament fabrication of PEEK: A review of process-structure-property relationships. *Polymers*, 12: 1665.

https://doi.org/10.3390/POLYM12081665

100. Aboulkhair NT, Simonelli M, Parry L, *et al*., 2019, 3D printing of aluminium alloys: Additive manufacturing of aluminium alloys using selective laser melting. *Prog Mater Sci*, 106: 100578.

https://doi.org/10.1016/J.PMATSCI.2019.100578

101. Tran TQ, Chinnappan A, Lee JK, *et al*., 2019, 3D printing of highly pure copper. *Metals*, 9: 756.

https://doi.org/10.3390/MET9070756

102. Godoi FC, Prakash S, Bhandari BR, 3D printing technologies applied for food design: Status and prospects. *J Food Eng*, 179: 44–54.

https://doi.org/10.1016/j.jfoodeng.2016.01.025

103. Mendes-Felipe C, Oliveira J, Etxebarria I, *et al*., 2019, State-of-the-art and future challenges of UV curable polymer-based smart materials for printing technologies. *Adv Mater Technol*, 4: 1800618.

https://doi.org/10.1002/ADMT.201800618

104. Zhang D, Liu X, Qiu J, 2020, 3D printing of glass by additive manufacturing techniques: A review. *Front Optoelectron*, 14: 263–277.

https://doi.org/10.1007/S12200-020-1009-Z

105. Madhavadas V, Srivastava D, Chadha U, *et al*., 2022, A review on metal additive manufacturing for intricately shaped aerospace components. *CIRP J Manuf Sci Technol*, 39: 18–36.

https://doi.org/10.1016/J.CIRPJ.2022.07.005

106. Ramkumar P, Rijwani T, 2022, Additive manufacturing of metals and ceramics using hybrid fused filament fabrication. *J Braz Soc Mech Sci Eng*, 44: 1–17.

https://doi.org/10.1007/S40430-022-03762-X/TABLES/1

107. Fu J, Li H, Song X, *et al*., 2022, Multi-scale defects in powder-based additively manufactured metals and alloys. *J Mater Sci Technol*, 122: 165–199.

https://doi.org/10.1016/J.JMST.2022.02.015

108. Uralde V, Veiga F, Aldalur E, *et al*., 2022, Symmetry and its application in metal additive manufacturing (MAM). *Symmetry*, 14: 1810.

https://doi.org/10.3390/SYM14091810

109. Muthuswamy P, 2022, Influence of powder characteristics on properties of parts manufactured by metal additive manufacturing. *Lasers Manuf Mater Process*, 9: 312–337.

https://doi.org/10.1007/S40516-022-00177-3/FIGURES/12

110. Phua A, Davies CH, Delaney GW, 2022, A digital twin hierarchy for metal additive manufacturing. *Comput Ind*, 140: 103667.

https://doi.org/10.1016/J.COMPIND.2022.103667

111. Zhou R, Liu H, Wang H, 2022, Modeling and simulation of metal selective laser melting process: A critical review. *Int J Adv Manuf Technol*, 121: 5693–5706.

https://doi.org/10.1007/S00170-022-09721-Z/FIGURES/10.

112. Sefene EM, Hailu YM, Tsegaw AA, 2022, Metal hybrid additive manufacturing: State-of-the-art. *Prog Addit Manuf*, 7; 737–749.

https://doi.org/10.1007/S40964-022-00262-1/TABLES/1

113. Zhang R, Jiang F, Xue L, Yu J, 2022, Review of additive manufacturing techniques for large-scale metal functionally graded materials. *Crystals*, 12: 858.

https://doi.org/10.3390/CRYST12060858

114. Chaghazardi Z, Wüthrich R, 2022, Review-electropolishing of additive manufactured metal parts. *J Electrochem Soc*, 169: 043510.

https://doi.org/10.1149/1945-7111/AC6450

115. Mostafaei A, Zhao C, He Y, *et al*., 2022, Defects and anomalies in powder bed fusion metal additive manufacturing. *Curr Opin Solid State Mater Sci*, 26: 100974.

https://doi.org/10.1016/J.COSSMS.2021.100974

116. Avateffazeli M, Haghshenas M, 2022, Ultrasonic fatigue of laser beam powder bed fused metals: A state-of-the-art review. *Eng Fail Anal*, 134: 106015.

https://doi.org/10.1016/J.ENGFAILANAL.2021.106015

117. Fu Y, Downey AR, Yuan L, *et al*., 2022, Machine learning algorithms for defect detection in metal laser-based additive manufacturing: A review. *J Manuf Process*, 75: 693–710.

https://doi.org/10.1016/J.JMAPRO.2021.12.061

118. Liu Z, Zhao D, Wang P, *et al*., 2022, Additive manufacturing of metals: Microstructure evolution and multistage control. *J Mater Sci Technol*, 100: 224–236.

https://doi.org/10.1016/J.JMST.2021.06.011

119. Selema A, Ibrahim MN, Sergeant P, 2022, Metal additive manufacturing for electrical machines: Technology review and latest advancements. *Energies*, 15: 1076.

https://doi.org/10.3390/EN15031076

120. Hashmi AW, Mali HS, Meena A, *et al*., 2022, Surface characteristics improvement methods for metal additively manufactured parts: A review. *Adv Mater Process Technol*.

https://doi.org/10.1080/2374068X.2022.2077535

121. Bandyopadhyay A, Ciliveri S, Bose S, 2022, Metal additive manufacturing for load-bearing implants. *J Indian Inst Sci*, 1021: 561–584.

https://doi.org/10.1007/S41745-021-00281-X

122. Zhang K, Qu H, Guan H, *et al*., 2021, Design and fabrication technology of metal mirrors based on additive manufacturing: A review. *Appl Sci*, 11: 10630.

https://doi.org/10.3390/APP112210630

123. Grasso M, Remani A, Dickins A, *et al*., 2021, *In-situ* measurement and monitoring methods for metal powder bed fusion: An updated review. *Meas Sci Technol*, 32: 112001.

https://doi.org/10.1088/1361-6501/AC0B6B

124. Becker TH, Kumar P, Ramamurty U, 2021, Fracture and fatigue in additively manufactured metals. *Acta Mater*, 219: 117240.

https://doi.org/10.1016/J.ACTAMAT.2021.117240

125. Ladani LJ, 2021, Applications of artificial intelligence and machine learning in metal additive manufacturing. *J Phys Mater*, 4: 042009.

https://doi.org/10.1088/2515-7639/AC2791

126. Gunasegaram DR, Murphy AB, Matthews MJ, *et al*., 2021, The case for digital twins in metal additive manufacturing. *J Phys Mater*, 4: 040401.

https://doi.org/10.1088/2515-7639/AC09FB

127. Ye C, Zhang C, Zhao J, *et al*., 2021, Effects of post-processing on the surface finish, porosity, residual stresses, and fatigue performance of additive Manufactured metals: A review. *J Mater Eng Perform*, 30: 6407–6425.

https://doi.org/10.1007/S11665-021-06021-7

128. Velásquez-García LF, Kornbluth Y, 2021, Biomedical applications of metal 3D printing. *Annu Rev Biomed Eng*, 23: 307–338.

https://doi.org/10.1146/ANNUREV-BIOENG-082020-032402

129. Mooraj S, Qi Z, Zhu C, *et al*., 2020, 3D printing of metal-based materials for renewable energy applications. *Nano Res*, 14: 2105–2132.

https://doi.org/10.1007/S12274-020-3230-X

130. Ansell TY, 2021, Current status of liquid metal printing.

J Manuf Mater Process, 5: 31.

https://doi.org/10.3390/JMMP5020031

131. Sing SL, Kuo CN, Shih CT, *et al*., 2021, Perspectives of using machine learning in laser powder bed fusion for metal additive manufacturing. *Virtual Phys Prototyp*, 16: 372–386.

https://doi.org/10.1080/17452759.2021.1944229

132. Galante R, Figueiredo-Pina CG, Serro AP, 2019, Additive manufacturing of ceramics for dental applications: A review. *Dent Mater*, 35: 825–846.

https://doi.org/10.1016/J.DENTAL.2019.02.026

133. Du X, Fu S, Zhu Y, 2018, 3D printing of ceramic-based scaffolds for bone tissue engineering: An overview. *J Mater Chem B*, 6: 4397–4412.

https://doi.org/10.1039/C8TB00677F

134. He R, Zhou N, Zhang K, *et al*., 2021, Progress and challenges towards additive manufacturing of SiC ceramic. *J Adv Ceram*, 10: 637–674.

https://doi.org/10.1007/S40145-021-0484-Z

135. Pinargote NW, Smirnov A, Peretyagin N, *et al*., 2020, Direct ink writing technology (3D printing) of graphene-based ceramic nanocomposites: A review. Nanomater, 10: 1300.

https://doi.org/10.3390/NANO10071300

136. Dommati H, Ray SS, Wang JJ, *et al*., 2019, A comprehensive review of recent developments in 3D printing technique for ceramic membrane fabrication for water purification. *RSC Adv*, 9: 16869–16883.

https://doi.org/10.1039/C9RA00872A

137. Pelanconi M, Rezaei E, Ortona A, 2020, Cellular ceramic architectures produced by hybrid additive manufacturing: A review on the evolution of their design. *J Ceram Soc Japan*, 128: 595–604.

https://doi.org/10.2109/JCERSJ2.20071

138. Dizon JR, Espera JH, Chen Q, *et al*., 2018, Mechanical characterization of 3D-printed polymers. *Addit Manuf*, 20: 44–67.

https://doi.org/10.1016/J.ADDMA.2017.12.002

139. De Leon AC, Chen Q, Palaganas NB, *et al*., High performance polymer nanocomposites for additive manufacturing applications. *React Funct Polym*, 103: 141–155.

https://doi.org/10.1016/J.REACTFUNCTPOLYM.2016.04.010

140. Manapat JZ, Chen Q, Ye P, *et al*., 2017, 3D Printing of polymer nanocomposites via stereolithography. *Macromol Mater Eng*, 302: 1600553.

https://doi.org/10.1002/MAME.201600553

141. Balla VK, Kate KH, Satyavolu J, *et al*., 2019, Additive manufacturing of natural fiber reinforced polymer composites: Processing and prospects. *Compos Part B Eng*, 174: 106956.

https://doi.org/10.1016/J.COMPOSITESB.2019.106956

142. Bracaglia LG, Smith BT, Watson E, *et al*., 3D printing for the design and fabrication of polymer-based gradient scaffolds. *Acta Biomater*, 56: 3–13.

https://doi.org/10.1016/J.ACTBIO.2017.03.030

143. Ettefagh AH, Guo S, Raush J, 2021, Corrosion performance of additively manufactured stainless steel parts: A review. *Addit Manuf*, 37: 101689.

https://doi.org/10.1016/J.ADDMA.2020.101689

144. Ko G, Kim W, Kwon K, *et al*., 2021, The corrosion of stainless steel made by additive manufacturing: A review. *Metals*, 11: 516.

https://doi.org/10.3390/MET11030516

145. Eshkabilov S, Ara I, Sevostianov I, *et al*., 2021, Mechanical and thermal properties of stainless steel parts, manufactured by various technologies, in relation to their microstructure. *Int J Eng Sci*, 159: 103398.

https://doi.org/10.1016/J.IJENGSCI.2020.103398

146. Klapczynski V, Le Maux D, Courtois M, *et al*., 2022, Surface tension measurements of liquid pure iron and 304L stainless steel under different gas mixtures. *J Mol Liq*, 350: 118558.

https://doi.org/10.1016/J.MOLLIQ.2022.118558

147. Yuan X, Guo X, Qiu H, *et al*., 2022, Mechanical properties and microstructure of 316 stainless steel processed by pulsed micro-plasma additive manufacturing. *J Therm Spray Technol*, 31: 623–635.

https://doi.org/10.1007/S11666-022-01335-X/FIGURES/10

148. Voisin T, Shi R, Zhu Y, *et al*., 2022, Pitting corrosion in 316L stainless steel fabricated by laser powder bed fusion additive manufacturing: A review and perspective. *JOM*, 74: 1668–1689.

https://doi.org/10.1007/S11837-022-05206-2/FIGURES/10

149. Douglas R, Lancaster R, Jones T, *et al*., 2022, The influence of powder reuse on the properties of laser powder bed-fused stainless steel 316L: A review. *Adv Eng Mater*, 24: 2200596.

https://doi.org/10.1002/ADEM.202200596

150. Nedjad HS, Yildiz M, Saboori A, 2022, Solidification behaviour of austenitic stainless steels during welding and directed energy deposition. *Sci Technol Welding Join*, 27: 8.

https://doi.org/10.1080/13621718.2022.2115664

151. Shao S, Khonsari MM, Guo S, *et al*., 2019, Overview: Additive manufacturing enabled accelerated design of ni-based alloys for improved fatigue life. *Addit Manuf*, 29: 100779.

https://doi.org/10.1016/J.ADDMA.2019.100779

152. Haines MP, Rielli VV, Primig S, *et al*., 2022, Powder bed fusion additive manufacturing of Ni-based superalloys:

A review of the main microstructural constituents and characterization techniques. *J Mater Sci*, 57: 14135–14187.

https://doi.org/10.1007/S10853-022-07501-4

153. Markanday JFS, 2022, Applications of alloy design to cracking resistance of additively manufactured Ni-based alloys. *Mater Sci Tech*, 38: 1300–1314.

https://doi.org/10.1080/02670836.2022.2068759

154. Guo C, Li G, Li S, *et al*., 2022, Additive Manufacturing of Ni-based superalloys: In: Residual stress, Mechanisms of Crack Formation and Strategies for Crack Inhibition, Nano Material Science. In Press.

https://doi.org/10.1016/J.NANOMS.2022.08.001

155. Qian M, Xu W, Brandt M,*et al*., Additive manufacturing and postprocessing of Ti-6Al-4V for superior mechanical properties. *MRS Bull*, 41: 775–784.

https://doi.org/10.1557/MRS.2016.215

156. Agius D, Kourousis KI, Wallbrink C, 2018, A review of the As-built SLM Ti-6Al-4V mechanical properties towards achieving fatigue resistant designs. *Metals*, 8: 75.

https://doi.org/10.3390/MET8010075

157. Harun WS, Manam NS, Kamariah MS, *et al*., 2018, A review of powdered additive manufacturing techniques for Ti-6al-4v biomedical applications. *Powder Technol*, 331: 74–97.

https://doi.org/10.1016/J.POWTEC.2018.03.010

158. Lyczkowska E, Szymczyk P, Dybała B, *et al*., 2014, Chemical polishing of scaffolds made of Ti-6Al-7Nb alloy by additive manufacturing. *Arch Civ Mech Eng*, 14: 586–594.

https://doi.org/10.1016/J.ACME.2014.03.001

159. Tong J, Bowen CR, Persson J, 2016, Plummer, mechanical properties of titanium-based Ti–6Al–4V alloys manufactured by powder bed additive manufacture. *Mater Sci Tech*, 33: 138–148.

https://doi.org/10.1080/02670836.2016.1172787

160. Carolo L, Ordoñez RE, 2022, A review on the influence of process variables on the surface roughness of Ti-6Al-4V by electron beam powder bed fusion. *Addit Manuf*, 59: 103103.

https://doi.org/10.1016/J.ADDMA.2022.103103

161. Hölzl K, Lin S, Tytgat L, *et al*., 2016, Bioink properties before, during and after 3D bioprinting. *Biofabrication*, 8: 032002.

https://doi.org/10.1088/1758-5090/8/3/032002

162. Derakhshanfar S, Mbeleck R, Xu K, *et al*., 2018, 3D bioprinting for biomedical devices and tissue engineering: A review of recent trends and advances. *Bioact Mater*, 3: 144–156.

https://doi.org/10.1016/j.bioactmat.2017.11.008

163. Schwab A, Levato A, D'Este M, *et al*., 2020, Printability and shape fidelity of bioinks in 3D bioprinting. *Chem Rev*, 120: 11028–11055.

https://doi.org/10.1021/ACS.CHEMREV.0C00084/ASSET/IMAGES/LARGE/CR0C00084_0009.JPEG

164. Lee JM, Yeong WY, Lee JM, *et al*., 2016, Design and printing strategies in 3D bioprinting of cell-hydrogels: A review. *Adv Healthc Mater*, 5: 2856–2865.

https://doi.org/10.1002/ADHM.201600435

165. Vijayavenkataraman S, Lu WF, Fuh JY, 2016, 3D bioprinting of skin: A state-of-the-art review on modelling, materials, and processes. *Biofabrication*, 8: 032001.

https://doi.org/10.1088/1758-5090/8/3/032001

166. Pereira RF, Bártolo PJ, 2015, 3D bioprinting of photocrosslinkable hydrogel constructs. *J Appl Polym Sci*, 132: 42458.

https://doi.org/10.1002/APP.42458

167. Alonzo M, AnilKumar S, Roman B, *et al*., 2019, 3D Bioprinting of cardiac tissue and cardiac stem cell therapy. *Transl Res*, 211: 64–83.

https://doi.org/10.1016/J.TRSL.2019.04.004

168. Yu C, Jiang J, 2020, A Perspective on using machine learning in 3D bioprinting. *Int J Bioprinting*, 6: 4–11.

https://doi.org/10.18063/ijb.v6i1.253

169. Fetah K, Tebon P, Goudie MJ, *et al*., 2019, The emergence of 3D bioprinting in organ-on-chip systems. *Prog Biomed Eng*, 1: 012001.

https://doi.org/10.1088/2516-1091/AB23DF

170. Kryou C, Leva V, Chatzipetrou M, *et al*., 2019, Bioprinting for liver transplantation. *Bioengineering*, 6: 95.

https://doi.org/10.3390/BIOENGINEERING6040095

171. Adhikari J, Roy A, Das A, *et al*., 2021, Effects of processing parameters of 3D bioprinting on the cellular activity of bioinks. *Macromol Biosci*, 21: 2000179.

https://doi.org/10.1002/MABI.202000179

172. Roussel N, Spangenberg J, Wallevik J, *et al*., 2020, Numerical simulations of concrete processing: From standard formative casting to additive manufacturing. *Cem Concr Res*, 135: 106075.

https://doi.org/10.1016/J.CEMCONRES.2020.106075

173. Valente M, Sibai A, Sambucci M, 2019, Extrusion-based additive manufacturing of concrete products: Revolutionizing and remodeling the construction industry. *J Compos Sci*, 3: 88.

https://doi.org/10.3390/JCS3030088

174. Du Plessis A, Babafemi AJ, Paul SC, *et al*., Biomimicry for 3D concrete printing: A review and perspective. *Addit Manuf*, 38: 101823.

https://doi.org/10.1016/J.ADDMA.2020.101823

175. Ahmed ZY, Bos FP, van Brunschot MC, *et al*., 2020,

On-demand additive manufacturing of functionally graded concrete. *Virtual Phys Prototyp*, 15: 194–210.

https://doi.org/10.1080/17452759.2019.1709009

176. van de Werken N, Tekinalp H, Khanbolouki P, *et al*., 2020, Additively manufactured carbon fiber-reinforced composites: State of the art and perspective. *Addit Manuf*, 31: 100962.

https://doi.org/10.1016/J.ADDMA.2019.100962

177. Li M, Pu Y, Thomas VM, *et al*., 2020, Recent advancements of plant-based natural fiber–reinforced composites and their applications. *Compos Part B Eng*, 200: 108254.

https://doi.org/10.1016/J.COMPOSITESB.2020.108254

178. Shanmugam V, Rajendran DJ, Babu K, *et al*., 2021, The mechanical testing and performance analysis of polymer-fibre composites prepared through the additive manufacturing. *Polym Test*, 93: 106925.

https://doi.org/10.1016/J.POLYMERTESTING.2020.106925

179. Ferreira I, Machado M, Alves F, *et al*., 2019, A review on fibre reinforced composite printing via FFF. *Rapid Prototyp J*, 25: 972–988.

https://doi.org/10.1108/RPJ-01-2019-0004/FULL/PDF

180. Ramesh M, Rajeshkumar L, Balaji D, 2021, Influence of process parameters on the properties of additively manufactured fiber-reinforced polymer composite Materials: A review. *J Mater Eng Perform*, 30: 4792–4807.

https://doi.org/10.1007/S11665-021-05832-Y/FIGURES/10

181. Goh GL, Zhang H, Chong TH, *et al*., 2021, 3D Printing of multilayered and multimaterial electronics: A review. *Adv Electron Mater*, 7: 2100445.

https://doi.org/10.1002/AELM.202100445

182. Mehrpouya M, Tuma D, Vaneker T, *et al*., 2022, Multimaterial powder bed fusion techniques. *Rapid Prototyp J*, 28: 1–19.

https://doi.org/10.1108/RPJ-01-2022-0014/FULL/PDF.

183. Rocha VG, Saiz E, Tirichenko IS, *et al*., 2020, Direct ink writing advances in multi-material structures for a sustainable future. *J Mater Chem A*, 8: 15646–15657.

https://doi.org/10.1039/D0TA04181E

184. Pajonk A, Prieto A, Blum U, *et al*., Multi-material additive manufacturing in architecture and construction: A review. *J Build Eng*, 45: 103603.

https://doi.org/10.1016/J.JOBE.2021.103603

185. García-Collado A, Blanco JM, Gupta MK, *et al*., 2022, Advances in polymers based multi-material additive-manufacturing techniques: State-of-art review on properties and applications. *Addit Manuf*, 50: 102577.

https://doi.org/10.1016/J.ADDMA.2021.102577

186. Peterson AM, 2019, Review of acrylonitrile butadiene styrene in fused filament fabrication: A plastics engineering-focused perspective. *Addit Manuf*, 27: 363–371.

https://doi.org/10.1016/J.ADDMA.2019.03.030

187. Chen X, Chen G, Wang G, *et al*., Recent progress on 3D-printed polylactic acid and its applications in bone repair. *Adv Eng Mater*, 22: 1901065.

https://doi.org/10.1002/ADEM.201901065.

188. Mehrpouya M, Vahabi H, Janbaz S, *et al*., 2021, 4D printing of shape memory polylactic acid (PLA). *Polymer* (*Guildf*), 230: 124080.

https://doi.org/10.1016/J.POLYMER.2021.124080

189. Cojocaru V, Frunzaverde V, Miclosina CO, *et al*., 2022, The influence of the process parameters on the mechanical properties of PLA specimens produced by fused filament fabrication— A review. *Polymers*, 14: 886.

https://doi.org/10.3390/POLYM14050886

190. El Magri A, Vanaei S, Vaudreuil S, 2021, An overview on the influence of process parameters through the characteristic of 3D-printed PEEK and PEI parts. *High Performance Polym*, 33: 862–880.

https://doi.org/10.1177/09540083211009961

191. Dua R, Rashad Z, Spears J, *et al*., Applications of 3D-printed PEEK via fused filament fabrication: A systematic review. *Polymers*, 13: 4046.

https://doi.org/10.3390/POLYM13224046

192. Ding Y, Muñiz-Lerma JA, Trask M, *et al*., 2016, Microstructure and mechanical property considerations in additive manufacturing of aluminum alloys. *MRS Bull*, 41: 745–751.

https://doi.org/10.1557/MRS.2016.214

193. Ponnusamy P, Rashid RA, Masood SH, *et al*., 2020, Mechanical properties of SLM-printed aluminium alloys: A review. *Materials*, 13: 4301.

https://doi.org/10.3390/MA13194301

194. Fiocchi J, Tuissi A, Biffi CA, 2021, Heat treatment of aluminium alloys produced by laser powder bed fusion: A review. *Mater Des*, 204: 109651.

https://doi.org/10.1016/J.MATDES.2021.109651

195. Thapliyal S, 2019, Challenges associated with the wire arc additive manufacturing (WAAM) of aluminum alloys. *Mater Res Express*, 6: 112006.

https://doi.org/10.1088/2053-1591/AB4DD4

196. Revilla RI, Verkens D, Rubben T, *et al*., 2020, Corrosion and corrosion protection of additively manufactured aluminium alloys-a critical review. *Materilas*, 13: 4804.

https://doi.org/10.3390/MA13214804

197. Jiang Q, Zhang P, Yu Z, *et al*., 2021, A review on additive manufacturing of pure copper. *Coatings*, 11: 740.

https://doi.org/10.3390/COATINGS11060740

198. Portanguen S, Tournayre P, Sicard J, *et al*., 2019, Toward the design of functional foods and biobased products by 3D printing: A review. *Trends Food Sci Technol*, 86: 188–198.

https://doi.org/10.1016/J.TIFS.2019.02.023

199. Wang M, Li D, Zang Z, *et al*., 2021, 3D food printing: Applications of plant-based materials in extrusion-based food printing. *Crit Rev Food Sci Nutr*, 6: 7184–7198.

https://doi.org/10.1080/10408398.2021.1911929

200. Li G, Hu L, Liu J, *et al*.,2022, A review on 3D printable food materials: Types and development trends. *Int J Food Sci Technol*, 57: 164–172.

https://doi.org/10.1111/IJFS.15391

201. Navaf M, Sunooj KV, Aaliya B, *et al*., 2022, 4D printing: A new approach for food printing; effect of various stimuli on 4D printed food properties. A comprehensive review. *Appl Food Res*, 2: 100150.

https://doi.org/10.1016/J.AFRES.2022.100150

202. Haleem A, Javaid M, Singh RP, *et al*., 2021, Significant roles of 4D printing using smart materials in the field of manufacturing. *Adv Ind Eng Polym Res*, 4: 301–311.

https://doi.org/10.1016/J.AIEPR.2021.05.001

203. Kwon JY, Park HE, Park YB, *et al*., 2017, Potentials of additive manufacturing with smart materials for chemical biomarkers in wearable applications. *Int J Precis Eng Manuf Technol*, 4: 335–347.

https://doi.org/10.1007/S40684-017-0039-5

204. Liu H, Jiang Q, Huo J, *et al*., 2020, Crystallization in additive manufacturing of metallic glasses: A review. *Addit Manuf*, 36: 101568.

https://doi.org/10.1016/J.ADDMA.2020.101568

205. Zhang H, Huang L, Tan M, *et al*., Overview of 3D-printed silica glass. *Micromachines*, 13: 81.

https://doi.org/10.3390/MI13010081

206. Das AK, Agar DA, Rudolfsson M, *et al*., 2021, A review on wood powders in 3D printing: Processes, properties and potential applications. *J Mater Res Technol*, 15: 241–255.

https://doi.org/10.1016/J.JMRT.2021.07.110

207. Wang C, Tan XP, Tor SB, *et al*., 2020, Machine learning in additive manufacturing: State-of-the-art and perspectives. *Addit Manuf*, 36: 101538.

https://doi.org/10.1016/J.ADDMA.2020.101538

208. Liu J, Gaynor AT, Chen S, *et al*., 2018, Current and future trends in topology optimization for additive manufacturing. *Struct Multidiscip Optim*, 57: 2457–2483.

https://doi.org/10.1007/s00158-018-1994-3

209. Ambrosi A, Pumera M, 2016, 3D-printing technologies for electrochemical applications. *Chem Soc Rev*, 45: 2740–2755.

https://doi.org/10.1039/C5CS00714C

210. Truby Rl, Lewis JA, 2016, Printing soft matter in three dimensions. *Nature*, 540: 371–378.

https://doi.org/10.1038/nature21003

211. Trenfield SJ, Awad A, Goyanes A, *et al*., 3D printing pharmaceuticals: Drug development to frontline care. *Trends Pharmacol Sci*, 39: 440–451.

https://doi.org/10.1016/J.TIPS.2018.02.006

212. Uriondo A, Esperon-Miguez M, Perinpanayagam S, 2022, The present and future of additive manufacturing in the aerospace sector: A review of important aspects. *Proceed Inst Mech Eng G J Aerospace Eng*, 229: 2132–2147.

https://doi.org/10.1177/0954410014568797

Author Guidelines

Before submitting for publication, please ensure that your paper and other supplementary files have been prepared and formatted in accordance with the guidelines below.

Submission structure, general style and format

Materials Science in Additive Manufacturing requests that every new submission should be made and accompanied by 3 separate core files, namely manuscript, title page and back matter, and cover letter, whereas resubmission of revision file should be accompanied by 4 separate core files, namely manuscript, title page and back matter, cover letter, and response/rebuttal letter (collectively known as the revision file). Provision of supplementary files and/or confidential accessory files is optional or dependent on the nature of study and findings relevance. The table below briefly summarizes the type of files in a submission, their respective requirements and included items:

Type of file	File format	Requirements	Included items
(1) Manuscript	DOC or DOCX	- Use 1.5-spacing and format text in one column - Use page numbers and continuous line numbers - Font and size: Times New Roman, 12 - Insert tables and figures at the back of manuscript	- Manuscript title - Abstract (for original research article, review article and perspective article) - Keywords - Text - References - Tables (including caption and legend) - Figures (including caption and legend)
(2) Title page and back matter *	DOC or DOCX	- Use 1.5-spacing and format text in one column - Font and size: Times New Roman, 12	**<u>On the first page (title page):</u>** - Manuscript title - Authorship list (first and last names must be spelled out) - Author's affiliation, including department, institution, city, state, postal code, and country (indicated with superscript number) - Corresponding author information, including asterisk indication, mailing address and email - Indication of equally contributing authors (if any) with dagger symbol **<u>On the second page (back matter):</u>** - Acknowledgments - Funding - Conflict of interest (mandatory) - Author contributions (formatted as per CRediT) - Further disclosure about presentation of essential findings in conference(s) and/or upload of the paper to a preprint server
(3) Cover letter	DOC or DOCX	- Use 1.5-spacing and format text in one column - Font and size: Times New Roman, 12	- A brief explanation of what was previously known, the conceptual advancement with the findings and its significance to broad readership - A statement that "neither the manuscript nor any significant part of it is under consideration for publication elsewhere or has appeared elsewhere in a manner that could be construed as a prior or duplication of the same work" with author confirmation - If any, associated accession numbers or DOIs of the corresponding preprint version of the submission - [Optional] Name, affiliation and email address of up to 4 academically qualified (recommended) reviewers and/or name and affiliation of individuals who should be excluded from reviewing the submitted works on the grounds of conflict of interest
(4) Supplementary files		- Supplementary files should **not exceed 20 MB** in total (15MB individual file limit)	

- Supplementary tables or figures	DOC or DOCX	- Use 1.5-spacing and format text in one column - Use page numbers and continuous line numbers - Font and size: Times New Roman, 12 - Include both supplementary tables (editable) and figures (in JPEG, PNG or TIFF format) in the same file	- Supplementary tables - Supplementary figures
- Data set	XLS or XLSX	- All data should be neatly presented using consistent fonts	
- Videos	MP4	- If necessary, trim the video clip to focus only on essential parts, such as experimental procedures and findings or observation that can only be demonstrated using video(s) - Avoid unnecessary narrations that can be presented in written form	
(5) Confidential accessory files			
- Sample consent form (for human research only)	DOC, DOCX, PDF, JPEG, PNG or TIFF	- This is a sample, unsigned consent form that should bear the institution letterhead	
- Research ethics proof (for human and/or animal research only)	DOC, DOCX, PDF, JPEG, PNG or TIFF	- Ideally, this document should contain the essential research ethics information, such as ethics approval identifiers and the name of Institutional Ethics Review Board or Institutional Review Board - The research described in **original research article** should match the proposed research or significantly fit within the framework of the specification stipulated in the research ethics proof	
(6) Response/rebuttal letter (only applicable to revisions)	DOC or DOCX	- All comments/feedback and responses/rebuttals must be clearly and concisely presented	- Reviewers' comments and feedback - Authors' responses

[#] Ideally, all information given in the title page and back matter file, except for the manuscript title, should remain the same from the point of submission to paper acceptance. Thus, authors are responsible to ensure that all information therein is accurate before making submission. Refer to **Authorship and Author Information** for more information about *Materials Science in Additive Manufacturing*'s authorship policy.

Submitting authors should refer to the relevant sections in the following for more detailed information.

Author metadata during submission

During the submission process, the submitting author must ensure that all particulars of author information, including full name, affiliation, and email address, are given in the author metadata column of the submission system. These particulars must exactly reflect those on the title page of the submission; this includes the author order of the authorship list. Provide authors' ORCID ID, if available.

Article types

(1) Original research article

An original research article is based on original, basic and applied research and/or analysis. This type of article aims to describe significant and novel research. Authors of original research articles must confirm that the essential findings presented have never been published or under consideration elsewhere.

This article type typically has at least 5 tables and/or figures in total, approximately 40 references, and 7,000 words (inclusive of Abstract and References).

(2) Review article

A review article provides scholarly survey as well as balanced summarization and highlights of recent developments in a research field or emerging/future trends. Authors should ensure that all perspectives from different works are linked in balanced and cohesive manner, taking into consideration different schools of thought.

This article type typically has at least 5 tables and/or figures in total, approximately 70 references, and 7,000 words (inclusive of Abstract and References).

(3) Perspective article

A perspective article contains the author's scholarly opinions on a particular subject area or topic. Unlike a review, a perspective article covers a more specific part of the field, aiming to provide new insights into the subject matter. However, these perspectives or opinions should be objective in line with the spirit of academia. A good perspective piece should stimulate further discussions and initiate novel experiments.

This article type typically has 5 tables and/or figures in total, approximately 70 references, and 7,000 words (inclusive of Abstract and References).

(4) Letters

This article type is a collection of unsolicited letters from the readers who wish to comment on specific articles published in *Materials Science in Additive Manufacturing* or another field-related journal. Alternatively, a letter can be written on an unrelated topic of interest to the journal's readership.

Ideally, a letter should present an in-depth, scholarly re-analysis of a previously published article in *Materials Science in Additive Manufacturing* or in another field-related journal, accompanied by the reader's constructive insights and comments. Letters containing new ideas, supporting data or data criticizing the indicated article may be subjected to peer review at editors' discretion. Authors should specify the intended recipient of the letters, i.e., Editor or specific author(s).

This article type typically has no more than 3 tables and/or figures in total, no more than 20 references, and 2,000 words (inclusive of References). No Abstract is required.

(5) Editorial

An editorial piece is a solicited, concise commentary that highlights prominent topics in particular issue. Alternatively, an editorial represents the official opinions of the editors on the journal or special issue.

An editorial piece should not exceed 1,000 words (inclusive of References). Typically, an Abstract is not required and only 1 figure or table is allowed.

(6) Erratum

Authors should contact the editors of *Materials Science in Additive Manufacturing* (editor.msam@whioce.com) if certain errors made by the journal are found. The editors will evaluate the impact of the errors and decide on the appropriate course of action. Any corrections to a paper are published at the sole discretion of the editors.

(7) Corrigendum

Authors should contact the editors of *Materials Science in Additive Manufacturing* (editor.msam@whioce.com) if certain errors made by the authors are found. The editors will evaluate the impact of the errors and decide on the appropriate course of action. Any corrections to a paper are published at the sole discretion of the editors.

Language

All submissions must be written entirely in good American English. Spelling and use of punctuations should conform to conventions in American English. Clarity and conciseness are critical requirements for publications; therefore, submissions that are not clearly written will be returned to authors. Authors must ensure that their manuscripts are submit-ready or publish-ready before making submission. The articles published in *Materials Science in Additive Manufacturing* are in adherence with the publishable standards of academic and scientific writing.

Please note that utilizing a language editing service is not a guarantee of acceptance.

Letter capitalization

Use sentence case capitalization in all aspects of the submission. In sentence case, most major and minor words are lowercase (proper nouns, including name of organizations and name of guidelines, are an exception in that they are always capitalized for the first letter of each word, except for minor words, such as conjunctions and short prepositions). The first letter of the first word should always be uppercase.

Manuscript title

The title should capture the conceptual significance for a broad audience. The title should not be more than 50 words and should be able to give readers an overall view of the paper's significance. Titles should avoid using uncommon jargons, abbreviations and punctuation.

Abstract

The purpose of abstract is to provide sufficient information and capture essential findings and/or messages of the paper. The length of an abstract should be in the range of 200-400 words. The abstract should be **unstructured**. Abstract is only needed in original research article, review article, and perspective article.

Keywords

Each submission should be accompanied by 3-6 keywords. Avoid using abbreviations and acronyms in keywords, unless they are established standard keywords. Separate keywords with semi-colons (i.e, term1; term2; term3).

Abbreviations and acronyms

Define abbreviations and acronyms upon their first appearance, **separately**, in the abstract, main text, table legends, and figure captions and legends.

Sections in article

(1) Section headings

Section headings should be in boldface. Examples of section headings of different levels are shown in the following:

Primary level : **1. Heart disease**

Secondary level : **1.3. Risk factors for heart disease**

Tertiary level : **1.3.2. Hypertension**

Authors are suggested **NOT** to introduce further sub-sections after the tertiary level section (e.g., **1.3.2.1. High-salt diet**).

(2) Special sectioning requirements for an original research article

- **Introduction.** The introduction should provide a background that gives a broad readership an overall outlook of the field and the research performed. It tackles a problem and states its important regarding with the significance of the study. Introduction can conclude with a brief statement of the aim of the work and a comment about whether that aim was achieved.

- **Materials and Methods.** This section provides the general experimental design and methodologies used. The aim is to provide enough detail to for other investigators to fully replicate the results. It is also required to facilitate better understanding of the results obtained. Protocols and procedures for new methods must be included in detail for the reproducibility of the experiments. Informed consent should be obtained from patients or parents before the experiments start and should be mentioned in this section. For human and/or research, research ethics information, such as ethics approval identifiers and the name of Institutional Ethics Review Board or Institutional Review Board, should be indicated in this section.

- **Results.** This section focuses on the results and findings of the experiments performed. After (statistical) analysis, all results, including tables and figures, must be neatly presented. If necessary, this section can be sub-divided into multiple topical sub-sections.

- **Discussion.** This section should provide the significance of the results and identify the impact of the research in a broader context. It should not be redundant or similar to the content of the results section.

- **Conclusion.** Use this section for interpretation only, and not to summarize information already presented in the text or abstract.

It is acceptable to merge both Results and Discussion as a single section.

Unit of measurements

Use SI units.

Data and image processing

Post-acquisition processing of images, photos and figures should be kept minimum to ensure that the final figures accurately reflect the original data as it was captured and/or produced. Any alterations should be applied to the entire image. Any kind of alteration, including but not limited to brightness, contrast and color balance, has to be clearly stated in the figure legend and in Materials and Methods section. For simulated or model figures, the software used for production, editing, and/or processing should be mentioned. Presenting images in the same figure must be made apparent and should be explicitly indicated in the appropriate figure legends.

Data comparisons should only be made from comparative experiments (or data from the same experiment). Same piece of data or figure should not be used in multiple instances, unless the images/data describe different aspects of the same experiment (reasons must be stated, wherever appropriate, in this regard). If inappropriate image/data manipulation is identified after publication, the editors reserve the right to ask for the original data and, if that is not satisfactory, to issue a correction or retract the paper, as appropriate.

Chemical compounds

Materials Science in Additive Manufacturing requires authors to fulfill the requirements below while reporting and/or describing a chemical compound in articles:

Scenario	Requirements
Naming chemical compounds	Use either IUPAC conventions or common names such as cholesterol and cephalosporins
Reporting a new chemical compound	Provide the exact structure of the compound as well as sufficient data regarding the purity and identity of the compound
Reporting the use of a known chemical compound	Provide sufficient data regarding the source, purity and identity of the compound

Figures

Include all figures, including photographs, scanned images, graphs, charts and schematic diagrams, at the back of manuscript. Avoid unnecessary decorative effects (e.g., 3D graphs) and minimize image processing (e.g., changes in brightness and contrast applied uniformly for the entire figure should be avoided or minimized). All images should be set against white background.

All figures should be numbered (e.g., **Figure 1**, **Figure 2**) in boldface. Label all figures (e.g., axis, structures), and add caption (a brief title) and legend as a description of the illustration below each figure. Explain all symbols and abbreviations used. Each figure should have a brief title (also known as caption) that describes the entire figure without citing specific panels, followed by a legend, which is either the description of each panel or further description about the single image. Identify each panel with uppercase letters in parenthesis (e.g. (A), (B), (C), etc.) Figures must be cited in chronological manner in the text.

The preferred file formats for any separately submitted figure(s) are JPEG, PNG and TIFF. All figures should be of optimal resolution. Optimal resolutions preferred are 300 dots per inch (dpi) for RBG colored, 600 dpi for grayscale and 1,200 dpi for line art. Although there is no file-size limitation imposed, authors are highly encouraged to compress their figures to an ideal size without unduly affecting the legibility and resolution of figures.

If necessary, the editors may request author(s) to supply high-resolution and/or unprocessed images after submission or paper acceptance for pre-screening/review and production purposes, respectively.

Tables

Include all tables at the back of manuscript. Editable tables created using Microsoft Word are preferred. A table should be accompanied by a caption on top of it. Captions and legends should be concise. All tables should be numbered (e.g. **Table 1**, **Table 2**) in boldface. Explain all symbols and abbreviations used. Tables must be cited in chronological manner in the text.

Lists and math formulae

Lists and math formulae should be properly aligned and included within the main body of the manuscript. List them using Roman numerals in parenthesis (e.g. (I), (II), (III), (IV), etc.) Lists and math formulae must be cited in chronological manner in the text.

Lists and math formulae should be given in editable text and not as images. Use the solidus (/) for small fractional terms, e.g., X/Y. In principle, variables should be italicized. Powers of e are often more conveniently denoted by exp.

Footnotes

Do not use footnotes.

In-text citations

Reference citations in the text should be numbered consecutively in superscript square brackets. Some examples:

- Negotiation research spans many disciplines[3,4].
- This result was later contradicted by Becker and Seligman[5].
- This effect has been widely studied[1–3,7].

Do not include citations in the Abstract.

Personal communications and unpublished works can only be used in the manuscript and are not to be placed in the References section. Authors are advised to limit such usage to the minimum. These should be made identifiable by stating the authors, year of personal communications or unpublished works, and the words “personal communication” or “unpublished” in parenthesis, e.g., (Smith J, 2000, unpublished).

References

This section is compulsory and should be placed at the end of all manuscripts. Do not use footnotes or endnotes as a substitute for a reference list. The list of references should only include works that are cited in the text and that have been published or accepted for publication. Personal communications and unpublished works should be excluded from this section.

Authors being referenced are listed with their surname or last name followed by their initials. All references should be numbered (e.g. 1, 2, 3, and so on) and sequenced according to the order they appear as the in-text citations. References (especially journal article’s) should follow the general pattern: author(s), followed by year of publication, title of publication, abbreviated journal name in italics, volume number, issue number in parenthesis and lastly, page range or article ID. If the referred article has more than 3 authors, list only the first 3 authors and abbreviate the remaining authors as italicized “*et al*.” (meaning "and others"). Use of DOI is highly encouraged; include DOI, if available, after the page range or article ID. Examples of references for different types of publications are as follows:

(1) Journals

Journal article (print) with 1-3 authors:

Younger P, 2004, Using the internet to conduct a literature search. *Nurs Stand*, 19(6): 45–51.

Journal article (print) with more than 3 authors:

Gamelin FX, Baquet G, Berthoin S, *et al*., 2009, Effect of high intensity intermittent training on heart rate variability in prepubescent children. *Eur J Appl Physiol,* 105(1): 731–738.

Journal article (online) with 1-3 authors:

Jackson D, Firtko A, Edenborough M, 2007, Personal resilience as a strategy for surviving and thriving in the face of workplace adversity: A literature review. *J Adv Nurs*, 60(1): 1–9. http://doi.org/10.1111/j.1365-2648.2007.04412.x

Journal article (online) with more than 3 authors:

Hargreave M, Jensen A, Nielsen TSS, *et al*., 2015, Maternal use of fertility drugs and risk of cancer in children — A nationwide population-based cohort study in Denmark. *Int J Cancer*, 136(8): 1931–1939. http://doi.org/10.1002/ijc.29235

(2) Books

Book with 1-3 authors:

Schneider Z, Whitehead D, Elliott D, 2007, *Nursing and Midwifery Research: Methods and Appraisal for Evidence-based Practice*, 3rd edn, Elsevier Australia, Marrickville, NSW, 112–130.

Book with more than 3 authors

Davis M, Charles L, Curry MJ, *et al*., 2003, *Challenging Spatial Norms*, Routledge, London, 12–30.

Chapter or article in book

Knowles MS, (eds) 1986, Independent study, in *Using Learning Contracts*, Jossey-Bass, San Francisco, 89–96.

(3) Preprints

Preprint article with 1-3 authors:

Ulgen A, Gurkut O, Li W, 2019, Potential Predictive Factors for Breast Cancer Subtypes from a North Cyprus Cohort Analysis. *medRxiv*. https://doi.org/10.1101/19010181

Preprint article with more than 3 authors:

Wu S, Sun P, Li R, *et al*., 2020, Epidemiological Development of Novel Coronavirus Pneumonia in China and Its Forecast. *medRxiv*. https://doi.org/10.1101/2020.02.21.20026229

(4) Others

Proceedings of meetings and symposiums, conference papers:

Chang SS, Liaw L, Ruppenhofer J, (eds) 2000, *Proceedings of the twenty-fifth annual meeting of the Berkeley Linguistics Society, February 12–15, 1999: General session and parasession on loan word phenomena*. Berkeley Linguistics Society, Berkeley, 12–13.

Conference proceedings (from electronic database):

Wang T, Cook C, Derby B, 2009, Fabrication of a glucose biosensor by piezoelectric inkjet printing. *Proceedings of the Third International Conference on Sensor Technologies and Applications, 2009 (SENSORCOM-M'09)*, 82–85.

Online document with author names:

Este J, Warren C, Connor L, *et al*., 2008, Life in the clickstream: The future of journalism, Media Entertainment and Arts Alliance, viewed May 27, 2009, http://www.alliance.org.au/documents/ foj_report_final.pdf

Online document without author name:

Developing an argument, n.d., viewed March 30, 2009, http://web.princeton.edu/sites/writing/Writing_Center/WCWritingResources.htm

Thesis/Dissertation:

Gale L, 2000, The relationship between leadership and employee empowerment for successful total quality management, thesis, *Australasian Digital Thesis database*, University of Western Sydney, 110–130.

Standards:

Standards Australia Online, 2006, Glass in buildings: selection and installation, AS 1288-2006, amended January 31, 2008, *SAI Global database*, viewed May 19, 2009.

Government report:

National Commission of Audit, 1996, *Report to the Commonwealth Government*, Australian Government Publishing Service, Canberra.

Government report (online):

Department of Health and Ageing, 2008, Ageing and aged care in Australia, viewed November 10, 2008, http://www.health.gov.au/internet/main/publishing.nsf/Content/ageing

No author:

Guide to agricultural meteorological practices, 1981, 2nd ed, Secretariat of the World Meteorological Organization, Geneva, 10–20.

Note: When referencing an entry from a dictionary or an encyclopedia with no author there is no requirement to include the source in the reference list. In these cases, only cite the title and year of the source in-text. For an authored dictionary/encyclopedia, treat the source as an authored book.

Acknowledgments*

*This should be included in the title page and back matter file

This is an optional section where authors can acknowledge people and/or institutions that provided non-financial support and/or helped with the research and/or preparation of the manuscript. Examples of non-financial support include externally-supplied equipment/biological sources, writing assistance, administrative support, and contributions from non-authors.

Funding*

*This should be included in the title page and back matter file

Authors should declare all financial support and sources that were used to perform the research, analysis, and/or article publication. Financial supports are generally in the form of grants, royalties, consulting fees and others.

Conflict of interest*

*This should be included in the title page and back matter file

At the time of submission, authors must declare any (potential) conflicts or competing interests with any institutes, organizations or agencies that might influence the integrity of results or objective interpretation of their submitted works. For more information, see our **Conflict of Interest** policy.

Author contributions*

*This should be included in the title page and back matter file

This section should be included in original research articles and review articles. In *Materials Science in Additive Manufacturing*, we encourage authors to use **Contributor Roles Taxonomy (CRediT)** in describing each contributor's specific contribution to the scholarly output in the Author Contributions section.

Definitions of each contributor role as per CRediT are as follows:

Contributor role	Definition
Conceptualization	Ideas; formulation or evolution of overarching research goals and aims.
Data curation	Management activities to annotate (produce metadata), scrub data and maintain research data (including software code, where it is necessary for interpreting the data itself) for initial use and later re-use.
Formal analysis	Application of statistical, mathematical, computational, or other formal techniques to analyze or synthesize study data.
Funding acquisition	Acquisition of the financial support for the project leading to this publication.
Investigation	Conducting a research and investigation process, specifically performing the experiments, or data/evidence collection.
Methodology	Development or design of methodology; creation of models.
Project administration	Management and coordination responsibility for the research activity planning and execution.
Resources	Provision of study materials, reagents, materials, patients, laboratory samples, animals, instrumentation, computing resources, or other analysis tools.
Software	Programming, software development; designing computer programs; implementation of the computer code and supporting algorithms; testing of existing code components.
Supervision	Oversight and leadership responsibility for the research activity planning and execution, including mentorship external to the core team.
Validation	Verification, whether as a part of the activity or separate, of the overall replication/reproducibility of results/experiments and other research outputs.
Visualization	Preparation, creation and/or presentation of the published work, specifically visualization/data presentation.
Writing – original draft	Preparation, creation and/or presentation of the published work, specifically writing the initial draft (including substantive translation).
Writing – review & editing	Preparation, creation and/or presentation of the published work by those from the original research group, specifically critical review, commentary or revision – including pre- or post-publication stages.

Below shows a sample Author Contributions section written based on the CRediT:

Conceptualization: Ali Jackson, Helen Meyer
Investigation: Ali Jackson, Tom Lewis-Hans, Han Xiang
Formal analysis: Han Xiang
Writing – original draft: Ali Jackson
Writing – review & editing: Helen Meyer, Joshua O'Brien

Supplementary files

This section is optional and contains all materials and figures that are excluded from the manuscript. These materials, figures or additional information are relevant to the manuscript but remain non-essential to readers' understanding of the manuscript's main content. All supplementary information should be submitted as a separate file during submission.

Supplementary figures and tables should be submitted in a single, separate supplementary file, and must be numbered, for example, **Figure S1** and **Table S1**. All tables must be editable (preferably created from Microsoft Word). The acceptable formats of images and illustrations used in figures are JPEG, PNG and TIFF. Citations of these items must be appropriately referenced in the manuscript in chronological manner,

for instance, “Additional information can be found in **Table S1**.” Note the additional letter **S** helps distinguish the normal from supplementary items.

Data set file are usually prepared using Microsoft Excel (in XLS or XLSX format).

Videos (MP4 format), with a constituent maximum size of 15 MB, can be uploaded as part of the supplementary file.

Revision and response/rebuttal letter

If the editorial decision for a submission is major revision or minor revision, authors are advised to revise the manuscript (and possibly, the supplementary files) as per the review reports and resubmit the revision file, including the manuscript, title page and back matter, cover letter, and response/rebuttal letter, before the due date.

Revisions should be done on the latest version of the manuscript (or in some rare cases, edited manuscript provided by the editor) with the track change on. The revisions made should be described and/or clarified in the response/rebuttal letter; ideally, explanation about the revisions should be made clear with the help of page number and line number. If authors do not agree with reviewers’ comments and suggestions, rebut their points with strong evidence and reasonable arguments.

Materials Science in Additive Manufacturing

Special Issue Alerts

Invitation for Special Issue Proposals

Organizing and editing for a Special Issue helps Guest Editors gain editorial experience and improve academic profile, in addition to being a part of organizing scientific communication of contemporary topics.

If you are published researcher and have an idea for a Special Issue, please write in via email to our Special Issue Commissioning Editor (felicia_wang@whioce.com). Please provide your CV, professional profile page and a topic of interest in your email. Our colleague will guide you in the process of writing a Special Issue proposal.

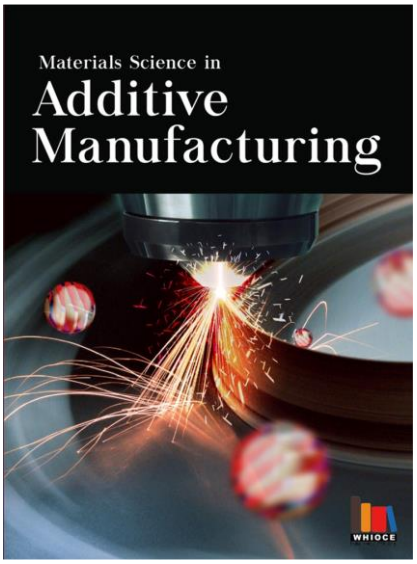

Frequently Asked Questions

1. **Are Special Issue submissions processed in the same way how Regular Issue papers are being pre-screened and reviewed?**
   Yes, all full-length article submissions to a Special Issue will go through the same editorial and peer-review process. The distinct difference here is that the Guest Editors will replace the usual editors and get involved in the making professional decisions on papers after peer review. Note that the specific roles of a Guest Editor could vary across Special Issues.

2. **How many Guest Editors are required to organize a Special Issue?**
   There is no fixed number; however, we suggest no more than 4 Guest Editors per Special Issue. More importantly, all Guest Editors should have excellent publication track records and demonstrated expertise in the topic(s) being proposed.

3. **Is the Special Issue governed by important deadlines?**
   Yes.

Benefits of Being A Guest Editor

- A chance to get involved in the conception and development of a specialty, contemporary topic that is of interest to the readers
- A chance to expand your professional network to the scholars and researchers who are similarly involved in the research of specialty topic
- A chance to hone your editorial skills
- A chance to gain first-hand experience of editing a thematic issue publication, which is a very valuable experience for those who aspire to edit their own journal in future
- A chance to improve your academic profile and help establish your academic influence within your discipline

OUR JOURNALS

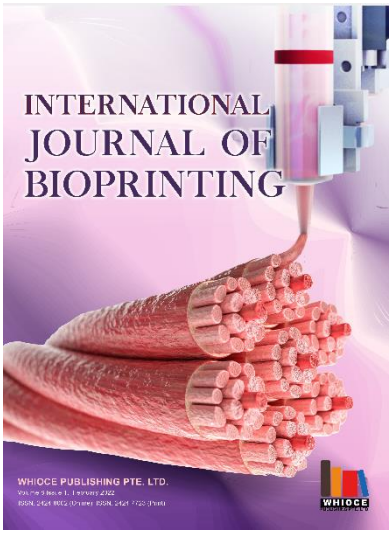

International Journal of Bioprinting is an international journal covering the technology, science and clinical application of the broadly defined field of bioprinting. Bioprinting is defined as the use of 3D printing technology with materials that incorporate viable living cells or biological elements to produce tissue or biotechnological products.

We are interested in the scientific topics spanning all stages of bioprinting process from concept creation to fabrication and beyond. Knowledge generated in these researches must be related to bioprinting.

The journal publishes original research articles on basic and applied research as well as associated social implications of this research. The journal also publishes brief commentaries and reviews. Articles focusing on the practical applications of 3D-printed products are similarly welcome.

The *Journal of Clinical and Translational Research* is an open access, peer-reviewed, multidisciplinary scientific journal that publishes studies with at least an ex vivo, in vivo, or clinical component. The published research is centered on any clearly defined clinical problem, which may comprise a disease or the basis of disease, a form of therapy or intervention, and clinical diagnostics or prognostics. Articles (original research, reviews, technical reports, medical hypotheses, commissioned articles, special issue articles, and editorials) are published continuously online. The key features of this journal are:

- Open access
- No submission or publication fees
- Reputable international editorial board
- Easy and fast submissions - no formatting rules ("your paper, your way")
- No word count or reference restrictions
- Double blind review process to minimize bias
- Rapid online publication of articles upon acceptance
- Outlet for academic institutions and industry

Start a new journal

Write to us via email if you are interested to start a new journal with Whioce Publishing. Please attach your CV, professional profile page and a brief pitch proposal in your email. We shall inform you of our decision whether we are interested to collaborate in starting a new journal.

Contact: info@whioce.com

Whioce Publishing Pte. Ltd.
Publishing Office:
8 Burn Road, #15-03 Trivex, Singapore 369977.

Editorial Office:
30-2, Jalan BS 1/2, Olive Hill Business Park, 43300 Seri Kembangan, Selangor. Malaysia.

msam.editor@whioce.com

https://msam.whioce.com/index.php/MSAM/index